Author:
Eales, Marcus G

Title:
Modulation of Bacteria and Stem Cells via Nanotopography and Antimicrobial Peptides

Author:
Eales, Marcus G

Title:
Modulation of Bacteria and Stem Cells via Nanotopography and Antimicrobial Peptides

Modulation of Bacteria and Stem cells on Titanium Surfaces via Nanotopography and Antimicrobial Peptides

by

Marcus G. Eales

A dissertation submitted to the University of Bristol in accordance with the requirements for award of the degree of

Doctor of Philosophy

Faculty of Health Sciences and Bristol Dental School

September 2019

Word Count: 52,402

To Mum and Dad.

To Tim and Jonny.

To Pippin.

Abstract

Titanium dental and orthopaedic implants are an essential component of modern healthcare with their use increasing rapidly over the last few decades. Bacterial infection is one of the most common causes of premature implant failure, and the subsequent revision surgery has serious ramifications for the patient, places financial burdens on healthcare systems and, with rising bacterial resistance, the infections are becoming more difficult to treat.

The aim of this project was to grow antibacterial nanotopographies on titanium and to then further enhance their properties by interfacial functionalisation with an antimicrobial peptide. A range of nanotopographies were formed on titanium using the alkaline hydrothermal method, and their physical properties characterised using a range of analytical techniques, including SEM, AFM, CLSM and OP. After 2-hours growth, distinct nanospikes had formed. These increased in height over time, eventually bending and intertwining to form a 'pocket' nanotopography after 4 hours. The crystal structures of the nanotopographies were confirmed to be titanium dioxide using XRD, EDX and XPS.

There is no single optimal quantitative viability technique for assessing nanotopographic surfaces. Consequently, a combination of viability assays and high-resolution imaging were employed. It was found that some of the nanotopographies exhibited anti-biofouling properties and impaired the growth of both Gram-negative and Gram-positive bacteria. Nanotopographies caused indentations in the bacterial cell membrane at points of contact, but there was limited evidence of puncturing of the bacterial cell envelope.

Synthetic antimicrobial peptide, ChoM, was functionalised onto flat and 2-hour nanospike surfaces by physical adsorption and could be released into the local environment in a dose-dependent manner to inhibit bacterial growth. Nanotopography was found to affect the peptide release kinetics relative to flat titanium, due, in part, to differences in hydrophilicity. Alongside effects on bacteria, stem cell studies showed nanotopography to be highly biocompatible which was unaffected by the functionalisation of ChoM.

This research highlights the potential to generate a synergistic antibacterial titanium surface comprising both physical and chemical mechanisms of action. Such an approach could be exploited to develop a next-generation implant surface to combat implant infections, and thus maximise the longevity of medical implants and improve the wellbeing of millions of patients worldwide.

Author’s Declaration

I declare that the work in this dissertation was carried out in accordance with the requirements of the University's Regulations and Code of Practice for Research Degree Programmes and that it has not been submitted for any other academic award. Except where indicated by specific reference in the text, the work is the candidate's own work. Work done in collaboration with, or with the assistance of, others, is indicated as such. Any views expressed in the dissertation are those of the author.

Signed: 

Date: 09/03/2020

Acknowledgements

The most exciting and privileged aspect of this multidisciplinary PhD was the opportunity to learn from many talented and inspiring people from diverse backgrounds and expertise.

First and foremost, I would like to thank to my supervisors Professor Bo Su and Dr Angela Nobbs for their continued guidance and support throughout this project. I am especially grateful for the opportunities they encouraged me to partake in including research placements, outreach events and conferences which have enriched and broadened my experience during this PhD.

I would like to thank Dr Wuge Briscoe and Dr Patryk Wasik in the department of Chemistry, University of Bristol for their organisation and involvement in XRD sample analysis on the European Synchrotron Radiation Facility (ESRF). Further gratitude to Dr Briscoe for organising a one-week research placement trip to KTH, Stockholm, Sweden for lateral friction force measurements with the help of Dr Illia Dobryden. Thanks also goes to Dr Rob Haniman for his assistance with AFM.

Immense gratitude goes to all members of the Oral Microbiology Group and the Biomaterials Engineering Research Group past and present who have always assisted, advised and inspired my work during group meetings, presentations and in the laboratory.

Gratitude goes to Dr Max Ryadnov at the National Physical Laboratory (NPL) who gave me the privileged opportunity of an industrial placement and was always available for advice. Thank you to the Biometrology group at NPL who made me feel very welcome and especially to Dr Brunello Nardone and Dr Smita Gunoo with their help making the peptides.

I would also like to thank Professor Matt Dalby and Laila Damiati at the University of Glasgow for their expertise in stem cell biology and carrying out experiments on my samples. Also, for Dr Thomas Keller, Dr Noei Heshmat and Dr Satish Kumar at DESY, Hamburg, Germany for their assistance with XPS and Focus-Ion Beam experiments and analysis.

I will be forever grateful and indebted to Dr Josh Jenkins and Dr Irill Ishak who always provided daily discussion, support and laughter. Both of you have made an immeasurable impact on this project and me. It is no understatement that I could not have done this without you, and I truly hope friendship will continue long into the future.

And finally, to my family and friends, who have been with me every single step of this journey and giving me unequivocal love and encouragement which I know can always be relied on.

Publications and Conferences

Publications

Publications

Damiati, L., **Eales, MG**., Nobbs, AH., Su, B., Tsimbouri, PM., Salmeron-Sanchez, M and Dalby, MJ. (2018) Impact of surface topography and coating on osteogenesis and bacterial attachment on titanium implants. *Journal of Tissue Engineering*, 9, p.1-16. Available at: https://journals.sagepub.com/doi/pdf/10.1177/2041731418790694.

Conferences, Presentations and Prizes

1. 9th May 2017- Oral Presentation at Euro bioMAT 2017, Weimar, Germany.
2. 21st June 2017- Poster Presentation at Infection and Immunity Early Career Researcher Event, University of Bristol, UK. (Best Poster Award).
3. 29th June 2017- Poster Presentation at Colloid Group PhD Day, University of Bristol, UK. (Best Year 2 Poster Award).
4. 15th August 2017- Poster Presentation at Faculty of Health Sciences Away Day, University of Bristol Students Union, UK.
5. 22nd August 2017- Poster Presentation at INASCON 2017, University of Bristol, Bristol, UK.
6. 28-29th June 2018- Poster Presentation at UKSB 2018, University of Bath, Bath, UK.
7. 1st-2nd October 2018- Oral Presentation at 7th Thesinge Biofilm Meeting, Thesinge, Netherlands.
8. Buehler 2020 Microstructure Calendar Image Competition.

'Gentlemen, it is the microbes who will have the last word.'

Louis Pasteur (1822-1895)

Table of Contents

Table of Figures

Table of Tables

1.

INTRODUCTION

Titanium dental and orthopaedic implants are an essential component of modern medical treatment. Dental implants are often used to treat missing teeth as a result of trauma or periodontal disease, while orthopaedic implants are used to replace joints such as the hip and knee as treatment for chronic diseases such as osteoarthritis. The usage of these implants is increasing rapidly due to ageing populations and rising obesity levels. Bacterial infection is one of the most common causes of premature implant failure. The subsequent revision surgery has serious ramifications for the patient, places burdens on the healthcare infrastructure and, with biofilm formation and increasing bacterial resistance, the infections are becoming more difficult to treat.

The aim of this project was to grow antibacterial nanotopographies on titanium and to further enhance their properties by functionalisation with an AMP, with the ultimate goal of developing a next generation implant surface to prevent bacterial infection of dental and orthopaedic implants. A range of nanotopographies were formed using the alkaline hydrothermal method and their physical properties characterised using a range of analytical techniques including SEM, AFM, CLSM and OP. The chemical and crystal structures of the nanotopographies were investigated using TEM, EDX and XPS. The antimicrobial properties of the different nanotopographical surfaces with Gram-positive and -negative bacteria were investigated using microscopy (SEM and FIM) and a range of analytical assays such as BacTiter-Glo and RealTime-Glo.

Despite previous research into modifying the surface of titanium to inhibit bacterial infection, there has been little work to date on the efficacy of AMPs functionalised on a nanotopographical surface and their capacity to have a synergistic effect on the surface antimicrobial properties. In this project, the titanium surface was functionalised with synthetic AMP, ChoM, by physical adsorption, which was released over time to inhibit bacterial growth. Preliminary experiments also assessed the biocompatibility and osteogenic potential of the AMP-functionalised nanotopography.

1.1.1 Thesis Outline

This thesis is divided into the following chapters:

- **Chapter 2 – Literature Review**: A literature review highlighting the context and importance of the research and discussing the variety of surface modification techniques currently being researched including the status of nanotopographical investigation and the application of antimicrobial peptides.

- **Chapter 3 – Experimental Methodology and Analysis Techniques**: Describes the methodology of the experiments and equipment used in this project in sufficient detail in order that results may be replicated.

- **Chapter 4 – Formation and Characterisation of Nanotopography**: Examines the formation of nanotopography on pure titanium surfaces and their physical, crystal and mechanical characterisation.

- **Chapter 5 – Bacterial Interaction with Nanotopography**: Reports on experimental work in optimising viability techniques and then assessing the viability of different bacteria on the created nanotopography.

- **Chapter 6 – Functionalisation of Nanotopography with Antimicrobial Peptide**: Reports on the synthesis of the antimicrobial peptide, ChoM, its functionalisation onto nanotopography and the assessment of its interface release and activity on Gram-negative and Gram-positive bacteria. This chapter also includes a preliminary investigation into the interaction and viability of human mesenchymal stem cells on antimicrobial peptide functionalised nanotopographical surfaces and the potential of the stimulation of osteogenic differentiation.

- **Chapter 7 – Conclusions and Recommended Future Work**: A summary of each research activity is provided together with recommendations for future work based on the conclusions presented in this thesis.

- **Chapter 8 – References**.

- **Chapter 9– Appendices**.

2.

LITERATURE REVIEW

Contents

2.1 Orthopaedic and Dental Implants

Since the early 19th century, synthetic implants have been an essential component of modern medical treatment. Their utilisation is ubiquitous across a significant range of medical disciplines (Lutwick *et al.*, 2019; Smart, Marshall and Daniels, 2012; Seriwala *et al.*, 2016; Pisoni *et al.*, 2017; Oh, Shiau and Reynolds, 2019; Hu *et al.*, 2019). Examples include:

- vascular treatment in the form of stents, heart valves and catheters
- soft tissue with sutures, hernia meshes and breast implants
- cardiovascular treatment utilising pacemakers, artificial hearts and ventricular assisted devices
- sensory and neurological medicine with cochlear and neural implants
- orthopaedic therapy in the form of joint replacements and anchors
- dentistry with dental implants and fillers

For this project the primary applications are in titanium orthopaedic and dental implants. Dental implants are often used to replace missing or removed teeth as a result of trauma, tooth decay, tooth and/or gum infection (Souza *et al.*, 2019; Prasad *et al.*, 2015). The most commonly used are the endosteal implants, which comprise of an artificial titanium tooth root inserted through the gum into the jawbone, with a protruding abutment onto which an artificial tooth is placed (**Figure 2.1A**) (Rupp *et al.*, 2018).

Orthopaedic implants are used to treat chronic bone and joint degenerative and inflammatory problems such as osteoarthritis and rheumatoid arthritis and acute trauma. These include reconstructive joint replacements, the most common being hip and knee arthroplasty (Cordeiro and Barão, 2016). A knee implant consists of two metal components, the femoral and tibial components, fixed into their respective bones with a spacer in between (**Figure 2.1B)** (Bahraminasab and Farahmand, 2017). The hip implant has a similar design, with the femoral step inserted into the femoral bone, and a protruding femoral head inserting into a lined acetabular cup, which is implanted into the acetabulum (**Figure 2.1C)** (Bahraminasab and Farahmand, 2017). Other titanium implants include fixation or fusion pins, rods, nails, wires, plates and screws.

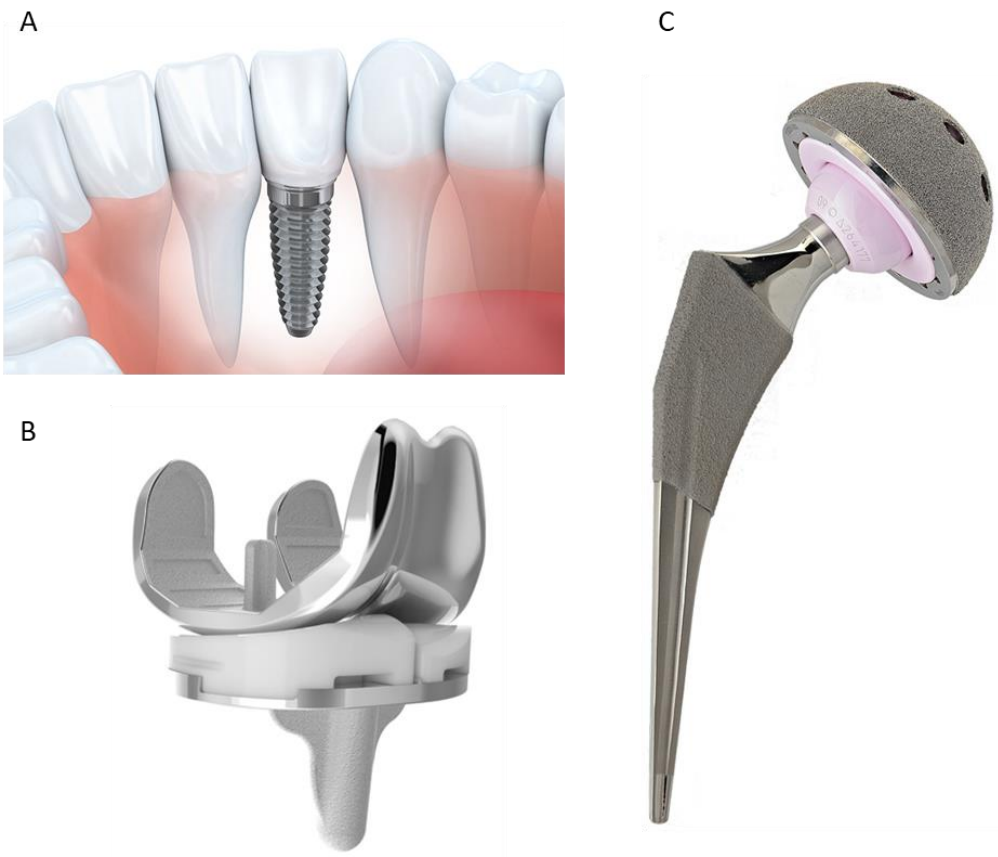

Figure 2.1- *Examples of titanium medical implants. A) Endosteal dental implant (Aqua Dental Clinic, 2019), B) Knee implant (Holzapfel et al., 2013), C) Hip Implant (Alibaba.com, 2019).*

2.1.1 Titanium Implants

Commercially pure titanium (cpTi) is regularly used in dental implants and contains between 98.9-99.6% titanium, together with oxygen, nitrogen and carbon (Prasad *et al.*, 2015). For orthopaedic implants, cpTi is still applied for the acetabular, femoral and tibial components in hip and knee arthroplasty and in fracture fixation, but the titanium alloy Ti64, containing 90% titanium, 6% aluminium and 4% vanadium, is now more commonly used (Kaur and Singh, 2019).

There are numerous beneficial properties of titanium that has led to its utilisation in the orthopaedic and dentistry disciplines. It is well known to being biocompatible which refers to the state of mutual coexistence between an implant and the physiological environment, without undesirable effects (Kaur and Singh., 2019). Titanium belongs to a group of elements called transition metals and has four weakly attracted valence electrons in its $3d^2$ and $4s^2$ energy sublevels, making titanium highly reactive with a standard reduction potential of -1.6V (Prasad *et al.*, 2015). Titanium, in the presence of water or air, instantaneously reacts with oxygen, with two valence electrons, to form a ~<10 nm thick chemically stable oxide layer (TiO_2) on the

surface (Wang *et al.*, 2016a). As a result of this surface passivation, the underlying titanium is protected, conferring high corrosion and rust resistance and therefore preventing the deterioration of the metal through chemical or electrochemical reactions with the local environment (Oldani and Dominguez, 2012; Sidambe, 2014). It is this oxide interface that enables titanium to exist inside the human body with minimal cytotoxicity potentially for decades, and why it is often used instead of metallic alternatives such as stainless steel and cobalt alloys (Koizumi *et al.*, 2019).

In addition to being biocompatible, titanium is also capable of facilitating osteointegration, defined as the direct connection and functional connection between living, ordered bone and the surface of a load carrying implant, which is essential for successful and long-term implantation (Mavrogenis *et al.*, 2009; Lin *et al.*, 2014; Jemat *et al.*, 2015a). The process of osteointegration is discussed further in **Section 2.2.2**.

Along with its unique biochemical properties, the mechanical properties of titanium allow its utilisation in various parts of the body, from load bearing joints to replacement of teeth (Cordeiro and Barão, 2016). This is in part due to its crystal structure. CpTi is allotropic, existing in two crystal orientations or phases, alpha (α) and beta (β). Normally cpTi exists in the α-phase as a hexagonal close packed crystal. If the metal is heated to temperatures above 882°C, the crystal structure transitions into the β-phase as a body centred cubic crystal (Prasad *et al.*, 2015).

The Ti64 alloy consists of both the α-phase, which is stabilised by the aluminium, and the β phase, stabilised by vanadium. The distinct crystal structures result in the Ti64 alloy having different mechanical properties to pure titanium, making it more suitable for load bearing joint replacements (Koizumi *et al.*, 2019; Shah *et al.*, 2016). The properties of cpTi and Ti64 alloy are compared in **Table 2.1**.

Young's modulus of human cortical bone is between 10-30 GPa. Titanium is around 105 GPa, which is relatively close to human bone compared to most other metals or metallic materials (Jemat *et al.*, 2015b; Oldani and Dominguez, 2012). If the modulus of the implant is far greater than bone it can lead to stress shielding, bone resorption or osteopenia due to the reduction of typical stresses experienced by the bone as the implant bears a greater proportion of the stress (Meng *et al.*, 2018; Geetha *et al.*, 2009).

Titanium is also very light, and with a density of 4.5 g/cm^3 it is very close to that of human bone at 3.88 g/cm^3. This enables the metal to be present inside the body without the patient being severely affected by weight impediments. The combination of these properties means that titanium has among the highest strength to weight ratios of any known metal (Koizumi *et al.*, 2019).

Material	Modulus of Elasticity (GPa)	Ultimate Tensile Strength (MPa)	Yield Strength (Mpa)	Fatigue Strength (Mpa)	Hardness	Elongation (%)
Pure Titanium	~105	241-500	172-480	120-275	70-100 HRB	15-24
Ti64 Alloy	~110	896	827	250-300	30-39 HRC	10

Table 2.1- *Mechanical properties of pure titanium and the Ti64 alloy* (Liu *et al.*, 2017; Ibrahim *et al.*, 2017).

Although cpTi and Ti64 have numerous beneficial properties, there are some limitations to their usage. Both have a poor shear strength or wearing resistance, which can lead to the destruction of the surface oxide layer. This causes metal ions, such as aluminium and vanadium, to be released into human tissue and initiate adverse cytotoxic and allergic reactions inside the human body (Kaur and Singh, 2019; Swiatkowska, Martin and Hart, 2019). Although the Young's modulus of titanium is relatively close to that of human bone, it is still higher, leading to potential bone resorption around the implant due to stress shielding and ultimately resulting in detachment and implant failure (Sidambe, 2014).

Titanium has relatively low fatigue strength to notches, which is the likelihood of the metal to fracture due to a surface inhomogeneity such as a notch, crack or scratch (Ibrahim *et al.*, 2017). Titanium has also a relatively low fretting fatigue strength. This refers to the wear and/or corrosion at the asperities of contact surfaces due to the load and recurrent surface motion, leading to the repetitive creation and abrasion of the oxide layer. This can result in premature wear of the implant (Ibrahim *et al.*, 2017; Capitanu *et al.*, 2018).

2.1.2 Trends in Orthopaedic and Dental Implant Practice

Both orthopaedic and dental implant usage is increasing worldwide. Societal expectation, the necessity of remaining active both in work and recreational activities, and being functionally independent later in life, increases the demand on healthcare and treatment. In the case of orthopaedics, the primary factors for this trend are increasing geriatric and obese populations. The average UK patient for primary hip and knee replacement surgery in 2018 was 69 years old and with an overweight/obese body mass index (BMI) of 29 for hip and 31 for knee (National Joint Registry, 2018).

In 2014 in the UK, there were 14.9 million people over 60, equating to 23% of the population; by 2039 this is predicted to rise to 21.9 million or 29.5% (FoaAP, 2016). This is due to the population boom after the Second World War (Randall, 2018), and the improvement in healthcare and technology causing falling mortality rates and an increasing average life span. In 2012, the national life expectancy in the UK was ca. 79.5 years for men and 83.3 years for women; by 2030 this is predicted to rise to 85.7 years and 87.6 years respectively (Bennett *et al.*, 2015).

Individuals over 60 years are more likely to begin experiencing symptoms of chronic bone and joint degenerative and inflammatory problems, such as osteoarthritis. Osteoarthritis is estimated to affect 10% of men and 13% of women in developed countries and is among the top ten most disabling diseases worldwide (Zhang and Jordan, 2010). Osteoarthritis accounts for 90% and 98% of hip and knee replacements respectively in the UK, with other reasons for surgery being trauma such as fractures, avascular necrosis, congenital dislocation/dysplasia of the joint and rheumatoid arthritis (National Joint Registry, 2018).

As nearly 20% of patients may receive their primary joint replacement before the age of 60 years, the increase in life expectancy also means that people could outlive their implants, which have an average life span of 20-25 years. This, in turn, would result in an increased frequency of revision surgery (National Joint Registry, 2018; Ibrahim *et al.*, 2017).

Being overweight or obese, defined as a BMI of over 25 and 30 respectively, is widely known to have major ramifications on human health, being associated with a significant increase in the prevalence of many chronic diseases such as diabetes, cardiovascular disease and osteoarthritis (Ofei, 2005; Agha and Agha, 2017). The excess weight on the load bearing joints over many decades, with the knee, hip and ankles being most susceptible, also leads to an increased chance of needing replacement surgery later in life (Harms *et al.*, 2007).

In 2016, it was estimated in the UK that 26% of adults were obese, up from 15% in 1993 (NHS Digital, 2018). While the UK has the highest obesity rates in Europe, obesity is a growing and

worldwide predicament with nearly a third of the world's population considered to be classified as overweight or obese (Chooi, Ding and Magkos, 2019).

There is also an increasing problem with obesity from an early age. In 2016, over a third of 10-11 years olds in the UK were overweight or obese (NHS Digital, 2018). These statistics highlight that the problem begins from an early age and is likely to lead to chronic bone problems at an earlier stage in life. High rates of obesity also have serious financial implications, with a cost to the National Health Service (NHS) of more than £5.1 billion per year (Scarborough *et al.*, 2011).

In 2004 in the UK there were 49,000 primary hip and knee replacement procedures. By 2010 this rose to 179,000 and in 2017 218,142 were carried out. This is a rise of over 350% from 2004 to 2017 (National Joint Registry, 2018) (**Figure 2.2)**. Equating this rise in financial terms, the global orthopaedic implants market accounted for approximately £35 billion in 2017, and by 2025 this is expected to rise to £50 billion (Allied Market Research, 2018).

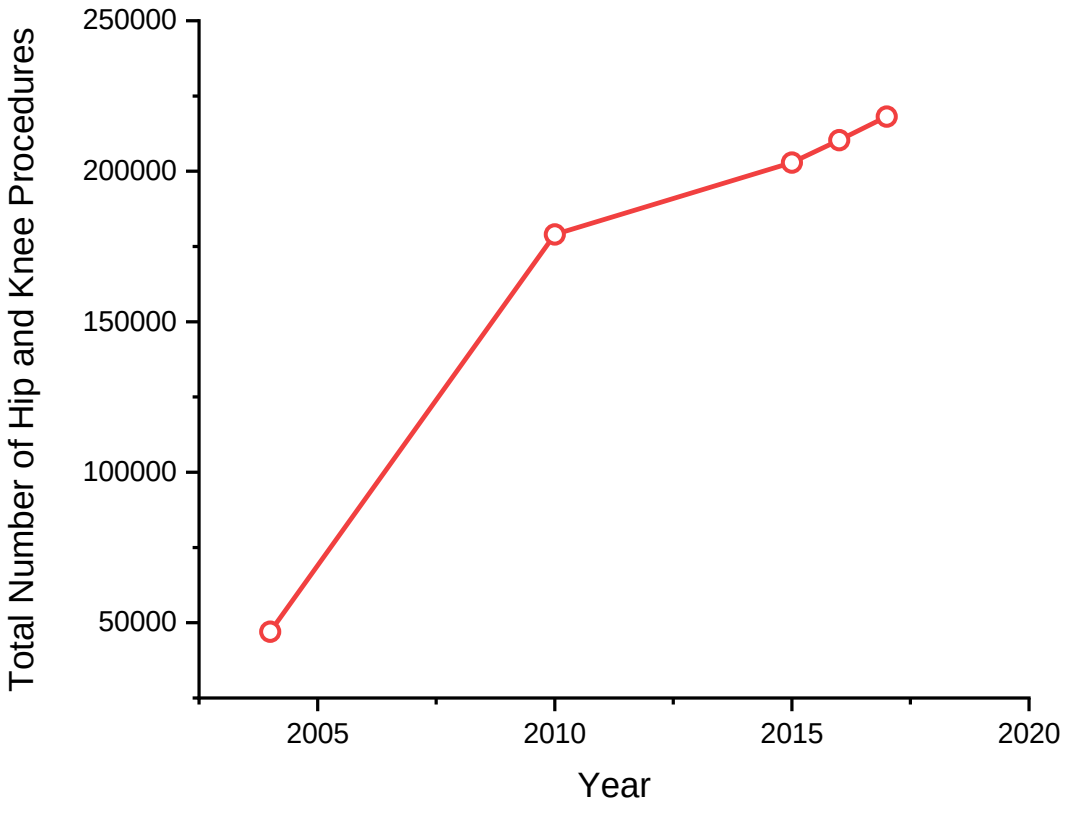

Figure 2.2- *Total number of hip and knee procedures in the UK from 2004 to 2017* (National Joint Registry, 2015, 2018).

Use of dental implants to replace missing or diseased teeth has also been rising rapidly over the last decade, due to ageing populations, unfavourable diets leading to tooth loss, cavities and

periodontitis, and the social demand for aesthetic teeth (Sargolzaie, Moeintaghavi and Shojaie, 2017). It was estimated in 2012 that more than 130,000 dental implants were inserted in the UK and this was predicted to double by 2018 (Ucer *et al.*, 2012). The global dental implant market was estimated at £2.74 billion in 2016 and is estimated to be worth nearly £5 billion by 2025 (Transparency Market Research, 2017).

2.2 The Problem of Premature Implant Failure

In the UK in 2017, revision surgeries accounted for 8.1% and 5.7% of all procedures for hip and knee respectively (National Joint Registry, 2018). Most implants are expected to last approximately 20-25 years (Ibrahim *et al.*, 2017), but there are numerous reasons why implants may fail prematurely. The National Joint Registry in 2018 indicate a cumulative risk of revision surgery with time. For example, hip implant revision at 1 year is 0.78%, increasing to 1.54% at year 3, 2.34% at year 5, 3.01% after 10 years and 4.87% after 14 years. Implants that fail within the first year are twice as likely to require re-revision than those that initially last more than 5 years (National Joint Registry, 2018).

In 2017 for hip and knee implants, infection caused 11.5% and 23% of revision surgeries, making it one of the most common causes (National Joint Registry, 2018). However, the most probable cause is aseptic loosening, which refers to the failure of the bond between an implant and bone in the absence of infection (Abu-Amer, Darwech and Clohisy, 2007); this accounted for 40% and 41% of knee and one stage hip revisions in 2017 respectively (National Joint Registry, 2018).

Further reasons for orthopaedic revision surgeries include pain complaints, adverse reactions to particulate debris, tissue lysis, implant instability, implant malalignment, polyethylene component wear, dislocation/subluxation and peri-prosthetic fracture (Raphel *et al.*, 2016b; Abu-Amer, Darwech and Clohisy, 2007; Chee and Jivraj, 2007; National Joint Registry, 2018).

Any revision to the primary surgery has potentially serious ramifications for the patient. The patient's wellbeing and health will be negatively affected with further highly invasive surgery. There will be prolonged hospitalisation, possible surgical complications such as reduced motion, pain and stiffness, bleeding, deep vein thrombosis and nerve damage, and further post-surgical treatment such as physiotherapy and exercise rehabilitation (Badarudeen *et al.*, 2017). There is also a doubled risk of recurrent infection with revision surgery (Ribeiro, Monteiro and Ferraz, 2012; Raphel *et al.*, 2016a; Widmer, 2006; Zimmerli, 2014; Trebse, Pisot and Trampuz, 2005).

Alongside patient considerations, there is a significant financial burden placed on healthcare systems due to the need to carry out revision surgery. This can range from £10,000 to, in some

instances, as high as £75,000 per patient, depending on the surgery type and treatment plan (Kallala *et al.*, 2015; Vanhegan *et al.*, 2012).

Dental implants have a survival rate of 90-95% over 10 years (Raikar *et al.*, 2017). There are several factors that cause implant failure. One is the implant itself, which includes physical characteristics such as being too rough or smooth, the anatomic site, and implant fit. Local patient factors include oral hygiene (e.g. presence of gingivitis/periodontitis), bone quality/quantity, presence and periodontal status of natural teeth, adjacent infection and inflammation, vascular integrity and soft tissue viability.

There are also patient systemic factors, such as alcohol consumption, smoking, chemotherapy/radiotherapy, illness (obesity, malnutrition, diabetes), impact of foreign material (e.g. excess residual cement or surgical debris in the implant site), and occlusal overload, which can lead to microfractures in the local bone or implant fracture (Pye *et al.*, 2009; Oh, Shiau and Reynolds, 2019).

2.2.1 Infection of Titanium Implants

Infection is estimated to cause, on average, a fifth of implant failures. It can develop at any time but is most likely to occur during the first year of implantation, before there is substantial osteointegration (National Joint Registry, 2018; Pye *et al.*, 2009). There are three principal ways an implant can become infected (Ribeiro, Monteiro and Ferraz, 2012; Raphel *et al.*, 2016b, 2016a):

(1) microbial contamination during surgery

(2) via the haematogenous route, where microorganisms are transported to the implant site through the blood or lymph systems

(3) infection in neighbouring tissues penetrates the implant site

Dental implant infections are classified as either peri-implant mucositis, involving inflammation of soft tissue around the implant, or peri-implantitis, which has accompanying bone loss (Holmberg *et al.*, 2013; Ramanauskaite and Juodzbalys, 2016). Infections by bacteria account for the largest proportion of these diseases. The most common causative agents are Gram-negative, anaerobic bacteria such as *Prevotella intermedia*, *Porphyromonas gingivalis*, *Aggregatibacter actinomycetemcomitans* and *Fusobacterium nucleatum*. Other microbes include *Staphylococcus* species, coliforms and the fungus *Candida* (Koyanagi *et al.*, 2010; Holmberg *et al.*, 2013; Pye *et al.*, 2009).

The most common microbes associated with orthopaedic implant infections are the Gram-positive staphylococci, particularly *Staphylococcus aureus* and *Staphylococcus epidermidis*, which account for 80% of all implant infections. The remaining infections are caused by other bacteria such as the Gram-negative *Pseudomonas aeruginosa* (8% incidence), *Klebsiella pneumoniae* and *Escherichia coli* (Ribeiro, Monteiro and Ferraz, 2012). Infections of orthopaedic implants can lead to bone-tissue infections such as osteomyelitis and septic arthritis, which both involve inflammatory destruction of joint and bone (Ribeiro, Monteiro and Ferraz, 2012; Zimmerli, 2014).

Treatment of infected dental implants includes pharmaceutical approaches, such as irrigation with antibiotics/chlorhexidine or systemic antibiotics, and mechanical debridement, such as through open flap surgery (Pye *et al.*, 2009). For infected orthopaedic implants, the most common treatment is a two-stage revision. The first stage involves complete removal of the implant and any necrotic tissue. The patient is treated with antibiotics during the implant-free period, which can last between 2 to 4 weeks, with differing therapy based on the causative agent. A new implant is then inserted (Trampuz and Widmer, 2006; Trebse, Pisot and Trampuz, 2005).

One-stage procedures are sometimes carried out, in which the implant is replaced immediately with concurrent antibiotic treatment. The estimated cure rate for revision surgery is approximately 80%. There may also be cases of palliative surgery, in which the implant is removed but not replaced, or in extreme cases, an amputation may be required (Trampuz and Widmer, 2006; Zimmerli, 2014).

2.2.1.1 Biofilm Formation on Implant

During the infection process, bacteria adhere to the implant surface, proliferate and commonly form a biofilm. This is an aggregate of microorganisms, often comprising a variety of species (i.e. polymicrobial), encased within a protective, self-secreted matrix known as the extracellular polymeric substance (EPS) (Raphel *et al.*, 2016a; Bjarnsholt, 2013; Alhede and Alhede, 2014; Flemming *et al.*, 2016).

The formation of a biofilm has four main stages (**Figure 2.3**). The first stage is the initial interaction between planktonic bacteria and the surface, and is a rapid and reversible interaction, usually involving electrostatic and physicochemical attractive forces. The second stage results in the strong and irreversible attachment of bacteria due to specific interactions between bacterial surface proteins, such as fimbriae and pili, and their cognate receptor molecules on the surface (Bjarnsholt, 2013; Alhede and Alhede, 2014). Upon attachment, a modulation of gene expression changes the bacterium from a planktonic to a sessile/biofilm state, facilitated through

mechanosensing, mechanotransduction and chemosensing of the local environment. The third stage involves rapid bacterial proliferation to form a mature biofilm, with excretion of EPS components such as proteins, polysaccharides, nucleic acids and lipids to generate a protective matrix layer encompassing the biofilm. The fourth stage is dispersal and detachment of bacteria from the biofilm to potentially form new biofilms at distal sites (Wu, Cheng and Cheng, 2019).

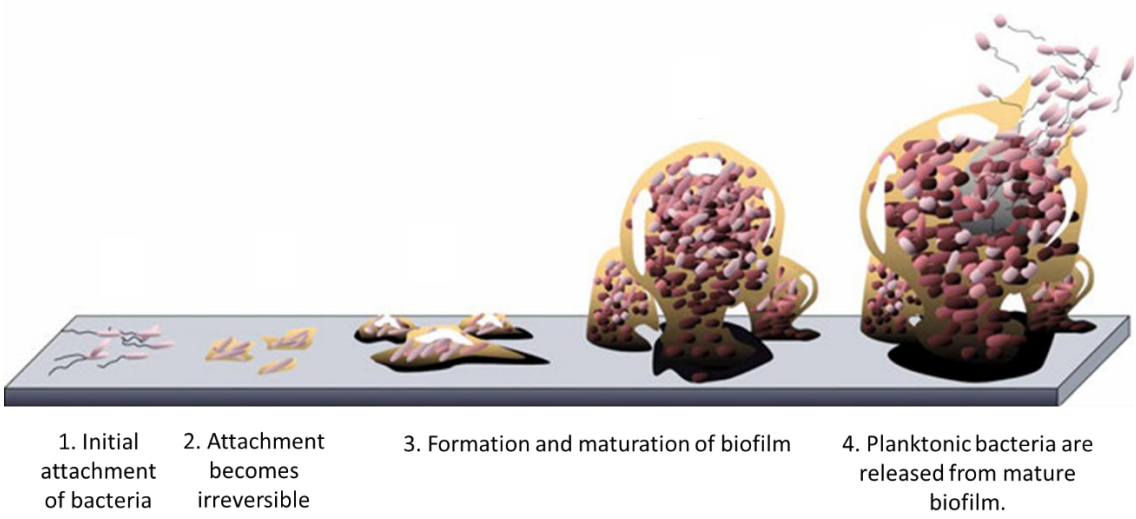

Figure 2.3- *Stages of biofilm development (Unosson, 2015).*

The environment of the biofilm confers a tolerance upon the constituent bacteria to a variety of stressors. For example, biofilms are estimated to be 10-1000 times more resistant to antibiotics than their planktonic counterparts (Mah and O'Toole, 2001). The EPS is made up of 97% water, and this protects the biofilm from desiccation. The EPS also facilitates diffusion reaction-inhibition, whereby effective antimicrobial concentration and activity are significantly reduced by chelation and enzymatic degradation. A significant proportion of bacterial cells within the biofilm are dormant or have reduced growth rates. This leads to reduced susceptibility to antimicrobials such as vancomycin, which depend upon bacterial metabolic activity for their potent activity (Flemming *et al.*, 2016).

Sub-lethal antimicrobial concentrations within a biofilm can also promote selection of resistant cells and enhance the uptake and transfer of resistance genes by horizontal gene transfer. High cell density, close cell-cell proximity, a stable physical and chemical environment that facilitates the binding and stability of plasmid DNA, and increased genetic competence, all promote the spread of antimicrobial resistance within a biofilm (Flemming *et al.*, 2016). This is particularly problematic given the ongoing global antimicrobial resistance crisis.

In 2016, it was estimated that 700,000 deaths worldwide were due to antimicrobial resistant infections, but this would rise to 10 million by 2050, at a cumulative cost over this period of £76 trillion in global economic output (The Review on Antimicrobial Resistance, 2016). Bacteria among the greatest concern are the 'ESKAPE' group, which comprises ***E****nterococcus faecium*, ***S.*** *aureus*, *K. pneumoniae*, ***A****cinetobacter baumannii*, ***P.*** *aeruginosa* and ***E****nterobacter* species. Many strains of these bacteria are multi-drug resistant or, in some cases, pan-resistant to all currently used antimicrobials. This group also includes those bacteria that are prevalent in orthopaedic joint implant infections (Santajit and Indrawattana, 2016).

In both orthopaedic and dental surgery, antimicrobial prophylaxis is widely used to prevent post-surgical infections. Historically, cephalosporins were most commonly used but due to fears of resistance, prophylaxis regimes have been modified in favour of combinational approaches such as using flucloxacillin and gentamicin (Aujla *et al.*, 2013).

2.2.2 Osteointegration with Titanium Implants

Osteointegration was first recognised by Brånemark *et al.* in 1969 and is defined as the direct structural and functional connection between ordered living bone and the surface of a load-bearing implant. The result is the long-term, stable anchorage of an implant within the host bone tissue through fusing with the titanium oxide layer (Brånemark *et al.*, 1969, 1977; Bosshardt, Chappuis and Buser, 2017; Listgarten *et al.*, 1991).

2.2.2.1 Osteointegration Biological Process

The initial phase of the osteointegration process is osteoconduction. Blood is the first biological component to encounter the implant. Platelets, red cells and inflammatory cells migrate to the tissue surrounding the implant and are activated. They release cytokines, growth and differentiation factors as PDGF, PCE2 and TGF-β. Platelets form clots and a fibrin matrix is formed, which acts as a scaffold for migrating osteogenic stem cells. This can occur within the first day of implantation (Mavrogenis *et al.*, 2009; Souza *et al.*, 2019).

The osteogenic cells are then directed to differentiate into osteoblasts and deposit calcified and osteoid tissue on the implant surface through osteoinduction. The calcified matrix remodels into woven and trabecular bone, ensuring early tissue anchorage 10-14 days after surgery. The woven bone slowly remodels into lamellar bone, which has greater mechanical competence, and at 3 months, a mixture of woven and lamellar bone can be observed. Progressive bone remodelling

and strengthening of the bone-implant interaction can continue for at least three years (Mavrogenis *et al.*, 2009; Souza *et al.*, 2019).

2.2.2.2 Factors that affect Osteointegration

Successful osteointegration is a dynamic process that relies on several factors over the implant lifespan (Bosshardt, Chappuis and Buser, 2017):

- Implant biocompatibility
- Implant design e.g. material, diameter, length and shape
- Implant surface treatment e.g. micro/nano roughness, topography, surface chemistry, bioactive coatings
- Patient health, bone quality and related risk factors
- Surgical implantation procedure e.g. position of implant within host bone, adjuvant treatment
- Mechanical stability and loading conditions
- Undisturbed healing phase

Implant geometry, such as the presence of trabecular design and a roughness of more than 1 µm, encourages bone ingrowth and provides mechanical interlocking (Parithimarkalaignan and Padmanabhan, 2013). The health of the host bone is also a major factor in osteointegration success. A healthy bone bed with minimal trauma is imperative, as this is the source of osteogenic cells, local regulatory factors, nutrients and vessels from which osteointegration will occur (Bosshardt, Chappuis and Buser, 2017).

Previous destructive treatment such as irradiation therapy, pharmacological treatment such as warfarin and cyclosporin A, and anti-inflammatory drugs, along with patient-related risk factors such as osteoporosis, rheumatoid arthritis, nutritional deficiency, smoking, and advanced age, can all lead to compromised bone tissue (Mavrogenis *et al.*, 2009).

Any micromotion of the implant due to overloading, especially during the initial phases of implantation, will also hinder the bone healing process (Parithimarkalaignan and Padmanabhan, 2013), while micromotion later on can lead to the formation of implant wear particles and debris. Debris can flow along the implant, interfering with the direct implant-tissue contact needed for osteointegration. Additionally, these particles may initiate an immune response leading to an inflammatory state with release of cytokines such as tumour necrosis factor α (TNF-α), resulting in local resorption of bone tissue. Adsorption and proliferation of pre-osteoblasts on the implant

surface are critical for long-term stability and lifespan of the implant (Raphel *et al.*, 2016b; Abu-Amer, Darwech and Clohisy, 2007).

2.3 Antibacterial Implant Surface Modification Strategies

There has been increased research over the last decade into modifying the surface of titanium to extend implant lifespan, with an aim of 40 years, by inhibiting bacterial infection and promoting osteointegration (Ibrahim *et al.*, 2017). Current research includes several strategies to modify the surface of the implant, as illustrated in **Figure 2.4** (Campoccia, Montanaro and Arciola, 2013a; Raphel *et al.*, 2016a; Goodman *et al.*, 2013; Busscher and van der Mei, 2012; Salwiczek *et al.*, 2014).

These may be broadly split into two groups. The first group incorporates physical techniques that include surface stiffness, roughness and micro/nanotopography, and rely on direct surface interaction. These can be applied to the generation of i) anti-fouling surfaces, which aim to prevent the attachment of any microbes or biomolecules that may promote microbial adhesion, and to release any adhered contaminants on the surface, and ii) surfaces that kill microbes upon contact, preventing proliferation and biofilm formation. The second group are chemical modifications to the surface, which include organic (e.g. antimicrobial peptides [AMPs]) or inorganic (e.g. metal) coatings that may have either surface contact or local environmental activity through short/long/delayed or triggered release.

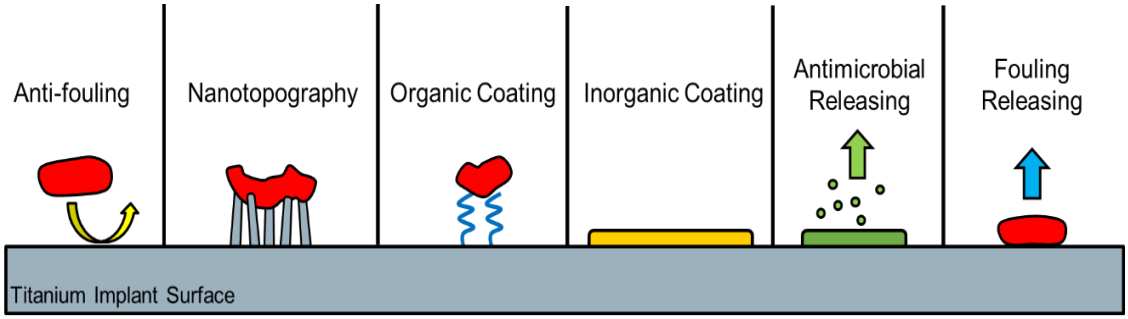

Figure 2.4- *Schematic summary of antibacterial surface modification strategies.*

2.3.1 Inspiration from Nature

Over millions of years, evolution has resulted in a huge variety of natural products with beneficial surface properties that can provide inspiration for antibacterial surface modifications on clinical implants (**Figure 2.5**). Shark skin, lotus leaves, butterfly wings and rice leaves exhibit super-hydrophobic and/or antifouling properties, preventing bacterial/contaminant adhesion or enabling the removal of contamination and thus displaying self-cleaning abilities (Bixler *et al.*, 2014; Chen *et al.*, 2016a).

Hydrophobic surfaces are observed on the lotus leaf and gecko skin, where high static water contact angles and low contact angle hysteresis, in tandem with micro and nanoscale topography and chemical properties (such as epicuticular wax in the case of lotus leaf), results in the 'Cassie-Baxter state'. This is where the microscopic architecture of the surfaces prevents water from penetrating the nanofolds on the surface, leaving air pockets below. This confers anti-adhesive properties and a self-cleaning mechanism, where water running off the leaf removes any contaminants (Kim *et al.*, 2018; Elbourne, Crawford and Ivanova, 2017; Watson *et al.*, 2015).

Shark skin has also been shown to have anti-fouling properties. Mann *et al.* (2014) showed that a shark-mimetic topography on acrylic film significantly reduced *S. aureus* adhesion by more than 98% compared to a smooth acrylic surface. Vasudevan *et al.* (2014) also found that a commercial shark skin mimetic (Sharklet™) could prevent or limit bacterial adhesion. Such effects were proposed to result from the specific patterns (such as recessed areas) impeding bacterial adhesion by maintaining a stable layer of trapped air between the liquid and solid interface, forming a composite water-air-solid interface.

Recently, nanotopographies exhibiting bactericidal properties have been observed from a variety of sources in nature (**Figure 2.6**). Insect wings of dragonflies, cicada and butterflies are the most common examples of structures incorporating nanotopographies that are apparently able to pierce bacterial cell membranes, particularly those of Gram-negative bacteria (Kelleher *et al.*, 2016; Pogodin *et al.*, 2013; Bhadra *et al.*, 2015; Webb *et al.*, 2011; Ivanova *et al.*, 2012). Several species of cicada have been assessed and shown to display nanotopographies of varying dimensions. *Psaltoda claripennis* wings showed bactericidal activity against *P. aeruginosa* and had nanotopography dimensions of ~200 nm in height, ~60 nm in diameter and a pitch spacing of ~170 nm between each pillar (Ivanova *et al.*, 2012). Kelleher *et al.*(2016) compared the wings of different species of cicada (*Megapomponia intermedia*, *Ayuthia spectabile*, *Cryptotympana aguila*) and reported that topographies typically less dense (pitch spacing of 187-251 nm compared to 165 nm) had better bactericidal efficiency against *Pseudomonas fluorescens*.

Dragonfly (*Diplacodes bipunctata*) wings had a typical nanotopography of 240 nm in height and 50-70 nm in diameter and were found to be bactericidal against Gram-negative *P. aeruginosa* and Gram-positive *S. aureus* and *Bacillus subtilis* (Ivanova *et al.*, 2013). The damselfly (*Calopteryx haemorrhoidalis*) wing surface topography exhibited high killing rates against both *P. aeruginosa* and *S. aureus* (Truong *et al.*, 2017). The naturally occurring nanotopographies on cicada and dragonfly wings have also been shown to have killing activity against fungus *Saccharomyces cerevisiae* (Nowlin *et al.*, 2014).

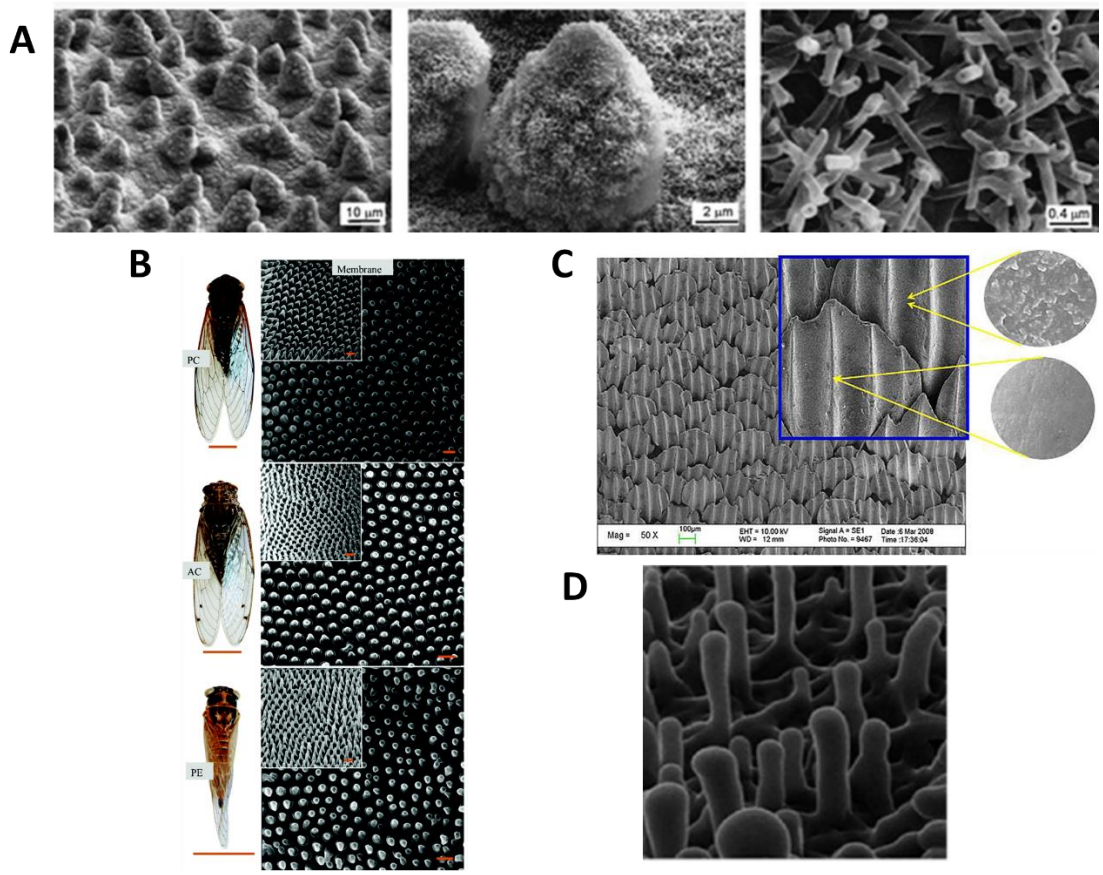

Figure 2.5- *Nanotopographies found in a range of natural environments. A) Increasing magnifications of topography on a lotus leaf (Nelumbo nucifera)* (Koch *et al.*, 2009)*; B) Nanotopographies on three cicada species (Psaltoda claripennis (PC) Alleta curvicosta (AC) Palapsalta eyrie (PE). ~210 nm in height and ~65 nm in diameter* (Shahali *et al.*, 2019)*; C) Shark skin riblet structures (Pu et al., 2016); D) Nanotopography on dragonfly wing (Orthetrum villosovittatum). ~190 nm in height and ~37 nm in diameter* (Bandara *et al.*, 2017).

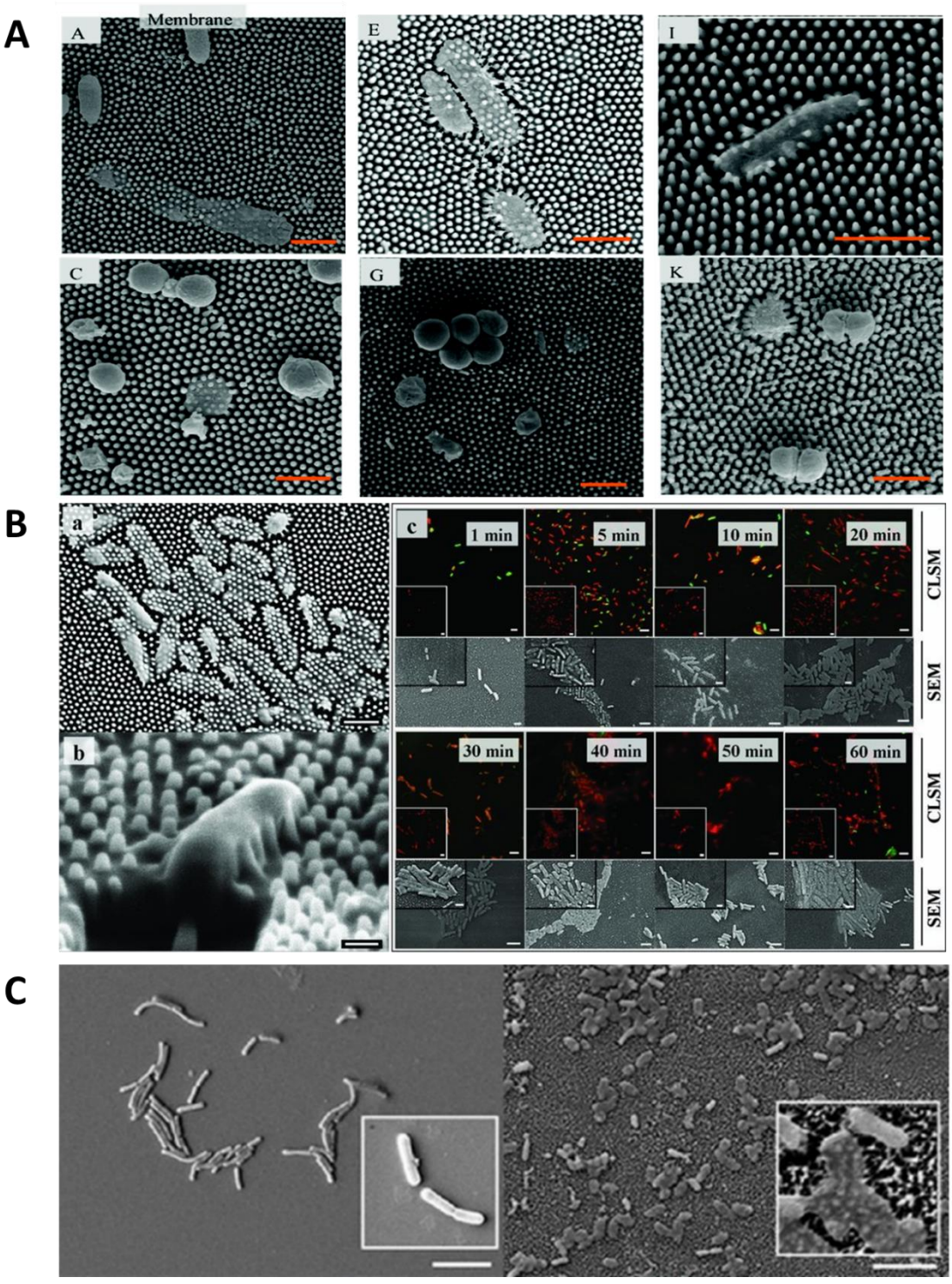

Figure 2.6- *Antibacterial activity of naturally occurring nanotopography.* ***A)*** *E. coli (top) and S. aureus (bottom) on three cicada wings, A, C: Psaltoda claripennis, E, G: Alleta curvicosta, I, K: Palapsalta eyrie after 18 hours (Shahali et al., 2019).* ***B)*** *A and B: P. aeruginosa after 18 hours on cicada wing (Psaltoda claripennis), C: Confocal microscope Live/Dead imaging of P. aeruginosa over time* (Ivanova *et al.*, 2012). ***C)*** *E. coli on dragonfly wing after 30 minutes suggesting bacterial membrane rupture (Bandara et al., 2017)*

Numerous studies have reported variability in the susceptibility of different bacterial species to being mechanically pierced by nanotopography with Gram positive bacteria such as *S. aureus* being less likely to be penetrated to that of Gram-negative bacteria such as *P. aeruginosa* and *E. coli* (Diu *et al.*, 2014; Tsimbouri *et al.*, 2016; Crawford *et al.*, 2012; Hasan *et al.*, 2013; Linklater *et al.*, 2017). This is likely due to the differences in bacterial envelope structure (**Figure 2.7**). Of the Gram-negative envelope there are three main layers: (1) the outer membrane consisting of a lipid bilayer, principally lipopolysaccharide (LPS), (2) a thin peptidoglycan layer or cell wall of <10nm and (3) an inner phospholipid bilayer membrane. The Gram-positive envelope differs structurally in several ways. The outer membrane is absent and instead the cell wall/peptidoglycan consists of several layers and between 30-100nm in thickness (Silhavy, Kahne and Walker, 2010). The thicker cell wall observed in Gram-positive bacteria is theorised to confer greater rigidity to the cells and make them less vulnerable to being mechanically pierced by nanotopography (Bunney *et al.*, 2017; Hasan *et al.*, 2013; Pogodin *et al.*, 2013; Ivanova *et al.*, 2012).

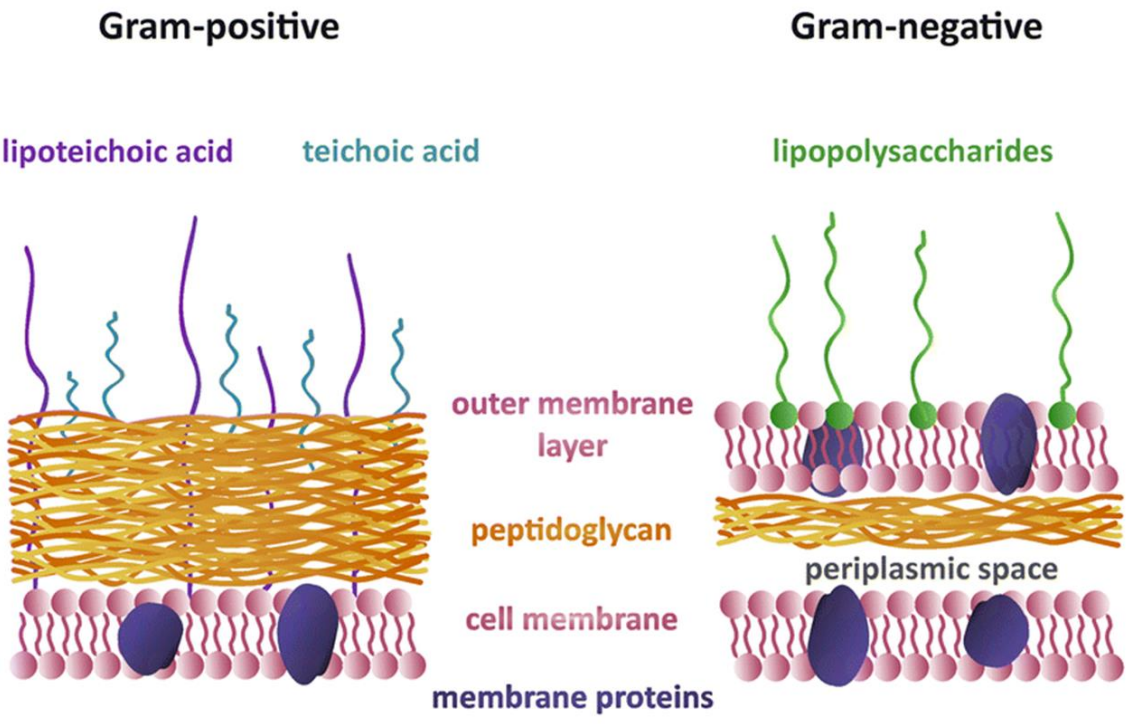

Figure 2.7- *Illustration highlighting differences between composition of cell envelopes of Gram positive and Gram-negative bacterium* (Pajerski *et al.*, 2019).

2.3.2 Physical Modifications for an Antibacterial Titanium Surface

2.3.2.1 Alkaline Hydrothermal Synthesis

In this project an alkaline hydrothermal synthesis was utilised to generate nanotopography on the surface of pure titanium. The technique was reported by Kasuga *et al.* (1998) and used to generate TiO_2 nanotubes on TiO_2 powder. This topography exhibited appealing properties such as photocatalytic activity, high surface area, and layered walls, facilitating its potential as a photocatalyst, i.e. a substance that is able to degrade emergent contaminants in the presence of light (Wong, Tan and Mohamed, 2011; López Zavala, Lozano Morales and Ávila-Santos, 2017).

Alkaline hydrothermal synthesis is an attractive method to generate insect-wing mimicking nanowires due to its experimental simplicity, together with its high and reliable yield of nanostructures. The process is also environmentally friendly due to relatively low temperature and closed system operating conditions, with water being used as the reaction medium (Wong, Tan and Mohamed, 2011).

The basis of the technique involves an aqueous alkaline solution, such as sodium hydroxide (NaOH), within an autoclave or acid-digestion vessel being heated to above water's boiling point to generate a saturated vapour pressure. The reaction with metal forms titanite topography and the physical structures and crystal composition can be manipulated or optimised by the changing of the operating conditions such as the temperature, time duration of synthesis, alkaline molarity and volume (Wong, Tan and Mohamed, 2011; Dong *et al.*, 2007, 2011; Diu *et al.*, 2014). The hydrothermal process involves three major steps. The first involves the generation of alkaline titanate nanostructures. The second involves the substitution of alkali ions within the titanate with hydrogen ions. The third and final step involves heat dehydration in ambient air.

Diu *et al.* (2014) tested two different nanotopographies generated by the alkaline hydrothermal technique described as 'brush-type' and 'niche-type'. Using confocal microscopy, brush-type and niche-type topography were observed to have heights of 2-5 µm and a diameter of ~100 nm. The brush-type, grown for 3 hours, had vertically orientated spikes; the niche type, grown for 8 hours, had intertwined spikes forming pockets of 10-15 µm in diameter. Differences in bacterial cell viability were observed when incubated with these surfaces, possibly related to their motility. *P. aeruginosa, E. coli* and *B. subtilis* were reported to have relatively high levels of killing. In contrast, there was apparently little cell death seen for the non-motile bacteria *S. aureus, K. pneumoniae* and *Enterococcus faecalis.*

Tsimbouri *et al.* (2016) used alkaline hydrothermal synthesis with a shorter duration of 2 hours. The spikes had a height of approximately 1 µm and diameter of ~25 nm (**Figure 2.8A**). Using the Live/Dead imaging technique, *P. aeruginosa* cell death was reported as up to ~50% in some

cases. Jaggessar *et al.* (2018) also observed comparable killing rates for *S. aureus* on nanostructures of around ~300 nm height and ~50 nm diameter.

2.3.2.2 Plasma/Ion Etching

Vertically orientated nanotopographies have been generated on silicon wafers (termed black silicon) using an ion/plasma etching technique (Linklater *et al.*, 2017; Ivanova *et al.*, 2013; Hasan, Jain and Chatterjee, 2017; Hazell *et al.*, 2018a; Vassallo *et al.*, 2017), with a height range between 280 nm to 20 µm and diameters of 60-300 nm. Linklater *et al.* (2017) showed a reduced pillar height from 610 nm to 280 nm, and a decrease in pillar diameter of 63 nm and density of 97 spikes per μm^2 led to higher bactericidal properties against *S. aureus* and *P. aeruginosa*. Hasan *et al.* (2018) used a wet etching technique on aluminium and observed high death rates for *E. coli*, although less effective against *S. aureus*.

Similarly, black titanium was reported by Hasan *et al.* (2017), using a chlorine based reactive ion etching process on titanium, to form structures of approximately 1 µm in height and 80 nm in diameter, which were found to have high bactericidal activity against both *E. coli* and *P. aeruginosa* after 4 hours and *S. aureus* after 24 hours (**Figure 2.8C**). Linklater *et al.* (2019) also used a plasma etching process to produce black titanium with topography between 1.5-3.5 µm in height and ~100 nm in diameter, which showed high bactericidal efficiencies against *P. aeruginosa* and *S. aureus* after 18 hours.

2.3.2.3 Thermal Oxidation

Titanium dioxide nanotopography has also been generated on Ti64 alloy using a thermal oxidation technique (**Figure 2.8B**). The process involved titanium being placed into a horizontal alumina tube furnace and subjected to high temperature (up to 850°C) for 15-45 minutes. Argon flows through a bubbler bottle containing acetone, which then goes through the tube furnace adjusted at different flow rates between 50-300 sccm. The synthesised nanospikes consisted of TiC with a carbon shell, which were then converted into titanium dioxide by heating at 600°C in air. A reduced viability of *E. coli* was found on the nanospikes after a 2-hour incubation (Sjöström, Nobbs and Su, 2016).

2.3.2.4 Sputter and Vapour Deposition

Nanotopography has been formed on titanium using glancing angle sputter deposition. Physical rupturing of *E. coli* cells was observed on these surfaces, but *S. aureus* membranes remained intact (Ziegler *et al.*, 2019).

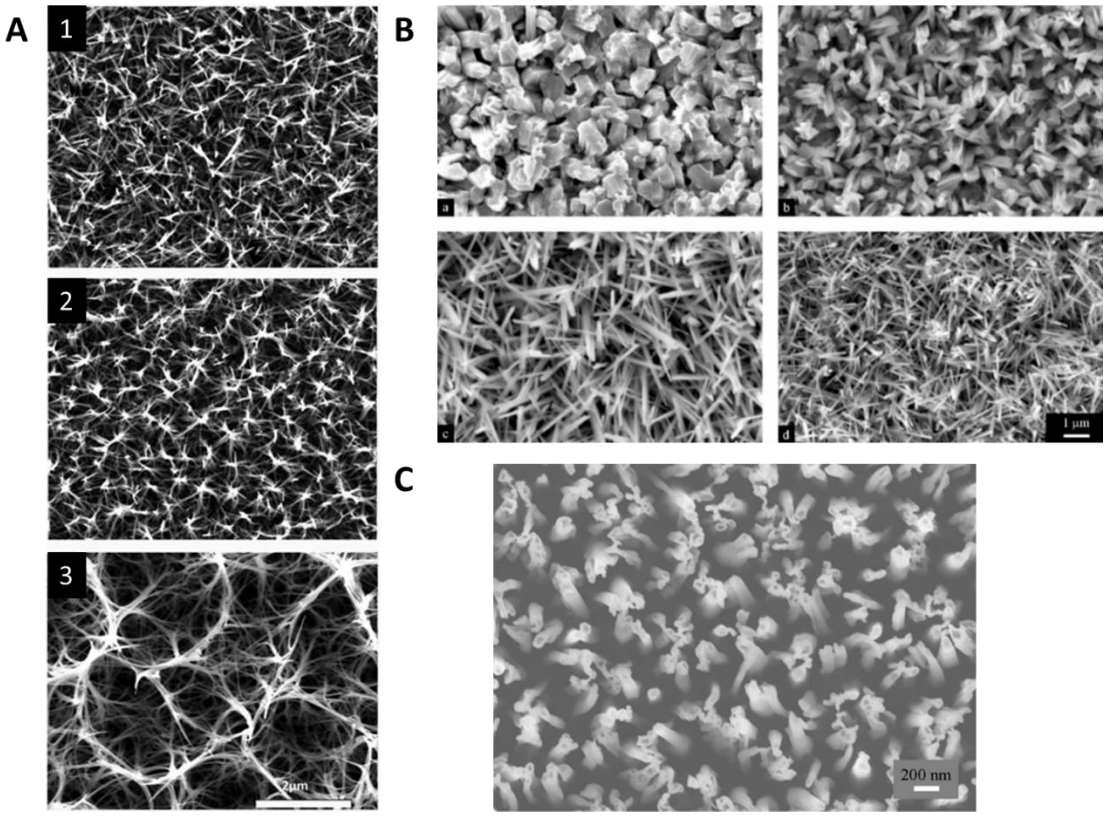

Figure 2.8- *Examples of different nanotopographies generated on titanium using different fabrication techniques. A) Alkaline hydrothermal method. Images 1-3 are different structures generated using increasing time duration (Tsimbouri et al., 2016); B) Thermal oxidation method. Images A-D are of different structures generated using increasing flow rate of acetone (Sjostrom et al., 2016); C) Chlorine based reactive ion technique (Hasan et al., 2017).*

2.3.3 Chemical Modifications for an Antibacterial Surface

2.3.3.1 Antifouling and Fouling-Releasing

The attachment of microbes may be modulated through many complex, multifactorial processes. These include the surface chemical composition, surface functional groups, electrical charge, surface wettability (hydrophobicity and hydrophilicity), macro/micro or nanoscale surface roughness, geometry, degree of hydration, and surface free energy. Also, effective attachment will depend on bacterial properties such as cell shape, surface charge, cell wall composition

(Gram-negative/positive), specific adhesin profile, and extracellular polymeric substance (EPS) secretion. Environmental conditions such as pH, temperature, fluid flow rate, electrolytes and presence of host proteins also play a prominent role (Campoccia, Montanaro and Arciola, 2013b).

Preventing bacterial adhesion to a surface may be achieved by modifying the material's interfacial chemistry, such as by adding coatings with specific functional groups. The functional groups interact with the local environment or directly with the bacterial cell, inhibiting its adhesion to the surface (Querido *et al.*, 2019; Gao *et al.*, 2011; Junter, Thébault and Lebrun, 2015; Tripathy *et al.*, 2017). Functionalised negatively charged surfaces may electrostatically repel bacteria that have a net negative charge (Querido *et al.*, 2019; Campoccia, Montanaro and Arciola, 2013b). Surfaces may also be coated with zwitterionic materials such as a betaine (phosphobetaine, carboxybetaine, sulfobetaine), which make the surface ultra-hydrophilic and have been shown to reduce bacterial adhesion (Mi and Jiang, 2014; Schlenoff, 2014; Sommerfeld Ross *et al.*, 2014; Venault, Subarja and Chang, 2017).

Hydrophilic polymers, such as polyethylene glycol (PEG) and polyethylene oxide (PEO), are often used in a brush-like formation. They form a repellent water layer with high steric hindrance due to water bound within the brush and the elasticity of the polymer chains themselves. This prevents protein adsorption and bacterial cell adhesion and biofilm formation on the modified surface (Gao *et al.*, 2011; Muszanska *et al.*, 2014). Skovdal *et al.* (2018) described an ultra-dense PEG coating that deterred *S. aureus* biofilm formation on titanium in vitro, even after 10 days.

Some polymers are able to be triggered in certain physiological conditions, such as a reduction in temperature or rise in salinity that induces a change in the polymer brush chain configuration to increase the hydrophilicity of the surface (Lee *et al.*, 2015; Chen *et al.*, 2016a). Cao *et al.* (2011) reported that a surface coating containing two reversible equilibrium states triggered by dry or aqueous conditions, could kill *E. coli* or prevent adhesion and encourage contaminant release. Heparin, a naturally occurring coagulant, has been used to reduce bacterial adhesion on catheters, artificial lenses and titanium by increasing the hydrophilicity of the local interface environment (Campoccia, Montanaro and Arciola, 2013b).

A technique called Slippery Liquid-Infused Porous Surfaces (SLIPS) involves generating a stabile liquid coating such as perluoropolyether on a porous microstructured silicon wafer interface. Utilising the extreme wetting characteristics of the generated film, the surface prevented significant *E. coli*, *S. aureus* and *P. aeruginosa* attachment over 7 days under both static and flow conditions (Epstein *et al.*, 2012).

2.3.3.2 Organic Coatings - Antibiotics

Antibiotics at the implant site may prevent biofilm formation via their bacteriostatic or bactericidal capabilities. High local doses may increase the chance of successful treatment, and by being deployed locally, can circumvent the problem of systemic toxicity. Dependent on the type of linkage used, antibiotic coatings for implants may be either long term and not released into the local environment, or shorter term, where they are released in bursts or gradually over a period of time. With the latter, however, depletion of the antimicrobial will eventually result in sub-optimal/sub-MIC levels (Chouirfa *et al.*, 2019).

Vancomycin, an antibiotic often used to treat infections caused by Gram-positive bacteria, has been immobilised onto titanium surfaces and shown to reduce biofilm formation (Jose *et al.*, 2005; Parvizi *et al.*, 2004; Lawson *et al.*, 2010; Beyenal *et al.*, 2004). Other antibiotics such as gentamicin, ceftriaxone, kanamycin, tetracycline and doxycycline have also been used (Hickok and Shapiro, 2012; Onaizi and Leong, 2011; Kazemzadeh-Narbat *et al.*, 2010; Yu, Ista and López, 2014). Tetracycline has been covalently coupled to titanium surfaces through silanization and AEEA linkers and shown to effectively inhibit surface colonisation by *E. coli* and partially by *S. aureus* after 24 hours (Davidson *et al.*, 2015).

2.3.3.3 Inorganic Coatings

Metals such as silver, zinc, cobalt, aluminium and copper have been reported to exhibit antimicrobial activity. Antimicrobial properties include the ability to affect enzyme activity, produce reactive oxygen species (ROS), impair membrane function, interfere with nutrient assimilation and to damage DNA (Lemire, Harrison and Turner, 2013). Fluorine, zinc, chlorine, copper, cerium, selenium and silver have been incorporated into titanium surfaces and displayed varying degrees of antibacterial success (Cochis *et al.*, 2015; Chimutengwende-Gordon *et al.*, 2014; Unosson *et al.*, 2015; Qu *et al.*, 2011; Orapiriyakul *et al.*, 2018).

2.3.3.4 Antimicrobial Release

Chlorhexidine is a widely used antibacterial compound in dentistry and medicine. It has been utilised on titanium implants and shown to reduce biofilm formation in the local environment after 12 hours (Garner and Barbour, 2015; Barbour *et al.*, 2009; Ready *et al.*, 2015). Other approaches have involved 'on-demand' techniques, such as layer-by-layer coatings that involve a release of antimicrobials due to stimuli such as pH, enzymes or temperature (Yao *et al.*, 2017; Wang *et al.*, 2017; Albright *et al.*, 2017; Pavlukhina *et al.*, 2014). When a bacterial infection

occurs the microenvironment changes, often with a reduction in pH, and this is reported to increase the activity of specific enzymes such as hyaluronidase and chymotrypsin. Layered coatings such as (MMT/PLL-GS) have been formed on glass and silicon wafers, with reported killing of *E. coli* and *S. aureus* over 12 hours, and reduced *S. aureus* biofilm over 7 days (Xu *et al.*, 2017).

2.4 Osteogenic Surface Modification Strategies

The ideal implant surface should be osteoconductive by encouraging the adhesion, proliferation and differentiation of mesenchymal stem cells (MSCs) into osteoblasts, to promote strong, long-term osteointegration between the host bone and the implant. Aseptic loosening is a major cause of implant failure, especially for load bearing orthopaedic implants. A primary cause is micromotion of the implant, which is aggravated over time and leads to implant wear and the release of wear particles. This not only prevents stable osteogenesis from occurring, but also causes inflammatory cascades that result in local bone resorption, thereby exacerbating the problem (Liu and Wang, 2017).

2.4.1 Physical Modifications for an Osteoinductive Surface

2.4.1.1 Surface Roughness

A greater surface area due to increased surface roughness facilitates the anchoring of cells and establishment of connections to the surrounding tissues (Alghamdi, 2018). To increase the implant surface area, micron scale roughness can be generated on the surface by grit-blasting and/or acid-etching procedures. Grit-blasting involves the use of abrasive oxide particles such as silicon, titanium or aluminium, typically 100-500 µm in size. Acid etching involves the use of an acid or a mixture such as hydrochloric acid, sulphuric acid, nitric acid and hydrofluoric acid. Changes in temperature and etching time determines interfacial roughness and morphology (Souza *et al.*, 2019). These procedures have demonstrated improved biocompatibility, enhanced cell differentiation and apposition of new bone (Nagasawa *et al.*, 2016; Souza *et al.*, 2019; Lagonegro *et al.*, 2018).

It has been reported that such modified surfaces lead to the activation of blood platelets and migration of osteogenic cells to the bone-implant interface (Lotz *et al.*, 2018; Souza *et al.*, 2019). This results in improved interconnection between the implant and host bone tissue and prolonged mechanical stability at the bone-implant interface. The formation of tuneable-geometric

nanopores or nanotubes, micro-scale in height and nanoscale in diameter, on the titanium interface is also an appealing method of surface modification. Nanotubes have been shown to have closer elastic moduli to cortical bone than pure titanium. This avoids stress shielding, which leads to bone weakening and loss (Shokuhfar *et al.*, 2009; Soares *et al.*, 2008).

Electrochemical techniques such as anodization can stimulate osteointegration. This results in surfaces with a porous, hydrophilic, high surface area interface capable of loading and delivering bioactive molecules and growth elements (e.g. calcium, phosphorous) into the local implant environment (Alves *et al.*, 2017; Ferreira *et al.*, 2017; Butt *et al.*, 2015; Gaviria *et al.*, 2014).

Lasers-based techniques have been used to produce a range of surface textures of different geometries, such as pits, grooves, ripples, pillars and columns, in a highly controlled manner. A variety of techniques exist such as laser ablation, laser melting, laser induced periodic surface structures (LIPSSs), and laser engineered net shaping (LENS™) (Jorge-Mora *et al.*, 2018).

2.4.1.2 Topography

The topography and mechanics of a material are known to influence stem cell proliferation, differentiation and senescence. The higher the elastic modulus of the surface, the more likely that the stem cells may differentiate into bone (Gonzalez-Fernandez, Sikorski and Leach, 2019).

Nanotube, nanopit, nanopore and nanogroove topographies have been shown to promote the adhesion, spread and osteogenic differentiation of stem cells. Nanotopography has also been used to promote cellular alignment and elongation (Bettinger, Langer and Borenstein, 2009). Relatively random topography has been reported to be better than highly order topography to promote osteogenic differentiation (Dalby *et al.*, 2007).

Anodization is an electrochemical process used to generate nanopillars/tubes on titanium and has been reported to promote osteogenic differentiation of MSCs (Sjöström *et al.*, 2009; Goriainov *et al.*, 2018). The formed nanotopography also has capabilities of loading and delivering bioactive molecules such as the bone morphogenetic protein 2 (Alves *et al.*, 2017; Grotberg *et al.*, 2016; Wei *et al.*, 2019). Chang *et al.* (2019) showed that the mechanical strain exerted by titanium nanotubes promoted osteogenesis by upregulating the FAK-ErK1/2-Runx2 pathway.

2.4.2 Chemical Modifications for an Osteogenic Surface

To promote osteointegration, implant surfaces have been coated with bioactive molecules such as calcium phosphate, collagen I, growth factors, bioglass and relevant drugs such as bisphosphonates and anabolic agents (Alghamdi, 2018; Raphel *et al.*, 2016a; Narayanan *et al.*, 2008; Souza *et al.*, 2019).

The deposition of collagen, the main organic component of bone extracellular matrix (ECM) and hydroxyapatite, has been shown to promote direct implant bonding to bone tissue and promote soft tissue growth (Feng *et al.*, 2010; Sartori *et al.*, 2015; Truc *et al.*, 2018; Zhang *et al.*, 2007; Gonzalez-Fernandez, Sikorski and Leach, 2019). Bone growth proteins such as fibroblast growth factor (FGF), vascular endothelial growth factor (VEGF) and transforming growth factor (TGF-β1) promote the expression of genes required for synthesis of collagen, alkaline phosphatase and osteopontin in local implant environments (Le Guéhennec *et al.*, 2007; Terheyden *et al.*, 2012; Carreira *et al.*, 2014; Kang *et al.*, 2010).

Short oligopeptides and peptidomimetics containing the RGD motif (arginine, glycine, and aspartate) have been functionalised onto titanium surfaces. This sequence is a common recognition motif for integrin receptors that mediate cell adhesion (Jenny Raynor *et al.*, 2007; Chen, Zhang and Lee, 2013; Mas-Moruno *et al.*, 2013). For osteoporotic bones, pharmacological drugs are sometimes incorporated onto the implant surface to help improve osteointegration. Bisphosphonates act as antiresorptive agents, while strontium ranelate is an anabolic agent. These drugs have been shown to promote osteoblast deposition and reduce osteoclast resorption and have been administered to patients with weak bone tissue (Alghamdi, 2018).

2.4.3 Hydrophilicity

Rendering an implant surface hydrophilic is believed to reduce the osteointegration time. Conditioning the surface by immersion in isotonic solutions such as sodium chloride after previous acid-etching treatment was shown to increase protein adsorption, platelet aggregation and monocyte/macrophage adhesion. This augmented the healing process, improved bone apposition and led to enhanced bone-implant connection (Wennerberg *et al.*, 2013, 2014).

2.5 Antimicrobial Peptides (AMPs)

2.5.1 Natural Function and Characteristics of AMPs

As antimicrobial resistance levels are continually escalating against the last resort and latest generation drugs, alternatives to traditional antibiotics are being pursued. These include antimicrobial peptides (AMPs). In the Antimicrobial Peptide Database (APD), in September 2019, there were 3,128 peptides from 6 taxonomic kingdoms, highlighting their widespread diversity, and this number is continually rising (Wang, Li and Wang, 2016).

In nature, AMPs function as part of the innate immune system and are found in bacteria, archaea, protists, fungi, plants and animals. In September 2019, 2,321 AMPs have been isolated from animals, including humans and other mammals, amphibians, fish, reptiles, birds and insects (Andersson, Hughes and Kubicek-Sutherland, 2016; Wang, Li and Wang, 2016). In humans, AMPs are expressed by numerous immune cells such as neutrophils, NK and T cells, and by epithelial cells. Their expression can be constitutive or induced by stimuli such as bacterial LPS and inflammatory cytokines such as TNF-α and interleukin-1 (IL-1) (Andersson, Hughes and Kubicek-Sutherland, 2016).

Most AMPs exhibit similar characteristics and are typically 10-100 amino acids in length (Wang, Li and Wang, 2016). Under physiological conditions they have a net positive charge, usually between +2 and +9, due to the presence of positively charged amino acid residues such as lysine, arginine and histidine. AMPs can adopt a variety of structures; most form either alpha helices or beta sheets, but others are cyclic, globular, alpha-beta mix or poorly structured (Wimley and Hristova, 2011). Where AMPs do form structures, they often are arranged amphipathically, with separate hydrophilic and hydrophobic regions. This facilitates their interaction with the phospholipid bilayers of bacterial and mammalian cell membranes (Andersson, Hughes and Kubicek-Sutherland, 2016; Lakshmanan, Zhang and Hauser, 2012; Alencar-Silva *et al.*, 2018).

2.5.2 Benefits of AMPs as Therapeutics

AMPs have rapid, potent and broad-spectrum antimicrobial activity against both Gram-positive and Gram-negative bacteria, viruses, single celled eukaryotes such as protozoa, and multicellular organisms such as parasites and fungi (Alencar-Silva *et al.*, 2018). As they are positively charged, AMPs have a natural electrostatic affinity for bacterial membranes, which carry a strong anionic charge due to the presence of anionic phospholipids, such phospatidylglycerol and cardiolipin (Andersson, Hughes and Kubicek-Sutherland, 2016; Hazam, Goyal and Ramakrishnan, 2019). By contrast, AMPs have only a very low affinity for mammalian cell membranes, which have a

net neutral charge conferred by zwitterionic phospholipids, such as phosphatidylethanolamine and phosphatidylcholine. The presence of cholesterol, the membrane potential and the asymmetric distribution of phospholipids in mammalian cell membranes confers further protection against the activity of AMPs, minimising their cytotoxic potential (Hazam, Goyal and Ramakrishnan, 2019; Andersson, Hughes and Kubicek-Sutherland, 2016).

AMPs have been shown to exhibit bactericidal activity against multi-drug resistant bacteria, highlighting their potential as alternatives to current antimicrobials that have become redundant due to the rise in resistance (Hazam, Goyal and Ramakrishnan, 2019; Eales *et al.*, 2018). The synergistic potential of AMPs with conventional antibiotics has also been demonstrated (Hazam, Goyal and Ramakrishnan, 2019; Gopal *et al.*, 2014; Lakshminarayanan *et al.*, 2016).

Furthermore, whereas bacteria within biofilms often show increased tolerance to antimicrobials, studies have found that AMPs may have significant inhibitory and anti-biofilm activity (Hazam, Goyal and Ramakrishnan, 2019; Chung and Khanum, 2017; Sánchez-Gómez and Martínez-de-Tejada, 2017). Eales *et al.* (2018) compared the bactericidal properties of two synthetic peptides bicarinalin, and BP100 with colistin which is commonly used as a last resort treatment for *Acinetobacter baumannii* infections. The synthetic peptides had significantly enhanced anti-biofilm potential compared with colistin.

Alongside their antimicrobial activity, AMPs have critical immunomodulatory functions as part of the innate immune system. These include coordinating the chemotaxis of immune cells, neutralisation of endotoxins, the induction of angiogenesis, and skin re-epithelialization to promote wound healing (Jenssen, Hamill and Hancock, 2006; Guaní-Guerra *et al.*, 2010; Alencar-Silva *et al.*, 2018). This characteristic gives the potential for AMPs to be used as immunostimulatory or endotoxin-neutralizing agents to augment natural innate immunity (Gordon, Romanowski and McDermott, 2005; Pfalzgraff, Brandenburg and Weindl, 2018).

When the amino acid sequence of an AMP is known, it may be synthesised using standard protocols such as solid phase peptide synthesis (SPPS) (Alencar-Silva *et al.*, 2018). This process offers the potential to improve the activity of the peptide by amino acid modification, including conjugations, cyclization, terminus modifications, heterochiral designs and peptidomimetics (Hazam, Goyal and Ramakrishnan, 2019).

2.5.3 Bactericidal Mechanisms of AMPs

The primary interaction between AMPs and bacteria is the electrostatic attraction between the cationic peptide and the anionic cell membrane (Andersson, Hughes and Kubicek-Sutherland, 2016; Malanovic and Lohner, 2016). AMPs are thought to be able to translocate through the outer membrane of Gram-negative bacteria by displacing the divalent cations, Ca^{2+} and Mg^{2+}, that stabilise the membrane by binding to the phosphate groups of the lipopolysaccharides within the membrane (Mahlapuu *et al.*, 2016). Upon contact with the cytoplasmic membrane, the AMP adopts an amphipathic secondary structure, which permits the peptide to interact with the phospholipid bilayer of the bacterial cell membrane. This leads to membrane destabilisation and/or the formation of pores within the membrane. Substantial disruption of the membrane morphology and structure occurs, resulting in surface blebbing, vesiculation and fragmentation (Wimley, 2010; Mahlapuu *et al.*, 2016; Wimley and Hristova, 2011), and ultimately bacterial cell death.

Three principal models have been proposed for the AMP/bacterial membrane interaction, alongside numerous variations and combinations of these (**Figure 2.9)**. The Barrel-stave model and Toroidal model both involve the formation of pores through the membrane. In the Barrel-stave model, the peptides interact with one another to insert and align themselves parallel with the phospholipids of the bacterial membrane, with their hydrophobic regions interacting with the hydrophobic phospholipid core. This generates a cylindrical transmembrane pore, the inner surface of which comprises the hydrophilic regions of the AMPs (Laverty, Gorman and Gilmore, 2011; Li *et al.*, 2012).

In the Toroidal model, the AMPs co-operatively cause local inward curvature of the bacterial membrane bilayer to generate a pore consisting of the AMPs and phospholipids of the membrane. In the Carpet model, the peptides lie parallel to the plane of the phospholipids within the bacterial membrane. Once a peptide to lipid ratio threshold has been reached, the peptide inserts into the membrane and, within a period of micro-seconds to minutes, the membrane is destabilised and forms micelles or vesicles (Nguyen, Haney and Vogel, 2011; Maria-Neto *et al.*, 2015).

While the predominant outcome, disruption of the bacterial cell membrane is not the only mechanism by which AMPs can mediate antibacterial effects. Some AMPs transit across the bacterial cell membrane to enter the cytoplasm. Here, AMPs have then been observed to interact with DNA, RNA or proteins and mediate bacterial cell death by interfering with cell wall or nucleic acid synthesis (Brogden, 2005; Li *et al.*, 2012).

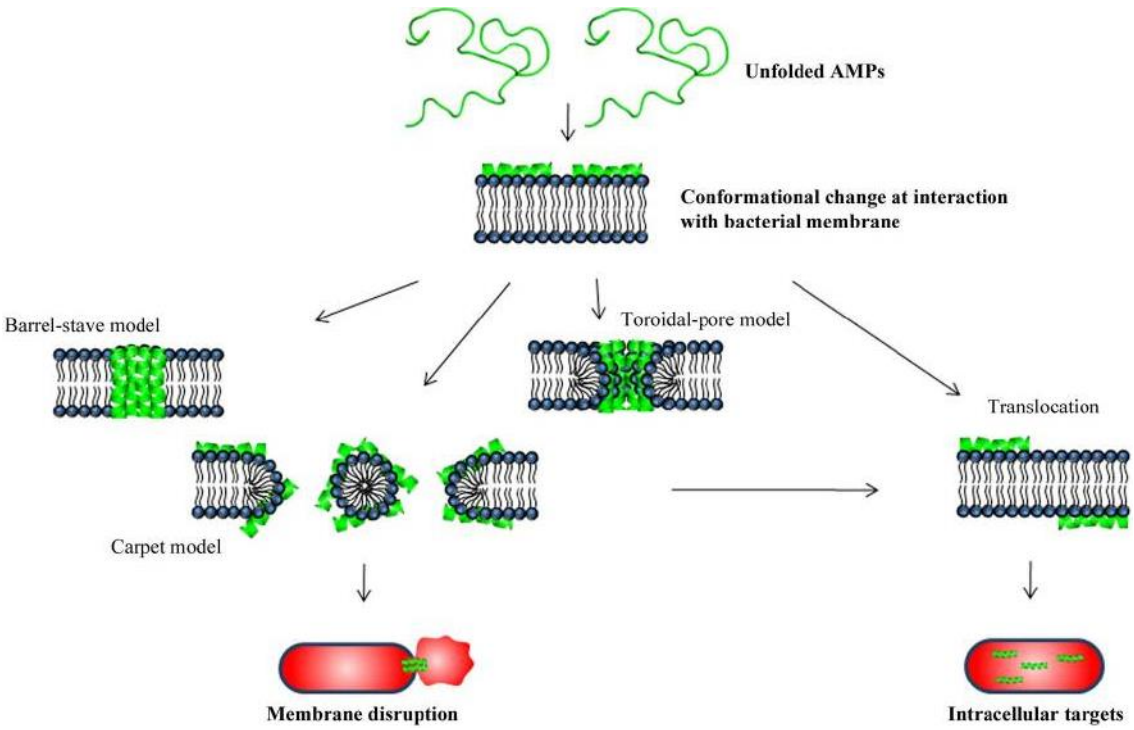

Figure 2.9- *Schematic of bacterial membrane disruption mechanisms by AMPs. 1) Barrel-stave model. Transmembrane pore consisting of perpendicularly orientated AMPs. 2) Toroidal-pore model. Transmembrane pore consisting of perpendicularly orientated AMPs and phospholipid groups. 3) Carpet model. Once a threshold concentration has been reached, the accumulation causes surface tension and disruption of membrane leading to micelle formation (Mahlapuu et al., 2016).*

2.5.4 Limitations of AMPs

Currently there are very few classified AMPs in clinical use. The most well-known are the polymyxins (polymyxin B and colistin [polymyxin E]), which are used as last resort drugs against various multi-drug resistant Gram-negative bacteria (Andersson, Hughes and Kubicek-Sutherland, 2016). Nonetheless, there are currently around 30 AMPs in clinical trials, with 8 in phase 3 trials. Ongoing AMP research into the treatment of acne, sepsis, HIV and AIDS, cystic fibrosis, tuberculosis and fungal infections, highlights their diverse potential (Hazam, Goyal and Ramakrishnan, 2019).

Despite their beneficial properties, several factors have hindered the potential development of AMPs as therapeutic drugs. AMPs are susceptible to proteolytic degradation and conformational changes under certain conditions (e.g. high/low pH, temperature, salinity). This can result in short half-lives and rapid elimination from the body leading to a decrease in bioavailability (Mahlapuu *et al.*, 2016; Lakshmaiah Narayana and Chen, 2015).

The broad-spectrum activity of AMPs against both prokaryotic and eukaryotic cells can be advantageous but in high concentrations, can cause cytotoxicity. This is observed with the

intravenous use of polymyxins, produced by the bacterium *Bacillus polymyxa* (Abdelraouf *et al.*, 2012). These AMPs have been used since the 1950s to treat Gram-negative bacteria that cause meningitis, bronchopulmonary, skin, eye and ear infections. Due to the increase in antimicrobial resistance, polymyxins are used as the last resort treatment despite high incidence rates of nephrotoxicity and neurotoxicity through systemic usage (Seo *et al.*, 2012; Andersson, Hughes and Kubicek-Sutherland, 2016).

Despite numerous theories about the antimicrobial mechanisms of AMPs, there is still a lack of understanding, especially in relevant physiological and *in vivo* conditions compared with *in vitro* conditions of the laboratory (Andersson, Hughes and Kubicek-Sutherland, 2016; Hazam, Goyal and Ramakrishnan, 2019).

Bacterial resistance, both intrinsic and acquired, to AMPs has been documented. Inherent resistance can occur passively or be induced by environmental stimuli such as low pH, low iron and magnesium, or low nutrient concentration. Through modifying the LPS of Gram-negative bacteria, or teichoic acids in Gram-positive bacteria, the negative charge of the bacterial envelope is reduced and hence the electrostatic attraction to AMPs. The upregulation of efflux pumps and proteolytic degradation systems have been observed (Gruenheid and Le Moual, 2012; Andersson, Hughes and Kubicek-Sutherland, 2016).

Acquired resistance through mutations and horizontal gene transfer leads to altered metabolism, slower growth rates and reduced transmembrane potential. Rates of resistance can occur rapidly. Samuelsen *et al.* (2005) reported a 30-fold increase in *S. aureus* resistance after four generations against the AMP lactoferricin B, while Perron *et al.* (2006) showed resistance in *E. coli* against pexiganan after 600 generations.

The potential high cost of AMP production and purification is likely to result in pressure to invest in cheaper alternatives such as designing shorter length chains. In addition, increasing safety and efficacy requirements will require significant financial pharmaceutical investment (Hazam, Goyal and Ramakrishnan, 2019).

2.5.5 AMP Incorporation onto Implant Surfaces

AMPs have been incorporated onto biomaterials by immobilisation either through covalent attachment, such as silanization, polydopamine and PEG brushes, or by physical immobilisation, such as physical adsorption or self-assembled monolayers.

2.5.5.1 Physical Immobilisation

Physical adsorption has been used primarily to coat a surface with bioactive compounds, such as fibrinogen and albumin, to improve osteointegration, rather than for an antibacterial function (Wronska *et al.*, 2016; Horasawa *et al.*, 2015). The adsorption process is dependent on a range of factors such as surface chemistry, solution chemistry, topography, hydrophilicity and the electrostatic interactions of the molecules with each other and the surface. It has been reported for albumin that the increase in hydrophilicity resulted in a lower adsorption. However, the opposite was reported for fibrinogen, with more being absorbed onto the relatively hydrophobic surfaces (Chen, Zhang and Lee, 2013).

Physical adsorption methods used for AMPs include the layer by layer approach, which relies on the positive electrostatic charge of the AMP (Shi *et al.*, 2015). The advantage of physical adsorption approaches is that they avoid the need for initial surface treatment, such as the generation of hydroxyl groups for silanization, or the use of linkages such as PEG and glutaraldehyde (Xu *et al.*, 2018). Consequently, physical adsorption is extremely time efficient and avoids the use of toxic and dangerous solutions such as piranha solution (a mixture of sulphuric acid and hydrogen peroxide) (Costa *et al.*, 2015, 2011).

Furthermore, while covalent tethering techniques are dependent on the number of available functional groups (e.g. amine) to tether peptides to the surface (Costa *et al.*, 2015), minimal experimental optimisation is required for physical adsorption. Since it does not involve linkages or functional groups, the exact concentration of required peptide can be applied to the surface. Potential cytotoxicity has also been reported for some linkers, and physical tethering can hinder peptide activity due to the requirement for a specific peptide orientation and mobility on the surface (Costa *et al.*, 2015). Such issues are avoided when using physical adsorption.

Physical adsorption methods allow the free release of AMPs into the local environment from the surface, enabling the peptides to exert effective short-term antimicrobial activity. However, this elution inevitably leads to depletion of AMPs over time (Chouirfa *et al.*, 2019). In a closed environment, this will lead to a high concentration of the peptide. In a dynamic environment, depletion of the peptide will occur more rapidly, and the peptide concentration may struggle to reach the threshold required for effective antimicrobial activity.

Peptides may interact with a surface through ionic bonds, hydrogen and van der Waals forces rather than via covalent attachment. For self-assembled peptides (SAPs), the AMPs are adsorbed onto the surface between polyanions such as polyacrylic acid and poly L-lysine. Repeated processing forms multiple layers and determines the amount of peptide ultimately in the coating (Pinto *et al.*, 2019; Lakshmanan, Zhang and Hauser, 2012; de Avila *et al.*, 2019; McCloskey, Gilmore and Laverty, 2014). Hernandez-Montelongo *et al.* (2018) described immobilisation of AMP Tet-124 with a polyethyleneimine film onto silicon wafers by electrostatic interactions between the amino groups of the film and the carboxylic groups of peptide amino acids. High death rates of *S. epidermidis* on these functionalised wafers were reported after 24 hours.

AMPs can also be incorporated into hydrogels. Casciaro *et al.* (2017) described fixation of Esc (1-21) onto hydrogel soft contact lenses. This resulted in a significant reduction of over 70% in the number of *P. aeruginosa* cells that were able to adhere to the lenses. No cytotoxicity was apparent against murine connective tissue, and the contact lens characteristics were unaffected.

2.5.5.2 Covalent Attachment

Covalent tethering is a potentially appealing method for a number of reasons. It has been shown to increase peptide stability, protecting it against enzymatic degradation, and can limit the leaching of peptide into the environment (Chen *et al.*, 2014; Qi *et al.*, 2011; Pinto *et al.*, 2019; Costa *et al.*, 2011). As a result, long-term bactericidal activity has been reported for surfaces that have been functionalised in this way over hours and days (Godoy-Gallardo *et al.*, 2015; Nie *et al.*, 2016; Córdoba *et al.*, 2016). Surfaces reaching sub-MBC AMP concentrations have shown a retardation of bacterial growth rate and an increased lag phase (Soares *et al.*, 2015), while the beneficial properties of biocompatibility and promoting osteogenesis were maintained (Pinto *et al.*, 2019; Costa *et al.*, 2011).

Silanization involves the attachment of amino silanes such as 3-aminoproyltriethoxysilane (APTES), 3-aminopropyltrimethoxysilane (APTMS) or 3-chloropropyltriethoxysilane (CPTES) to hydroxyl groups on the material interface (Holmberg *et al.*, 2013; Chen *et al.*, 2014; Godoy-Gallardo *et al.*, 2015; Majhi, Arora and Mishra, 2019). Surface preparation involves the generation of hydroxyl groups through, for example, treatment with piranha solution, which is a mixture of sulphuric acid and hydrogen peroxide (Peng *et al.*, 2017).

The silane acts as an anchor through the available functional amino groups, to which compounds like AMPs can covalently attach (Chouirfa *et al.*, 2019; Chen *et al.*, 2016b). Other molecules such as catechol (Chouirfa *et al.*, 2019) and phosphate (Córdoba *et al.*, 2016) have also been used to anchor peptides to the surface. Godoy-Gallardo *et al.* (2014) compared the bactericidal activity

of a covalently tethered AMP, hLf1-11, with physically adsorbed peptide. More peptide was found on the silanized surface, resulting in better antibacterial activity against *Streptococcus sanguinis*, although comparable levels of attachment were seen for *Lactobacillus salivarius*.

Polymer brushes with linkers such as poly(ethylene glycol) (PEG) have been widely used to attach peptides such as LL37 and nisin to solid surfaces. This is due to their stability, non-toxic and non-immunogenic properties (Qi *et al.*, 2011; Gabriel *et al.*, 2006; Mishra and Wang, 2017). The immobilisation of nisin with PEG onto carbon nanotubes was reported to show a seven-fold higher antimicrobial activity against both Gram-negative and Gram-positive bacteria after 1 hour (Qi *et al.*, 2011).

2.5.5.3 Factors affecting Covalent Tethering

Higher MICs are usually reported for immobilised peptides compared to their soluble alternatives (Costa *et al.*, 2011; Tan *et al.*, 2014). There are many complex factors affecting optimisation of the tethering, such as what the peptide is being attached to, its orientation and stability, and if any surface preparation is required e.g. cleaning or increasing the number of hydroxyl groups (Costa *et al.*, 2011; Aumsuwan *et al.*, 2008). Silanes, for example, suffer from hydrolytic instability in aqueous environments at physiological pHs (Córdoba *et al.*, 2016; Silverman, Wieghaus and Schwartz, 2005). Additional considerations include the flexibility and length of the spacer, which can be incorporated to allow more movement and preferential orientation of the peptide (Lozeau, Alexander and Camesano, 2015). Potential cytotoxicity has also been reported involving linkers required for effective tethering (Gu *et al.*, 2017).

2.6 Synergistic Surface Modifications

Some studies have investigated the effects of incorporating two or more surface modification techniques to improve an implant's antibacterial activity and biocompatibility. For example, Zhou *et al.* (2015) functionalised the antimicrobial peptide GL13K onto microgroove titanium surfaces by silanization. This resulted in a reduction in *P. gingivalis* viability and the promotion of adhesion and proliferation by human gingival fibroblasts. Titanium nanotubes have demonstrated improved antibacterial activity when doped with gentamicin, silver or zinc, whilst remaining biocompatible (Mei *et al.*, 2014).

2.7 Project Aims and Objectives

Much of the recent research into devising implant materials that are resistant to infection seeks to combine one antibacterial modification with another that may also promote stem cell adhesion and proliferation. An aspect that has not been widely researched is using two antimicrobial strategies on a surface that will synergise to prevent infection. The aim of this project was to generate a pure titanium implant surface with synergistic physical (nanotopography) and chemical (AMP) modifications, which would effectively reduce bacterial colonisation yet remain biocompatible. This was to be achieved via the following main objectives:

1. Form and characterise a range of different nanotopographies generated by the alkaline hydrothermal method on a pure titanium surface.

2. Assess the bactericidal potential of these nanotopographies with a range of different bacterial viability techniques on both Gram-positive and Gram-negative bacteria.

3. Functionalise the optimal topography with an AMP, ChoM, and assess the impact of this functionalisation on the bactericidal potential of the surface.

4. Assess the biocompatibility and potential osteogenic properties of the functionalised surface.

3.

EXPERIMENTAL METHODOLOGY AND ANALYSIS TECHNIQUES

Contents

3.1 Formation of TiO_2 Nanotopography on Titanium Substrates

3.1.1 Polishing Titanium Disks

Titanium disks were polished to a mirror shine to obtain <10 nm roughness across the disk in order to optimise nanotopography orientation during the subsequent alkaline hydrothermal growth.

Grade 1 sheets of commercially pure titanium (Ti-Tek (UK) Ltd) of 0.7 mm thickness were laser cut, by Laserit, into circular disks, initially 14 mm in diameter. These were subsequently reduced to 11 mm to enable more disks to be cut from a sheet of titanium and polished in a single batch. Grade 5 Ti-6Al-4V (Titek) was cut into 1 cm squares with a guillotine (Fortex).

The disks were mounted onto a custom-made polishing holder as shown in **Figure 3.1**. Acrylic cylinders (laboratory made) were superglued to a circular glass disk (Dixon Science). Double sided sticky tape (Tesa) was used to stick parafilm (Bemis) onto the glass. The titanium disks were then superglued onto the parafilm, ensuring all the disks were uniformly flat.

The disks were polished on a Struers TegraPol-15 with silicon carbide grinding paper (Struers) at increasing grit levels of 80, 500, 1200, 2000 and 4000 on MD Fuga pads (Struers) at 30 N, 300 rpm for 4 minutes each. Initially the disks were polished to SiC level 2000 and then diamond polished using Struers MD Largo pads and diamond suspension (Struers DiaPro Largo 3) at 30 N, 150 rpm for 4 minutes. This stage was removed due to repeated scratching of the disks and subsequently a SiC level 4000 was used.

To obtain the required mirror shine, the disks were polished with MD Chem pads (Struers) at 35 N, 150 rpm for about 15 minutes. Approximately 4 ml of 10% hydrogen peroxide (Acros

Organics) in colloidal silica suspension (Struers) was pipetted onto the MD Chem pads every 45 seconds with the occasional spray of deionised water to prevent clumping of the colloidal suspension. The disks were visually quality controlled and checked for scratches every 5 minutes.

The disks were removed from the parafilm, the superglue scraped off with a scalpel (Swann Morton), and the disks sonicated (Grant XUB5) for 15 minutes in deionised water, preheated to 40°C. Finally, the disks were immersed in absolute ethanol (Merck) for 10 minutes before blow-drying with compressed air. The disks were stored in a clean plastic Petri dish (Greiner Bio-one, 632180) until used.

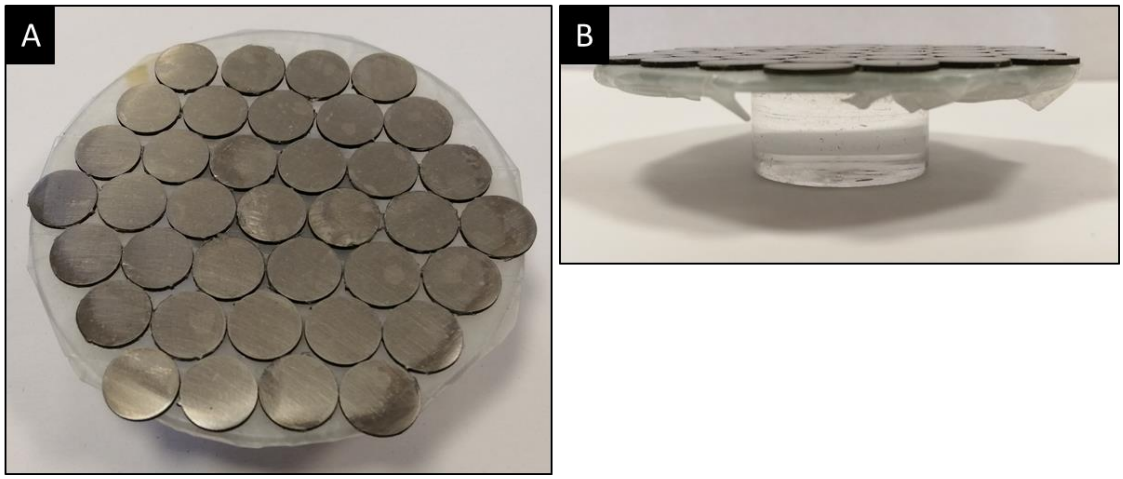

Figure 3.1- *Custom-made polishing holder with titanium disks glued on top. A thin circular glass slide was superglued to an acrylic stub. Using double sided sticky tape, parafilm was stuck to the glass slide. Titanium disks of 11 mm in diameter and 0.7 mm in thickness were immobilised onto the parafilm using superglue and air dried. During polishing the stub was placed upside down. A) Top view of 37 titanium disks glued to parafilm which is stuck onto a circular glass disk with double sided sticky tape. B) Side view of polishing holder.*

3.1.2 Alkaline Hydrothermal Treatment

Sodium titanate nanotopography was generated on the titanium surface by the following alkaline hydrothermal process.

Polished titanium disks (24) were prepared as described in **Section 3.1.1** and slotted into custom-made PTFE holders, to ensure the disks remained upright, and placed into a 125 ml PTFE cup. The cup was then inserted into an acid digestion vessel (Parr Instrument Company-Model 4748) containing a determined volume (e.g. 52 ml) and concentration (e.g. 1 M) of NaOH (Fisher). The vessel was tightly sealed and placed in a preheated oven (Gallenkamp Plus II) for a fixed time duration (e.g. 2 hours) and temperature (e.g. 240°C). The Teflon cup, disk holders and acid digestion vessels are shown in **Figure 3.2**.

After the alkaline hydrothermal treatment, the acid digestion vessel was removed from the oven and left to cool to room temperature. The disks were then removed from the holders and soaked in deionised water and absolute ethanol for 10 minutes each. The disks were finally placed on ceramic blocks and left to dry overnight in a sheltered environment.

Systematic parameter changes were carried out in order to optimise the nanotopography formation:

- Time Duration within oven at 240°C in 1 M, 52 ml NaOH

  30 minutes, 1 hour, 1.5 hours, 2 hours, 3 hours, 4 hours, 5 hours, 6 hours, 7 hours.

- Temperature of oven for 2 hours in 1 M, 52 ml NaOH

  180°C, 200°C, 220°C, 240°C.

- Molarity of 52 ml sodium hydroxide within the Teflon vessel heated at 240°C for 2 hours.

  0.5 M, 1 M, 2 M, 4 M, 5 M.

- Volume of 1 M sodium hydroxide within the Teflon vessel heated at 240°C for 2 hours.

  28 ml, 36 ml, 44 ml, 52 ml, 60 ml, 68 ml.

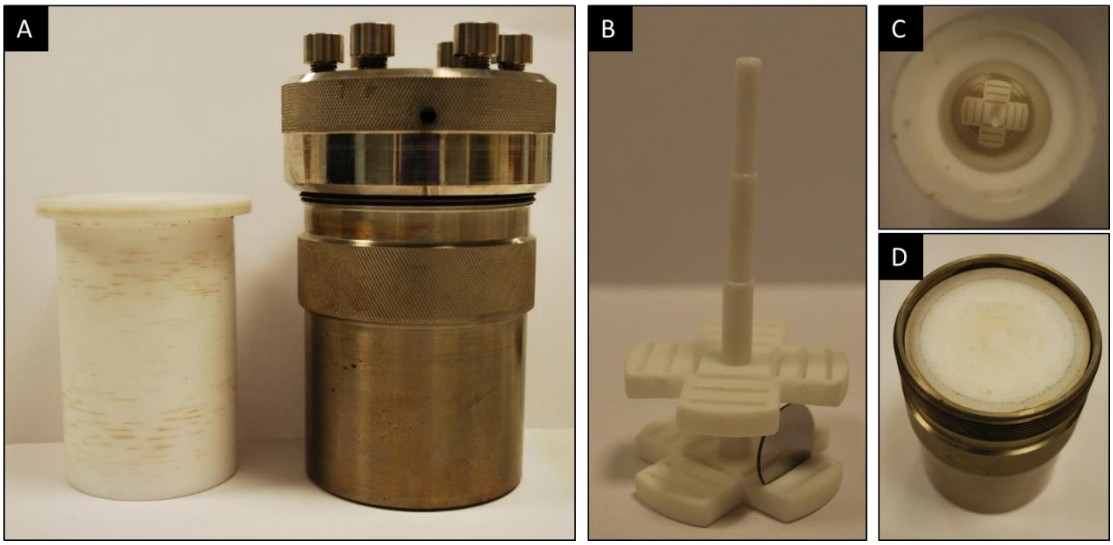

Figure 3.2- *Components used for alkaline hydrothermal treatment. Polished titanium disks (24) were placed upright in a Teflon disk holder before being immersed in NaOH within a Teflon cup. The Teflon cup was placed within an acid-digestion vessel and the lid tightly closed. The vessel was then placed in a preheated oven for alkaline hydrothermal treatment. (A) Teflon cup (left) and acid digestion vessel (right) with lid, (B) Double tiered Teflon disk holder, (C) Overhead view of Teflon disk holder within Teflon cup, (D) the Teflon cup within the acid digestion vessel.*

3.1.2.1 Nanotopography Transformation and Resolution

Due to wear and tear of the Teflon vessels over time, a change in the nanotopography was observed. It was found that these replacement vessels were typically ~3 mm shorter and therefore allowed a greater expansion during the alkaline hydrothermal treatment. To mitigate this expansion, the mobile base of the acid-digestion vessel was moved upwards by placing three titanium metal spacers of 5 mm thickness and 22 mm in diameter, in 'triangle formation', underneath the acid digestion vessel during the alkaline hydrothermal treatment and cooling stages. This procedure rectified the problem and the spacers were used in all subsequent hydrothermal treatments.

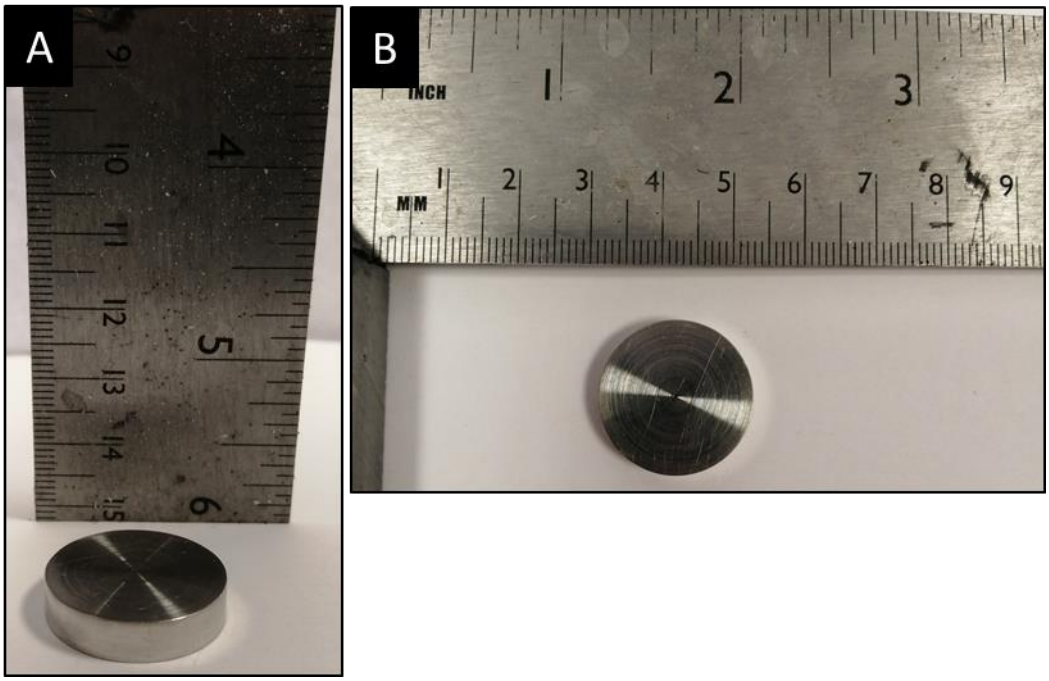

Figure 3.3- *Titanium spacer used during alkaline hydrothermal treatment.*

3.1.3 Post Alkaline Hydrothermal Treatment

After the alkaline hydrothermal treatment, the sodium titanate nanotopography was converted into hydrogen titanate by the following processes:

The disks were initially heated at 300°C (temperature ramp of 10°C/min) for 1 hour using a chamber furnace (Elite Thermal Systems Ltd (Oven Model-BMF 11/7)) to ensure the nanotopography fixed to the titanium disk interface. Without this step, the top layer was prone to peeling during subsequent steps.

When cooled, the disks were immersed in 0.6 M hydrochloric acid (HCl) (Fisher) for 1 hour in a fume hood, where the sodium in the nanotopography was exchanged with the hydrogen in the HCl to form hydrogen titanate. The disks were then rinsed with deionised water and absolute ethanol for 10 minutes each and air dried.

The final step involved placing the disks in the chamber furnace for calcination for 2 hours at 600°C, where the hydrogen titanate topography was converted into TiO_2. The disks were cooled and stored in a clean, closed plastic Petri dish until utilised.

3.2 Characterisation of TiO_2 Nanotopography

3.2.1 Scanning Electron Microscopy (SEM)

Disks were prepared for electron microscopy by sputter coating (Emitech K757X) the surface with a conductive metal layer of ~6 nm thick consisting of 20% palladium and 80% gold. The samples were imaged on a FEI Quanta 200 scanning electron microscope at various magnifications. The height, density, diameter of the nanospikes and average pocket/niche diameter were measured. Three different areas of two disks in each batch were imaged.

3.2.2 Atomic Force Microscopy (AFM)

The nanotopography was imaged and the average height, surface area and RMS roughness were quantitatively measured using AFM. Nanospikes were imaged using an AFM (Digital Instruments INC Nanoscope IIIa Atomic Force Microscope) and contact probe tips (MikroMash). An area of 25 μm^2 with a scan rate of 0.5 Hz and 512 lines was investigated.

3.2.3 Optical Profilometry (OP)

The maximum and RMS (average-root mean square) surface roughness and average heights of the nanospikes were measured using optical profilometry. Nanospike disks were placed onto the optical profilometer (Proscan 2100) and an area of 400 μm^2 was investigated. The RMS and maximum roughness were calculated. The maximum roughness is the vertical distance between the lowest valley and highest peak observed along the profile length.

3.2.4 Confocal Microscopy (CM)

The nanospike dimensions and surface roughness were measured using confocal microscopy. Nanospike disks were placed onto a confocal microscope (Olympus LEXT OLS3100) and the maximum, minimum and average peak heights and surface roughness were recorded. An area of 100 x 100 µm was measured.

3.2.5 Transmission Electron Microscopy (TEM)

TEM was used to visualise the internal crystal structure of single TiO_2 nanospikes. 2-hour nanospikes were grown on pure titanium substrate. The nanotopography was then scraped off using a new scalpel into absolute ethanol. The solution was sonicated for 30 seconds to help disperse the nanospikes. A drop was pipetted onto lacey copper mesh TEM support grids (Agar Scientific, AGS166) and allowed to dry. The nanospikes were analysed on a Jeol 1400 TEM.

3.2.6 X-Ray Photoelectron Spectroscopy (XPS)

The surface elemental composition of mirror polished pure titanium disks and 2-hour nanospike disks were analysed by XPS. A monochromatic Al Kα X-Ray source was used with a photon energy of 1486.6 eV and anode operating energy of 15 kV. The base pressure was ~2×10^{-10} bar. A survey scan (settings of 0.5 eV steps, 0.1 s dwell time, epass 40 and range between 1100 and -10 eV) was initially carried out to determine the elemental peaks in the sample. Ti2p, O1s, C1s, N1s peaks were observed. Further scans were carried out for each of these elements:

- Ti2p: 20 scans, range of 482.5 to 449 eV, 0.1 eV step, 0.1s dwell time and epass 30
- O1s: 50 scans, range of 536.5 to 511.5 eV, 0.1 eV step, 0.1s dwell time and epass 30
- C1s: 50 scans, range of 295 to 278 eV, 0.1 eV step, 0.1s dwell time and epass 30
- N1s: 40 scans, range of 405 to 393 eV, 0.1 eV step, 0.1s dwell time and epass 30

Peaks were fitted using the CasaXPS software.

3.2.7 X-Ray Diffraction (XRD)

Grazing incident X-Ray diffraction was carried out to investigate the crystal structure of the nanospikes at each stage of the alkaline hydrothermal treatment and post hydrothermal treatment.

The XRD data collection and analysis were carried out by Dr Patryk Wasik, University of Bristol on the beamline BM28 (XMaS) at the European Synchrotron Radiation Facility (Grenoble, France). Samples were tilted at 0.7° and the X-Ray beam had a wavelength of 0.09nm. The sample-detector distance was 0.243 m, which was located at 8° and 30°. ZnO powder (Sigma-

Aldrich) was used as a calibrant. The images collected were converted into 1D profiles using the azimuthal integration procedure with the pyFAI software package (Kieffer and Karkoulis, 2013).

The Spurs and Myers Equation (**Equation 3.1**) was used to calculate the percentage of anatase and rutile titanium dioxide present after the final calcination step and post alkaline hydrothermal treatment.

$$Anatase\ Percentage\ (\%)\ [A] = \frac{100 \text{ x } I_A}{I_A + 1.265 \text{ x } I_R}$$

$$Rutile\ Percentage\ (\%)\ [R] = 100 - [\text{A}]$$

Where:

I_R = Intensity of rutile 110 peak

I_A = Intensity of 101 peak

Equation 3.1

3.2.8 Energy-Dispersive X-Ray Spectroscopy (EDX)

EDX was carried out to determine the elemental composition of the 2-hour nanospikes. The nanospikes were prepared and fixed onto a copper mesh as described in **Section 3.2.5**. Two points on a nanospike were chosen and an electrical voltage spectrum between 0 and 20 keV was analysed.

3.3 Bacterial Interactions with Nanotopographical Surfaces

3.3.1 Growth and Preparation of Bacteria

Bacterial strains used in these studies are listed in **Table 3.1**. Broth cultures (10 ml) were incubated for 16 hours at 37°C, 220 rpm. These were then sub-cultured into 20 ml pre-warmed broth in a 50 ml conical flask to an optical density at 600 nm (OD_{600}) of 0.1 and further incubated at 37°C, 220 rpm until the start of exponential phase growth (usually after 1.5-3 hours). Bacteria were then adjusted to the desired cell density. Bacteria were routinely cultured in Luria Bertani (LB) broth or Mueller Hinton (MH) broth (Sigma-Aldrich).

BACTERIAL STRAIN	MORPHOLOGY	GRAM IDENTITY	MOTILITY	STRAIN ID
Pseudomonas aeruginosa PAO1	Bacillus	Gram negative	Motile	Provided by J. Spencer (UB 2888)
Escherichia coli DH5α	Bacillus	Gram negative	Motile	Provided by H. Jenkinson (UB 776)
Klebsiella pneumoniae IS-2662A	Bacillus	Gram negative	Non-motile	Provided by M. Avison (UB 2703)
Staphylococcus aureus Newman	Coccus	Gram positive	Non-motile	Provided by T. Foster (UB 1621)

Table 3.1- *Bacterial strains used and relevant characteristics.*

3.3.2 Assessing Bacterial Viability on Surfaces

A key approach to assess the bactericidal properties of nanotopographical disks is to quantify the percentage of dead and viable bacteria on the disks. Previous research has shown that there is no single method to achieve this accurately, especially when applied to surfaces with nanotopography. Several methods were therefore investigated here to optimise the quantification of bacterial viability upon interaction with the surfaces.

To sterilise the titanium disks prior to inoculation, disks were immersed in absolute ethanol for 10 minutes within a clean plastic Petri dish, thoroughly washed with 0.01 M Tris-HCl, and then air dried within a flow hood (Brassaire). Once dried, the disks were stored in sterile Petri dishes until utilised.

3.3.2.1 Viability qPCR

Viability quantitative polymerase chain reaction (v-qPCR) was assessed as a potential method to quantify the viability of bacteria adhering to the nanospike disks.

Flat mirror polished disks and 2-hour nanospike disks (4 of each) were placed within a 12-well plate, immersed in 1 ml of LB broth containing 10^7 CFU *P. aeruginosa* and incubated for 3 hours at 37°C. The disks were rinsed in Tris-HCl and transferred to a 24-well plate containing 400 µl phosphate buffered saline (PBS). Propidium monoazide (PMAxx) was added to two disks of each surface type at a final concentration of 50 µM and then left for 10 minutes in the dark to allow for complete dye uptake. To photolyse the PMA, the plate was placed on a bed of ice on a rotating platform (Stuart Scientific mini orbital shaker S05) set at 50 rpm and exposed to a 650 W halogen lamp (Britek H80615), positioned 20 cm above, for 5 minutes within a dark room.

Each disk was then transferred to a well of a new 24-well plate and genomic DNA extraction was carried out using the Qiagen QIAamp DNA extraction kit. Each disk was immersed in 400 µl ATL buffer and 20 µl Proteinase K and incubated at 56°C, 100 rpm for 1 hour. The plate was then removed and 40 µl of 10 mg/ml RNase was added for 10 minutes at ambient room temperature, with occasional mixing. AL buffer (400 µl) was added and incubated at 70°C for 10 minutes. Finally, 400 µl of absolute ethanol was added to the solution and mixed. The lysate was then transferred into a spin column and the DNA precipitated and washed, according to manufacturer's instructions. DNA was eluted in 50 µl of AE buffer, quantified using a nanodrop (Simplinano) and stored at -20°C.

Reactions (20 µl final volume) for qPCR comprised 200 nmol universal 16S rDNA primers U16SRT-F and U16SRT-R (Clifford *et al.*, 2012), 1x iQ SYBR Green super mix (Bio-Rad) and 5 µl DNA template. A positive control of 5 µl of *P. aeruginosa* genomic DNA and a negative control using PCR water were included. The qPCR reactions were performed in a MyCycler™ thermocycler (Bio-Rad) according to the following parameters: 3 minutes at 95°C; 40 cycles of 30 s at 95°C, 30 s at 56°C and 30 s at 72°C; melt curve analysis with successive 2 s cycles at incremental temperature increases of 0.2°C from 56°C to 90°C. The purity of the amplicons generated was confirmed by gel electrophoresis analysis of 5 µl of each sample. The electrophoresis was run at 100 V for 50 minutes, and the gel visualised by UV on an Amersham Imager 680 (GE Healthcare).

To investigate the potential of the v-qPCR technique to distinguish between viable and dead bacteria, standard *P. aeruginosa* templates were prepared: 100% viable; 100% non-viable, prepared by heat inactivation at 70°C for 20 minutes in a water bath (Grant Instruments); 50% viable, prepared by mixing at a 50:50 ratio the 100% viable and non-viable samples. The non-viable sample was confirmed by lack of growth on LB agar. PMAxx (5 µl) was then added to

each microtube and incubated in the dark for 10 minutes at ambient room temperature. Photolysis of PMA was performed, the suspension centrifuged at 12,000 *g* for 4 minutes, and the resulting pellet resuspended in ATL buffer. DNA was then extracted as described previously and quantified using a nanodrop (SimpliNano). DNA was normalised to the lowest concentration measured, and 5 µl used as template DNA, as described previously. A standard curve was also produced by performing a 10-fold serial dilution of *P. aeruginosa* genomic DNA from 50, 5, 0.5, 0.005 and 0.0005 ng. The curve was produced by plotting a log quantity of initial genomic DNA against the threshold cycle.

3.3.2.2 Lactate Dehydrogenase (LDH) assay

Lactate dehydrogenase (LDH) assay is a colorimetric assay that quantifies the amount of LDH in a solution as it reduces NAD to NADH. Since LDH is a cytoplasmic enzyme, this assay has the potential to be a measure of bacterial lysis on the nanospike disks.

Flat control and nanospike disks, in duplicate, were immersed in 400 µl of *P. aeruginosa* suspension (10^6 CFU/ml) within a 24-well plate and incubated for 1 or 3 hours at 37°C. There were two background controls: one with only LB broth and a maximum lysis control, where all the bacteria were lysed by addition of SDS/Triton-X100 (Sigma). Aliquots (50 µl) from each well were then transferred into a 96-well plate (Greiner Bio-one) and mixed with 50 µl Cytotox96 reagent (Promega, G1780). The plate was left for 30 minutes in the dark at room temperature before addition of 50 µl Stop Solution (Promega, G1780). Viability was calculated from A_{490} readings on a microplate reader (BioRad I-Mark) according to **Equation 3.2**:

$$Viability\ (\%) = 100 * \frac{Experimental\ LDH\ release\ (at\ 490\ nm)}{Max\ LDH\ release\ (at\ 490\ nm)}$$

Equation 3.2

3.3.2.3 Live/Dead Staining

*Bac*Light™ live/dead staining (Invitrogen) was used to investigate the membrane integrity of adherent bacteria on the nanotopographical surfaces.

The surface of each disk was inoculated with 40 µl of a bacterial suspension of known cell density and incubated at 37°C for 3 hours. Disks were washed with Tris-HCl by gentle agitation with a pipette. A 3 µl aliquot of SYTO9/Propidium iodide (Thermo-Fisher) was added to 1 ml Tris-HCl

and mixed. This solution (40 µl) was then added to each surface and left for 15 minutes in the dark at ambient room temperature. Disks were then washed twice with Tris-HCl to remove excess stain. The disks were placed onto a glass slide and covered with a glass cover slip and imaged under a fluorescence microscope at wavelengths 450-490 nm and 515-560 nm. The relative numbers of bacterial cells with intact membranes, fluorescing green, and membrane compromised cells, fluorescing red, were quantified using the Image J (NIH) software.

3.3.2.4 BacTiter-Glo™

BacTiter-Glo™ assay (Promega) is an endpoint assay that provides a method for determining the number of viable bacterial cells by measuring the amount of ATP present in a solution via luminescence. The bacterial cells are lysed, and ATP released into the solution. Beetle luciferin in the presence of ATP, oxygen, magnesium and luciferase then produces a luminescence signal that is proportional to the amount of ATP present in the solution and thus an indication of the number of viable cells.

Aliquots (40 µl) of bacterial suspension ($1x10^6$ CFU/ml) were pipetted onto the surface of flat and nanospike disks within a white, opaque 24-well plate and incubated within a humidity chamber at 37°C for 0.5-3 hours. BacTiter-Glo reagent (40 µl) was added to the bacterial suspension and the luminescence measured in a plate reader (Teccan Infinite F200 Pro) with automatic attenuation and 1000 ms integration time.

In a variation of this method when using ChoM-functionalised disks, the disks were submerged in 400 µl bacterial suspension ($5x10^5$ CFU/ml) and incubated for 3 hours. Aliquots of suspension (40 µl) in duplicate were then transferred to a 24-well plate, mixed with 40 µl BacTiter-Glo reagent, and luminescence measured as above. To investigate the effects of agitation on ChoM release, this experiment was also performed using an orbital shaking incubator, with disks incubated for 3 hours at 100 rpm.

The delayed release of ChoM was investigated by incubating disks in 400 µl MH broth for 3 or 12 hours. Aliquots (50 µl) were then transferred in duplicate into a 24 well plate and mixed with an equal volume of bacterium (such as *E. coli, K. pneumoniae* or *S. aureus)* suspension ($1x10^6$ CFU/ml). Plates were incubated at 37°C for 1 hour, and 40 µl of each suspension was then transferred in duplicate into a white, opaque 24-well plate (Perkin Elmer, 24-50-6005168) and bacterial viability determined using BacTiter-Glo, as described above.

3.3.2.5 BacTiter-Glo™ Standard Curves

Bacterial suspensions were grown up to mid-exponential phase and 10 dilutions of a 1:4 dilution was carried out from the neat concentration. In triplicate, 50 µl of each diluted inoculum was transferred to a white opaque 96-well microplate (Perkin Elmer, 6005680) and the bacterial viability determined using BacTiter-Glo, as described above. In tandem, the CFU for each dilution was found by Miles and Misra spot technique. The number of CFU were counted and a luminescence-CFU standard curve plotted.

3.3.2.6 RealTime-Glo™

RealTime-Glo assay (Promega) allows continuous monitoring of the metabolic activity of mammalian or bacterial cells. Viable cells reduce the RealTime-Glo substrate, which then diffuses out of the cell into the surrounding medium. NanoLuc luciferase uses this reduced substrate to produce a luminescence signal that can be quantified and is proportional to the number of viable cells. Dead cells are unable to reduce the substrate and so no luminescence is produced.

Exponential phase bacterial inocula (1 ml) were prepared, mixed with 1 µl of MT Cell Viability Substrate and 1 µl of NanoLuc Enzyme, and incubated in the dark for 1 hour at 37°C, 220 rpm. This was to allow the bacteria to take up the RealTime-Glo reagents and initiate generation of a detectable luminescence signal. Bacterial suspensions (40 µl) were pipetted onto disks within a white, opaque 24-well plate, which was then sealed with transparent film (Greiner Bio-one EasySeal Plate Sealer) to ensure sterility and to prevent the surfaces from drying out. The plate was placed in a preheated (37°C) plate reader (Tecan infinite F200 Pro) and luminescence recorded every 10 minutes for approximately 11 hours with 1000 ms integration time, wait time of 0.1 seconds and settle time of 150 ms.

3.3.3 Visualising Bacterial Interactions with Nanospike Surfaces

3.3.3.1 SEM Imaging

The methodology for bacterial fixation was refined over the course of this project due to observations of bacterial membrane dehydration leading to potential inaccuracies and false positives. Initially, bacteria were incubated on the surface for a determined time duration. Disks were then immersed, within a 24-well plate, in 2.5% glutaraldehyde (FisherBiotech)/0.1 M potassium phosphate buffer (KH_2PO_4:K_2HPO_4, pH 7.2) (monobasic-Calbiochem, 52968, dibasic-Analak, 104363A) for 2 hours at room temperature. The disks were dehydrated by immersing in

increasing concentrations of ethanol (20%, 40%, 60%, 80% and 100%) for 10 minutes each. Finally, the disks were immersed in hexamethyldisilazane (Sigma-Aldrich) for 10 minutes.

This methodology was modified after membrane dehydration was observed. The samples were instead immersed in 2.5% glutaraldehyde/0.1 M sodium cacodylate for 2 hours at 4°C, then incrementally dehydrated as before until the 100% ethanol stage. Instead of hexamethyldisilazane treatment, the samples were critically point dried (Leica CPD300). Disks were then mounted onto 0.5" aluminium specimen stubs (Agar Scientific) with sticky double-sided carbon tabs (Agar Scientific) and sputter coated as described in **Section 3.2.1**.

3.3.3.2 Focussed Ion Beam Milling

This protocol was performed by Joshua Jenkins of the University of Bristol to investigate the interaction between the underside of the bacterial cell and the nanospikes. Focussed ion beam milling was used to sequentially slice the bacterium while taking SEM images. These slices were later collated to generate a 3D model.

Nanospike surfaces were sputter coated, as described in **Section 3.2.1**, sterilised, and inoculated with *E. coli* or *S. aureus*, as described in **Section 3.3.1**. Following incubation at 37°C for 3 hours, samples were fixed for 12 hours with 2.5% glutaraldehyde/ 0.1 M NaC buffer at 4°C. Samples were washed in 0.1 M NaC buffer three times for 5 minutes on ice then incubated in 2% reduced osmium for 60 minutes on ice. Subsequently, samples were washed in deionised water three times for 5 minutes, incubated in thiocarbohydrazide for 20 minutes and washed in deionised water three times for 5 minutes at room temperature.

Samples were then incubated in 2% aqueous osmium for 30 minutes at room temperature, washed in deionised water three times for 5 minutes at room temperature, and incubated in aqueous 1% uranyl acetate for 1 hour at 4°C. Finally, samples were washed in deionised water three times for 5 minutes at room temperature, incubated in lead aspartate for 30 minutes at 60°C, and washed in deionised water three times for 5 minutes at room temperature. Samples were dehydrated in pre-chilled (4°C) ethanol at 20, 50, 70, 90 and 100% for 10 minutes each. Samples were then critically point dried and finally sputter coated with gold and palladium.

Titanium disks were loaded into the chamber of the Scios DualBeam (FEI) and the system was pumped to generate a vacuum. Before cross sectional analysis, the stage was tilted by 52°, moving the titanium disks perpendicular to the gallium ion beam. Area scanning was performed using an electron beam with an accelerating voltage of 5 kV and current of 50 pA. Prior to ion beam milling, a protective platinum layer (500 nm) was deposited on each bacterium. Rough cut trenches were milled around coated bacteria to depths of 250 nm, using an accelerating voltage

of 30 kV, and current of 1 nA. Auto Slice and View software was used to carry out sequential sectioning of *E. coli* and *S. aureus* in 20 nm slices. This was performed with an ion beam accelerating voltage of 30 kV, and current of 30 pA. Images of each section were acquired using electron beam accelerating voltages of 5 kV and current of 50 pA. 3D models of each bacterium upon nanospikes were made using Avizo modelling software.

3.4 Antimicrobial Peptide Synthesis, Biofunctionalisation and Release

The AMP, ChoM, was synthesised at the National Physical Laboratory (NPL) by Dr Smita Gunoo and Dr Brunello Nardone using solid phase peptide synthesis. ChoM was biofunctionalised onto 2-hour nanospikes and its release and activity against several species of bacteria were investigated.

3.4.1 Solid Phase Peptide Synthesis (SPPS)

Solid phase peptide synthesis (SPPS) was used to generate ChoM, with a peptide sequence of KWKVFKKIEKMIRNIRNKIVK. Amino acids (Novabiochem) were weighed and dissolved in dimethylformamide (DMF) to a concentration of 0.2 M (**Table 3.2**). Resin (250 mg; Iris Biotech TG S RAM (90 µm)) was swelled in DMF, 297 ml piperidine, 35 ml 1 M activator base Oxyma, 65 ml activator disoproylcarbodiimide (DIC).

Amino Acid	POWDER WEIGHT (g)	DMF VOLUME (ml)
Arginine (R)	1.56	12
Asparagine (N)	0.72	6
Glutamate (Q)	0.26	3
Isoleucine (E)	0.85	12
Lysine (K)	2.25	24
Methionine (M)	0.23	3
Phenylalanine (F)	0.24	3
Tryptophan (W)	0.32	3
Valine (V)	0.41	6

Table 3.2- *Preparation of amino acids for SPPS synthesis.*

The peptide was assembled on a Liberty-1 microwave peptide synthesizer (CEM Corp). The synthesis of the peptide chain involved six main steps as illustrated in **Figure 3.1**. Rink amide-4-methylbenzhydrylamine resin (Novabiochem, UK) was used as the insoluble polymer resin, which acts as the 'anchor' from which the peptide chain grows.

Step 1 involves cleaving the Fmoc group (Fluorenylmethyloxycarbonyl) from the resin with piperidine (Merck), a weak base, to allow the amino acids to subsequently bond. The removal of the Fmoc group from the resin and amino acids was monitored after each cycle by UV absorbance at 301 nm. DMF was then used to wash away any soluble by-products, cleavage agents and excess reagents.

Steps 2, 3 and 4 involves the attachment of an amino acid, with its amine group (protected by Fmoc), through a coupling reaction of the now newly free amino group onto the linker (resin or previously attached amino acid). The coupling reagent 2-(1H-benzotriazol-1-yl)-1,1,3,3,-tetramethyluronium hexafluorophosphate (HBTU) was required to initiate the condensation reaction as the carboxylate group, on the to-be-bound amino acid (B), is not very reactive. The carboxylic acid on amino acid (B) reacted with the reagent HBTU to yield a reactive intermediate that binds to the amino group of amino acid (A) to form a covalent amide bond. DMF was again used to remove side products and excess reagents.

Step 5 is a repeat of steps 1, 2 and 3 to attach further amino acids to the sequentially grown peptide chain. Each amino acid has unique side chains from its alpha carbon atom that are protected by tBu (tert-Butyl esters) to prevent unwanted reactions from occurring. tBu is not washed away during the piperidine addition as it is base stable.

Step 6 involves cleavage of the peptide from the resin and removal of the tBu protection of the amino acid side chains using 95% trifluoracetic acid (TFA) (Merck)/2.5% Triisopropylsilane (TIS) (Sigma-Aldrich)/2.5% deionised water.

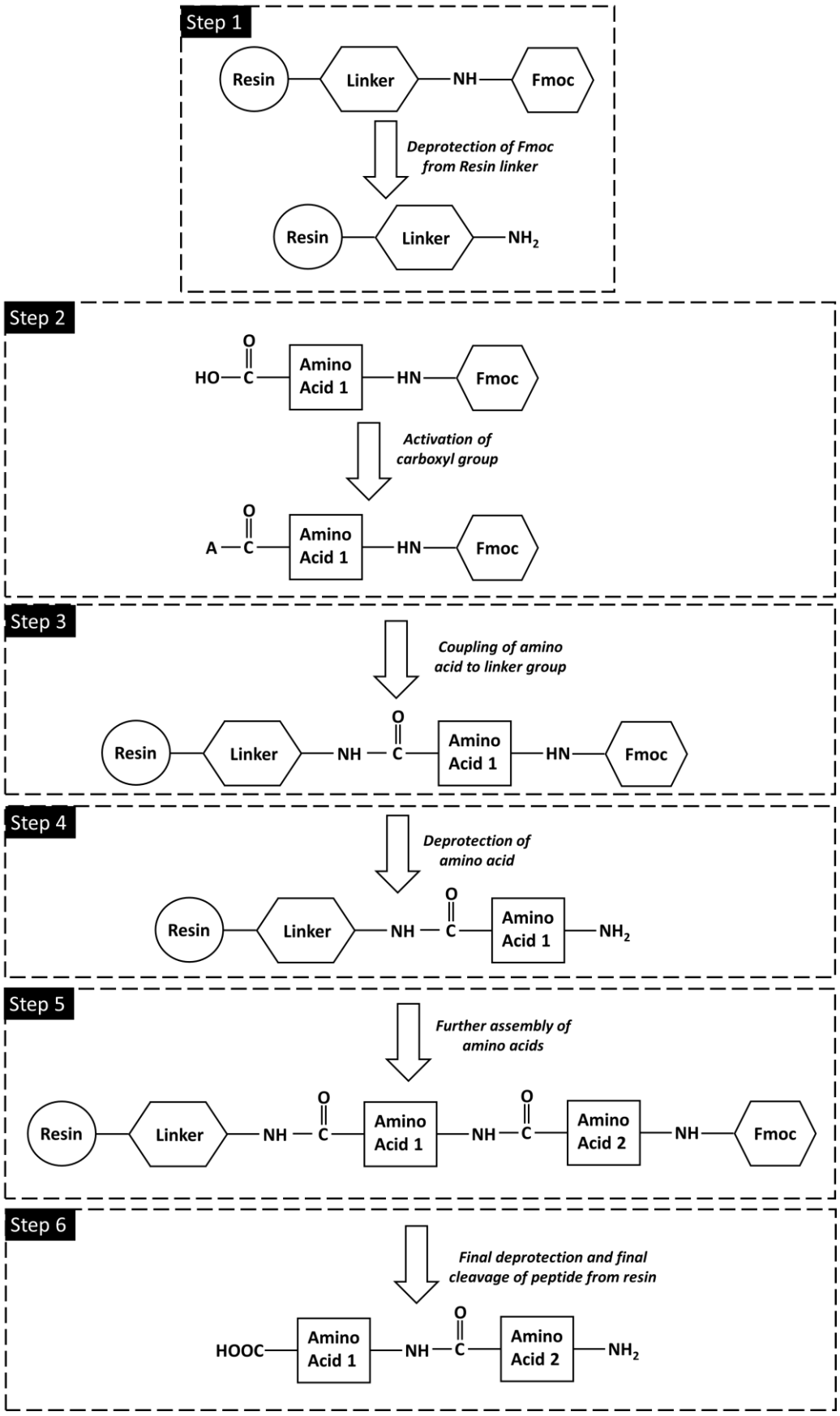

Figure 3.4- *Illustration of SPPS steps.*

3.4.2 MALDI-TOF

Matrix Assisted Laser desorption/ionization-Time of Flight Mass Spectroscopy (MALDI-TOF) was used to confirm the peptide product synthesised by calculating its mass to charge ratio (m/z).

Peptide solution (2 µl) was mixed with 2 µl of dihydrobenzoic acid (DHB) (Merck) as the matrix, and 2 µl of TFA as a counter ion source to generate the M+H ions. This solution (2 µl) was pipetted onto a metal plate and air dried. The plate was placed within a MALDI-TOF machine (Bruker autoflex III), where the compound was subjected to approximately 1000 UV nitrogen laser beam flashes. The mass to charge ratio was calculated.

3.4.3 Reverse Phase-High Performance Liquid Chromatography (RP-HPLC)

Two different HPLC techniques were used in this project. HPLC separates molecules within a solution based on their relative hydrophobicity. The more hydrophobic a molecule is the longer it takes to travel through the column. The first approach was semi-preparative HPLC, which was used to purify the peptide solution.

Crude ChoM was resuspended in 20% ACN (80% deionised water, 20% CAN, 0.001% TFA). The peptide was injected into a Vydac C18 semi-preparative (5 µm) column at 4.7 ml/min and 150 bar pressure with runs of 10− 60% B gradient over 50 min. Buffer A – 5% (vol/vol) and buffer B – 95% (vol/vol) aqueous CH_3CN, 0.1% TFA. The column eluate was aliquoted into glass tubes every 30 s. The contents of the tubes were analysed with MALDI-TOF as described in **Section 0** to determine the purest ChoM peptide fractions. These fractions were pooled and freeze dried to obtain a powder. The second technique was analytical HPLC (ThermoFisher UltiMate 3000) and was used to quantify the purity of the final peptide solution. The peptide was injected into Vydac C18 analytical (5 µm) column at used a 10− 60% B gradient over 50 min at 1 ml/min with detection at 230 and 220 nm. Buffer A – 5% (vol/vol) and buffer B – 95% (vol/vol) aqueous CH_3CN, 0.1% TFA.

3.4.4 Minimum Inhibitory Concentration (MIC) Assay

This assay was undertaken to find the minimum concentration of peptide required to inhibit the growth of bacteria over a 24-hour period.

Peptide stocks were 2-fold serially diluted in fresh MH broth to final concentrations of 100 µM to 0.4 µM in a 96-well plate. Exponential phase bacterial inocula (100 µl, 10^6 CFU/ml) were

added and the plate incubated at 37°C for 24 hours. A negative control comprising bacteria without peptide and a blank control of MH broth alone were included. Wells were measured by absorbance at 595 nm. The ChoM concentration at which there was no difference in absorbance compared to the blank control was denoted as the MIC.

3.4.5 Functionalisation of Surface with AMP

Peptide aliquots (40 µl) were pipetted onto a surface and left to dry at ambient room temperature under sterile conditions (within a flow hood) until visually dried (typically around 3 hours). The surface was stored at 4°C until required.

3.4.6 ChoM Release Quantification using Nanodrop

The release of ChoM from flat and 2-hour nanospike disks was quantified on the Nanodrop (SimpliNano) at 280 nm. Deionised water (40 µl) was pipetted onto the surface and incubated at 37°C for a determined time duration. Aliquots (2 µl) were transferred at periodic intervals to the Nanodrop for A_{280} measurements.

3.4.7 ChoM Release Quantification by Bacterial Growth

For this assay the peptide release profile was assessed as a function of bacterial growth.

Flat and 2-hour nanospike disks were functionalised with 40 µl of 50 µM ChoM as described in **Section 3.4.5**. The disks were placed in duplicate in a 24-well plate, to which 40 µl of MH broth was added and incubated at 37°C in a humidity chamber. At the chosen time point (10, 30 minutes, 1, 2 or 3 hours), 20 µl of the broth from each of the disks was removed and transferred into a 96-well plate. A 5-point, two-fold dilution was carried out with MH broth, and then mixed with 20 µl of bacterial inoculum ($1x10^6$ CFU/ml). Plates were incubated at 37°C for about 20 hours with gentle agitation (100 rpm). The absorbance of each well was measured at 595 nm to quantify bacterial growth.

3.4.8 Effect of Ultrasound Stimulation on ChoM Release

Stimulated ChoM release from the disks was investigated with low sonication power through a nanokick device (University of Glasgow) with a frequency of 1 kHz.

Functionalised disks were incubated with 400 µl of bacterial suspension ($5x10^5$ CFU/ml) for 3 hours at 37°C on top of a nanokick device covered with a magnetic strip (MagnetExpert). Levels of bacterial viability were then determined using BacTiter-Glo, as described in **Section 3.3.2.6**.

3.4.9 SEM Imaging of Functionalised Surfaces

SEM imaging was used to visualise the flat and nanospike functionalised surfaces before and after incubation with broth. Functionalised disks were incubated in broth from 10 min to 3 hours and then removed. Disks were left to air dry, sputter coated and imaged as described in **Section 3.2.1**.

3.4.10 Wettability

Disks were mounted onto a drop shape analyser (Kruss DSA30R) and a 2 µl drop of deionised water was pipetted onto the surface. Three samples of each disk type were analysed, and the resulting angle of three different drops were recorded on each surface. As the water droplet completely spread over the nanotopography sample, a high-speed camera was used to film the spreading of the drop over time. Images were taken every 0.001 seconds.

3.5 Biocompatibility and Osteogenic Potential

The following experiments were carried out by Laila Damiati at the University of Glasgow. Here the biocompatibility and osteogenic potential of non-functionalised and 100 µM ChoM-functionalised flat titanium and 2-hour nanotopography surfaces were assessed. The flat titanium and 2-hour nanospike disks were created at the University of Bristol.

3.5.1 Cell Culture

Human mesenchymal stem cells (hMSCs) (Promo cell) were cultured in Dulbecco's modified essential medium (DMEM) (Sigma-Aldrich) supplemented with 1% penicillin/streptomycin (Invitrogen), 1% sodium pyruvate (Sigma-Aldrich), 1% non-essential amino acids (Sigma-Aldrich), and 10% foetal bovine serum (FBS) (Invitrogen) at 37°C in 5% CO_2. No cells beyond passage 4 were used. During the cell culture on the titanium substrates, wells were supplemented with 500 µl of 5% FBS and the medium replenished every 3 days.

3.5.2 Alamar Blue Assay

AlamarBlue solution (Bio-Rad) was mixed 1:10 in DMEM, 900 µl was added to each coverslip, and then incubated for 6 hours at 37ºC in 5% CO_2. Aliquots (3 x 200 µl) of solution were transferred to a 96 well plate and analysed using a Thermo- Scientific Multiskan FC. Absorbance was analysed at A1= 570 nm and A2 = 600 nm. The percentage reduction was calculated according to **Equation 3.3**:

$$\%\ Reduced = \frac{(O600\ X\ A570) - (O570\ X\ A600)}{(R570\ X\ N600) - (R600\ X\ N570)}\ X\ 100$$

Equation 3.3

Where:

$O600$ = molar extinction coefficient (E) of oxidized alamarBlue® (Blue) at 600 nm

$O570$= E of oxidized alamarBlue® at 570 nm

$R570$ = E of reduced alamarBlue® at 570 nm

$R600$= E of reduced alamarBlue® at 600 nm

$A570$ = absorbance of test wells at 570 nm

$A600$= absorbance of test wells at 600 nm

$N570$ = absorbance negative control well (media plus alamarBlue®, no cells) at 570 nm $N600$ = absorbance negative control well (media plus alamarBlue®, no cells) at 600 nm

3.5.3 Immunofluorescence Staining

For focal adhesions, hMSCs were seeded onto the disks at a cell density of 3000 cells/cm^2. The samples were incubated for 3 days then washed with PBS (Sigma-Aldrich), fixed with 3.7% v/v formaldehyde/PBS for 15 minutes at 37ºC, permeabilized and stained for vinculin using monoclonal anti-vinculin antibody (1:100 dilution) (Sigma-Aldrich) and actin diluted in 1:500 PBS/BSA. Antibody was removed, and cells washed three times for 5 min with PBS/0.5% v/v Tween. Secondary antibody (horse anti-mouse IgG, Biotinylated, Vector laboratories, UK Z0715) was added for 1h at 37ºC. Antibody was removed, and cells washed 3x for 5 min with PBS/0.5% v/v Tween. Streptavidin-FITC (Vector laboratories, UK SA-5001) was added and incubated at 4ºC for 30 mins then washed three times for 5 min with PBS/0.5% v/v Tween. A small drop of Vectorshield-DAPI (Vector Laboratories) was added before microscopy.

3.5.4 Alizarin Red S Staining

Alizarin Red S (ARS) staining was used to qualitatively indicate calcium deposition within the cells, indicative of osteogenic differentiation. Culture medium was removed from the titanium surface, which was gently washed three times with PBS. The cells were then fixed with 4% formaldehyde for 15 minutes at room temperature. The fixative was removed, and the surfaces washed three times with diH_2O. The water was removed and 1 ml of 40 mM ARS (Sigma-Aldrich) was added to each surface and incubated at room temperature for 20 - 30 min with gentle shaking. The dye was removed, and the cells washed five times with diH_2O. Excess water was removed, and the cells were imaged using a phase microscope.

3.5.5 von Kossa staining

von Kossa staining was carried out to visualise deposits of phosphate. The titanium surfaces were first washed in PBS followed by fixation in 3.7% v/v formaldehyde/PBS for 15 minutes at 37°C. A solution of 5% silver nitrate (Sigma-Aldrich) was added, and the plates were exposed to UV light for 30 min. The plates were then rinsed three times with diH_2O before adding 5% sodium thiosulfate (Sigma-Aldrich) for 10 min. The plate was washed with tepid running tap water for 10 min, followed by three further washes in diH_2O. Samples were quickly dehydrated by adding 70% EtOH prior to light microscopy to detect any mineralization.

3.5.6 Giemsa staining

Giemsa staining was used to visualise and assess the morphology and confluency of the hMSCs. After cell fixation, the cells were stained with Giemsa stock solution (Gurr) for 1 minute and washed thoroughly with distilled water. The samples were air-dried and observed using a Zeiss immunofluorescence microscope under fluorescent illumination at 495 nm/519 nm (excitation and emission) and under normal light.

3.5.7 qRT-PCR

Quantitative reverse transcriptase-polymerase chain reaction (qRT-PCR) was used to measure the expression of three genes: osteocalcin (OCN), osteopontin (OPN), osteonectin (ON), which are indicative of osteogenic differentiation.

Total RNA was extracted at day 28 of cell culture using a Qiagen RNeasy Micro kit and protocol. To standardise for quantitative analysis, equal amounts of RNA from each sample were used for cDNA synthesis using the Qiagen QuantiTect RT-PCR kit and protocol. qRT-PCR was carried out using the Qiagen Quantifast SYBR Green kit and the reactions run in a 7500 Real Time PCR cycler (Applied Biosystems). Reaction parameters were 10 minutes at 95°C; 40 cycles of 15 s at 95°C and 60 s at 60°C. Four biological and two technical replicates from each sample were analysed. Expression of OCN, OPN and ON was normalised against the housekeeping gene glyceraldehyde 3-phosphate dehydrogenase (GAPDH). The primers used are shown in **Table 3.3**.

Gene Name	PRIMER SEQUENCE
GAPDH	*Forward: TCAAGGCTGAGAACGGGAA*
	Reverse: TGGGTGGCAGTGATGGCA
Osteonectin (ON)	*Forward: AGAATGAGAAGCGCCTGGAG*
	Reverse: CTGCCAGTGTACAGGGAAGA
Osteopontin (OPN)	*Forward: ACAGCCGTGGGAAGGACAGT*
	Reverse: GACTGCTTGTGGCTGTGGGT
Osteocalcin (OCN)	*Forward: GCCCTCACACTCCTCGCC*
	Reverse: CTACCTCGCTGCCCTCCTG

Table 3.3- *Primers used for qRT-PCR*

3.5.8 Statistical Analysis

Statistical analysis was carried out with one-way ANOVA test followed by Tukey and Bonferroni post-hoc tests using SPPS 24 software (IBM). A p value of ≤ 0.05 was considered to be statistically significant.

4.

FORMATION AND CHARACTERISATION OF NANOTOPOGRAPHY

Contents

4.1 Introduction

In 1998 the alkaline hydrothermal technique was first used to grow TiO_2 nanotubes on TiO_2-based powder (Kasuga *et al.*, 1998). This TiO_2 nanotopography exhibited appealing properties such as photocatalytic activity, high surface area and layered walls, facilitating its potential as photocatalysts and humidity sensors (López Zavala, Lozano Morales and Ávila-Santos, 2017; Wong, Tan and Mohamed, 2011; Simović *et al.*, 2019; Liu *et al.*, 2014). The alkaline hydrothermal process has also been used to grow nanowires/nanotubes on substrates that mimic the topography observed on insect wings and have potential antimicrobial properties (Diu *et al.*, 2014; Tsimbouri *et al.*, 2016; Cao *et al.*, 2018).

Hydrothermal synthesis is an attractive method for the generation of nanostructures due to its simplicity and high and reliable yield. It is also environmentally friendly due to the relatively low temperatures and closed system operating conditions with water-diluted alkaline as the reaction medium (Wong, Tan and Mohamed, 2011; Simović *et al.*, 2019). The basis of the technique involves immersion of a titanium metal substrate into an aqueous alkaline solution, such as sodium hydroxide (NaOH), within an autoclave or acid-digestion vessel. This is heated to above boiling point to generate a saturated vapour pressure. The alkaline reaction with titanium forms titanite topography, and the physical structures and crystal composition can be manipulated or optimised by changing the operating conditions such as the temperature, duration of synthesis, alkaline molarity and volume and then with the subsequent heating and post treatment steps (Dong *et al.*, 2007; Wong, Tan and Mohamed, 2011).

The hydrothermal process consists of three major steps. The first results in the generation of alkaline titanate nanostructures. The second involves the substitution of alkali ions within the titanate with hydrogen ions by immersion in an acid. The third and final step involves heat dehydration in ambient air and crystallisation at an elevated temperature. On pure titanium, the conditions for the physical formation of nanotopography, reminiscent of topography seen on the surface of insect wings, have been studied by Dong *et al.* (2007) and Diu *et al.* (2014).

The nanotopographies generated have most commonly been visualised using SEM (Dong *et al.*, 2007; Simovic *et al.*, 2019), and their physical characteristics (such as nanospike height and diameter and roughness) quantified using SEM (Dong *et al.*, 2007), TEM (Song *et al.*, 2007), AFM (Guo *et al.*, 2017), optical profilometry (Ekoi *et al.*, 2019) and CLSM (Diu *et al.*, 2014). The elemental and crystal structure of various nanotopographies have been analysed through various techniques such as XRD (Dong *et al.*, 2011, 2007), EDX (Wang *et al.*, 2011; Lai *et al.*, 2015), XPS (Guo *et al.*, 2017; Song *et al.*, 2005) and TEM (Wang *et al.*, 2011; Dong *et al.*, 2011).

The objective of the studies presented in this chapter was to build upon the work of Dong *et al.* (2007), Diu *et al.* (2014) and Tsimbouri *et al.* (2016) and perform a systematic characterisation of nanotopography formation on titanium substrates using the alkaline hydrothermal method. Through systematic parameter changes of duration, temperature, sodium hydroxide molarity and volume, the surfaces were optimised for subsequent bactericidal analyses and antimicrobial peptide functionalisation. The nanotopography was visualised and physically characterised by multiple techniques (SEM, AFM, CM and optical profilometry) to compare quantitative measurements and more accurately estimate the dimensions of the topography. The crystal structure and chemistry of the nanotopography was analysed throughout the stages of the alkaline hydrothermal process using a range of techniques (EDX, TEM, XRD and XPS).

4.2 Formation of Nanotopography

4.2.1 Nanotopography at Different Stages of the Alkaline Hydrothermal Process

These experiments were carried out to analyse the formation of nanotopography during the different stages of alkaline hydrothermal treatment, and to investigate if there was any visual change in the topography with the subsequent post treatment. The alkaline hydrothermal method consisted of four stages:

1. Alkaline hydrothermal treatment to generate sodium titanate nanotopography.
2. Heat fixation at 300°C for 1 hour to ensure stabilisation of nanotopography to the pure titanium substrate.
3. Ion exchange in 0.6 M HCl between sodium ions in sodium titanate and hydrogen ions in the hydrochloric acid.
4. Calcination at 600°C for 2 hours to convert hydrogen titanate into titanium dioxide.

Figure 4.1 shows representative SEM images of nanospike structures at each stage of the alkaline hydrothermal process including the post treatment steps. These were made on mirror polished pure titanium substrate, as shown in **Figure 4.1A**. The first step involved the alkaline hydrothermal treatment at the conditions of 240°C, 1 M and 52 ml NaOH for 2 hours. As shown in **Figure 4.1B**, topography was formed at the first stage and could be observed across the whole surface as perpendicular spikes protruding from the surface. The following post-treatment steps

(**Figure 4.1C-E)** showed very little change in the conformity of the nanospikes, indicating that the nanotopography remained stable after the first alkaline hydrothermal treatment stage.

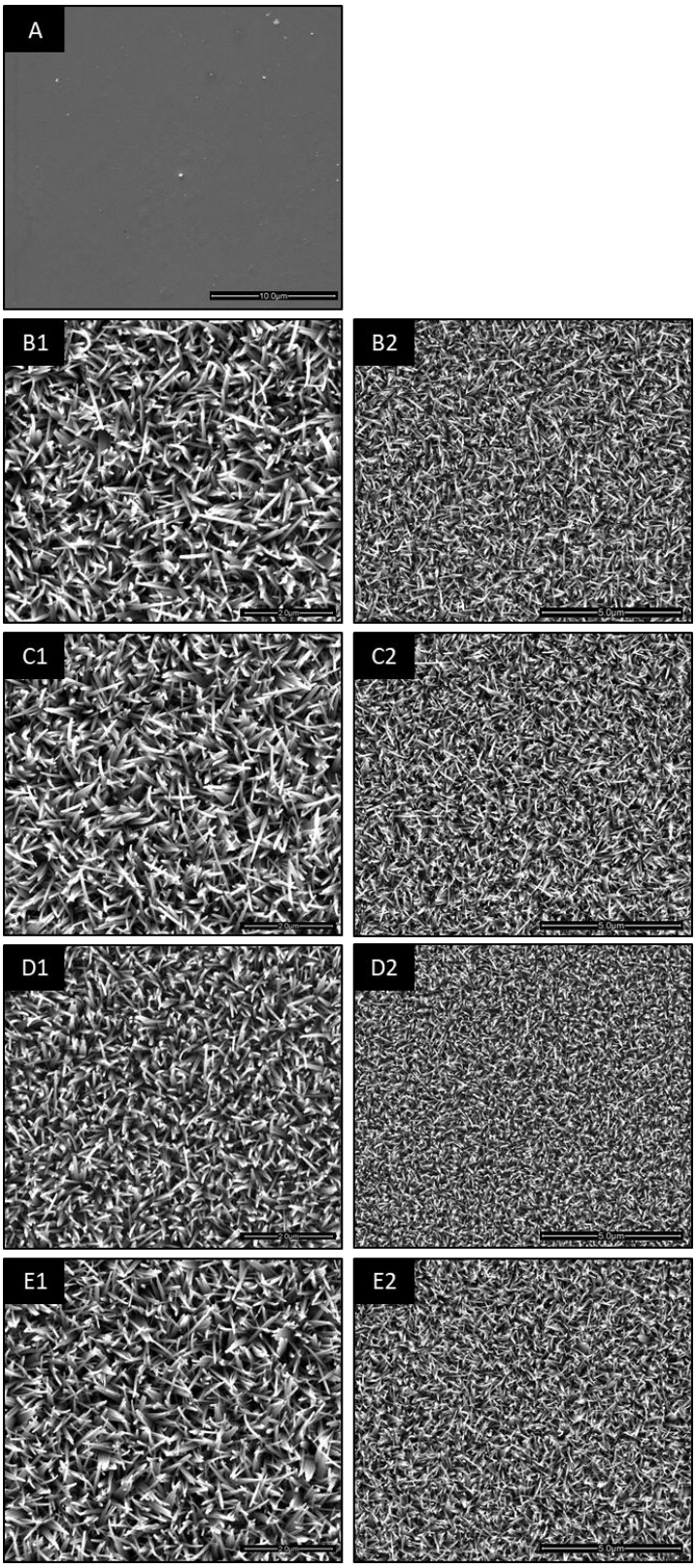

Figure 4.1- *SEM images showing nanotopography on titanium substrate at the four stages of alkaline hydrothermal treatment. A) Mirror polished flat titanium surface, B) Alkaline hydrothermal process at*

240°C, 2 hours, 1 M and 52 ml NaOH, C) After 300°C heat treatment, D) After 0.6 M HCl for 1 hour, E) After heat treatment at 600°C for 2 hours. Columns 1 and 2 show different magnifications.

4.2.2 Systematic Studies of the Alkaline Hydrothermal Process

After confirming the formation of nanotopography by the alkaline hydrothermal treatment process, further experiments were carried out by systematically changing the processing parameters at the alkaline hydrothermal treatment stage, to investigate the range of nanostructures that could be generated. Four key parameters that potentially could determine the nanotopography during the alkaline hydrothermal treatment were duration, temperature, sodium hydroxide (NaOH) molarity and volume. The post treatments were subsequently carried out after the initial alkaline hydrothermal treatment. The parameter changes that were investigated are summarised below:

Duration at 240°C with 1 M and 52 ml NaOH:

30 minutes, 1 hour, 1 hour 30 minutes, 2 hours, 2 hours 30 minutes, 3 hours, 4 hours, 5 hours, 6 hours, 7 hours.

Temperature with 1 M and 52 ml NaOH for 2 hours:

180°C, 200°C, 220°C and 240°C.

Sodium Hydroxide Molarity at 240°C, in 52 ml of NaOH for 2 hours:

1 M, 2 M, 3 M, 4 M and 5 M.

Volume of Sodium Hydroxide at 240°C, with 1 M NaOH for 2 hours:

28 ml, 36 ml, 44 ml, 52 ml, 60 ml and 66 ml.

The surfaces were imaged by SEM. This technique gives a highly magnified and detailed representation of an interface by analysing the secondary electrons emitted from a sample surface after being subjected to a focused electron beam.

4.2.2.1 Duration

The time-duration experiment was carried out to observe the growth of nanotopography over a range of time intervals during the alkaline hydrothermal process. Ten time points were chosen, and the post treatment steps subsequently carried out. The resultant nanotopography was then visualised using SEM.

After 30 minutes hydrothermal treatment (**Figure 4.2A**), the nanospikes were in their infancy, with short, stubby or spherical protrusions starting to appear from the surface. The nascent growth was not homogenous, with some areas appearing flatter with no growth visible. Lower magnification images revealed that similar growth characteristics occurred over a wide area. After 1-hour, the nanospikes were markedly longer than the 30-minute disks, highlighting epitaxial growth in specific regions (**Figure 4.2B**). The growth was heterogeneous and flatter areas were still visible. There was generally a random angle of nanospike growth, with some spikes protruding directly perpendicular to the substrate, while others were more acute to the surface.

After 1 hour 30 minutes of alkaline treatment, the nanospikes had continued upwards growth and some growth was also observed in areas where previously there was limited growth. A greater proportion of nanospikes had started to protrude upwards from the surface (**Figure 4.2C**). After 2 hours of alkaline treatment, the titanium surface had a greater homogeneous covering of nanospikes with little of the flatter areas previously observed. Most of the nanospikes were generally protruding upright from the surface but not necessarily directly perpendicular. Most of the nanospikes were straight and round along their lengths and tips (**Figure 4.2D**).

With 2.5 hours of hydrothermal treatment, the nanospikes were significantly longer and bending and intertwining between multiple nanospikes was observed. The reduced density of long nanospikes was also evident (**Figure 4.2E**). After 3 hours, further lengthening and interweaving of the nanotopography was observed, forming 'pockets' or 'nests'. The walls of these pockets were smooth, consisting of the sides of the nanospikes, with the nanospike tips comprising braided singular spikes that protruded directly upwards (**Figure 4.2F**).

After 4 hours, most of the nanospikes had intertwined completely at the tips and edges to form pockets of varying sizes and shapes. Flat ridges of interconnecting nanospikes had formed and the columellar protrusions previously noted at 3 hours were absent (**Figure 4.2G**). For the 5 hours (**Figure 4.2H**), 6 hours (**Figure 4.2I**) and 7 hours disks (**Figure 4.2J**), the nanotopography continued to form intertwining pockets that progressively increased in diameter. The height of the nanotopography also continued to increase over time.

4.2.2.2 Temperature

The temperature at which the alkaline hydrothermal process was carried out was systematically changed to investigate its effect on nanospike growth and configuration. Four temperatures were chosen during the alkaline hydrothermal with the post treatment steps subsequently carried out.

The 2-hour time point was selected as, from the duration experiment, this was the optimal incubation period to form pronounced nanospikes without intertwining. Intertwining led to the

decrease in density of spikes protruding from the surface. It was hypothesised that this may reduce potential antimicrobial activity through physical rupturing of the bacterial membrane due to fewer contact points on the membrane.

At 180°C (**Figure 4.3A**), there was heterogeneous growth, with the nanotopography resembling flakes or ribbons. The tips of these protrusions were noticeably blunt. The hydrothermal treatment at 200°C (**Figure 4.3B**) showed similar nanospike conformity and arrangement to that at 180°C. Although taller, the growth was dominated by flake-like structures. At 220°C (**Figure 4.3C**), the nanospikes were more homogeneous in height and more rounded. The spike diameters were similar from the base to the tip. The orientation of the nanospikes was more perpendicular than observed at the lower temperatures. A temperature of 240°C is close to the maximum advised for the acid digestion vessels of 250°C; the topography had a similar character to that at 220°C but was noticeably taller (**Figure 4.3D**).

4.2.2.3 Sodium Hydroxide Molarity

The aim of this experiment was to investigate the growth of the nanospikes with increasing NaOH concentrations. Six NaOH concentrations were chosen during the alkaline hydrothermal stage followed by the post treatment steps. The 2-hour/240°C parameters were selected as the previous experiments indicated these to be the optimal duration/temperature to form the most pronounced nanospikes without intertwining.

At 0.5 M NaOH concentration, the nanotopography was very dense and the spikes were flaky in appearance and blunt at the tip, as if they were fused together. The height between the spikes was consistent (**Figure 4.4A**). The 1 M NaOH disks were similar, with homogeneous growth of separate, rounded nanospikes (**Figure 4.2B**). With 2 M NaOH**,** the nanospikes were taller and less dense, comparable to the 2.5-hour duration experiment. The tips of the nanospikes could be observed to start to bend and intertwine with neighbouring nanospikes. The spikes appeared thinner compared with the 1 M NaOH samples (**Figure 4.4C**).

With 3 M NaOH, the nanotopography arrangement differed significantly from the previous disks and was similar to the 4-hour topography seen in the duration study. Pockets of intertwined nanospikes were observed and the nanospikes themselves appeared disjointed and 'blebby'. This indicated that at the high molar NaOH concentration, the nanospike growth may lead to structural weaknesses (**Figure 4.4D**). Both the 4 M and 5 M NaOH disks showed pocket arrangements of intertwined nanospikes. As with the 3 M NaOH disks, the nanospikes looked deformed and 'blebby' but more extreme, causing the walls of the pockets to structurally break down (**Figure 4.4E** and **F**).

4.2.2.4 Sodium Hydroxide Volume

The sodium hydroxide volume, in which the titanium disks were submerged during the alkaline hydrothermal process, was systematically changed to investigate its effects on the nanospike growth and character. Six volumes were chosen during the alkaline hydrothermal stage with the post treatment steps subsequently carried out. The nanospikes were grown within the acid digestion vessel for 2 hours in 1 M NaOH at 240°C, as optimised from the previous experiments to form nanospikes without intertwining. The results indicated there was minimal sensitivity to nanotopography growth with the different NaOH volumes (**Figure 4.5**). At each of the volumes tested, the structure and arrangement of the nanotopography were very similar. All disks showed separate, rounded nanospikes, with the same diameter along their length, and generally protruding upwards from the surface.

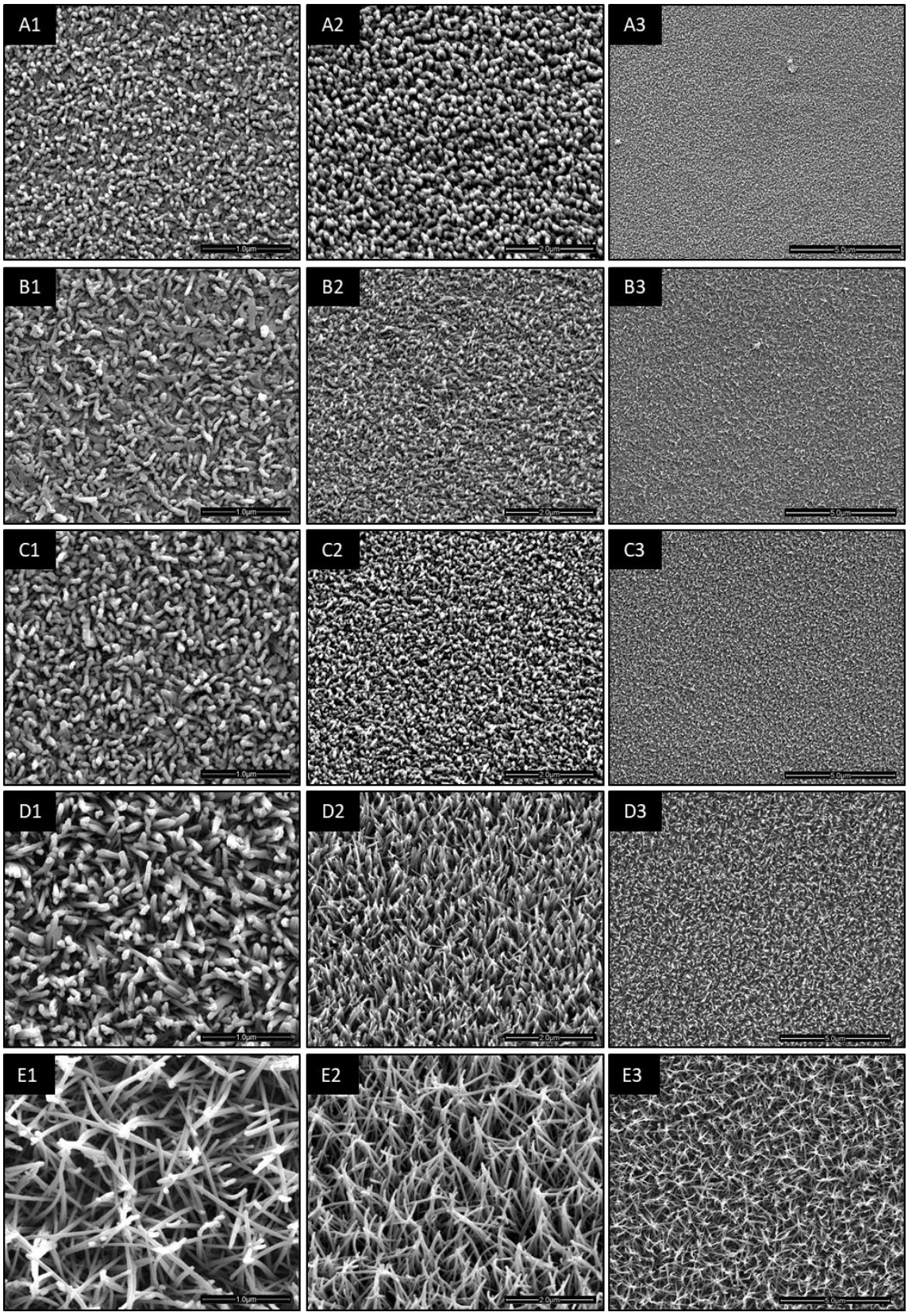
A1
A2
A3
B1
B2
B3
C1
C2
C3
D1
D2
D3
E1
E2
E3

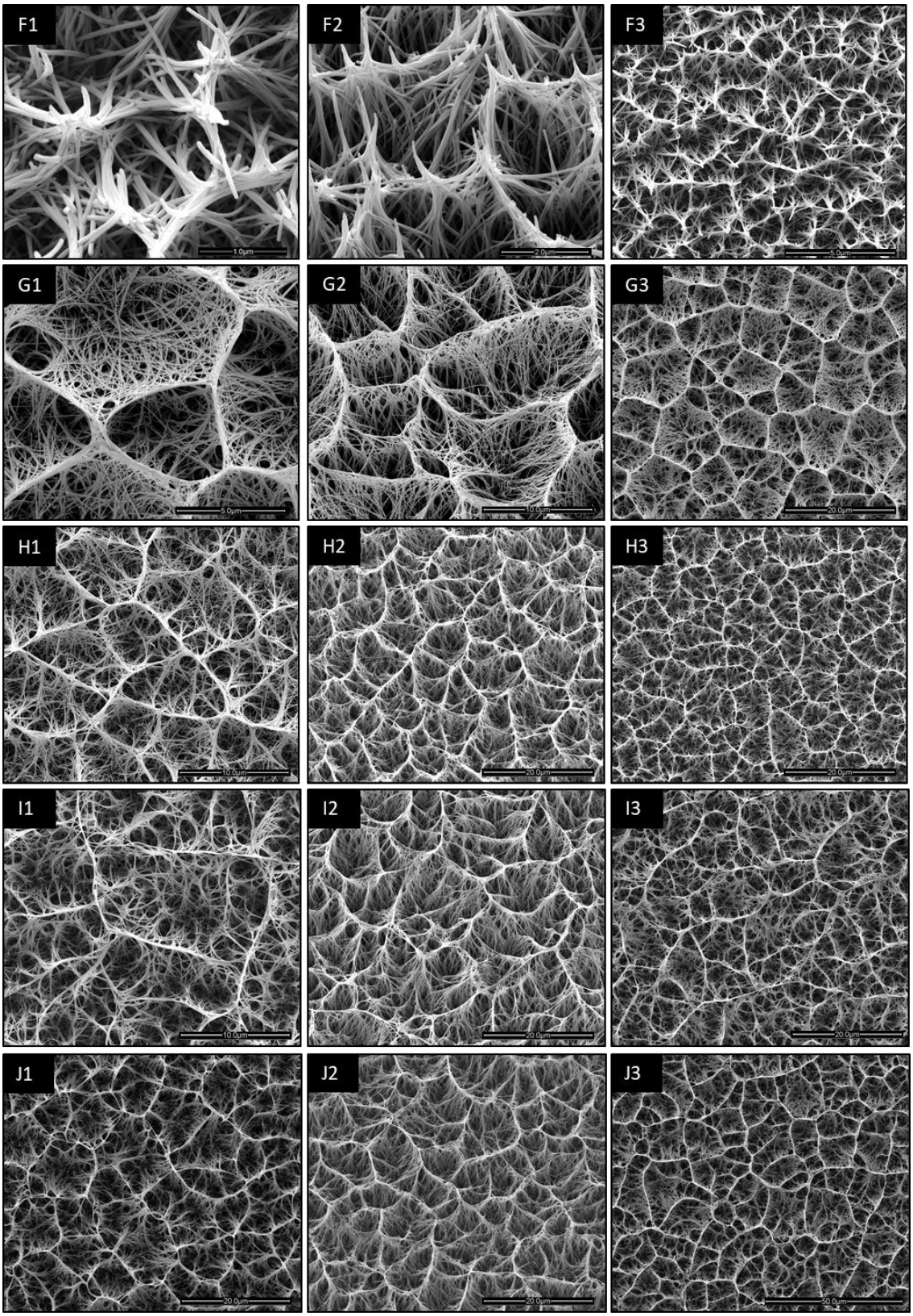

Figure 4.2- *Representative SEM images of nanotopographical growth over time using the alkaline hydrothermal process. Nanotopography was grown on pure titanium substrates within a Teflon-lined acid digestion vessel with the conditions of 52 ml 1 M NaOH at 240°C. A) 30 minutes, B) 1-hour, C) 1 hour 30 minutes, D) 2-hours, E) 2 hours 30 minutes, F) 3-hours, G) 4-hours, H) 5-hours, I) 6-hours, J) 7-hours. Columns 1 and 3 show images at different magnifications and column 2 shows 30° tilted images.*

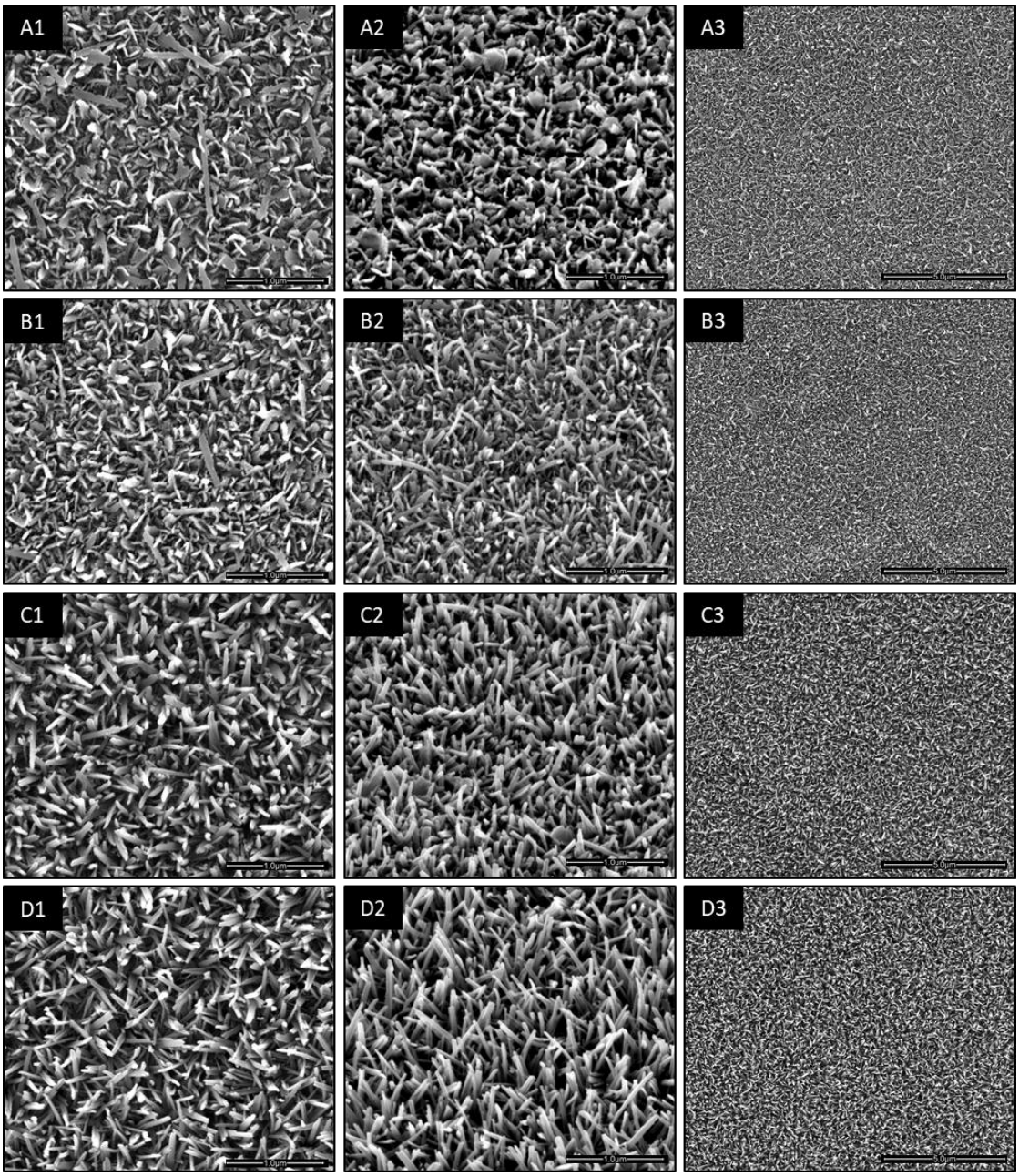

Figure 4.3- *Representative SEM images of nanotopographical growth with increasing temperature during the alkaline hydrothermal process. Nanotopography was grown on pure titanium substrates within a Teflon-lined acid digestion vessel with the conditions of 52 ml 1 M NaOH for 2 hours and A) 180°C, B) 200°C, C) 220°C, or D) 240°C. Columns 1 and 3 show images at different magnifications and column 2 shows 30° tilt images.*

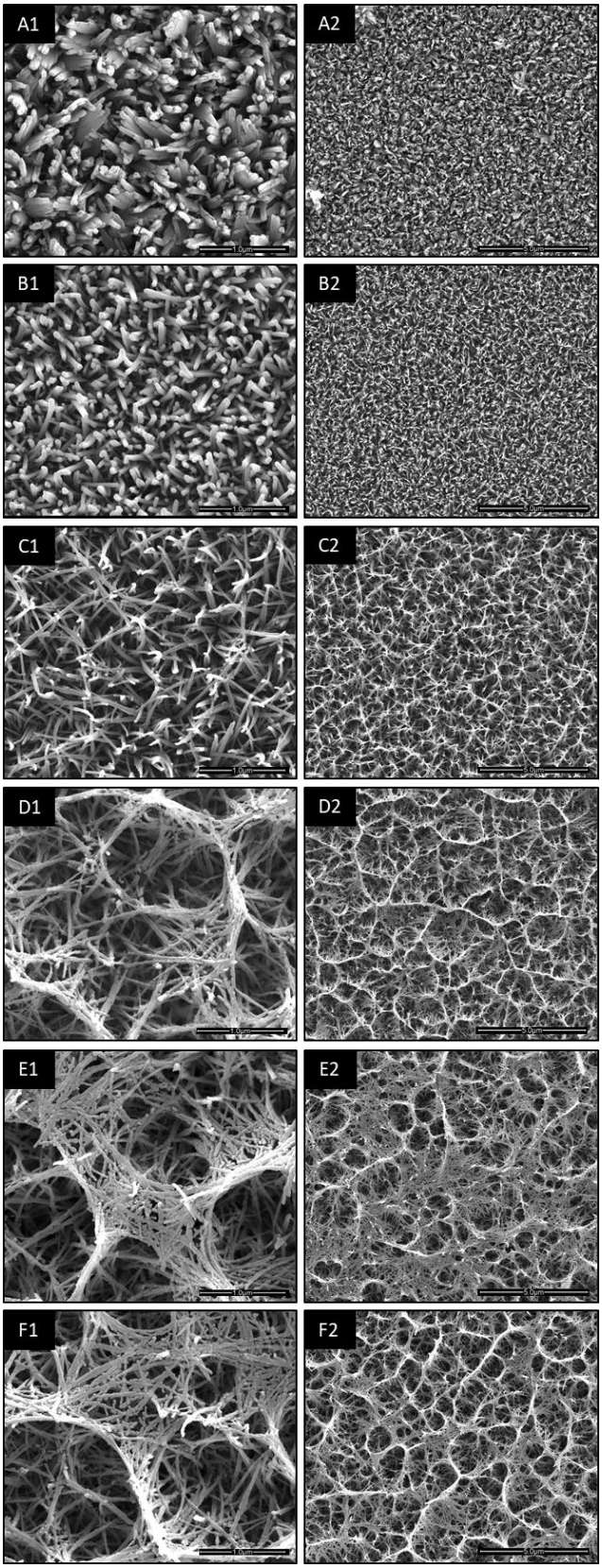

Figure 4.4- *Representative SEM images of nanotopographical growth with increasing NaOH molarity during alkaline hydrothermal process. Nanotopography was grown on pure titanium substrates within a Teflon-lined acid digestion vessel with the conditions of 52 ml NaOH at 240 °C for 2 hours. Molarities of NaOH used were A) 0.5 M, B) 1 M, C) 2 M, D) 3 M, E) 4 M and F) 5 M. Columns 1 and 2 show images at different magnifications.*

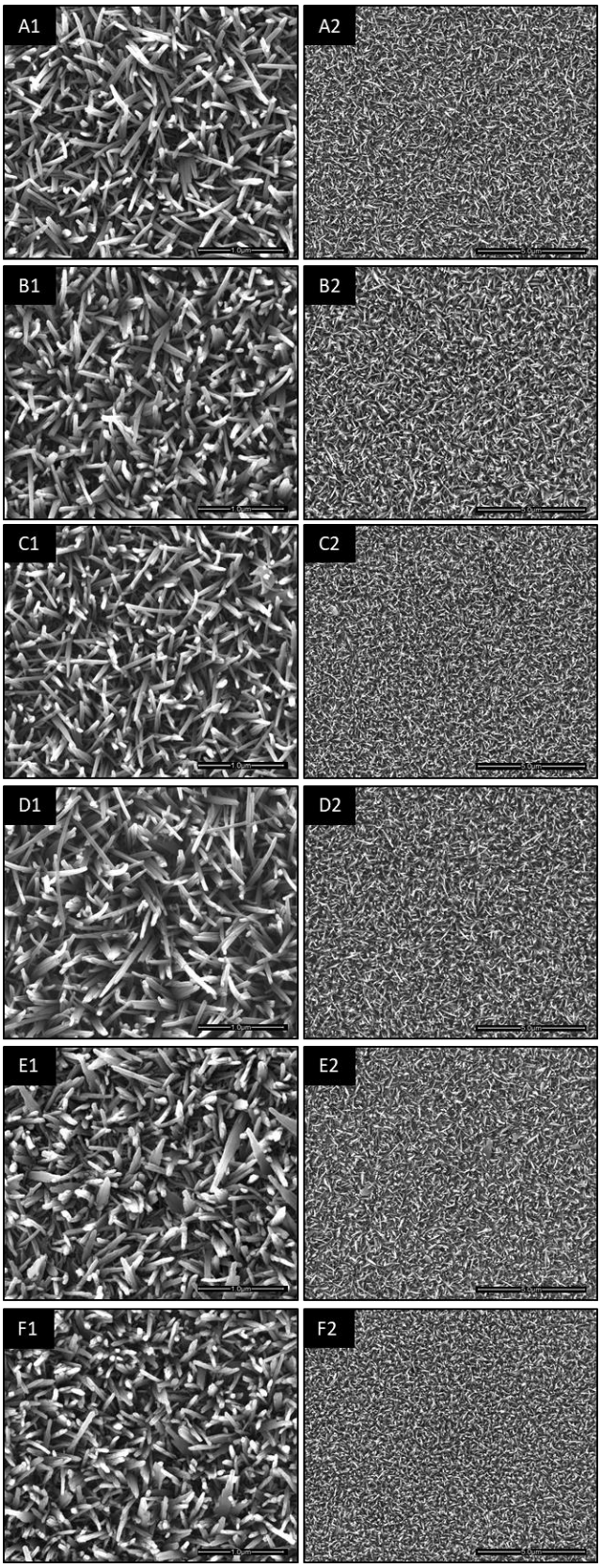

Figure 4.5- *Representative SEM images of nanotopographical growth with increasing NaOH volume during the alkaline hydrothermal process. Nanotopography was grown on pure titanium substrates within a Teflon-lined acid digestion vessel with the conditions of 1 M NaOH at 240°C for 2 hours. Volumes of NaOH were A) 28 ml, B) 36 ml, C) 44 ml, D) 52 ml, E) 60 ml and F) 68 ml. Columns 1 and 2 show images at different magnifications.*

4.2.3 Reproducibility of Nanotopography Growth

Disks within the same batch and between different batches were imaged to assess the reproducibility of nanotopography growth, using the conditions of 2 hours, 240°C, 52 ml of 1 M NaOH. **Figure 4.6A** shows the nanotopography on two separate disks from the same batch at the same magnification. Very similar nanotopography was observed between these two surfaces.

Figure 4.6B shows the nanotopography on two separate disks from a different batch to that shown in Row A. Again, the intra-batch nanotopography was similar, but there was a difference between batches. For the second batch (Row B), the nanospikes appeared a little thinner, and with some potentially fusing. The nanospikes also appeared to have a greater variety in angular orientation to those from the first batch (Row A). Visual differences may be due to quality of imaging and sputter coating.

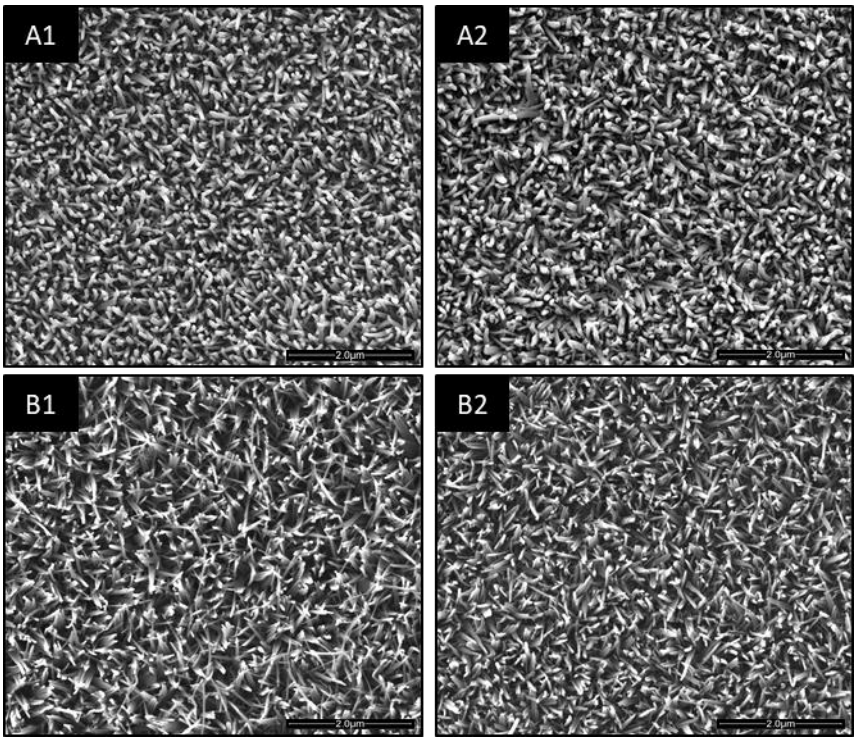

***Figure 4.6**- Intra- and inter-batch variability of nanospike growth. Nanotopography was grown on pure titanium substrates within a Teflon-lined acid digestion vessel with the conditions of 52 ml 1 M NaOH at 240°C for 2 hours. SEM images of nanotopography grown within the same batch (1 and 2) and between different batches (A and B).*

The Teflon vessels used during the alkaline hydrothermal treatment noticeably degraded over time. This is highlighted in **Figure 4.7**, where there is observable discolouration from the pristine white of a new vessel. The walls at the top of the old vessels (**Figure 4.7B1**) and lids (**Figure 4.7C1**) became deformed and elongated, potentially affecting the closed system seal of the acid

digestion vessels. This vessel degradation over time was a key factor in the variability between different batches of nanotopography.

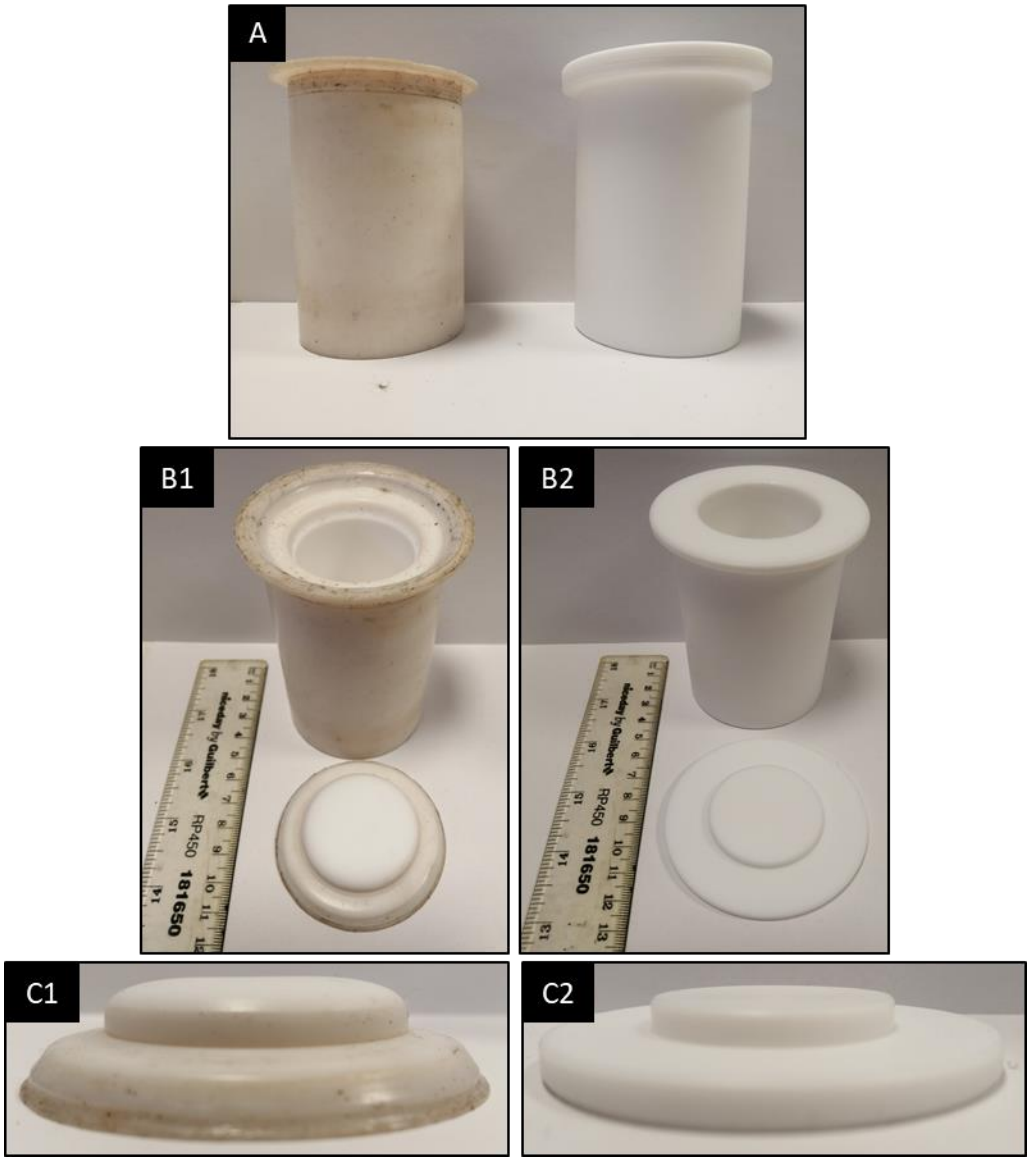

***Figure 4.7**- Images of Teflon vessels highlighting degradation with use. Discolouration and deformation of the vessel is evident together with the elongation of the vessel lids. A) Used vessel (left) and unused vessel (right), B1/2) Vessels with lid removed, C1/2) Vessel lids.*

4.2.4 Nanotopography Change and Resolution

Due to wear and tear of the vessels over time (**Figure 4.7**), a change in the nanotopography was observed. **Figure 4.8A** shows a 2-hour disk that was generated early in this project, before noticeable warping of the vessels, and represents the 'typical' 2-hour nanotopography. The effect of the vessel warping on nanotopography is shown in **Figure 4.8B**, with heterogeneous nanospike growth appearing stunted, and with fusing spikes and flakes. It is believed that this decline in spike quality may be due to warping of the vessel causing the tight seal to fail, leading to a loss or fluctuation of pressure.

New vessels were purchased, but the nanotopography formed with these new vessels was notably different from that previously generated. Thick, flat, flaky, heterogeneous structures, with poorly developed spikes, were observed (**Figure 4.8C**). Analysis of the new Teflon vessels revealed that they were ~3 mm shorter than the old vessels. This meant that within the acid digestion bombs, the Teflon had a greater volume to expand during heating.

It was hypothesised that this would lead to a decrease and fluctuation in pressure. To counteract this, a 'spacer' was placed underneath the acid-digestion vessel to raise the adjustable floor and completely remove the available space for the Teflon vessel to expand into. Following this modification, single, smooth protruding nanospikes were generated that were very similar to those previously obtained (**Figure 4.8D**).

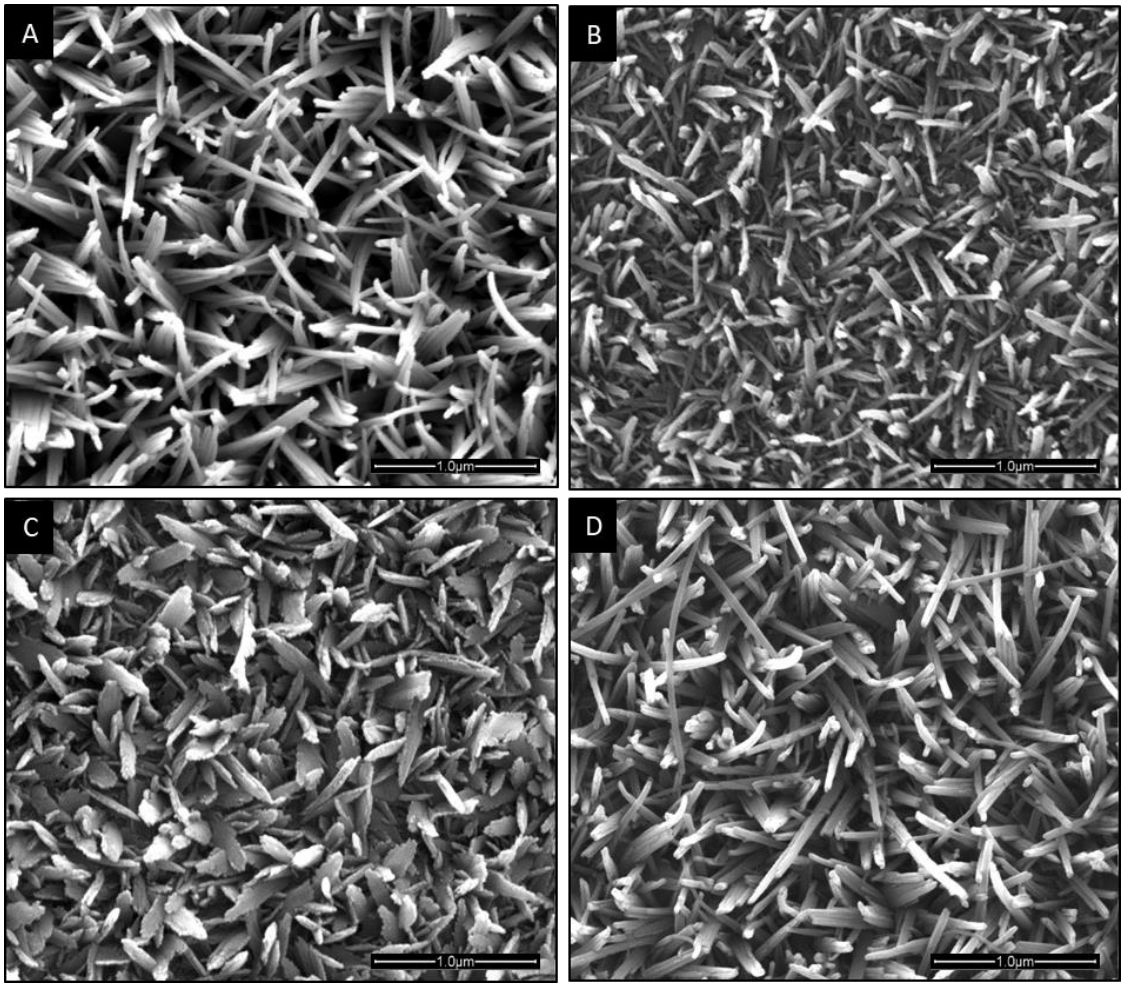

Figure 4.8- *SEM images showing difference in 2-hour nanospikes when grown in a used-degraded Teflon vessel, new Teflon vessel and Teflon vessel with spacer. Nanotopography was grown on pure titanium substrates within a Teflon-lined acid digestion vessel with the conditions of 52 ml 1 M NaOH at 240°C for 2 hours. A) 'Typical' 2-hour nanospikes, B) 2-hour nanospikes grown in used-degraded vessel, C) 2-hour nanospikes grown in new vessel, D) 2-hour nanospikes grown in new vessel with spacer.*

4.2.5 Formation of Nanotopography on Ti64 Alloy

Ti64 alloy is primarily used for orthopaedic implants. Nanospike growth using the alkaline hydrothermal method was therefore also tested on this alloy. **Figure 4.9A** shows SEM images of 2-hour growth on the Ti64 alloy (with 6% aluminium and 4% vanadium). The arrangement was similar to growth at 2-hours on the pure titanium. The 3-hour growth on Ti64 appeared similar to the 2 hours 30 minutes pure titanium disks (**Figure 4.9B**).

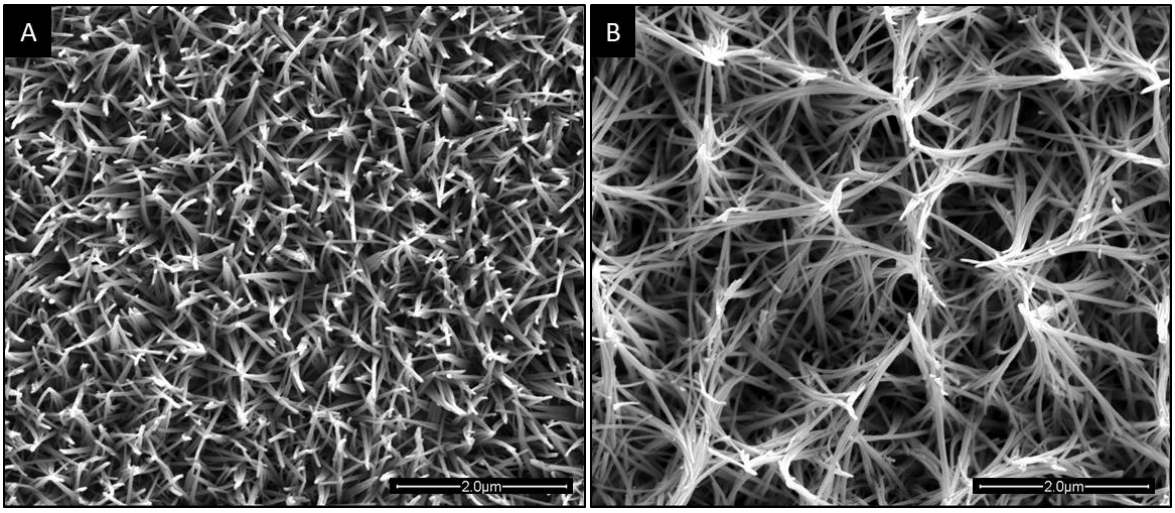

***Figure 4.9**- SEM images of nanotopography generated on Ti64 substrate. Nanotopography was grown on Ti-6Al-4V alloy substrates within a Teflon-lined acid digestion vessel with the conditions of 52 ml 1 M NaOH at 240°C. A) 2-hour nanotopography, B) 3-hour nanotopography.*

4.2.6 Mechanical Robustness of Nanotopography

The nanotopography formed on the titanium surface is susceptible to being damaged from handling. During the implantation of a dental or orthopaedic implant, the surface will be touched, which may lead to any interfacial topography being destroyed. This experiment was carried out to highlight the potential result of human handling on the topography.

The effects of three different physical touches on 2-hour nanospike surfaces were investigated (**Figure 4.10**). After a gentle swipe of the finger across the surface, the nanotopography had been completely flattened, with no independent nanospikes compared with the control (**Figure 4.10A-B**). A scratch by a metal scalpel effectively destroyed the nanotopography (**Figure 4.10C**). For disks that had been subjected to a gentle finger compression on the surface, some of the nanotopography remained intact and unharmed, while other regions had been destroyed (**Figure 4.10D**).

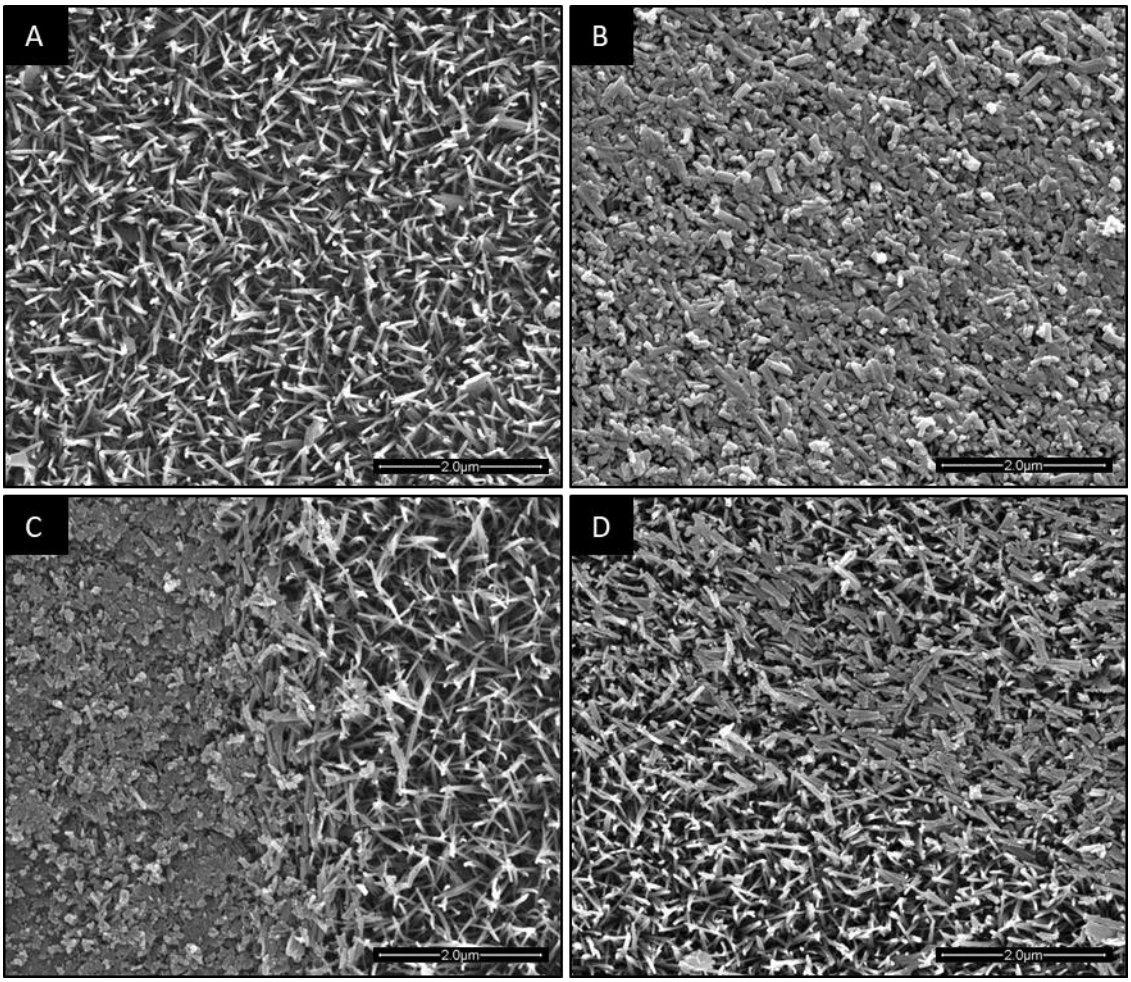

***Figure 4.10**- Representative SEM images showing physical damage of nanotopography. Nanotopography was grown on pure titanium substrates within a Teflon-lined acid digestion vessel with the conditions of 52 ml 1 M NaOH at 240°C for 2 hours. The resulting nanospikes were then subjected to different types of physical damage: A) Untouched control, B) Gentle finger swipe, C) Scratch with a metal scalpel, D) Gentle compression with finger.*

4.3 Physical Characterisation of Nanotopography

The nanotopographies formed from 30 minutes to 7 hours on pure titanium disks exhibited a wide range of structures. To better characterise and accurately quantify the physical attributes of these nanotopographies, several analytical microscopy-based techniques were utilised.

4.3.1 Scanning Electron Microscopy (SEM)

SEM was used to image the surfaces generated in **Section 4.2.2.1**. Image J, an image processing program, was used to quantify:

1. average nanospike height
2. average nanospike diameter
3. nanospike density per μm^2
4. average pocket diameter for durations 3 - 7 hours

As shown in **Figure 4.11A**, the height of the nanotopography increased over time. Initially, there was gradual growth and after 30 minutes, the median height of the nascent nanotopography was 80 nm. Growth then became more rapid and after 2 hours, the average height was 445 nm, a ~5.5-fold increase from 30 minutes. This rapid growth continued, with a ~8-fold increase from 2 to 3 hours, resulting in an average spike height of 3.46 µm. By 2.5 hours the nanospikes had started to bend and intertwine. By 7 hours growth, the height of the nanotopography had increased to 7 µm, with the growth rate slowing between 3 to 7 hours.

In contrast to nanospike height, the diameter of the nanotopography remained constant at approximately 45 nm over the 7-hour duration (**Figure 4.11B)**.

The density of identifiable nanospikes decreased with time (**Figure 4.11C**). After 30 minutes growth, the average density observed was 226 nanospikes/μm^2. The density continued to decrease and at 2 hours growth, had reduced to 37 nanospikes/μm^2. At 3 hours, the last time point with distinct nanospikes, there was an average of 2 nanospikes/μm^2. At further time points, no 'spikes' were observed, as the nanotopography had intertwined to form ridges.

As the nanospikes intertwined they formed pockets/niches that increased in diameter over time **(Figure 4.11D)**. At 3 hours the pockets were the smallest, with an average diameter of 1.6 µm. The variability in diameter was also small, with a standard deviation of 0.4 µm. There was over a four-fold increase in median pocket diameter from 3 to 4 hours, but expansion then slowed from

4 to 6 hours. A larger increase of 1.6-fold was seen from 6 to 7 hours, the latter having a median diameter of 13.3 µm. As the time increased, a greater variability between the pocket diameters was also observed.

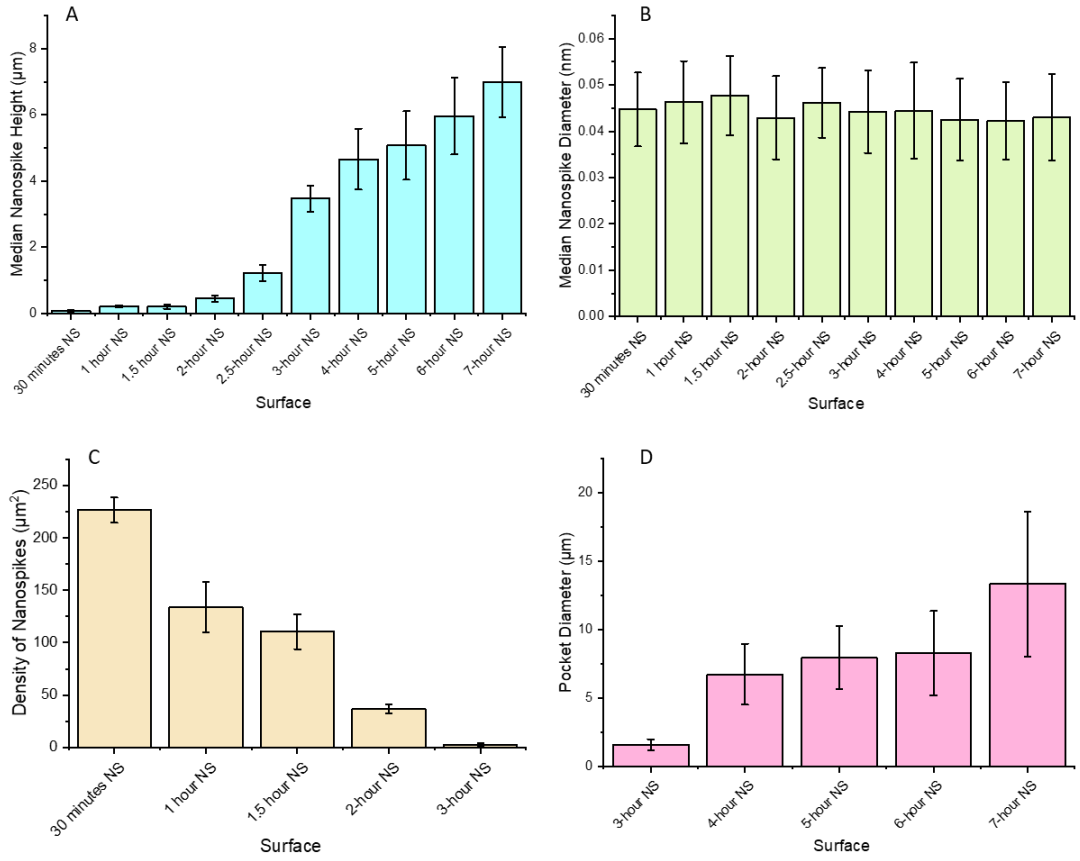

***Figure 4.11**- SEM quantification of nanotopography grown with the alkaline hydrothermal process over 30 mins to 7 hours. Nanotopography was grown on pure titanium substrates within a Teflon-lined acid digestion vessel with the conditions of 52 ml 1 M NaOH at 240°C. Using Image J, physical characteristics of the nanotopographies were determined based on 60 measurements from 3 disks from different batches. A) Average nanospike height, B) Average nanospike diameter, C) Average nanospike density per µm^2, D) Average pocket diameter.*

4.3.2 Atomic Force Microscopy (AFM)

AFM utilises a small sharp probe which interacts directly with the sample interface. The movement of the probe is measured by a laser beam angled onto the probe and directed into a detector. The technique allows 3D imaging with high vertical resolution of around 0.1 nm and direct measurement of the sample surface which is not possible with SEM.

As this technique requires direct contact with the surface, high aspect ratio topographies such as those grown for 3 or more hours can lead to inaccurate imaging and measurements as a result of tip convolution, topography movement and random nanospike orientation. Taking these into consideration, the AFM was only used to image the 30 minutes to 2-hour nanotopographical surfaces. The calculated RMS roughness is the standard deviation of the distribution of surface heights and is more sensitive to large deviations than the average height measurements (Soliman *et al.*, 2002).

The following topography characteristics were quantified using AFM:

1. Average nanospike height
2. RMS surface roughness
3. surface area increase

The resulting images are illustrated in **Figure 4.12**. The mirror polished titanium surface had an average height of 8.9 nm and an RMS roughness of 3.1 nm, indicating a very flat surface for the nanotopography to grow upon (**Figure 4.13**). The height of the nanospikes generally increased with time. However, between 1 and 1.5 hours there was little change, whereas from 1.5 to 2 hours the average nanospike height increased by two-fold to 432 nm (**Figure 4.13A**).

The RMS roughness showed a similar trend to that of the height (**Figure 4.13B**). The 2-hour nanospikes had the highest surface RMS roughness of 112 nm. The surface area increased from 25 μm^2 over time, again showing a similar trend to that of nanospike height (**Figure 4.13C**).

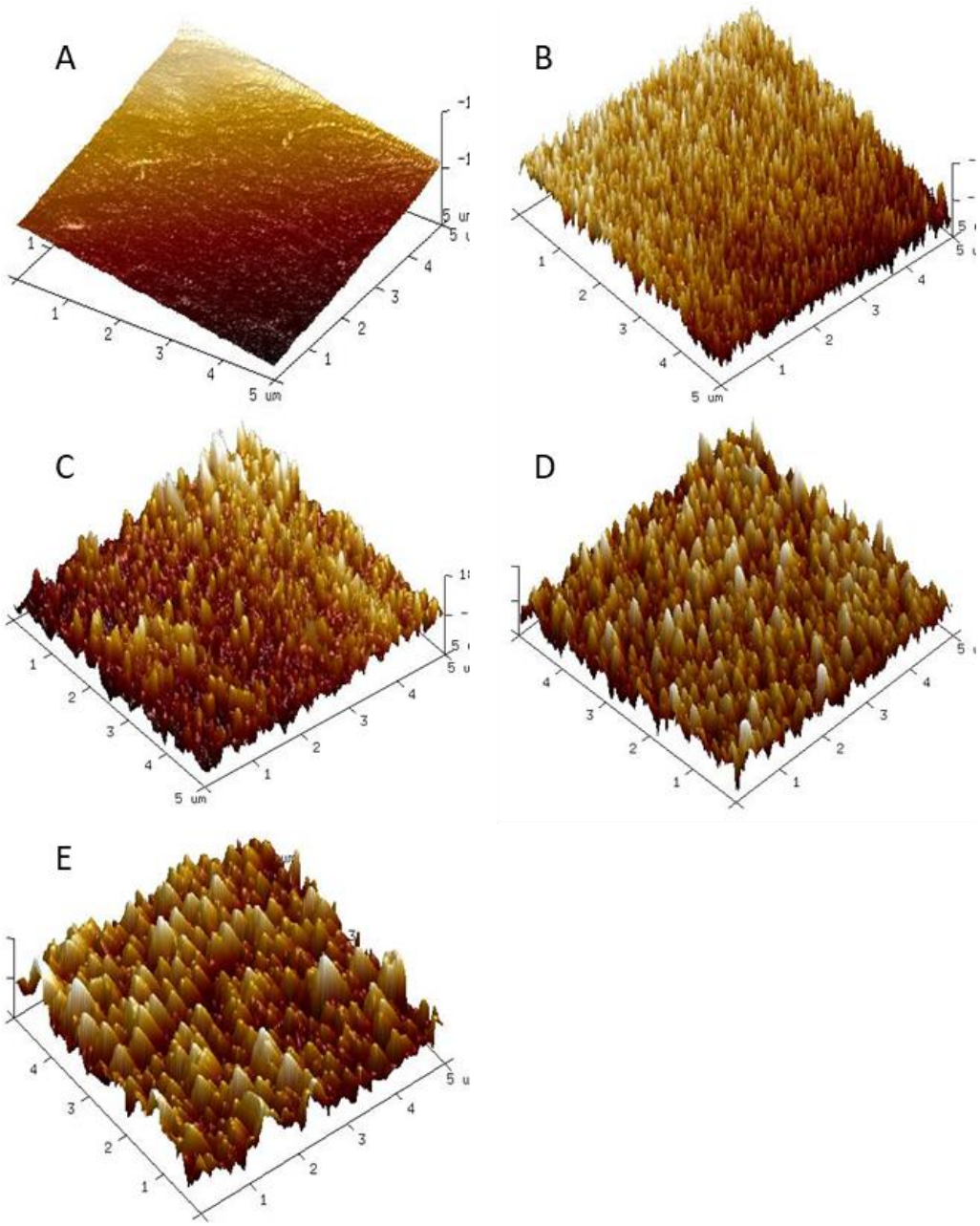

Figure 4.12- *AFM imaging of nanotopography grown with the alkaline hydrothermal process from 30 mins to 2 hours. Nanotopography was grown on pure titanium substrates within a Teflon-lined acid digestion vessel with the conditions of 52 ml 1 M NaOH at 240°C. A) Flat mirror polished surface, B) 30-minutes nanospikes, C) 1-hour nanospikes, D) 1.5-hour nanospikes, E) 2-hour nanospikes. Imaging area of 5 µm by 5 µm.*

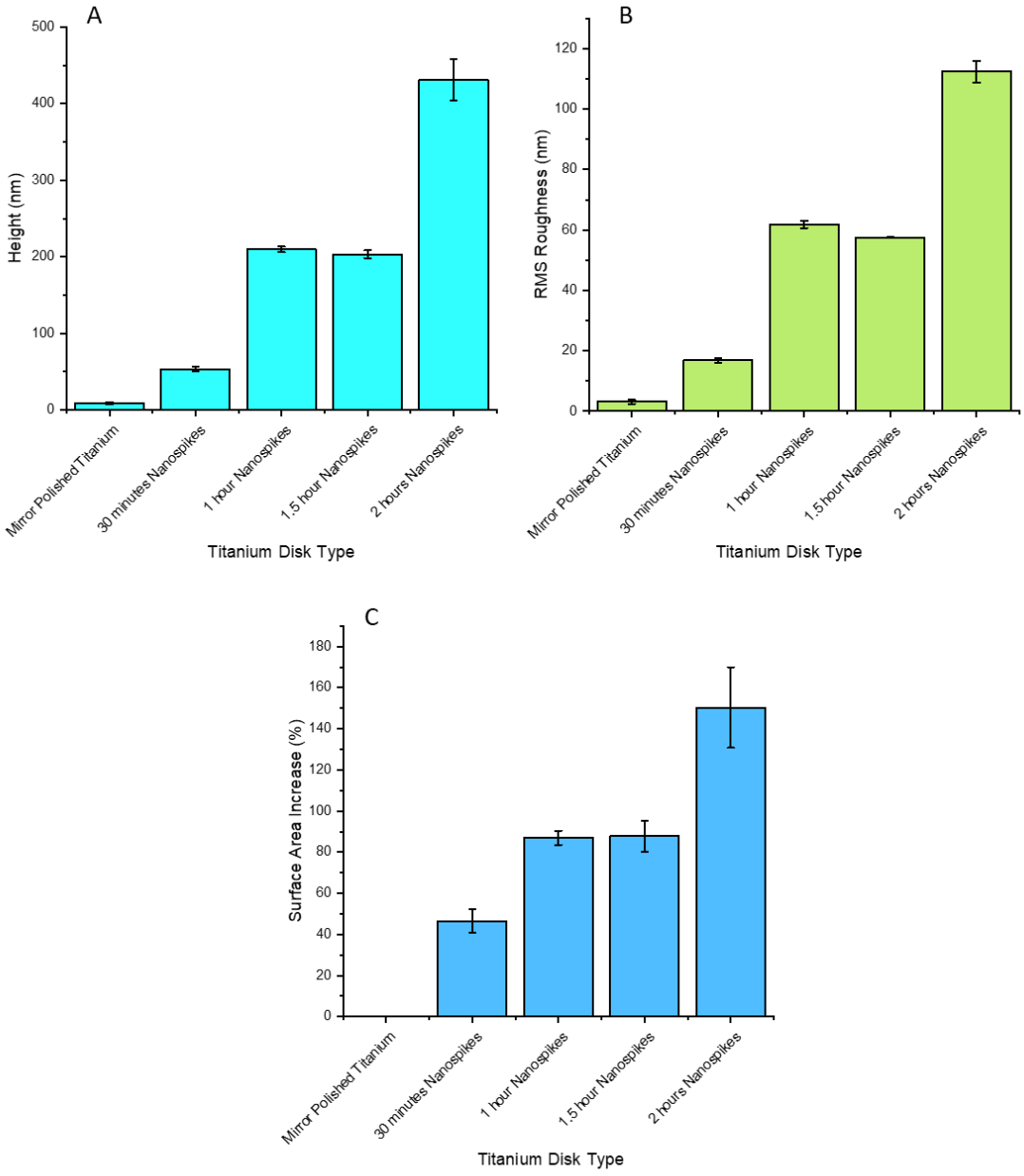

Figure 4.13- *AFM quantification of nanotopography grown with the alkaline hydrothermal process from 30 mins to 2 hours. Nanotopography was grown on pure titanium substrates within a Teflon-lined acid digestion vessel with the conditions of 52 ml 1 M NaOH at 240°C. Using NanoScope software, physical characteristics of the nanotopographies were measured. A) Median nanospike height, B) RMS Roughness, C) Surface area % increase.*

4.3.3 Optical Profilometry (OP)

AFM could only be used to analyse topography grown at the shorter time durations and therefore another technique had to be used to analyse the larger topography grown from 3 hours. Optical profilometry (OP) is a non-contact visualisation technique widely used in material science to analyse surface topography in 3D.

In this project OP was used to measure the surface roughness, both RMS and maximum roughness, and average height of the nanotopography/ridges grown between 3-7 hours. The maximum roughness is the vertical distance between the lowest valley observed and highest peak along the profile length (Soliman *et al.*, 2002). As it uses light and dependent on the objective, the resolution is relatively low compared to SEM and AFM. This meant it was only possible to image topography that had been grown for more than three hours and with a large surface area. OP was used to quantify the following characteristics:

1. Average height of nanotopography (ridges)
2. RMS surface roughness
3. maximum surface roughness

Top and 3D views of the 3-7-hour disks are shown in **Figure 4.14**. These illustrate the pocket walls, highlighted in red, with the bottom of the pockets shown in blue. The columnar peaks of the multiple intertwined nanospikes can be seen in green. There was a clear trend of the pocket area (blue) to widen over time, with a corresponding decrease in peaks (green) and walls (red). The height of nanospikes increased over time, with a median height of 2.3 µm at 3 hours, increasing by 2.7-fold to 6.1 µm at 7 hours (**Figure 4.15A**). Similar profiles were seen for RMS roughness, which increased from 0.4 µm at 3 hours to 1.32 µm at 7 hours (**Figure 4.15B**), and for maximum roughness (**Figure 4.15C**).

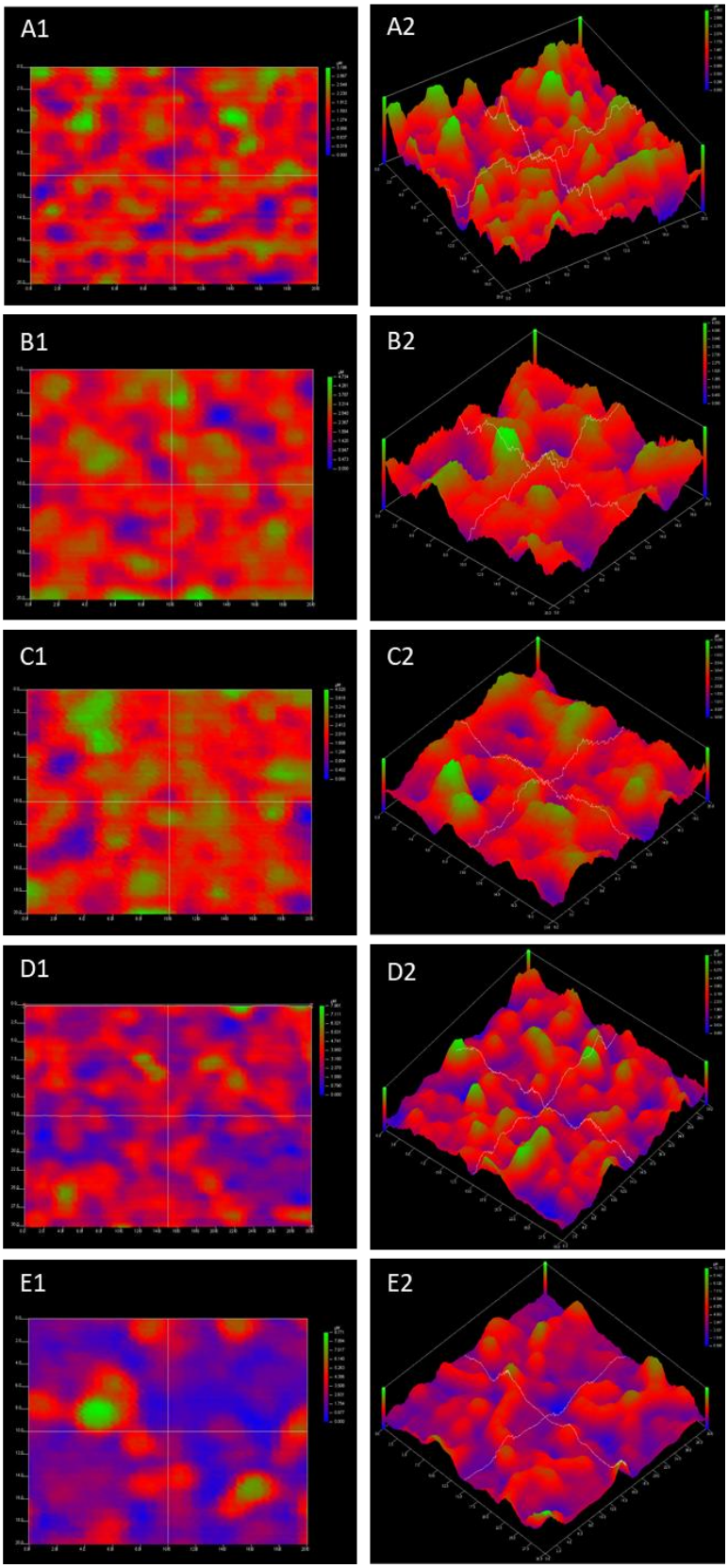

Figure 4.14*- Optical profilometry imaging of nanotopography grown with the alkaline hydrothermal process from 3 to 7 hours. Nanotopography was grown on pure titanium substrates within a Teflon-lined acid digestion vessel with the conditions of 52 ml 1 M NaOH at 240°C. Optical profilometry scans (20x20 µm) with top view (1) and tilted 3D models (2) of A) 3-hour nanospikes, B) 4-hour nanospikes, C) 5-hour nanospikes, D) 6-hour nanospikes and E) 7-hour nanospikes.*

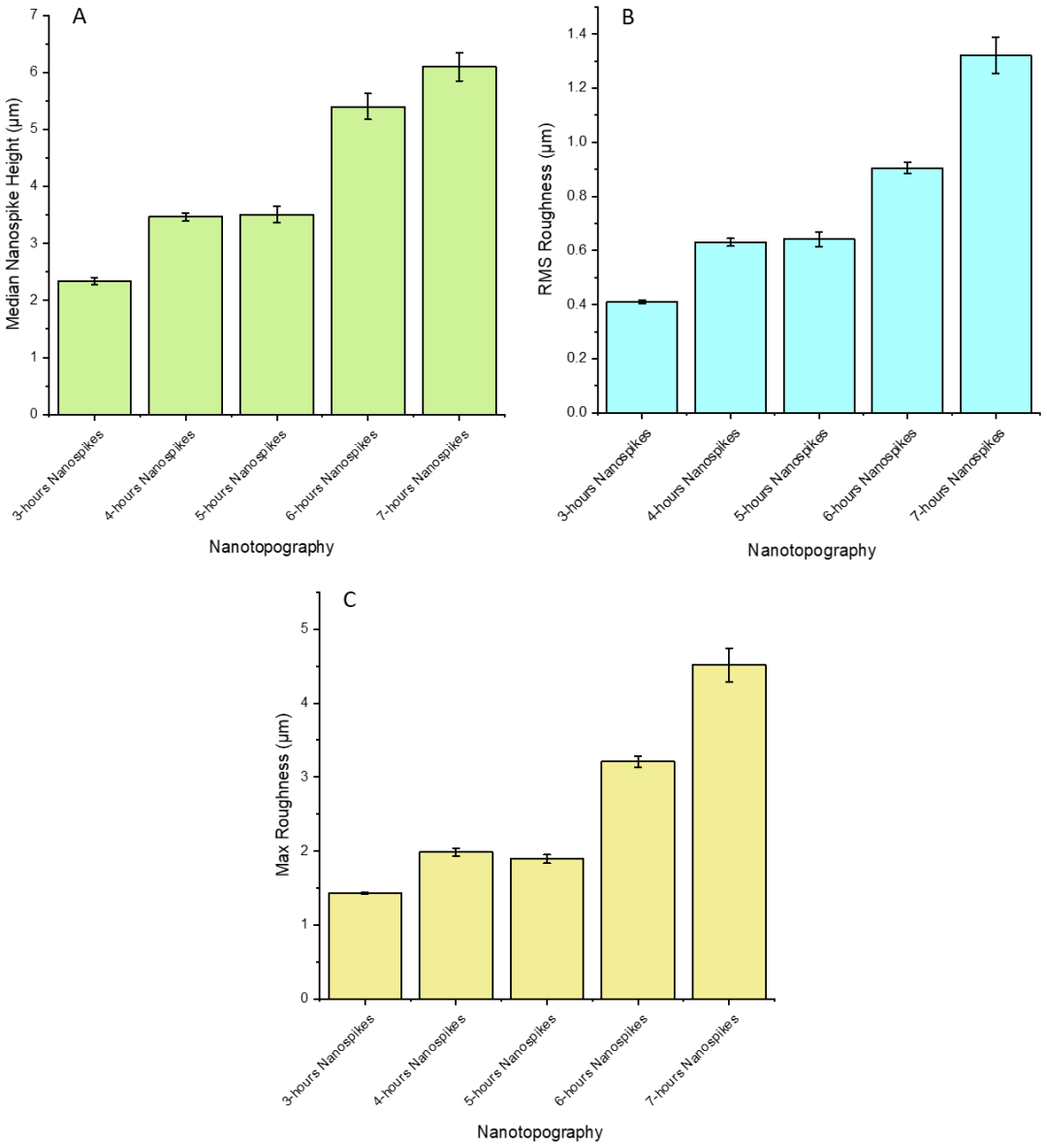

Figure 4.15- *Optical profilometry quantification of nanotopography grown with the alkaline hydrothermal process from 3 to 7 hours. Nanotopography was grown on pure titanium substrates within a Teflon-lined acid digestion vessel with the conditions of 52 ml 1 M NaOH at 240°C. A) Median nanospike height, B) RMS Roughness, C) Maximum Roughness.*

4.3.4 Confocal Microscopy (CM)

CM enables accurate and representative imaging with high resolution by only using light at a specific Z-plane on the sample. This is achieved by two pinholes preventing out-of-focus light reaching the detector and giving a lateral resolution of less than 0.2 µm, better than the optical profilometer. Due to sample availability and the location of the confocal microscope at the National Physical Laboratory (NPL), the CM was only used to measure the 3- and 4-hour nanotopographies.

CM was used to visualise the nanotopography and the following characteristics were quantified:

1. Average height of nanotopography (ridges)
2. RMS roughness

The 3-hour nanotopography had small pockets of intertwined nanotopography (**Figure 4.16A**), which appeared to widen, with the formation and thickening of ridges, at 4 hours (**Figure 4.16B**). The median height of the nanotopography at 3 hours was measured at 1.44 µm, increasing 2.6-fold to 3.8 µm at 4 hours (**Figure 4.17A**). The RMS roughness similarly increased with time, by 35% from 0.82 µm to 1.1 µm (**Figure 4.17B**).

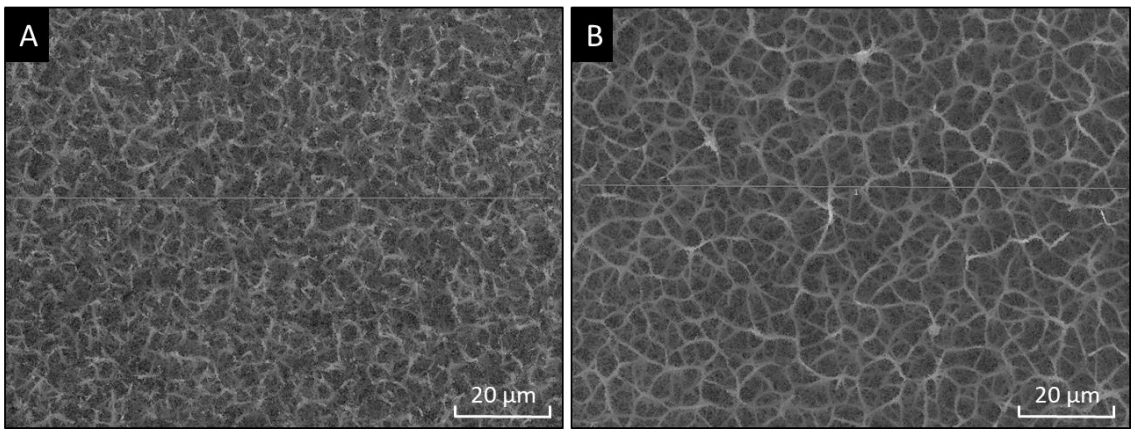

Figure 4.16- *Confocal micrographs of nanotopography grown with the alkaline hydrothermal process for 3 and 4 hours. Nanotopography was grown on pure titanium substrates within a Teflon-lined acid digestion vessel with the conditions of 52 ml 1 M NaOH at 240°C. A) 3-hour nanospikes, B) 4-hour nanospikes.*

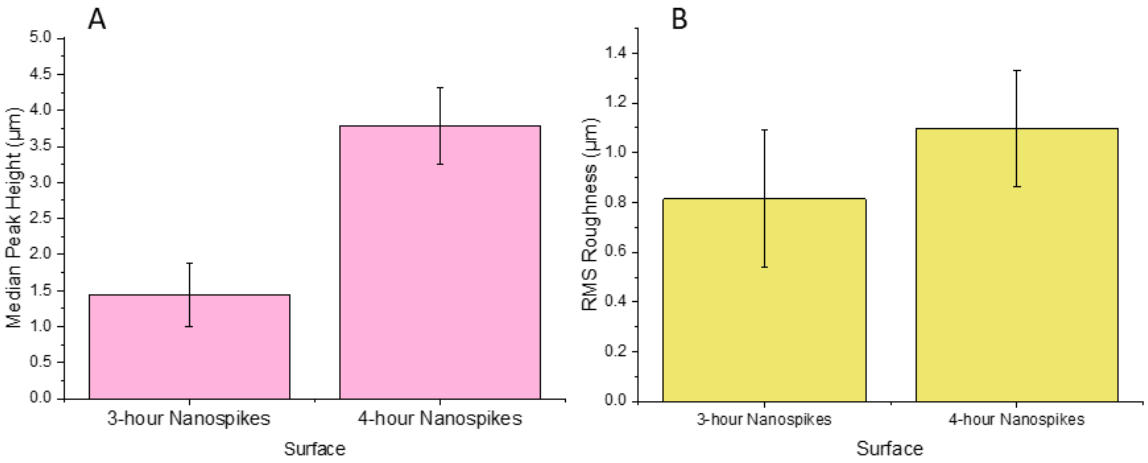

Figure 4.17- *Confocal microscope quantification of nanotopography grown with the alkaline hydrothermal process for 3 and 4 hours. Nanotopography was grown on pure titanium substrates within a Teflon-lined acid digestion vessel with the conditions of 52 ml 1 M NaOH at 240°C. A) Mean peak height, B) RMS roughness.*

4.4 Crystal Characterisation of Nanotopography

During the alkaline hydrothermal process, the nanotopography formed is hypothesised to be transformed through different chemical and crystal configurations with the final product being titanium dioxide. Numerous analytical techniques were used to analyse these transformations.

4.4.1 X-Ray Diffraction (XRD)

Grazing incident X-Ray diffraction was carried out to investigate the crystal structure of the nanotopography formed at each stage of the alkaline hydrothermal process. The four major steps of the alkaline hydrothermal method (see **Section 4.2.1**) were expected to result in different chemistries and crystal structures.

1. Alkaline hydrothermal treatment to generate sodium titanate nanotopography.
2. Heat fixation at 300°C for 1 hour to ensure stabilisation of the nanotopography to the pure titanium substrate.
3. Ion exchange in 0.6 M HCl between sodium ions in sodium titanate and hydrogen ions in the hydrochloric acid to form hydrogen titanate.
4. Calcination at 600°C for 2 hours to convert hydrogen titanate into titanium dioxide.

Figure 4.18 shows initially pure titanium (black) with diffraction peaks at 100, 002, 101, 102, 110, 103, 200 and 201. After alkaline hydrothermal treatment with sodium hydroxide, diffraction peaks of 200, 110, 310, 020 and 220 appeared (red) corresponding to the sodium titanate crystal structure. The peaks present in the pure titanium sample could also be seen, corresponding to the underlying titanium substrate from which the nanotopography was grown. After 300°C fixation for 1 hour (blue) and 1-hour immersion in 0.6 M HCl (pink), the same peaks were observed, indicating no change in the crystal structure. At the end of the process, polymorphous titanium dioxide was observed (green), with the presence of anatase (A) peaks such as 101, 200, 105 and rutile (R) peaks such as 110 and 111.

As a polymorphic composition of both anatase and rutile was observed, the relative amounts of each phase by weight were estimated from the Spurr and Myers equation (Spurr and Myers, 1957; Su *et al.*, 2011). Using the relative intensity values from the XRD spectra (**Figure 4.18** (green)) of the anatase 101 peak (108.75) and the rutile 110 peak (38.20), the percentage anatase present was calculated using **Equation 3.1**. The results indicated that the titanium dioxide consisted of approximately 70% anatase and 30% rutile.

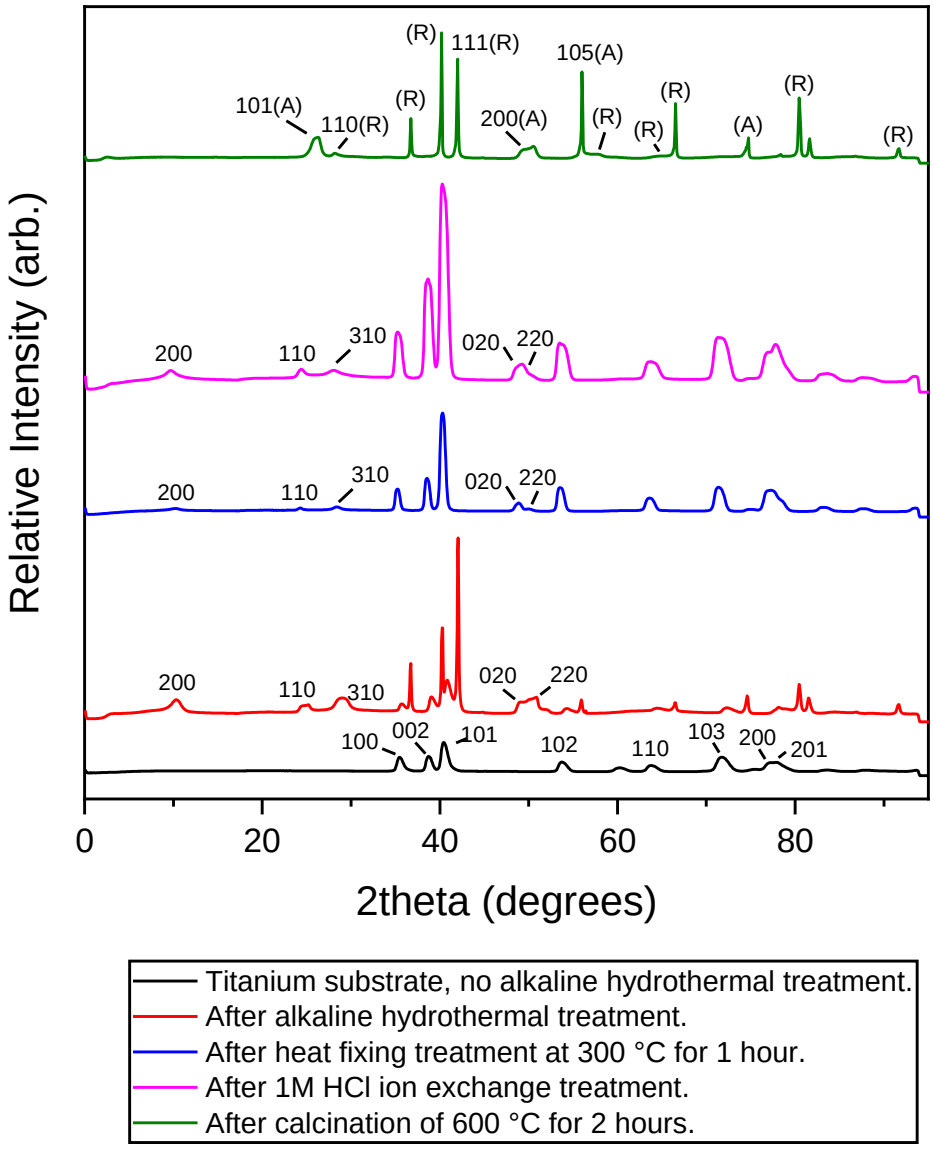

Figure 4.18- *XRD analysis at each stage of the alkaline hydrothermal process. Nanotopography was grown on pure titanium substrates within a Teflon-lined acid digestion vessel with the conditions of 52 ml 1 M NaOH at 240°C for 2 hours. Disks were systematically removed at each stage for analysis.*

4.4.2 Transmission Electron Microscope (TEM)

TEM allows the visualisation of the internal crystalline structure of a sample. The crystal lattice structure of the 2-hour nanospikes generated by the alkaline hydrothermal process was analysed for anatase and rutile phases. As this technique also enabled imaging of the nanospike, the diameter was also measured.

Visualisation of a 2-hour nanospike by TEM showed the presence of a polymorphous crystal lattice with many different planes, shown in red and orange, indicating different crystal orientations within the spikes (**Figure 4.19**). The nanospikes were predominantly anatase (red), as most of the planes had a lattice spacing of 0.332 nm. Some of the planes had a lattice spacing of ~0.238 nm, consistent with the rutile phase (orange). The TEM images also confirmed that the 2-hour nanospikes had an average diameter of ~45 nm consistent with the SEM measurements.

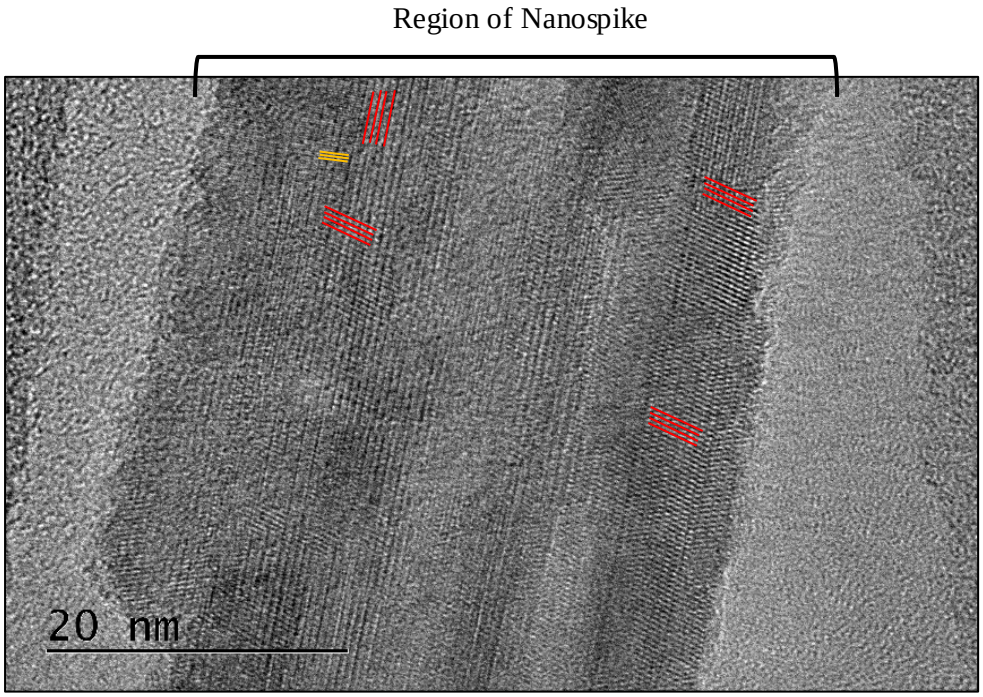

Figure 4.19- *TEM image of 2-hour nanospike showing crystal lattice. Nanotopography was grown on pure titanium substrates within a Teflon-lined acid digestion vessel with the conditions of 52 ml 1 M NaOH at 240°C for 2 hours. The nanotopography was scraped off the disk and fixed onto a copper lattice for TEM imaging. Anatase lattice indicated in red and rutile in yellow.*

4.4.3 Energy Dispersive X-Ray Spectroscopy (EDX)

EDX is widely used to investigate the elemental composition of a sample. In this project it was used to analyse the elemental composition of the nanospikes after the 2-hour alkaline hydrothermal process and post treatment.

Two regions of a nanospike were analysed (**Figure 4.20A**) and gave comparable results, indicating that the nanospikes were essentially homogeneous (**Figure 4.20B**). Both regions showed that titanium (~45%) and oxygen (~35%) were the most common elements present. Copper (~20%) was also present in both regions, due to contamination from the copper mesh on which the nanospikes were fixed. EDX analysis confirmed that the nanospikes consist of pure titanium dioxide. No sodium from the sodium titanate was present, indicating that the complete ion exchange with hydrochloric acid during the post treatment process was successful.

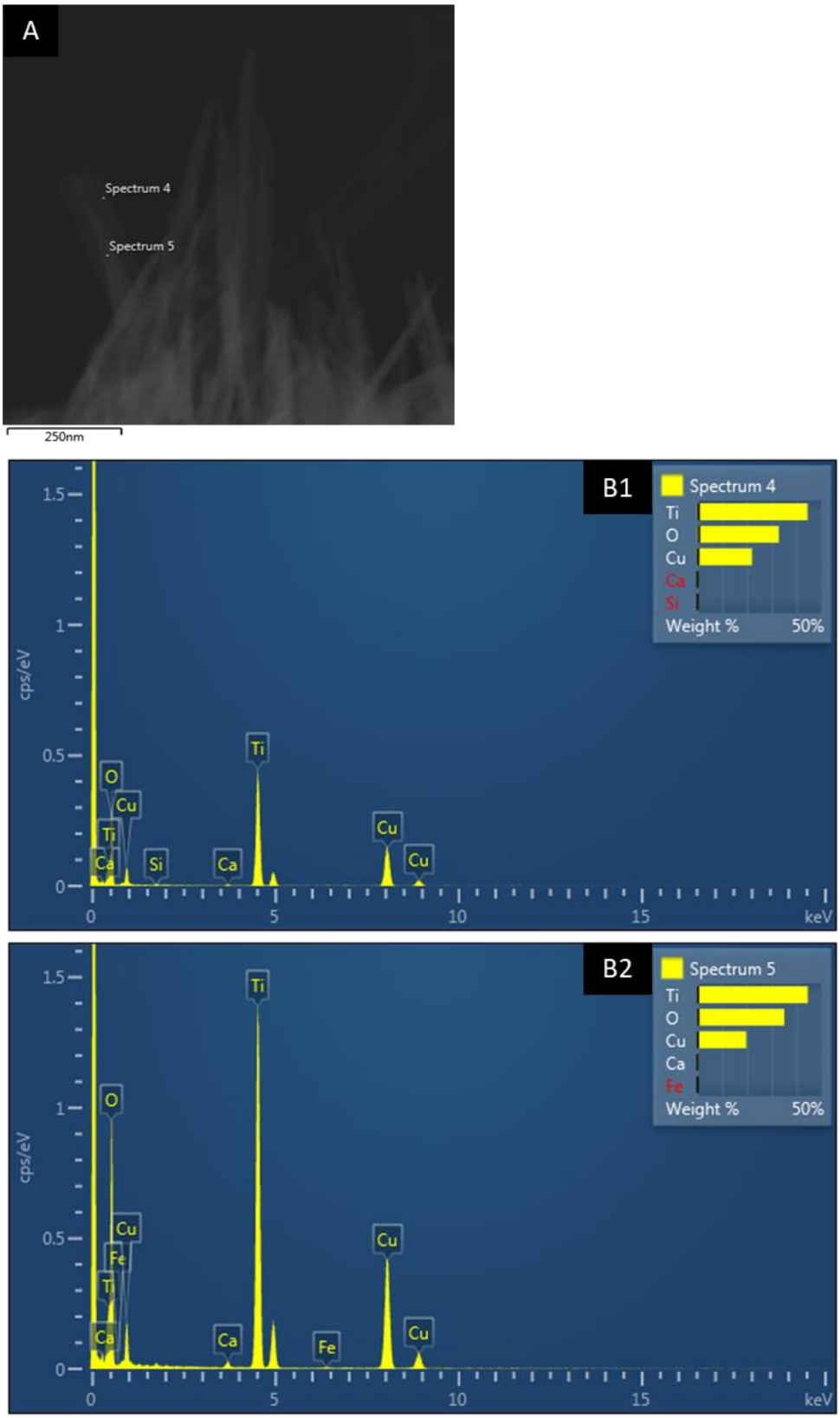

Figure 4.20- *EDX analysis of 2-hour nanospikes. Nanotopography was grown on pure titanium substrates within a Teflon-lined acid digestion vessel with the conditions of 52 ml 1 M NaOH at 240°C for 2 hours. A) SEM showing nanotopography and regions of EDX analysis. B1) and B2) EDX spectra of nanospikes from the two different regions.*

4.4.4 X-Ray Photoelectron Spectroscopy (XPS)

XPS is used to analyse elemental surface composition and bonding states between elements within a sample. XPS was utilised in this project to corroborate the EDX and XRD results that indicated titanium dioxide as the final product of nanospike growth and also to give information regarding the elemental binding states.

Three main elements were present in the pure titanium substrate in the form of oxygen ~530 eV, titanium ~454 eV and carbon ~285 eV (**Figure 4.21**). Nitrogen was also included to enable comparison with AMP-functionalised surfaces in subsequent studies. The titanium spectra indicated that titanium dioxide was present, along with the underlying titanium metal. The oxygen spectra showed the presence of metal oxides, likely to be titanium oxide. There was a little nitrogen present on the surface, as shown by the lower intensity values compared to titanium and oxygen. There was also a minor presence of carbon in the form of C-C and C-C=O bonds likely due to natural contamination of the surfaces by air adsorption.

The survey scan of the 2-hour nanotopography, as with the pure titanium substrate, indicated that the dominant elements of the nanotopography were titanium, oxygen and carbon (**Figure 4.21**). The titanium was present primarily as titanium dioxide. The underlying metal of pure titanium was not measured, as the nanotopography was more than 5 nm in height and therefore exceeded the analytical depth of XPS. Oxygen was present as a metal oxide, likely to be titanium dioxide, with the presence of additional metal hydroxides. There was also contamination with some nitrogen in small amounts and carbon with C-C and C-C=O bonds as seen on the pure titanium.

Taken together, these results highlighted that the nanotopography was most likely to be titanium dioxide, supporting the results of the XRD and EDX analyses.

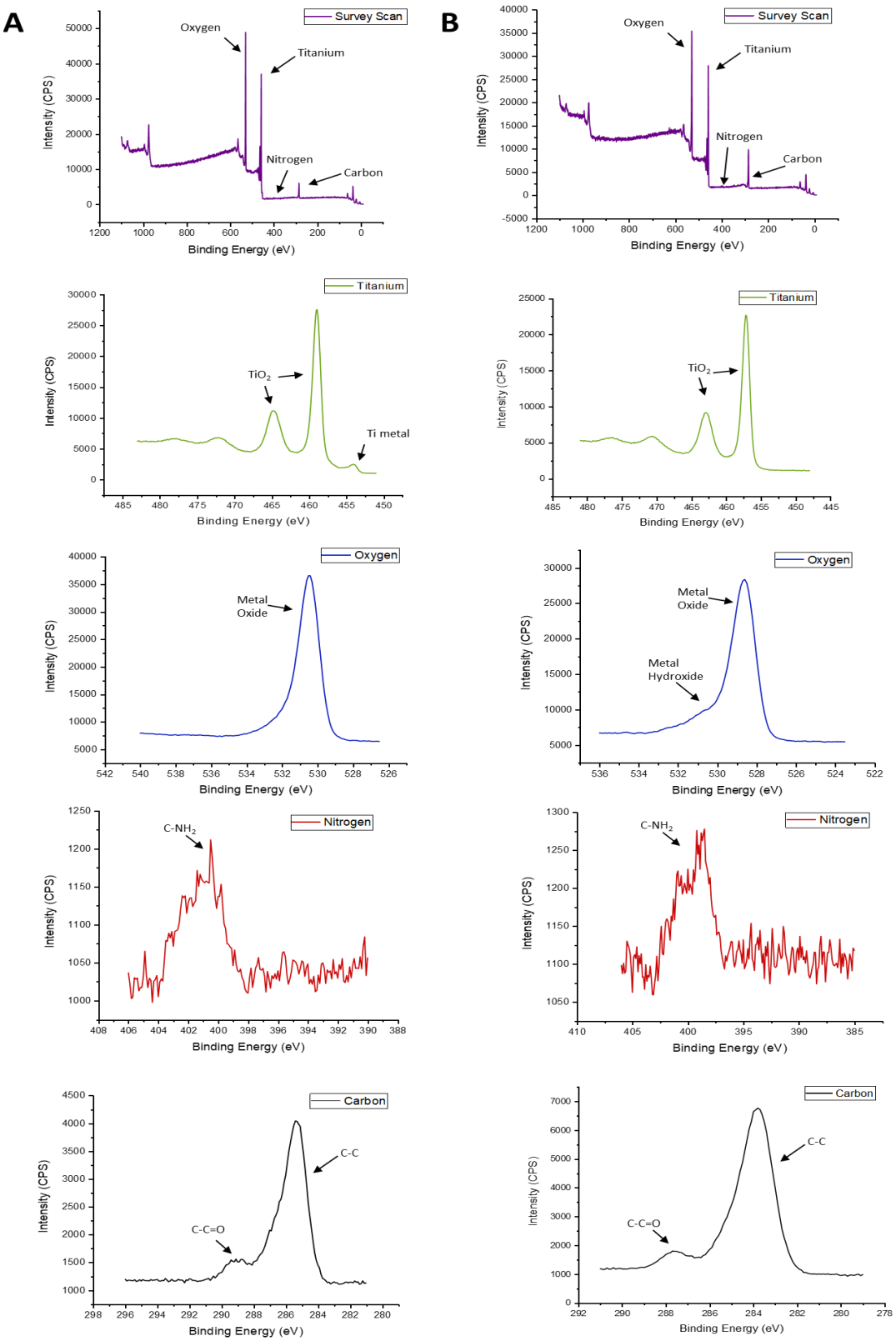

Figure 4.21- *XPS spectra of pure titanium and 2-hour nanotopography. Nanotopography was grown on pure titanium substrates within Teflon-lined acid digestion vessels with the conditions of 52 ml 1 M NaOH at 240°C for 2 hours. XPS analysis was carried out on pure titanium (column A) and 2-hour nanospikes (column B). Includes survey scan and highlighted regions of titanium, oxygen, nitrogen and carbon. CPS=counts per second.*

4.5 Discussion

4.5.1 Effects of Processing Conditions on Nanotopography

In this project, the alkaline hydrothermal technique was used to generate titanium dioxide nanotopographies on the surface of pure titanium substrate. This method has been widely used with varying temperatures, durations and sodium hydroxide molarities to generate different nanotopography structures on titanium substrates (Dong *et al.*, 2007; Diu *et al.*, 2014; Guo *et al.*, 2017; Song *et al.*, 2005; Simović *et al.*, 2019). The protocols used in this project were similar to those of Dong *et al.* (2007), Diu *et al.* (2014) and Tsimbouri *et al.* (2016). The hydrothermal process involved four stages. The first stage involved the generation of the nanotopography by immersing in sodium hydroxide, followed by heat treatment at 300°C, immersion in 0.6 M HCl and a final calcination of 600°C. There was little visual change in the nanotopography during these stages, confirming that the nanotopography generated at the first stage could withstand post treatment conditions.

Building on the work of Dong *et al.* (2007), systematic studies were then conducted to determine the optimal sodium hydroxide volumes, concentration, temperature and growth times required to form a nanotopography most alike to the bactericidal nanospikes reported on insect wings. The nanospikes grew progressively in length with time. It has been suggested that the nanospikes grow both upwards and downwards, the downwards growth ensuring stability in the corroded layer and a generally perpendicular orientation upwards (Dong *et al.*, 2007). From 2.5 hours onwards, the nanospikes started to bend and intertwine, which led to the formation of 'pockets' or 'nests'. These comprised of smooth sides and nanospike tips of braided singular spikes protruding directly upwards, which increased in diameter and height with time. Such observations were generally consistent with previous studies (Tsimbouri *et al.*; 2016; Diu *et al.*, 2014; Dong *et al.*, 2007), with the intertwining proposed by some workers to be encouraged by the high-tension environment static charge between nanospikes (Dong *et al.*, 2007; Sun *et al.*, 2006; Kong *et al.*, 2004).

The nanospikes became taller, more perpendicular and sharper with temperature. This may have been a result of increasing temperature promoting the nucleation and crystal growth and higher pressure within the vessel (Liu *et al.*, 2014). The growth of the nanotopography was also more rapid and may have been due to the increasing temperatures above 130°C that are required to break the titanium oxygen bonds, which is an initial step to form sodium titanate during the alkaline treatment (Liu *et al.*, 2014; Ou and Lo, 2007; Lai *et al.*, 2015). A maximum temperature of 250°C was limited by the specification of the acid-digestion vessels.

Optimum nanospikes were observed using 1 M NaOH, consistent with Dong *et al.* (2007). Increasing molarity leads to the reaction being accelerated due to enhanced titanium dissolution and the formation of sodium titanate (Liu *et al.*, 2014). At the high NaOH molarity of 3-5 M, the nanostructures became less well formed probably due to excessive titanium dissolution (Ou and Lo, 2007; Liu *et al.*, 2014; Wang *et al.*, 2011).

Changing the volume of 1 M NaOH had minimal effects on the nanotopography formed. This may have been due to the saturated vapour pressure that occurs within the closed Teflon vessel, as water evaporates at the high temperature of 240°C, with an equilibrium between the rate of evaporation and condensation of the water in the vessel. Any minor changes may be due to the small pressure changes generated within the Teflon vessel with increasing liquid volumes (Wong, Tan and Mohamed, 2011; Huang, 2018).

With use, the Teflon vessel degraded gradually due to the high temperatures and pressures that were exerted upon it, close to the maximum operational temperature of 260°C for the Teflon vessels (Venkateswarlu *et al.*, 2014). As a result, the quality of the nanospike growth decreased. The results from the old vessels, new vessels and the addition of the spacers suggest that pressure maintenance is imperative for high quality and reliable growth of the nanotopography, affecting titanium dissolution and the sodium titanate formation processes. The ability to form separate thin nanospikes is affected by a lower pressure environment. Therefore, variability in the pressure, due to leakage from a compromised seal or fluctuation in vessel volume during heating and cooling, would compromise this process.

4.5.2 Application of Nanotopography in the Clinical Setting

The alkaline hydrothermal method was also tested on the Ti64 alloy, which is primarily used for orthopaedic implants. The nanospikes for pure titanium and Ti64 were similar for the 2-hour disks, but for the 3-hour disks, the nested topography on Ti64 appeared similar to topography generated on pure titanium after 2.5 hours, indicating that marginally longer time periods may be required for optimised growth on Ti64. Variability in growth between batches could have accounted for the observed differences but more likely reflects the fact that there is less titanium in the alloy. Nonetheless, the results indicate that the alkaline hydrothermal method has potential to be used on different Ti64 alloy substrates and thus possibly for a wide range of applications.

The nanotopography was found to be easily damaged by physical touch. Orthopaedic and dental implants require significant handling during surgery. Based on the observations presented here, this could lead to destruction of some nanotopography before or during implant surgery. Although the titanium dioxide is biocompatible, damaged nanospikes could cause adverse effects such as

inflammation and osteolysis and ultimately lead to implant failure (Guo *et al.*, 2019; Hallab, Cunningham and Jacobs, 2003; Eger *et al.*, 2018). Hallab *et al.* (2003) found the wear and corrosion from titanium spinal implants resulted in high levels of pro-inflammatory cytokines such as tumour necrosis factor-alpha (TNF-α) and osteoclasts, and elevated levels of osteolysis, which led to bone resorption. To mitigate these potential problems, strict handling procedures should be investigated, with specific areas designed on an implant that are available to touch and where no nanotopography is present. Trabecular implants, generate a 3D porous environment, and nanotopography growth within this environment could shield the nanotopography from destruction during insertion into the body (Bencharit *et al.*, 2014).

4.5.3 Comparison of Different Quantification Techniques

Physical characterisation of the nanotopography was measured by a wide range of techniques to determine nanotopography height, diameter and density, together with surface roughness and surface area. Certain measurements could only be obtained from a specific technique, but most of the physical attributes could be determined using multiple approaches, enabling comparisons to be made.

4.5.3.1 Average Nanospike Height

To measure the height of the nanotopography, SEM was used for all surfaces (30 mins to 7 hours), while AFM was used only for the shorter time periods of 30 minutes to 2 hours. Optical profilometry and CM was used to quantify height for 3-hour nanotopographies and above. **Figure 4.22** summarises the average height measurements obtained with each technique.

For the short time durations, between 30 minutes and 2 hours, the SEM and AFM results were generally similar. Both techniques also highlighted inhibited growth between 1 and 1.5 hours. This may be due to the time required for sufficient corrosion of the titanium surface to occur to encourage nanotopography growth (Dong *et al.*, 2007). The longer time duration measurements using SEM, optical profilometry and CM had a greater variation as heights increased. Generally, the SEM measurements were higher, and this is likely due to the difficulty in determining the depth of the topography using a 30° tilt image with the Image J software, leading to an overestimation. Optical profilometry and CM produced similar height measurements for the 3-hour and 4-hour disks. CM has a high resolution (~0.2 µm) compared to OP (~0.5 µm), but differences may also be due to natural batch variation during alkaline hydrothermal growth (Fouquet *et al.*, 2015). Measurements were taken from SEM images of decreasing magnification due to the changes in the dimensions of the nanotopography over time. For example, 2-hour

nanotopography were imaged with SEM at 80,000x magnification while 7-hour topography were imaged at 10,000x magnification. For AFM, CM and OP the surface area remained the same for each duration imaged and nanotopography dimensions measured. Different surface areas were measured between the techniques. For AFM a 5µm^2 surface area was measured as the nanotopography were on the nanoscale; a small surface area was required to accurate image the nanotopography. For OP and CM, a surface area of 20µm^2 and 100µm^2 were measured respectively. Here the topography was microscale in height so a larger area was required to visualise the fabricated structures.

Diu *et al.* (2014) measured two nanotopographies grown at 240°C in 1 M NaOH and, using CM, reported average nanospike heights of ~3 µm after 3-hours growth and ~7 µm after 8-hours growth. This is consistent with the SEM measurements from this project. Dong *et al.* (2007) also reported the height of nanospikes generated at 240°C with 1 M NaOH. Using SEM images, they measured the topography to be 200 nm at 30 minutes, 400 nm at 1 hour, 2-5 µm at 2 and 4 hours. These values are higher at the shorter times than observed in this project, but the exact quantification methodology used by Dong *et al.* (2007) is not known. Likewise, although unclear how the measurement was taken, Jaggessar *et al.* (2018) reported a length of 298±33 nm at 3 hours growth with 240°C and 1 M NaOH.

As anticipated, the increase in nanospike height over time correlated with a concomitant increase in surface area as measured by AFM.

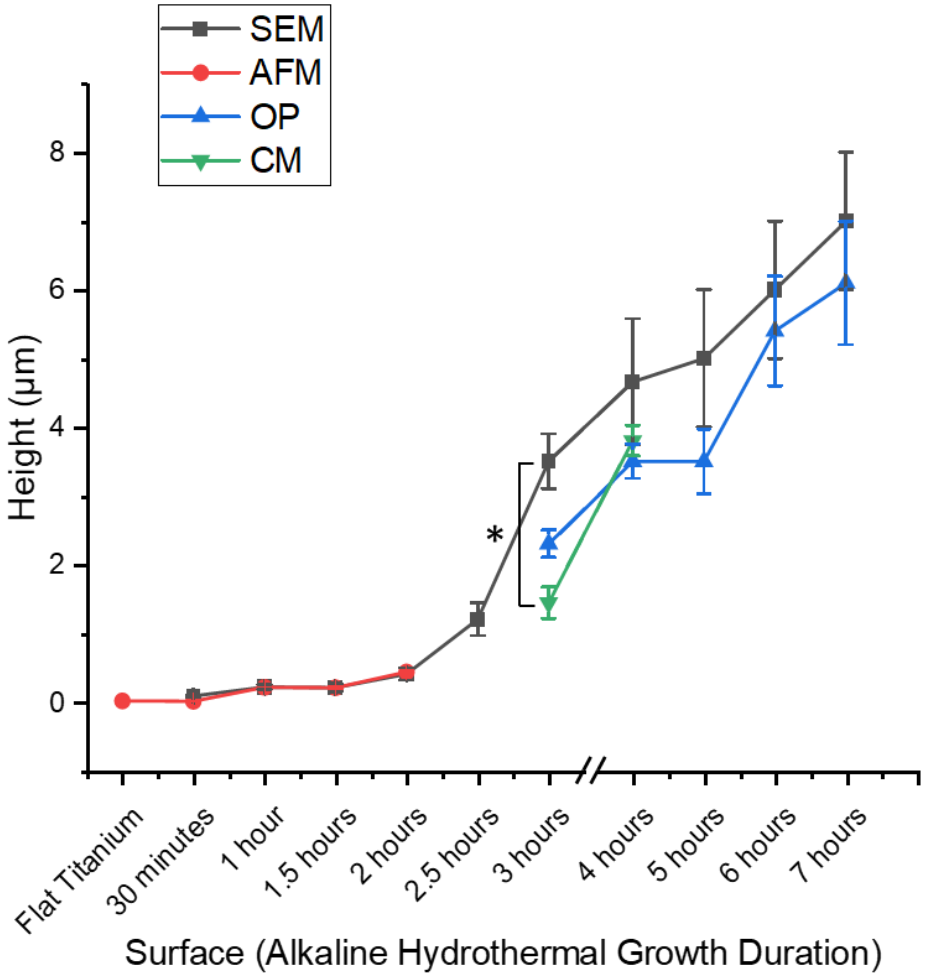

Figure 4.22- *Comparison of average nanotopography height using four surface characterisation techniques. Statistical significance determined by ANOVA with post-hoc Tukey and Bonferroni tests, * $p \leq 0.05$. n=3 from 20 measurements.*

Average Nanospike Diameter

The mean diameter of the nanospikes was found to be ~45 nm, as determined by both SEM and TEM, and remained constant during the alkaline hydrothermal growth which highlights the epitaxial growth (Liu *et al.*, 2014). Both these techniques have high resolution so the topography could be accurately imaged and then measured using image J software.

To obtain suitable images from SEM microscopy, a thin conductive coating of ~6 nm of gold-palladium was applied to the surface. If the coating is not used the electron beam may damage the sample and over charging may lead to poor imaging. A consideration when adding the coating is that it may potentially change/mask some aspects of the structures being visualised (Adamski, Rybska and Błoszyk, 2012). This is an important factor when measuring the diameter of the

nanotopography. In this project the diameter was measured, and 12 nm removed to give an accurate estimate of the diameter of the original nanotopography before the coating was applied.

The diameter measured in this project differs from some reported diameters from other studies using similar hydrothermal techniques. Dong *et al.* (2007) reported 50-100 nm over time but it is unclear how this was measured. Diu *et al.* (2014) reported ~100 nm at 3-hour and 8-hour growth and is believed to have used the confocal microscope. The confocal microscope uses light and so has a relatively poor lateral resolution of 180 nm compared to electron microscope techniques such as SEM and TEM, which can have a resolution as low as 1 nm (Bogner *et al.*, 2006). This may have led to a 2-fold higher estimate of the nanotopography diameter.

Tsimbouri *et al.* (2016) reported 25 nm in diameter for 2-hour to 3-hour nanospike growth and was probably measured by SEM. The samples were unlikely to be sputter coated, which potentially results in low resolution images that can be challenging to accurately measure using programs such as image J.

Cao *et al.* (2018) reported 70 nm at 2-hours growth and 100 nm at 3-hours growth, measured by AFM. As described previously, when imaging and measuring topographies of high aspect ratio such as these nanostructures with AFM, tip convolution may lead to inaccurate representations of the features. The AFM, along with the confocal microscope, may not be able to distinguish between nanospikes when they are intertwined together, leading to an overestimation of the diameter, as it consists of multiple spikes. Although unclear how the measurement was taken, Jaggessar *et al.* (2018) recorded an average diameter of 52±12 nm for 3-hour nanotopography.

Nanospike Density and Pocket Formation

Nanospike density was measured by SEM and progressively reduced with time. This may be due to the coalescing of sodium titanate crystals formed during the alkaline hydrothermal process, as upward growth occurs over time (Goudeli and Pratsinis, 2017). After 3 hours growth, there was intertwining of the nanotopography, which was then quantitatively counted as a single spike. This braiding may be due to the surface tension effects when in liquid or static charge between the nanospikes (Sun *et al.*, 2006; Kong *et al.*, 2004).

At periods in excess of 3 hours, no individual spikes were observed as the nanotopography had intertwined to form ridges; over time, the pockets or niches increased in height and average diameter. At 4-hour growth, Dong *et al.* (2007) reported a pocket diameter of 2-10 µm; for 8-hour nanotopography Diu *et al.* (2014) reported an average pocket diameter of 10-15 µm. Both these studies correlate with the measurements for this project. The increase in topography height

and pocket diameter over time reflects the growth of the nanospikes and as the intertwining of the nanospikes are orientated laterally, the pockets increase in diameter.

Roughness

The RMS roughness of the shorter time durations, 30 minutes to 2 hours, were measured with AFM, while the longer time durations (>3 hours) were measured by OP and confocal microscopy. RMS and maximum roughness increased progressively with nanotopography development over time, reflecting the upward growth and increasing height of the nanotopography.

The RMS roughness was ~120 nm for the 2-hour nanospikes (from AFM), increasing to ~600 nm for the 4-hour nanotopography and ~1400 nm at 7-hours (from OP). The CM values tended to be higher (1100 nm at 4-hour nanotopography), possibly due to the significantly higher CM resolution compared to OP. Cao *et al.* (2018) reported roughness of 245 nm at 2-hours growth and 619 nm at 3-hour growth. Differences may be due to the techniques used, as Cao *et al.* (2018) used AFM for both surfaces. For AFM, differences in tips used, scan rate and scan area size can have a significant effect on tip convolution and subsequent quantification. The maximum roughness values (as measured by OP) is generally 2-3 times greater than the RMS values (as measured by CM and OP). The maximum roughness is a measurement of the vertical extremes of a surface, while the RMS roughness is the standard deviation of the distribution of surface heights (Soliman *et al.*, 2002).

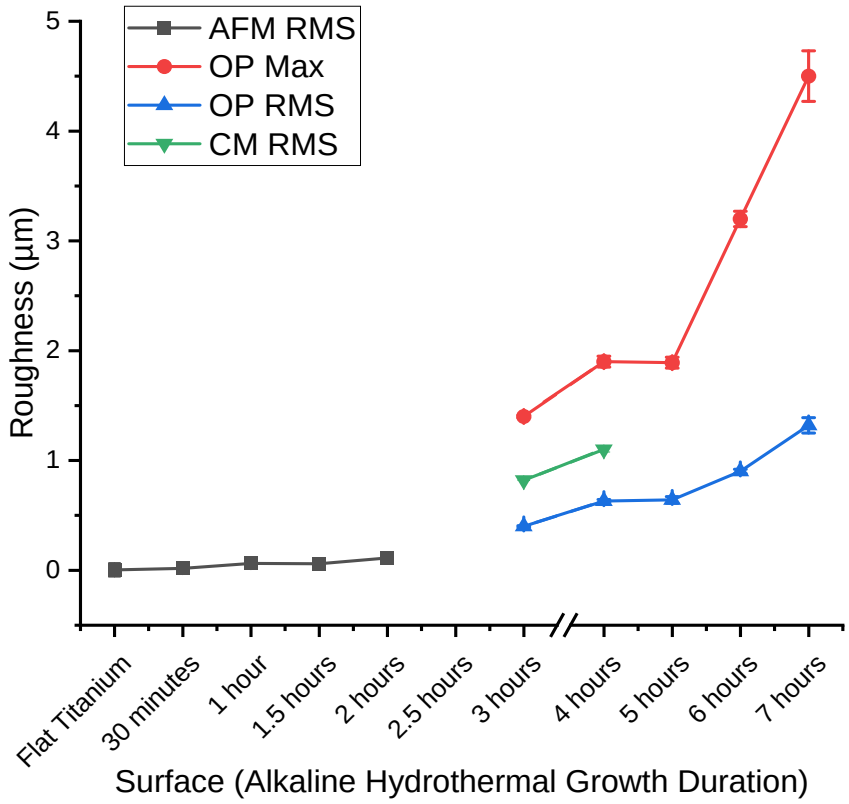

Figure 4.23- *Comparison of roughness measurements using three surface characterisation techniques. RMS: Root-mean-square roughness; Max: Maximum roughness*

4.5.4 Composition and Crystal Structure of Nanotopography

Analysis of the crystal structure of the nanotopography confirmed the predicted stages of the alkaline hydrothermal method, and that the final product comprised of titanium oxide, primarily in the form of anatase.

When the titanium disks are submerged in NaOH, the surface of the titanium undergoes progressive corrosion and sodium titanate nanospikes ($Na_2Ti_2O_5 \cdot H_2O$) grow perpendicularly from the substrate (**Equation 4.1**). This was confirmed by XRD by the presence of the 200, 110, 310, 020 and 220 peaks, which correspond to sodium titanate (Liu, Boercker and Aydil, 2008; Boercker, Enache-Pommer and Aydil, 2008). The spikes have been shown to have a body centred orthorhombic structure made up of TiO_6 octahedral sheets, which are electrostatically held together by Na^+ ions (Boercker, Enache-Pommer and Aydil, 2008; Kiatkittipong *et al.*, 2013; Wang *et al.*, 2011).

$$2Ti + 2NaOH + 4H_2O \longrightarrow Na_2Ti_2O_5{\cdot}H_2O + 4H_2$$

Equation 4.1- *Alkaline hydrothermal reaction between titanium and sodium hydroxide to form sodium titanate and hydrogen.*

Immersing the disks in hydrochloric acid leads to ion exchange between the sodium ions in the sodium titanium nanospikes and hydrogen ions in the HCl to generate hydrogen titanate ($H_2Ti_2O_5{\cdot}H_2O$) nanospikes (**Equation 4.2**) (Liu, Boercker and Aydil, 2008; Boercker, Enache-Pommer and Aydil, 2008). Hydrogen titanate has the same crystal structure as the sodium titanate nanospikes, as shown by the same XRD peaks of 200, 110, 310, 020 and 220 (Liu, Boercker and Aydil, 2008; Boercker, Enache-Pommer and Aydil, 2008; Kiatkittipong *et al.*, 2013). Previous research (Liu *et al.*, 2008) has observed a shift to the left of the 200 and 310 diffraction peaks, indicating a slight change in lattice spacing that may be due to the exchange between sodium and hydrogen ions between the titanium oxide octahedral sheets. However, this shift may have been due to data processing, and no discernible shift was seen in the XRD data reported here.

$$Na_2Ti_2O_5{\cdot}H_2O + 2HCl \longrightarrow H_2Ti_2O_5{\cdot}H_2O + 2NaCl$$

Equation 4.2- *Ion Exchange reaction to convert sodium titanate into hydrogen titanate and sodium chloride.*

The final step of the alkaline hydrothermal process involves calcination/dehydration of the nanospikes in air at 600°C for 2 hours, during which the nanospikes should be converted into TiO_2 nanospikes through topotactic transformation (**Equation 4.3**). During heating, the TiO_6 octahedral sheets within the hydrogen titanate come together and rearrange to form TiO_2. This transformation was confirmed by the presence of peaks resembling titanium dioxide in XRD spectra, and the presence of the chemical bond of titanium dioxide, as detected by XPS (Liu, Boercker and Aydil, 2008; Boercker, Enache-Pommer and Aydil, 2008; Ijadpanah-Saravy *et al.*, 2014).

$$H_2Ti_2O_5{\cdot}H_2O \longrightarrow 2TiO_2 + 2H_2O$$

Equation 4.3- *Calcination step where hydrogen titanate is converted into titanium dioxide.*

EDX and XPS analysis confirmed that the nanospikes consisted of pure titanium dioxide. No sodium from the sodium titanate was present, indicating that the ion exchange with hydrochloric acid during the post treatment process was successful. The XRD and TEM results indicated that the titanium dioxide consisted of approximately 70% anatase and 30% rutile. The anatase to rutile transformation occurs at around 600°C so more rutile may be expected at higher temperatures (Byrne *et al.*, 2016)

5.

BACTERIAL INTERACTION WITH NANOTOPOGRAPHY

Contents

5.1 Introduction

The objective of this chapter is to evaluate the antimicrobial potential of the nanotopographical arrays produced by the alkaline hydrothermal method as described in the previous chapter. From previous studies (Diu *et al.*, 2014; Cao *et al.*, 2018; Tsimbouri *et al.*, 2016) there are indications that the nanotopography formed had antimicrobial activity and so it was therefore anticipated that the nanotopography generated for this project may also exhibit antimicrobial properties against both Gram-positive and -negative bacteria.

Many of the previous studies used only Live/Dead staining as the method of assessing bactericidal potential of the nanotopography (Diu *et al.*, 2014; Tsimbouri *et al.*, 2016; Ivanova *et al.*, 2013; Linklater *et al.*, 2017; Hasan *et al.*, 2013). While a valid and well-recognised technique, using a single approach limits the extent of the data that can be obtained and can risk potential methodology-based bias in data interpretation.

In this project, a number of viability techniques were therefore tested against both Gram-negative (*E. coli, P. aeruginosa* and *K. pneumoniae*) and Gram-positive (*S. aureus*) bacteria. These included Live/Dead staining, viability quantitative PCR (v-qPCR), lactate dehydrogenase (LDH) assay, and metabolic-based assays BacTiter-Glo and RealTime-Glo. The interaction of the bacteria with the nanotopography were also visualised by SEM and SEM-FIM.

5.2 Viability Assays and Techniques

5.2.1 Live/Dead *Bac*Light Bacterial Viability Assay

The Live/Dead *Bac*Light assay is a widely used image-based technique using fluorescence microscopy or CLSM for visual assessment of intact or disrupted bacterial cell membranes within a population adhering to an interface (Ivanova *et al.*, 2012; Bhadra *et al.*, 2015; Pogodin *et al.*, 2013). The assay involves two fluorescent dyes of different cell permeability and light excitation

and emission wavelengths. SYTO9, with excitation/emission spectra of 480/500 nm, is a membrane permeable stain that fluoresces green when bound to nucleic acid and consequently identifies all bacteria within the population.

Propidium iodide (PI), with an excitation/emission spectra of 490/635 nm, is membrane impermeable and thus may only enters cells with a disrupted membrane. PI binds to bacterial nucleic acid and has the capacity to displace any bound SYTO9, so that dead or damaged bacterial cells may fluoresce red (Stiefel *et al.*, 2015; Stocks, 2004; Robertson *et al.*, 2019; Rosenberg, Azevedo and Ivask, 2019).

5.2.2 Viability qPCR

Viability polymerase chain reaction (v-PCR) is a technique to assess the viability of bacteria within a suspension or on a surface. To discriminate between DNA harvested from viable or non-viable cells, v-qPCR utilises a non-membrane permeable intercalating DNA dye, propidium monoazide (PMA) (Zhou *et al.*, 2019; Telli and Doğruer, 2019). PMA enters bacterial cells with a disrupted membrane and in the presence of intense visible light, the dye photolyzes and covalently binds to DNA. The DNA is irreversibly modified and consequently PMA inhibits its normal amplification by Taq polymerase. A schematic of this process is shown in **Figure 5.1**.

Within an experiment, samples are split into PMA-treated and non-treated reactions, which are used to calculate the quantity of DNA derived from viable cells and all cells (total DNA) respectively. During the qPCR reaction, samples with high levels of cell death will have relatively low levels of amplifiable DNA following PMA modification, and therefore will give a high threshold cycle (C_T) value. The difference in C_T values between the PMA-treated and untreated reactions potentially allows quantification of the proportion of viable/non-viable cells in a population. A standard curve of DNA extracted from bacterial suspensions of known cell number against C_T values can be used to quantify the number of viable cells present in the test sample (Telli and Doğruer, 2019).

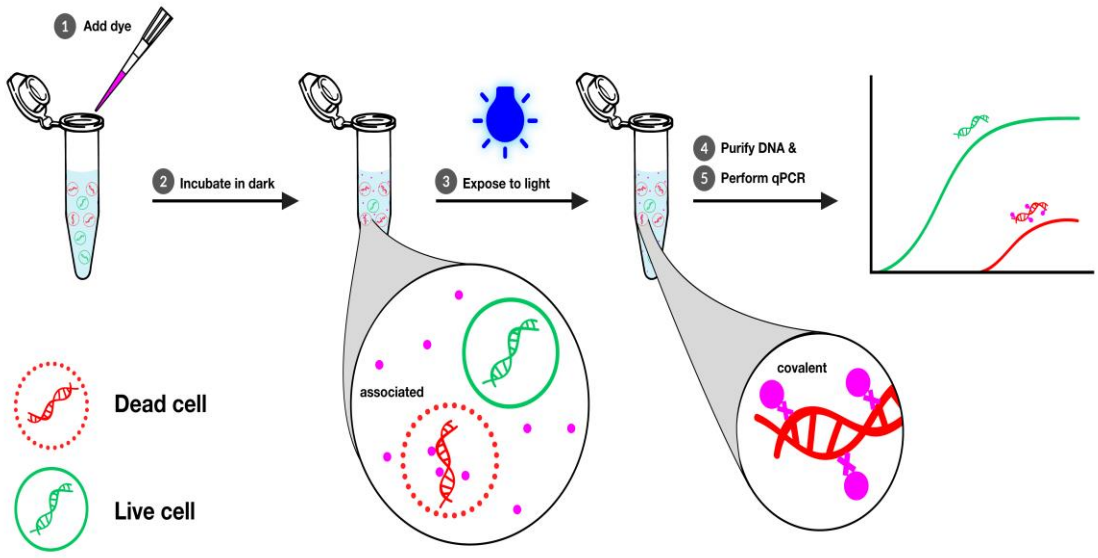

Figure 5.1- *v-PCR schematic. (Biotium, 2019)*

5.2.3 Lactate Dehydrogenase Activity Assay

The lactate dehydrogenase (LDH) activity assay is a colorimetric method developed by Merck and is most commonly used for assessing the viability of mammalian cells. For this study, the suitability of this method for bacteria was investigated, as it offered the benefit of not requiring bacteria to be recovered from the nanotopography for analysis. LDH is an enzyme present in cells that catalyses the reaction between pyruvate and lactate. When the cell membrane is damaged, LDH is released into the environment, where it can be detected. High levels of LDH therefore indicate high levels of membrane-compromised cells.

The assay quantifies the amount of LDH present in the environment by applying the substrate NAD, which LDH reduces to NADH. NADH is then oxidised by reacting with a tetrazolium salt into a red formazan product that can be quantified by absorbance measurements at 450 nm. The process is shown schematically in **Figure 5.2**. The absorbance is related to the amount of LDH present and to the number of dead or damaged cells (Kumar, Nagarajan and Uchil, 2018; Kaja *et al.*, 2017, 2015).

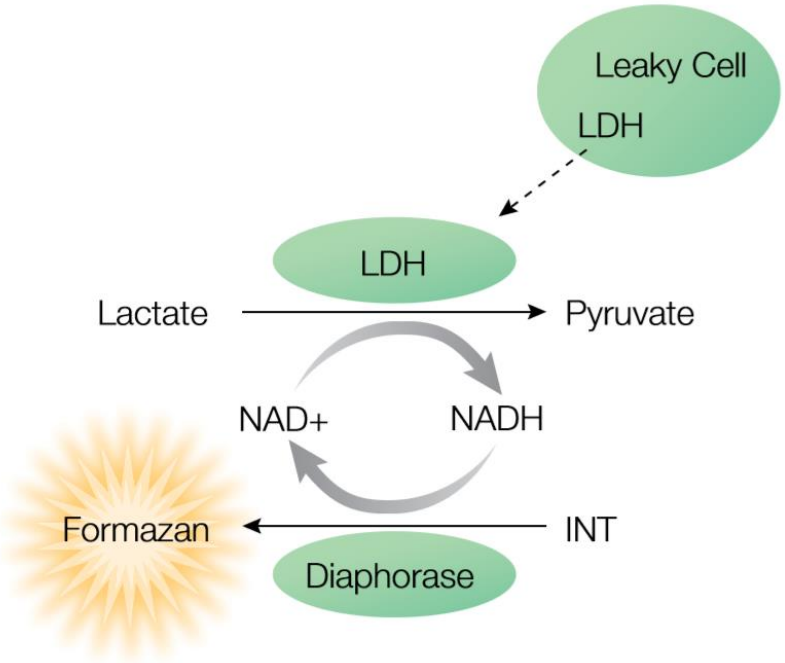

Figure 5.2- *Schematic of the LDH activity assay (Promega, 2012)*

5.2.4 BacTiter-Glo

The BacTiter-Glo assay was developed by Promega and provides a quantitative technique based on ATP levels to determine the number of metabolically viable microbial cells present in a solution. This assay has been used in several recent studies to assess bacterial viability (Reyneke *et al.*, 2016; Tschang and Thoma, 2019; Santivañez-Veliz *et al.*, 2016). Bacterial cells are lysed to release their ATP. Lysates are then mixed with beetle luciferin and a recombinant firefly luciferase. ATP allows the oxygenation of the luciferin by the luciferase enzyme, releasing a 'glow-type' luminescence signal that can be quantified (**Figure 5.3**).

Viable, metabolising cells have high levels of ATP, while dead or low metabolising cells have low levels of ATP present. The level of luminescence is related to the number of viable cells within a solution, which can be determined using standard curves of luminescent signal against bacterial CFU (Promega, 2016a).

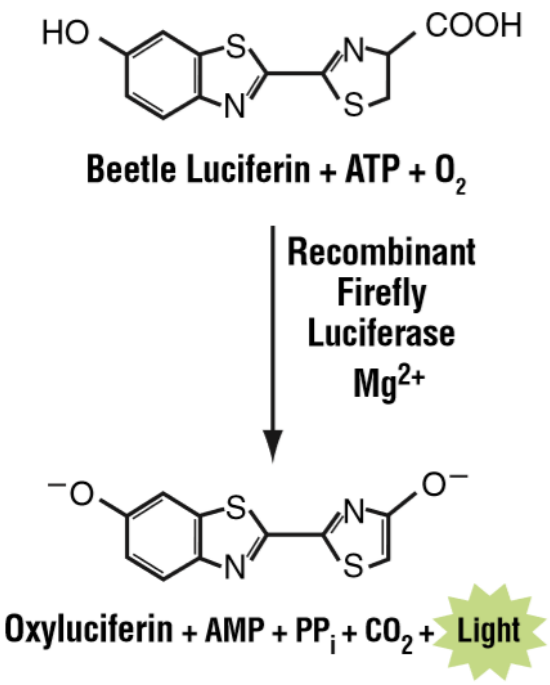

Figure 5.3- *Schematic of the BacTiter-Glo assay mechanism (Promega, 2016a)*

5.2.5 RealTime-Glo

RealTime Glo is another microbial viability assay developed by Promega, which measures the metabolic reducing potential of the cell as an indicator of viability and is often used for mammalian cell studies (**Figure 5.4**) (Lowin *et al.*, 2018; Petersen, Tang and Fields, 2019; Slotta *et al.*, 2018). The assay includes a cell-permeable MT Cell Viability Substrate and a NanoLuc luciferase enzyme. The MT Cell Viability Substrate is added to a bacterial suspension and if cells are viable, the substrate is reduced within the bacterial cell into a NanoLuc Substrate. This substrate subsequently diffuses out from the cells and rapidly reacts with the NanoLuc luciferase enzyme, resulting in a bioluminescent signal that can be measured. Non-viable cells are unable to reduce the pro-substrate and so cannot produce a luminescent signal. As the assay is non-lytic, it allows continuous assessment of bacterial viability over time (Promega, 2016b).

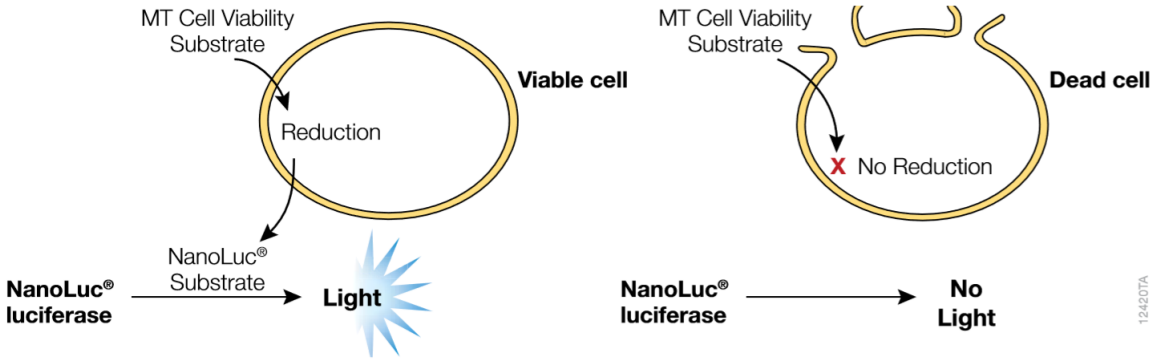

Figure 5.4- *Schematic of the RealTime-Glo assay mechanism (Promega, 2016b).*

5.2.6 SEM and FIB-SEM

Scanning electron microscopy (SEM) is an imaging technique dating back to 1935. It involves firing a focussed beam of accelerated electrons within a vacuum at a specimen and detecting the secondary electrons that are emitted from the surface to visualise the surface morphology and topography. This is now a routine technique widely utilised in material science, with a high resolution of 1-20 nm (Bogner *et al.*, 2007). In this project the SEM was used to visualise the interaction of bacteria on the nanotopography. A limitation of the SEM when imaging this interaction is the inability to visualise the underneath or inside the bacterium. To overcome this problem the focus ion beam-SEM (FIB-SEM) was utilised.

In FIB-SEM, a focused argon ion beam is sequentially used to slice or mill sample layers, as small as 3 nm thick. The SEM takes images of the sample after each slice of the FIB (Romero-Brey and Bartenschlager, 2015). Using modelling programs such as Avizo, the images can be collated to generate 3D models of the sample to give an enhanced 3D perspective.

5.3 Assessment of Viability Technique Suitability

5.3.1 v-qPCR

5.3.1.1 Generation of a Standard Curve

v-qPCR relies on the differences in the amount of amplifiable DNA template present within samples to quantify bacterial viability. As a first step, a standard curve was generated using known quantities (0.005-50 ng) of genomic DNA extracted from *P. aeruginosa* (**Figure 5.5)**. This would allow Ct values from subsequent test samples to be converted into the corresponding amount of amplifiable DNA. A log plot of the known concentrations against their respective Ct values demonstrated a very high correlation between DNA concentration and fluorescence (**Figure 5.6**).

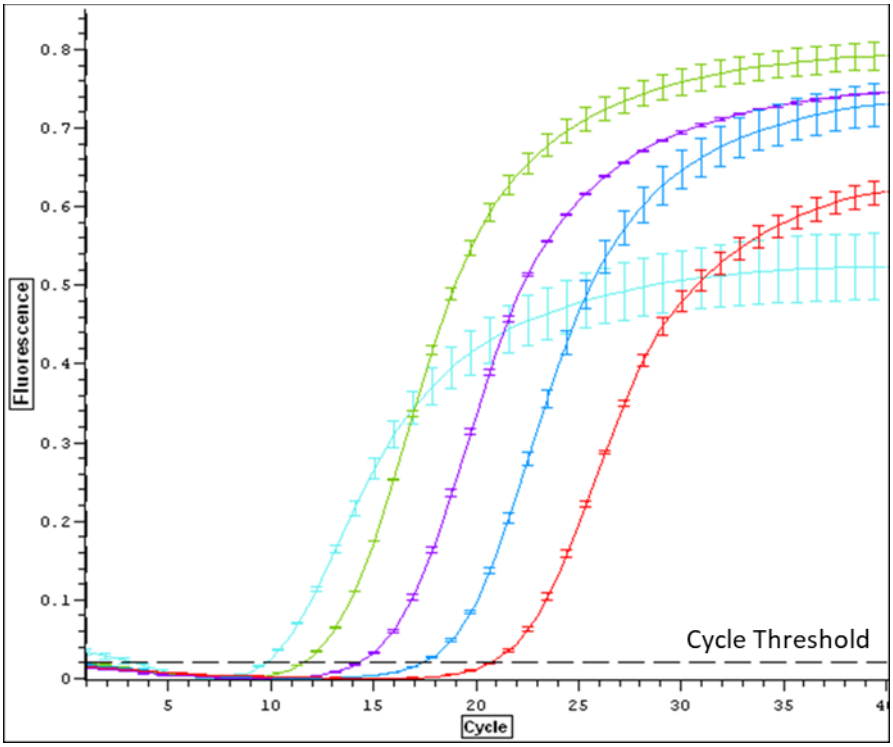

Figure 5.5- *Amplification plots for standard concentrations of DNA. Known concentrations of DNA from P. aeruginosa were amplified using qPCR to determine threshold cycle values. Systematic increases in Ct value with known DNA concentration decreases were seen. Turquoise: 50 ng, Green: 5 ng, Purple: 0.5 ng, Blue: 0.05 ng and Red: 0.005 ng.*

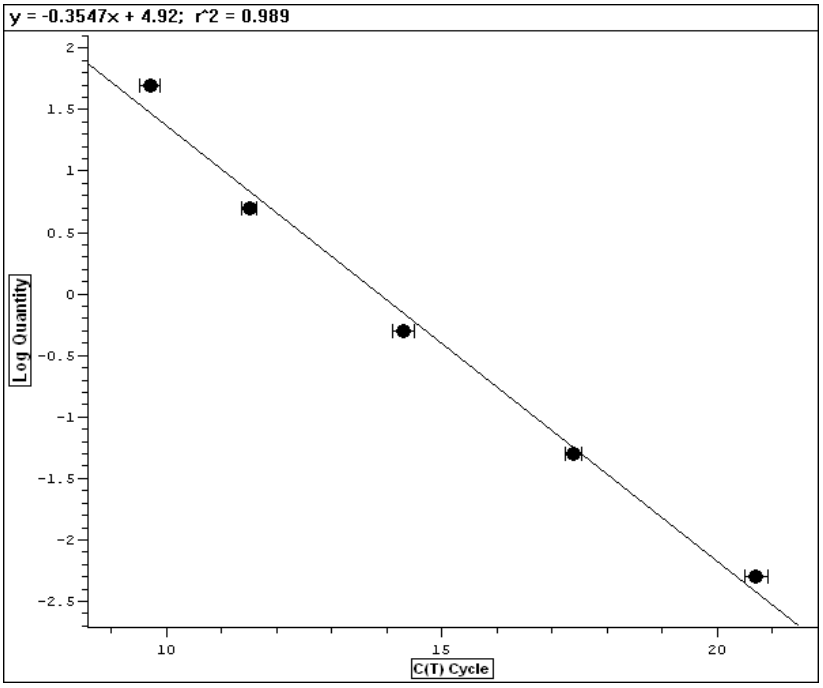

Figure 5.6- *Log of DNA concentration against Ct value with line of best fit. The Ct values found from known concentrations of DNA were plotted against the log of the respective DNA concentration in nanograms.*

5.3.1.2 Validation of v-qPCR Method

To assess the capacity of v-qPCR to distinguish between viable and non-viable bacteria, v-qPCR experiments were performed using *P. aeruginosa* suspensions of known viability levels (0%, 50% and 100% viability). Bacteria harvested from a mid-exponential phase broth culture were used as the 100% viable sample. To obtain a 0% viable sample, the bacterial suspension was heated at 70°C for 20 minutes, and loss of viability confirmed by viable count. To obtain the 50% viable sample, the 100% and 0% viable samples were mixed at a 1:1 ratio.

For the samples with added PMA, the highest Ct, as expected, was the 0% viability sample with a value of 22.1, followed by the 50% viability sample and then the 100% viability sample, with a Ct value of 13.28 (**Figure 5.7**). Confirming comparable cell numbers in each suspension, this latter Ct value was similar to the Ct values without PMA for 50% (13.04) and 0% (13.28) viability. A mistake during dilution of the genomic DNA in the 100% viability without PMA sample resulted in a lower Ct value of 11.11. Using the standard curve shown in **Figure 5.6,** the quantity of initial template DNA was calculated and is shown in **Figure 5.7**.

Table 4.1 shows that only very minor amplifiable DNA (0.05%) is present in the 0% viability sample. As this sample had only dead cells the PMA dye should arrest all DNA being amplified. This technique is considered potentially useful but accurate bacterial viability may be

difficult to quantify as the 50% and 100% viability samples recorded values ~15% less at 36% and 85% respectively. This may imply that while the v-qPCR could distinguish between different levels of viability, it may only be accurate within a certain range of DNA template concentrations. These aspects would need to be taken into consideration for subsequent experiments.

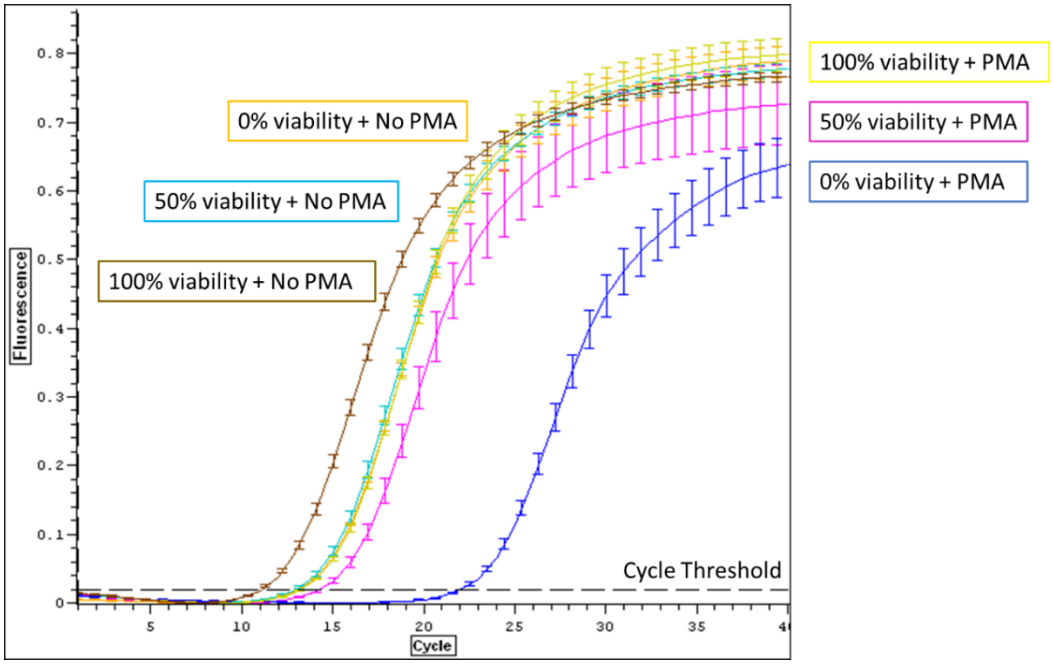

Figure 5.7- *Amplification plots of P. aeruginosa suspensions at different viability levels. Three suspensions of P. aeruginosa were prepared at 0%, 50% and 100% viability. DNA was extracted, normalised to the lowest concentration and used as template in v-qPCR. Blue: 0% viability+PMA, Pink: 50% viability+PMA, Yellow: 100% viability+PMA, Orange: 0% viability-no PMA, Turquoise; 50% viability-no PMA; Brown: 100% viability-no PMA.*

Sample	AVERAGE THRESHOLD CYCLE (C_T)	INITIAL AMPLIFIABLE DNA (ng)
Negative Control	25.27	9.07×10^{-5}
Positive Control	12.27	3.67
0% viability PMA	22.1	0.001205
0% viability No-PMA	13.1	1.831
50% viability PMA	14.3	0.7037
50% viability No-PMA	13.04	1.972
100% viability PMA	13.28	1.611
100% viability No-PMA	11.11	ND*

Table 5.1- *Quantity of amplifiable template DNA from P. aeruginosa suspensions at different viability levels. *ND, not done (due to dilution error)*

5.3.1.3 v-qPCR Pilot Study with Nanotopographical Surfaces

In a pilot experiment, v-qPCR was used to investigate if a higher percentage of non-viable *P. aeruginosa* cells were present following a 3-hour incubation on 2-hour nanospike disks compared to flat disks (**Table 5.2**). A 3-hour timepoint was chosen due to previous research indicating bactericidal activity within this timeframe (Diu *et al.*, 2014; Tsimbouri *et al.*, 2016; Hazell *et al.*, 2018c; Jaggessar *et al.*, 2018b).

For both disk types, a higher Ct value was obtained for the samples with PMA compared to samples without PMA, indicating some cell death. Quantities of initial amplifiable DNA were then calculated, and the relative live/dead cell percentages estimated (**Table 5.2)**. The results indicated that there were 10% more dead bacteria on the nanospikes compared to the flat titanium. However, the percentages of non-viable bacteria were unexpectedly high, especially for the control, at 70-80%. This was inconsistent with viability data obtained concomitantly using other methodologies. The merits of this technique is discussed in **Section 4.6.1** but it was decided it was not sufficiently reliable so was not taken forward for further viability analyses.

Sample	AVERAGE THRESHOLD CYCLE (C_T)	INITIAL AMPLIFIABLE DNA (ng)	% VIABILITY
Flat Titanium with PMA	14.09	0.9523	Live: 28 Dead: 72
Flat Titanium without PMA	12.06	3.425	
2-hr Nanospikes with PMA	14.92	0.4682	Live: 18 Dead: 82
2-hr Nanospikes without PMA	12.9	2.646	

Table 5.2- *Viability of P. aeruginosa on flat titanium and 2-hour nanospikes*

5.3.2 Lactate Dehydrogenase Assay

The lactate dehydrogenase (LDH) technique is a colorimetric assay that quantifies the amount of lactate dehydrogenase, released from a cell when it lyses. The higher the absorbance, the more LDH is present in the suspension indicating a higher proportion of non-viable cells.

Two Gram negative bacteria, *P. aeruginosa* and *K. pneumoniae* , were incubated for 1 and 3 hours on flat mirror-polished titanium disks or on five different nanotopographies generated over 30 minutes to 7 hours (**Figure 9.1**). For *P. aeruginosa,* after 1-hour incubation, the A_{450} values were approximately 0.1 for all surfaces, rising to 0.3 after 3 hours. Likewise, A_{450} values were approximately 0.2 for *K. pneumoniae*, increasing to over 0.5 for all the test surfaces after 3 hours. Most of the nanotopographical surfaces had very slightly higher OD values than the flat titanium suggesting a higher proportional of dead cells.

To convert these A_{450} values into % of dead cells, a total lysis sample was needed for each test surface to calculate the maximum quantity of LDH that could be released using the equation as shown in **Section 3.3.2.2**. Triton X-100 and a range of SDS-NaOH concentrations were tested, as the lysis solution supplied with the LDH assay was only compatible with eukaryotic cells. Only the Triton X-100 solution was able to lyse all the bacterial cells, and only for *P. aeruginosa*. These calculations implied that after 1-hour incubation, the percentage of dead cells was approximately 60% for all the surfaces, rising to nearly 100% after 3 hours (**Figure 9.2**).

These data were inconsistent with those obtained using other methodologies. It was noted that there was a distinct colour difference between the test surfaces and positive control, possibly indicating that the Triton X-100 was interfering with the formation of formazan and thus the absorbance reading. Due to this complication, the LDH assay was not taken forward for further viability analyses.

5.4 Bacterial Viability on Nanotopography

5.4.1 Live/Dead Stain

Live/Dead imaging was used for *K. pneumoniae* and *E. coli* to qualitatively assess the distribution and number of cells adhering to the nanotopography compared to the flat titanium control, and the extent of any membrane disruption.

On the control, most *K. pneumoniae* cells were viable, with a few non-viable cells present (**Figure 5.8**). Likewise, across the different nanotopographies, most cells were still viable, with their membrane seemingly intact. This suggested that *K. pneumoniae* cell membranes were not penetrated by the nanospikes within the 3-hour incubation period. Furthermore, there were significantly fewer bacteria adhering, in excess of a 50% reduction, on the 2-, 3- and 4-hour nanospikes than on the flat titanium (**Figure 5.8**). Bacterial attachment on 3-hour and 4-hour nanotopographies, which have niches of ~1-2 µm and 5-7 µm in diameter, respectively, suggested that the topographies may sequester the bacteria within the niches (**Figure 5.8D-E**), as opposed to the more homogeneous coverage seen on flat titanium and short nanotopographies.

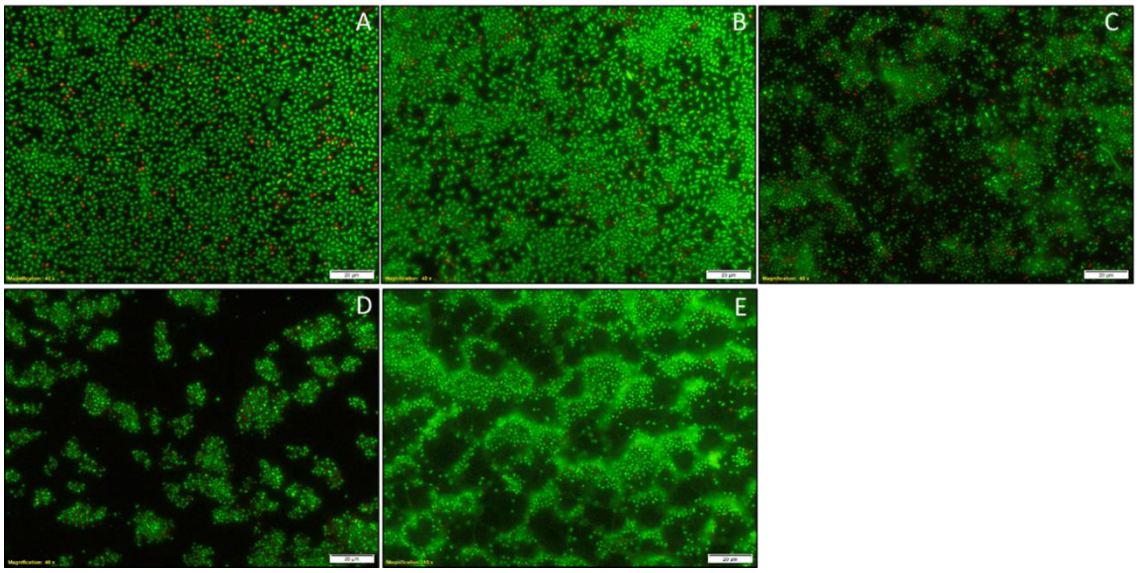

Figure 5.8- *Live/Dead staining of K. pneumoniae after 3-hours incubation on different surfaces. Bacterial inoculum (40 µl) was pipetted onto A) flat titanium, B) 1.5-hour nanospikes, C) 2-hour nanospikes, D) 3-hour nanotopography, or E) 4-hour nanotopography surfaces and incubated at 37°C for 3 hours. The surfaces were washed in Tris-HCl and then incubated with SYTO9/PI stain for 15 minutes. After washing to remove excess stain, the disks were then imaged under a fluorescence microscope.*

For *E. coli*, on all the surfaces, most cells were green, indicating viable cells with intact membranes, and only a few red cells were visible (**Figure 5.9**). There was also evidence of bacteria being sequestered within the niches of the 3- and 4-hour nanotopography. There was a relatively homogeneous spread of *E. coli* cells on the flat titanium, but this was reduced considerably for the nanotopography, especially for the 3- and 4-hour disks, and even more than the cases for *K. pneumoniae*.

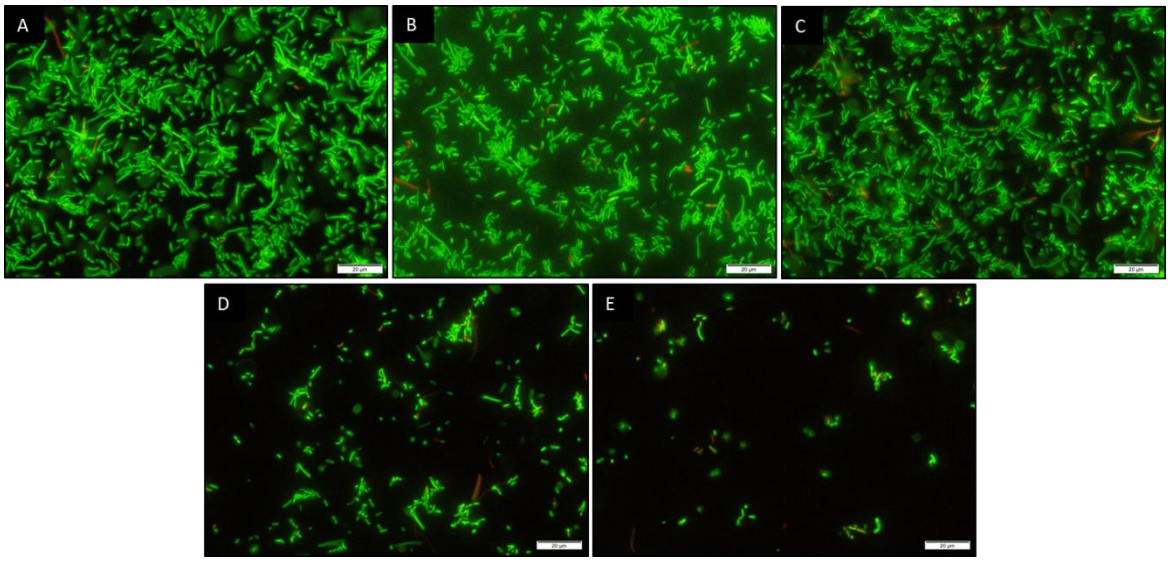

Figure 5.9- *Live/Dead staining of E. coli after 3-hours incubation on different surfaces. Bacterial inoculum (40 µl) was pipetted onto A) flat titanium, B) 1.5-hour nanospikes, C) 2-hour nanospikes, D) 3-hour nanotopography, or E) 4-hour nanotopography surfaces and incubated at 37°C for 3 hours. The surfaces were washed in Tris-HCl and then incubated with SYTO9/PI stain for 15 minutes. After washing to remove excess stain, the disks were then imaged under a fluorescence microscope.*

5.4.2 BacTiter-Glo

5.4.2.1 Standard Curves

BacTiter-Glo is a metabolic end-point assay that quantifies the presence of ATP as luminescence in a solution after it has been released from lysed bacteria. The assay measures the viability of the bacteria in the overlying solution and on the disks while the Live/Dead staining investigates the cells adhered on the disks. To be able to correlate luminescence with CFU, standard curves for each test strain were generated.

Mid-exponential phase inocula of *E. coli*, *K. pneumoniae* and *S. aureus* were serially diluted, mixed with BacTiter-Glo reagent, and the luminescence measured on a plate reader. Mid-exponential bacteria were used due to high metabolic rates during this phase, important for metabolic assays such as BacTiter-Glo. *E. coli*, *K. pneumoniae* and *S. aureus* were all used due to their prevalence in orthopaedic implant infections (**Section 2.2.1**) while *P. aeruginosa* was discarded due to possible mutation within bacterial stocks. Concomitant viable counts were carried out and the CFU calculated. Standard curves were then made by plotting the log of the luminescence against CFU (**Figure 5.10**). The graphs show a linear relationship between the log of the luminescence and corresponding CFUs for all three bacterial species. The slope of the line was used to convert measured luminescence values in subsequent experiments to CFU.

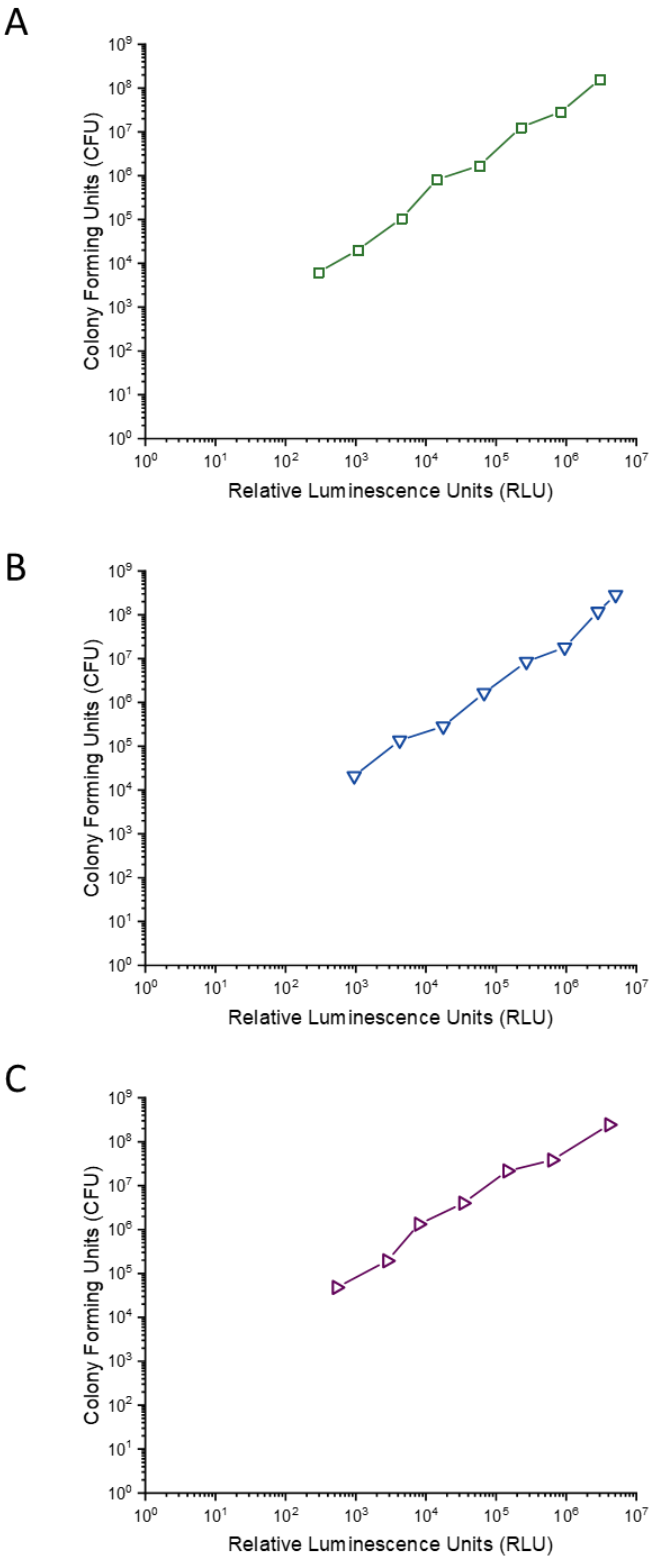

Figure 5.10- *BacTiter Glo standard curves for E. coli, K. pneumoniae and S. aureus. Mid-exponential phase inocula of A) E. coli, B) K. pneumoniae and C) S. aureus were serially diluted, mixed with BacTiter-Glo reagent, and the luminescence measured on a plate reader. These values were then plotted against corresponding viable counts. n=3 in triplicate.*

5.4.2.2 Viability of Bacteria on Nanotopography

Bacteria were incubated on five surfaces, including four nanotopographies (1.5-hour, 2-hour 3-hour and 4-hour), for 3 hours, and levels of viability determined by BacTiter-Glo assay. For *E. coli* (**Figure 5.11**), *K. pneumoniae* (**Figure 5.12**) and *S. aureus* (**Figure 5.13**), numbers of viable cells on the nanotopographies were generally lower but not significantly different compared to the titanium control. This suggests that the metabolic activity of the bacterial cells was not significantly affected by the presence of nanotopographical surfaces within the 3-hour incubation period. Nonetheless, there was a trend for lower CFU values to be seen for *E. coli* on the niche-type disks, and for *K. pneumoniae* across all of the nanotopographies. The most encouraging trend was exhibited by *K. pneumoniae* which indicated up to 50% fewer cells in the solution on the nanotopography than on the flat titanium. Of note, the trend was not apparent for *S. aureus*, a Gram-positive bacterium within the first 3 hours of incubation. *S. aureus* was then analysed for a 9-hour period by the RealTime-Glo assay as described **Section 5.4.3**.

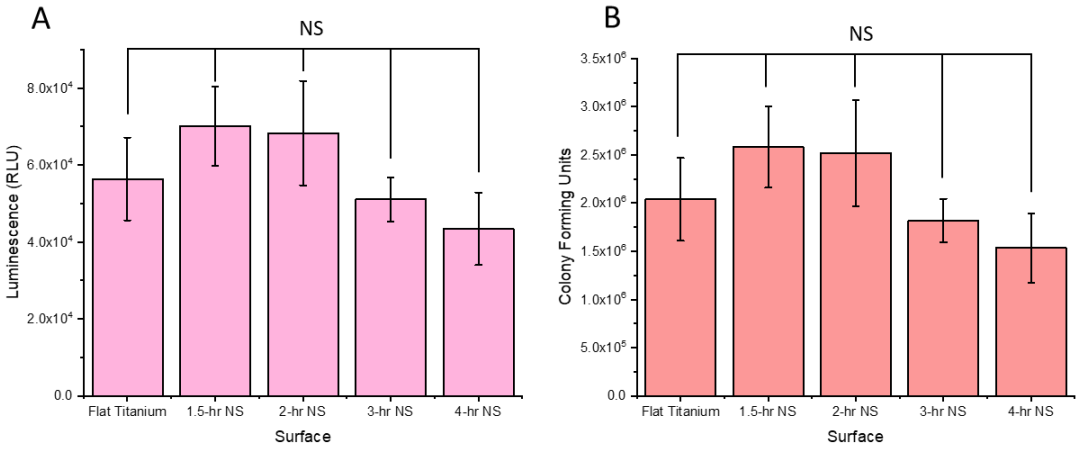

Figure 5.11- *Viability of E. coli on different nanotopographical surfaces as assessed by BacTiter-Glo. Bacterial inocula (40 µl) were pipetted onto control (flat) or nanospike (NS) surfaces and incubated for 3 hours at 37°C. BacTiter-Glo reagent was then added and the luminescence measured on a plate reader after 5 minutes (A). Luminescence values were converted into CFU using a standard curve (B). As determined by ANOVA with post-hoc Tukey and Bonferroni tests, NS=not significant. n=4 in duplicate.*

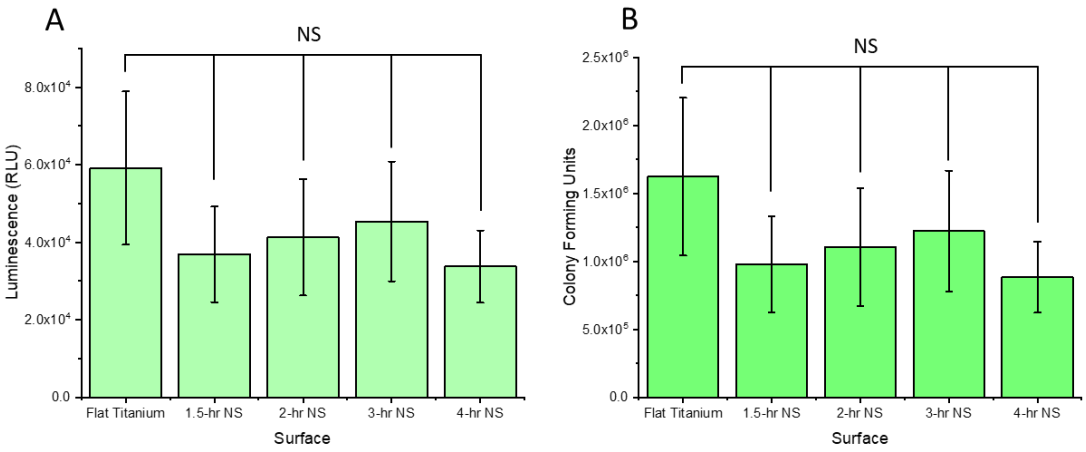

Figure 5.12-*Viability of K. pneumoniae on different nanotopographical surfaces as assessed by BacTiter-Glo. Bacterial inocula (40 µl) were pipetted onto control (flat) or nanospike (NS) surfaces and incubated for 3 hours at 37°C. BacTiter-Glo reagent was then added and the luminescence measured on a plate reader after 5 minutes (A). Luminescence values were converted into CFU using a standard curve (B). As determined by ANOVA with post-hoc Tukey and Bonferroni tests, NS=not significant. n=4 in duplicate.*

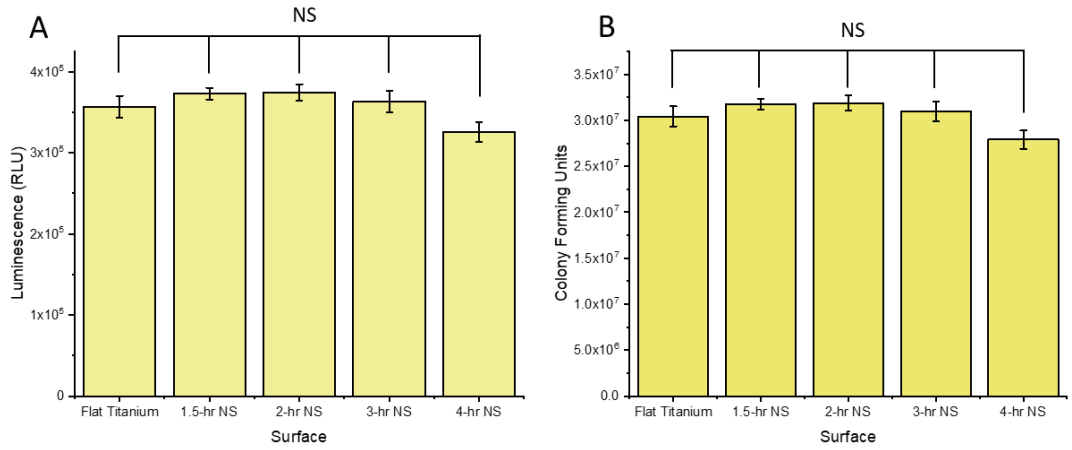

Figure 5.13- *Viability of S. aureus on different nanotopographical surfaces as assessed by BacTiter-Glo. Bacterial inocula (40 µl) were pipetted onto control (flat) or nanospike (NS) surfaces and incubated for 3 hours at 37°C. BacTiter-Glo reagent was then added and the luminescence measured on a plate reader after 5 minutes (A). Luminescence values were converted into CFU using a standard curve (B). Statistical significance determined by ANOVA with post-hoc Tukey and Bonferroni tests, NS=not significant. n=4 in duplicate.*

5.4.3 RealTime-Glo

RealTime-Glo was used to measure the vitality of *S. aureus* every 10 minutes on flat titanium and five nanotopographical surfaces: 1-hour, 1.5-hour, 2-hours, 3-hours, and 4-hour. A duration of 9 hours was used as, beyond this timepoint, the luminescence on each surface, including control,

decreased. This indicated that factors independent of surface morphology were affecting bacterial metabolism.

Up to 3 hours, there was little difference observed between the disks, and bacterial growth on each of the surfaces entered the exponential phase at around 4 hours (**Figure 9.3**). Subsequently the highest luminescence readings were seen for both the 1-hour nanotopography and flat titanium disks, suggesting that these surfaces were most favourable for bacterial growth. The vitality of *S. aureus* on 1.5-hour and 3-hour nanotopography was similar, and significantly less than the flat titanium and 1-hour nanospike disks (**Figure 9.3**). This indicated that the longer nanospikes of the 1.5-hour nanotopography and the formation of pockets for the 3-hour nanotopography may be affecting bacterial growth. Luminescence readings for 2- and 4-hour nanotopographies remained very low over the 9 hours and maximum RLU values were only 5% and 17% respectively of those recorded for the flat titanium control (**Figure 9.3**). These results taken together with the BacTiter-Glo data suggest that the longer nanospikes and niche morphologies significantly impaired *S. aureus* metabolic activity but only after a 4-hour incubation period.

5.5 Imaging Bacterial Interactions with Nanotopographies

5.5.1 SEM Imaging of Bacterial Interactions with Surfaces

Live/Dead staining had suggested that little membrane piercing, or disruption occurred when *E. coli* or *K. pneumoniae* interacted with the different nanotopographical surfaces over 3 hours. To better assess this by visualising the interactions at high magnification, SEM was utilised to image Gram-negative bacteria *P. aeruginosa*, *E. coli*, and *K. pneumoniae*, and the Gram-positive bacterium *S. aureus*, on flat titanium and three different nanotopographies: 2-hour, 3-hour and 4-hour.

5.5.1.1 *P. aeruginosa* Images

On flat titanium **(Figure 5.14A)** there was evidence of cell division and the presence of adhesins assisting the attachment of *P. aeruginosa* to the surface. This suggests that the cells were healthy and growing. However, there was also evidence of excessive dehydration, as cells appeared flat, excessively wrinkled, and with membrane subsidence evident. Likewise, on the 2-hour nanospikes, the *P. aeruginosa* cells had collapsed and deflated onto the spikes (**Figure 5.14B)**.

On the 3-hour and 4-hour nanotopography **(Figure 5.14C** and **D),** the cells had fallen into the formed pockets and adhered to the walls. However, once again, the cells appeared very flat;

membrane wrinkling and collapsing could be observed, resulting in relatively flat rather than the characteristic rod-shaped cells.

Taken together, these data suggested that the fixation method, which involved fixing the bacteria in glutaraldehyde and potassium phosphate buffer, was insufficient, and/or the dehydration process in hexamethyldisilazane was too extreme. This risked giving a false impression regarding the capacity for the nanospikes to cause membrane disruption and deflation of the bacterial cells due to a loss of internal turgor pressure. The protocol was therefore modified for subsequent samples, using fixation in glutaraldehyde and sodium cacodylate, and critical point drying as a final dehydration step.

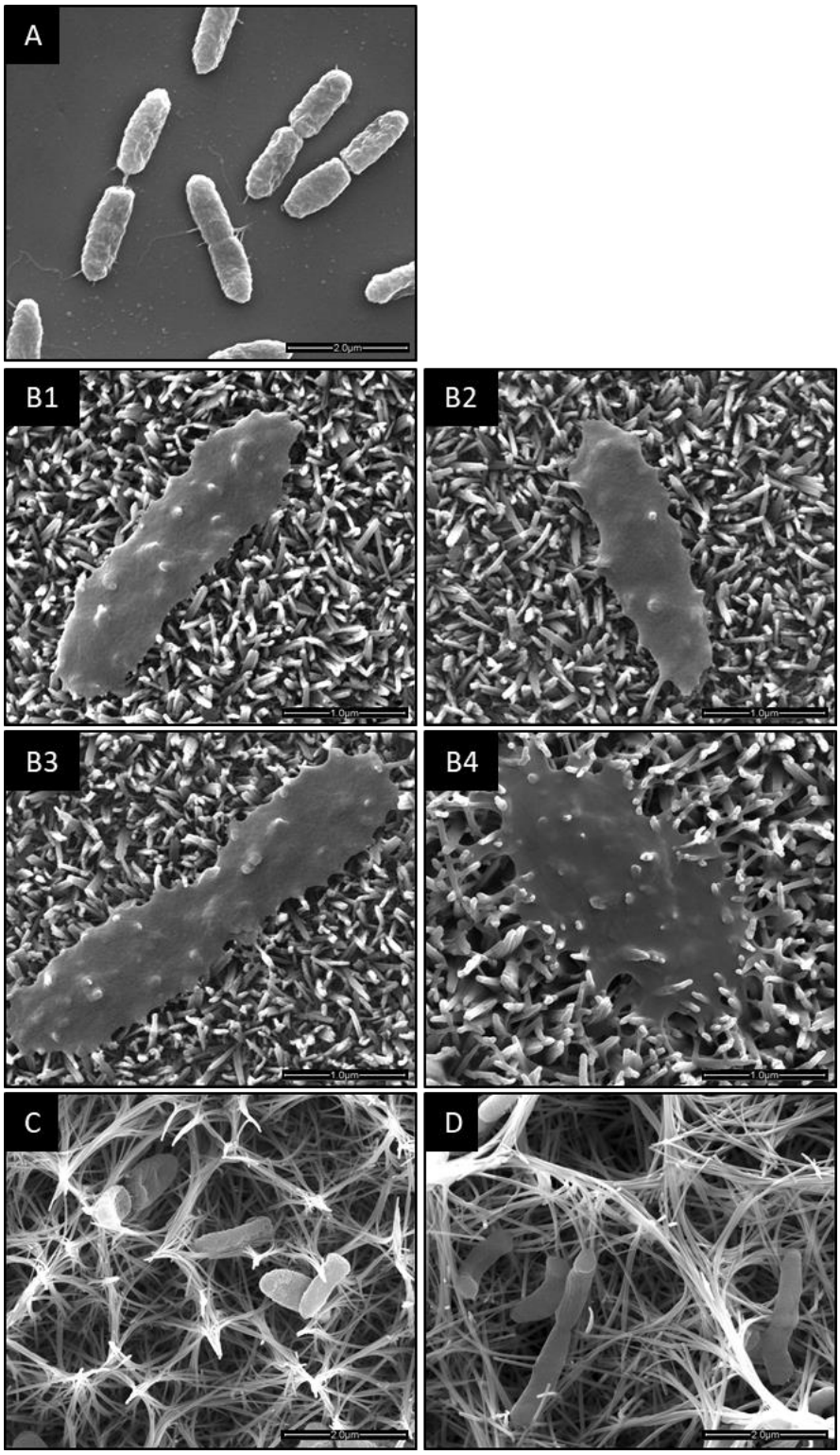

Figure 5.14- *SEM images of P. aeruginosa on flat titanium and 3 nanotopographical surfaces after 3-hours incubation. P. aeruginosa cells were incubated for 3 hours at 37°C on A) flat titanium, B) 2-hour nanospikes, C) 3-hour nanotopography, or D) 4-hour nanotopography. Samples were then fixed, dehydrated and visualised by SEM.*

5.5.1.2 *E. coli* Images

SEM images of *E. coli* cells on flat titanium and three nanotopographies, after the processing had been optimised, are shown in **Figure 5.15**. On the flat titanium **(Figure 4.18A)**, there were healthy cells with surface-expressed adhesins mediating attachment, along with evidence of binary fission having taken place. The cells were bacillus shaped, with no evidence of dehydration or membrane collapsing, indicating that the revised protocol had resolved the issues observed for *P. aeruginosa*. On the 2-hour nanospikes (**Figure 5.15B**), the cells had a healthy appearance, with no evidence of membrane disruption or piercing. There were several elongated cells, which may be indicative of the first stages of cell division or a sign of unfavourable conditions. There was also a notable absence of adhesins expressed by the bacteria.

On the 3-hour nanotopography (**Figure 5.15C**), many cells had fallen into the pockets, but some had adhered to the ridges of the topography. Due to their length, some *E. coli* cells were able to traverse the pockets. The low density of the spikes of the intertwined nanotopography, and the size of the bacteria, implied that effective piecing of the bacterial cells would be unlikely.

For the 4-hour nanotopography (**Figure 5.15D**), most cells had adhered to the walls of the pockets or the ridges, while some had formed micro-colonies, adhering to each other and avoiding direct attachment to the nanotopography. Some cells were also elongated, again suggesting possible cell stress, while other bacterial cells appeared to have undergone or be undergoing binary fission.

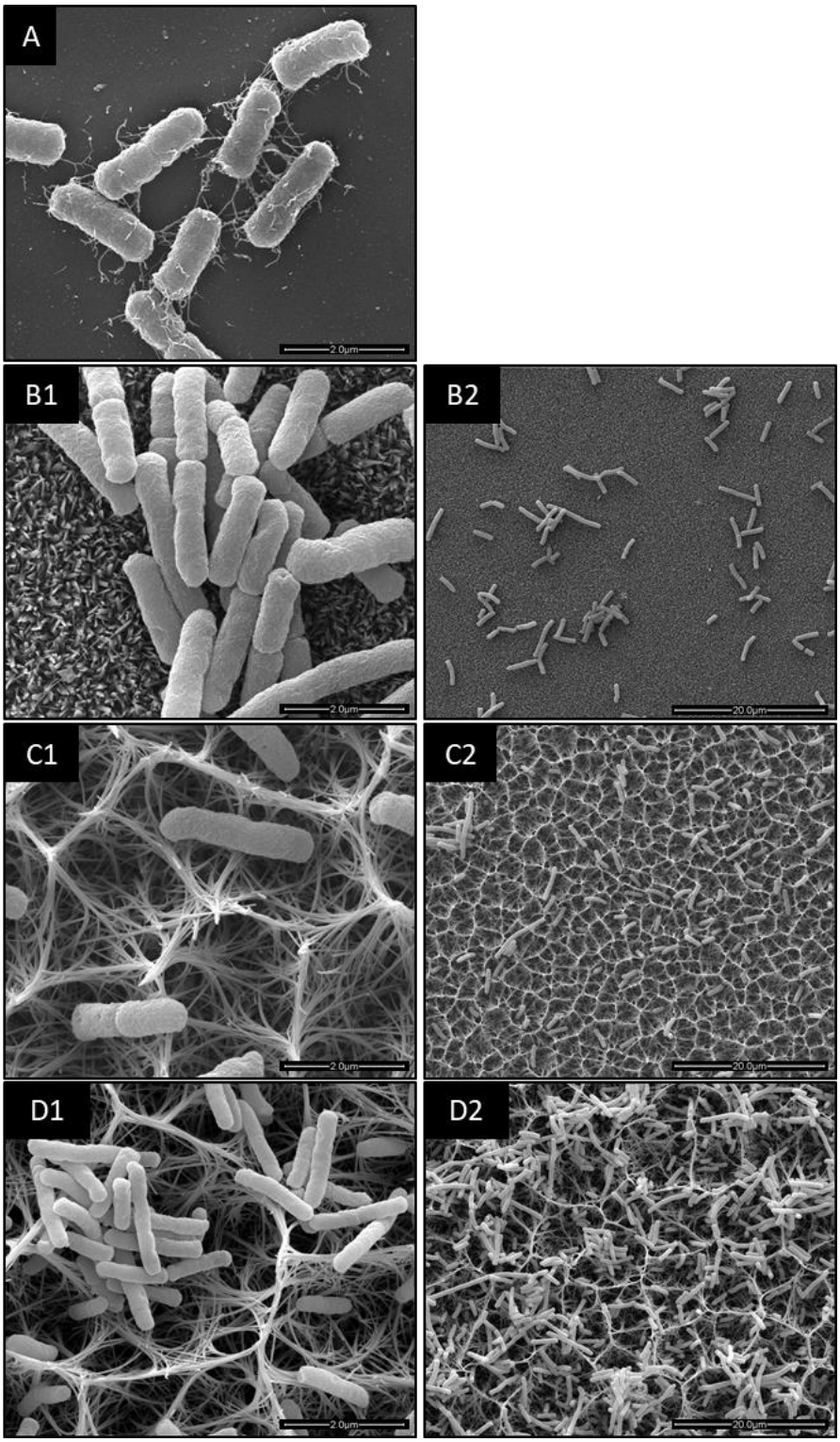

Figure 5.15- *E. coli cells on flat titanium and 3 nanotopographical surfaces after 3-hours incubation. E. coli cells were incubated for 3 hours at 37°C on A) flat titanium, B) 2-hour nanospikes, C) 3-hour nanotopography, or D) 4-hour nanotopography. Samples were then fixed, dehydrated and visualised by SEM.*

5.5.1.3 *K. pneumoniae* Images

On the flat titanium **(Figure 5.16A)**, *K. pneumoniae* exhibited a healthy, bacillus shape, with no evidence of membrane collapse or dehydration, and in some places, small aggregates of cells were forming. There was also evidence of adhesins facilitating attachment to the interface. On the 2-hour nanospikes (**Figure 5.16B**), some cells appeared to have some distortions in their morphology, suggesting possible membrane disturbance due to their interaction with the nanospikes. Some spikes were seen to indent the membranes, causing an irregular morphology, but complete piercing was not evident (**Figure 4.20**). Again, some micro-colonies could be observed.

For the 3-hour nanotopography (**Figure 5.16C**), a few *K. pneumoniae* cells were present inside the pockets, although most had attached near the top of the pockets or along the ridges. Adhesins were evident, facilitating bacterial attachment to the nanotopography. Cell elongation and binary fission was also evident, suggesting that bacterial growth was occurring. The size of the bacteria enabled them to avoid the low-density upright nanospikes. There was also evidence that the nanotopography walls were causing the bacteria to assemble into distinct clusters of cells. On the 4-hour nanotopography (**Figure 5.16D**), the *K. pneumoniae* cells primarily adhered to the ridges or upper regions of the walls, with adhesins seen to be assisting their attachment. Overall coverage of the surface by the bacterial cells was less than seen on the flat titanium and the 2-hour nanotopography, suggesting that the pocket nanotopography may be hindering bacterial attachment.

The SEM images are consistent with the results from the Live/Dead and BacTiter-Glo assays for Gram-negative *E. coli* and *K. pneumoniae*. The results together indicate that, although there are not significant cell deaths within 3-hours, the nanotopography causes stress and indentations. There is also reduced cell attachment especially for the pocket nanotopography.

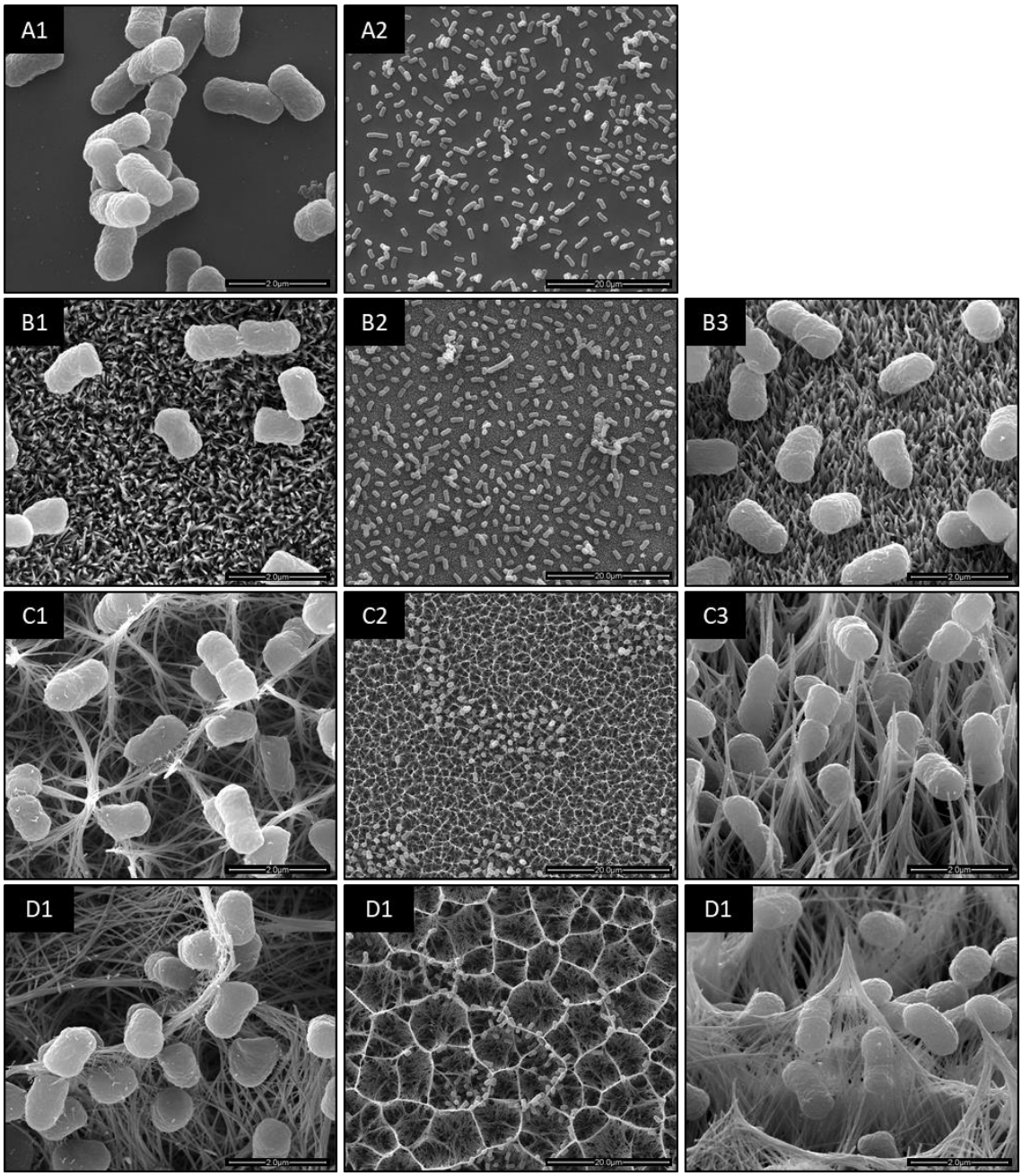

Figure 5.16- *K. pneumoniae cells on flat titanium and 3 nanotopographical surfaces after 3-hours incubation. K. pneumoniae cells were incubated for 3 hours at 37°C on A) flat titanium, B) 2-hour nanospikes, C) 3-hour nanotopography, or D) 4-hour nanotopography. Samples were then fixed, dehydrated and visualised by SEM. Column 3 images are tilted at 30°.*

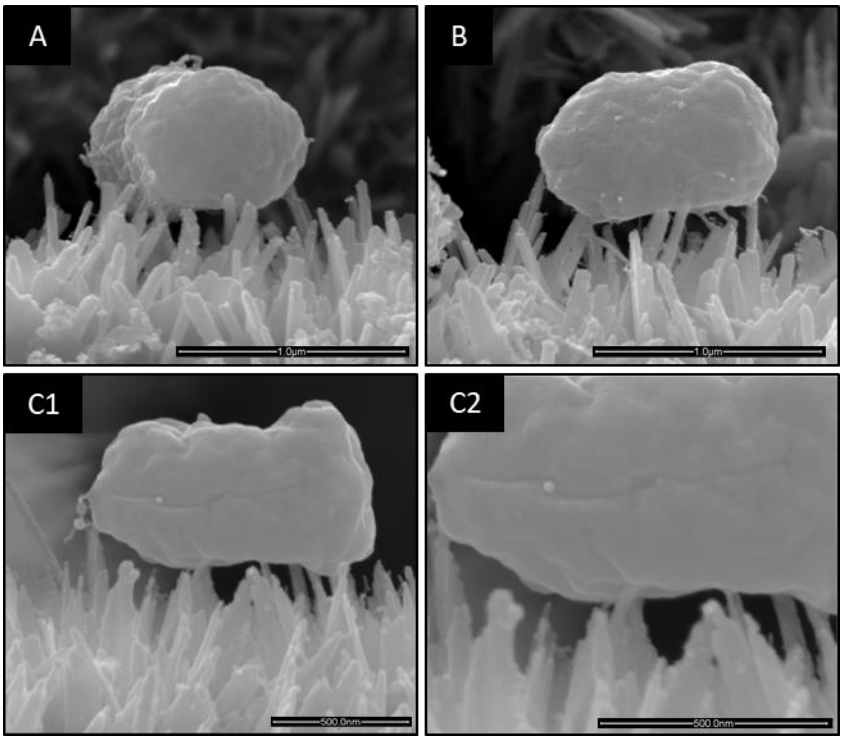

Figure 5.17- *High resolution images of K. pneumoniae cells on 2-hour nanospikes after 3 hours incubation. K. pneumoniae cells were incubated for 3 hours at 37°C on 2-hour nanospikes, fixed, dehydrated and visualised by SEM. Images were taken on the edge of the disk. A, B and C are different cells and C2 is a higher magnification of the cell in C1.*

5.5.1.4 *S. aureus* Images

On the flat titanium **(Figure 5.18A),** the *S. aureus* cells exhibited a normal coccoid shape. Extreme charging was experienced by the electron beam during SEM imaging, which resulted in a fuzzy image. On the 2-hour nanotopography **(Figure 5.18B),** the bacterial cells retained their morphology and no significant membrane indentations were visualised. Cell division and characteristic clustering of the *S. aureus* cells were also evident. On the 3-hour nanotopography **(Figure 5.18C),** the *S. aureus* cells primarily attached around the bottom of the intertwined spikes, rather than inside the pockets, or along the ridges/walls.

Some pockets had no cells, indicating a heterogeneous coverage of bacteria across the surface. Due to the low density of the nanotopography, the size of the cells and the preferred areas of attachment, no piercing of the cells by the nanotopography was observed. On the 4-hour nanotopography **(Figure 5.18D),** the *S. aureus* cells adhered primarily along the ridges of the pockets, but many also attached deep down into the pockets.

The SEM images are consistent with the results from BacTiter-Glo assay for Gram-positive *S. aureus*. The results together indicate that there are not significant cell deaths or cell wall stress

within 3-hours. The RealTime-Glo assay indicates significant bactericidal effects but only after 4 hours of incubation.

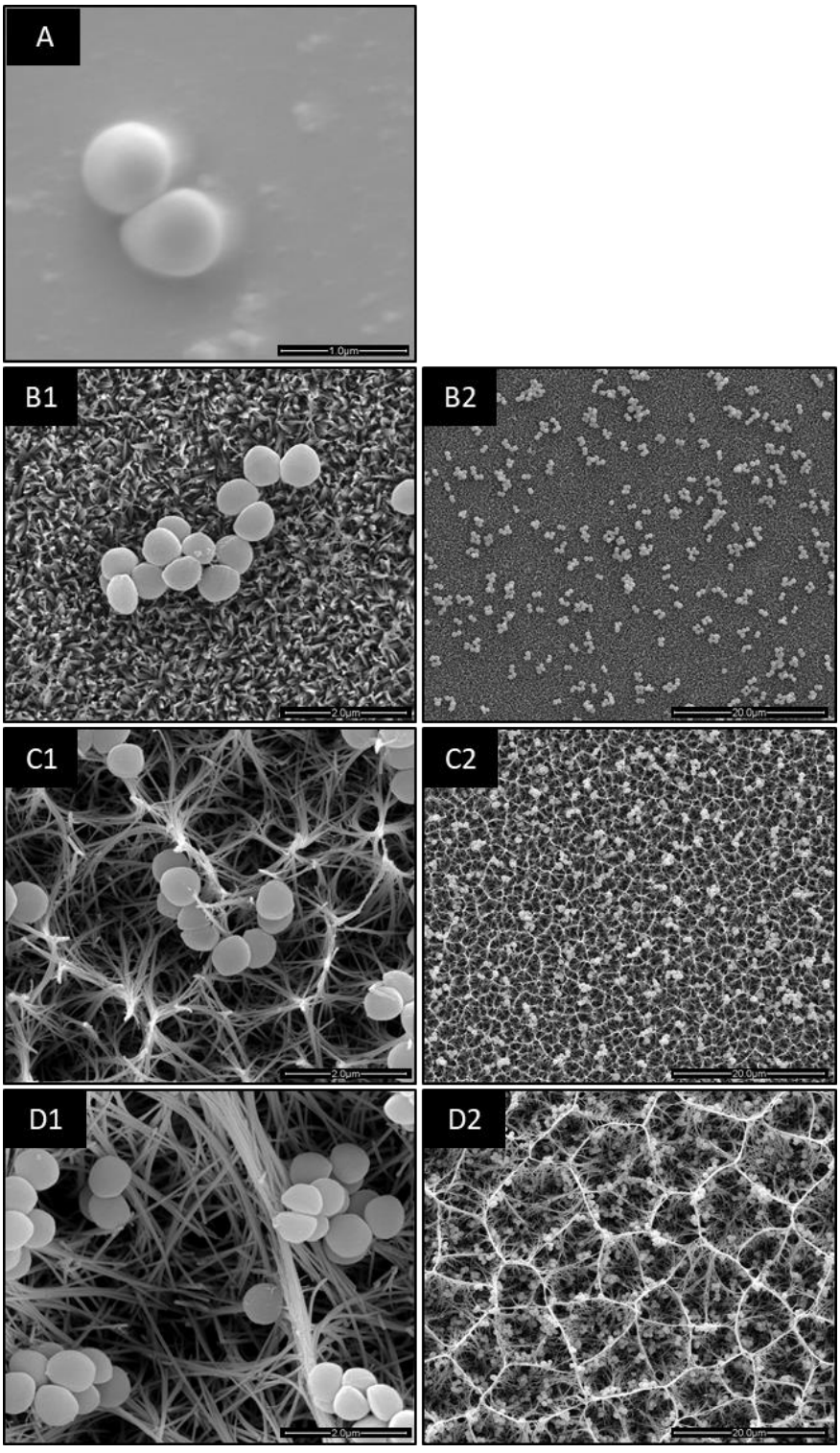

Figure 5.18- *S. aureus cells on flat titanium and 3 nanotopographical surfaces after 3-hours incubation. S. aureus cells were incubated for 3 hours at 37°C on A) flat titanium, B) 2-hour nanospikes, C) 3-hour nanotopography, or D) 4-hour nanotopography. Samples were then fixed, dehydrated and visualised by SEM.*

5.5.2 Focus Ion-Beam Sectioning

Most of the SEM images were taken as a top view or a tilt of 30°. These perspectives were unable to visualise the direct interaction of the underside of the bacterium on the nanotopography. Focus Ion Beam (FIB) was therefore utilised to further investigate the interaction between 2-hour nanotopography and two bacterial species, *E. coli* and *S. aureus*.

Using the Avizo modelling program the images were collated to generate 3D models of the sample to give an enhanced 3D perspective. This enables analysis of the interaction of the nanotopography with the cell from an internal perspective and also underneath the cell, which may be unclear with SEM imaging.

5.5.2.1 *E. coli* Images

Sequential FIB slicing of an *E. coli* cell lying upon the nanotopography showed multiple spikes interacting with the membrane (**Figure 5.19**). Some indentations were visible, but no complete piercing. A similar interaction was seen for an *E. coli* cell that had been coated with platinum for protection from the argon beam during successive 20 nm milling (**Figure 5.20**). The nanotopography was in contact along the length of the cell and some indentations of the cell wall were observed, but there was no evidence of spike penetration into the cell. A 3D reconstruction of a cell further demonstrates that there were 10 nanospikes directly interacting with the cell, causing indentations underneath, but no clear nanospike penetration (**Figure 4.24**).

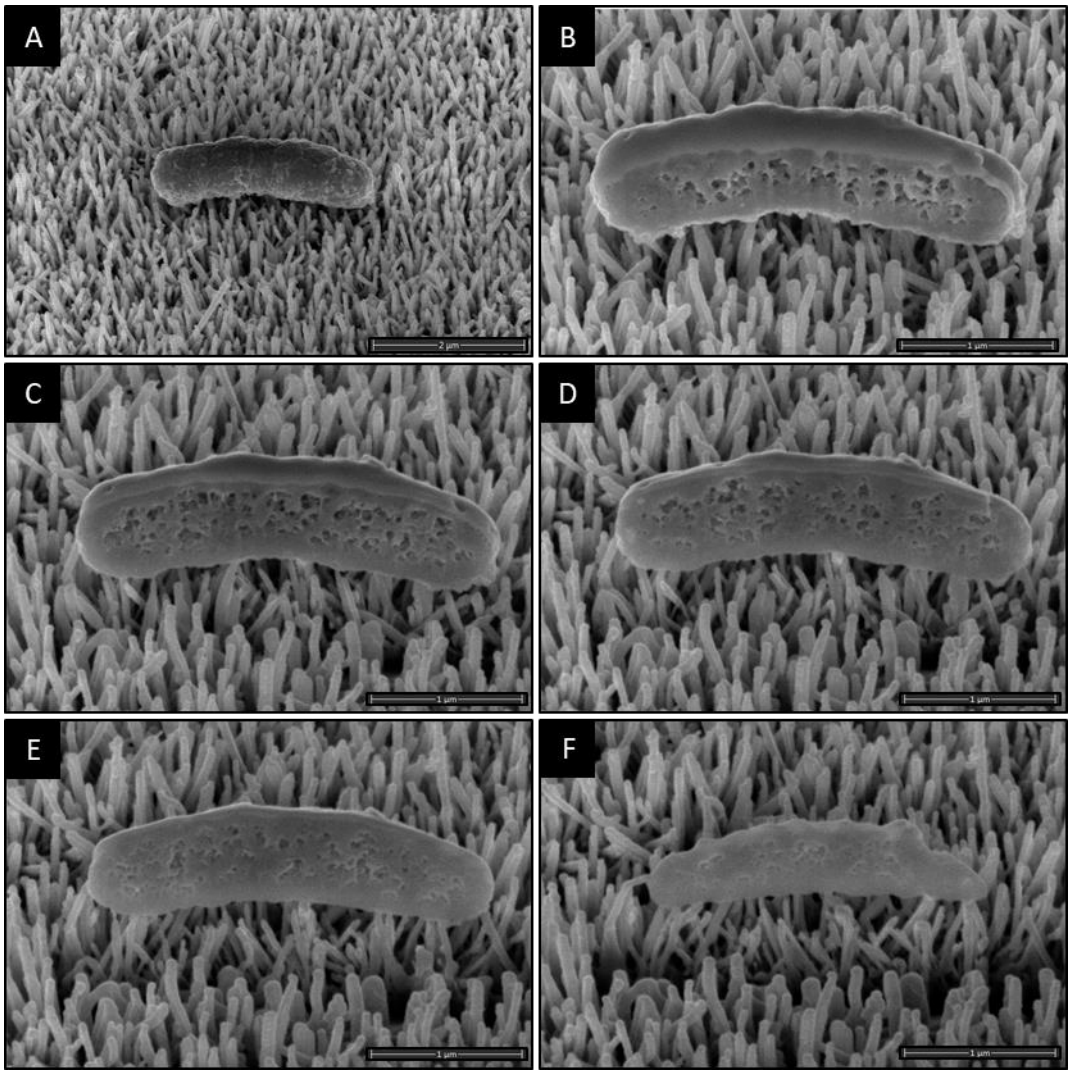

Figure 5.19- *Representative SEM images of four slices imaged during the FIB sectioning of an E. coli cell on 2-hour nanotopography after 3-hours incubation. E. coli cells were incubated for 3 hours at 37°C on 2-hour nanospikes, fixed, dehydrated and critically point dried before visualisation by FIB-SEM. A-F) Sequential images of E. coli being sliced.*

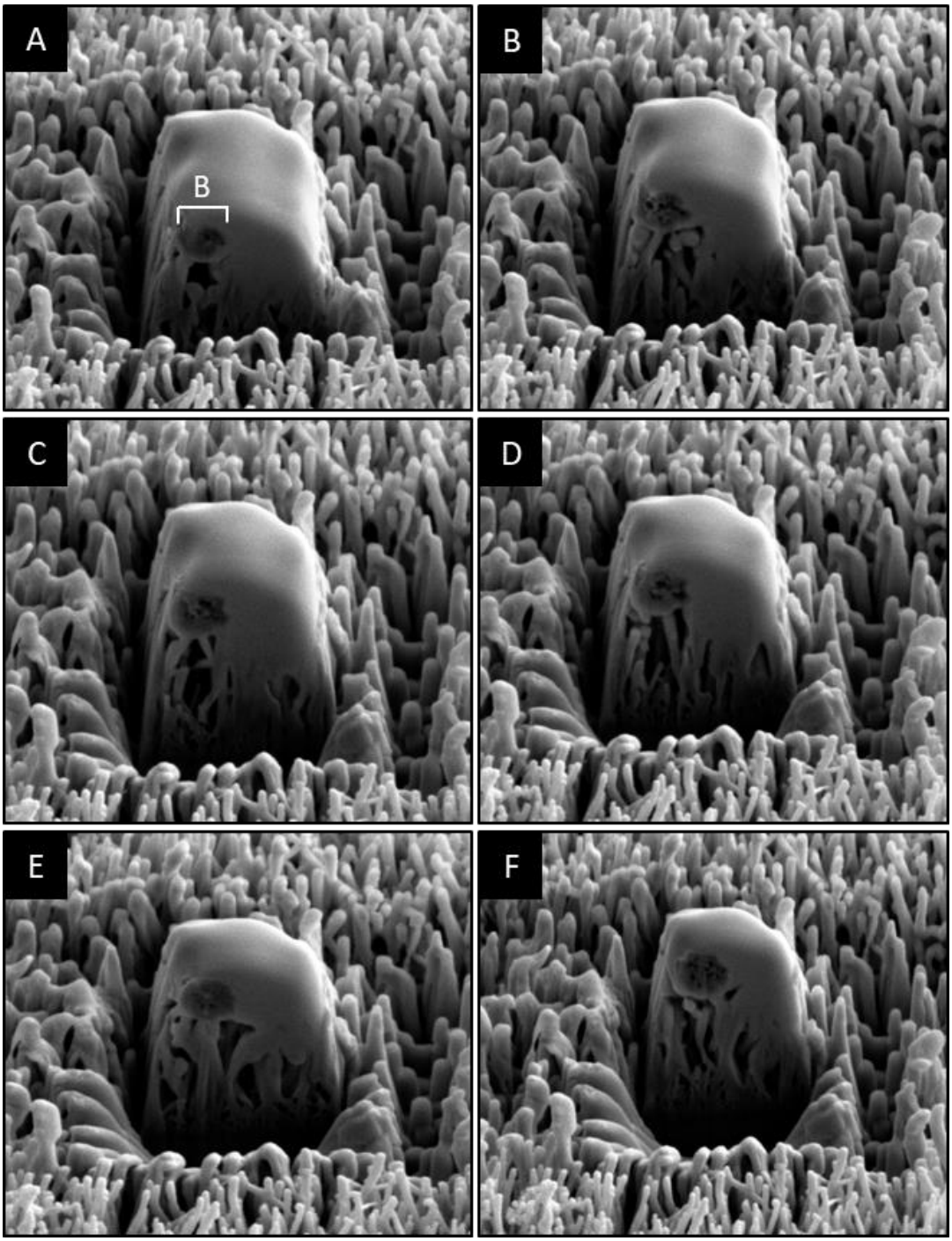

Figure 5.20- *Representative SEM images of six phases imaged during the FIB sequential sectioning of an E. coli cell on 2-hour nanotopography after 3-hours incubation. E. coli cells were incubated for 3 hours at 37°C on 2-hour nanospikes, fixed, dehydrated and critically point dried. The bacterium was coated with a protective palladium layer and sequential 20 nm slices of the bacterium were cut and imaged using FIB-SEM. B=Area of bacterium.*

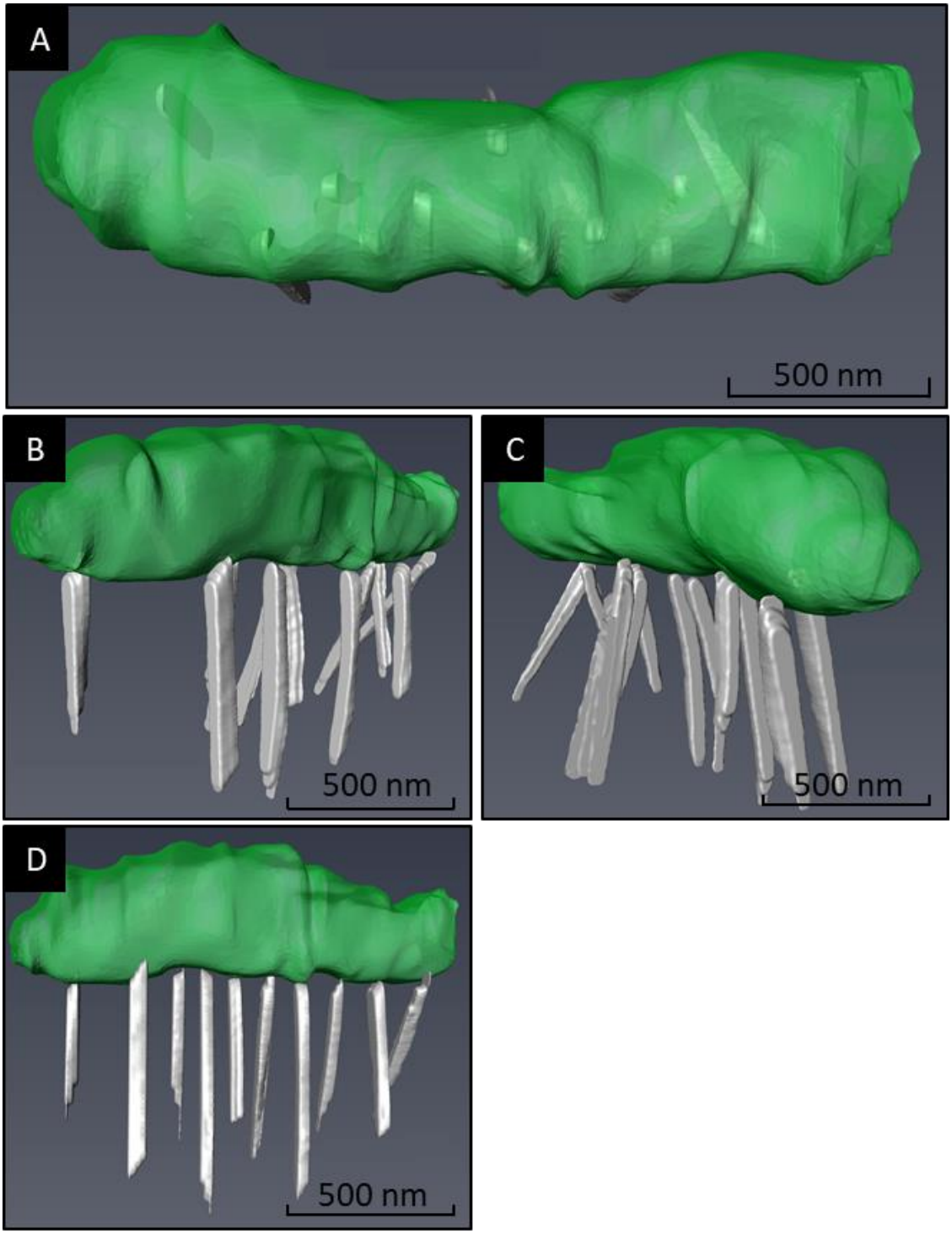

Figure 5.21- *3D model of E. coli cell on 2-hour nanotopography after 3-hours incubation. E. coli cells were incubated for 3 hours at 37°C on 2-hour nanospikes, fixed, dehydrated and critically point dried. Sequential 20 nm slices of the bacterium were cut and imaged using FIB-SEM, and a 3D model of the bacterium on nanospikes generated using Avizo software. Images A-D represent different viewpoint angles of the same bacterial cell. Image A is a top view perspective.*

5.5.2.2 *S. aureus* Images

Sequential FIB slicing of an *S. aureus* cell upon the nanotopography indicated multiple spikes interacting with the membrane, with minor indentations to the cell, but no piercing (**Figure 5.22**). This was also seen for two *S. aureus* cells that had been coated with platinum (**Figure 5.23**). A 3D reconstruction of the cells indicated that five spikes were directly in contact with the first cell and three with the second (**Figure 5.24**). Minor membrane indentations, but no nanospike penetration, were observed for either cell.

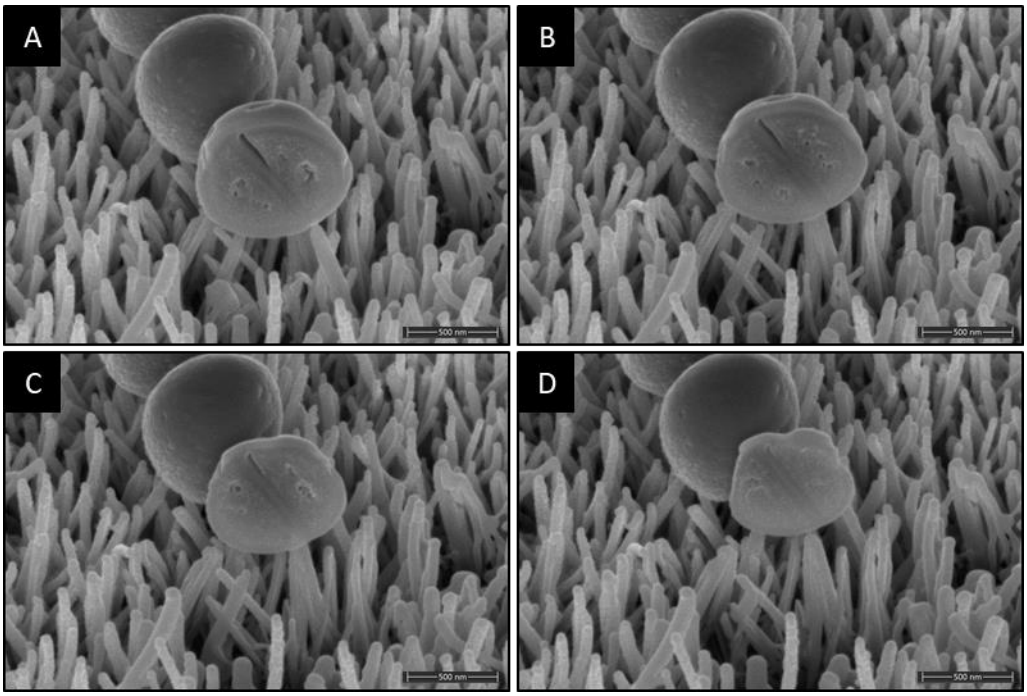

Figure 5.22- *Representative SEM images of four slices imaged during the FIB sectioning of S. aureus cells on 2-hour nanotopography after 3 hours incubation. S. aureus cells were incubated for 3 hours at 37°C on 2-hour nanospikes, fixed, dehydrated and critically point dried before visualisation by FIB-SEM. A-D) Sequential images of S. aureus being sliced.*

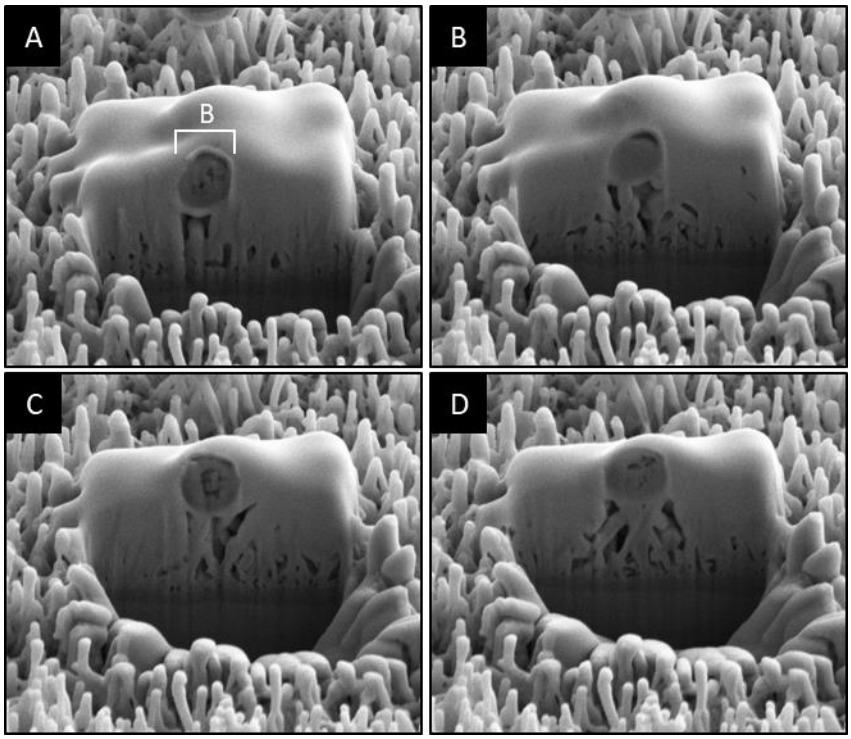

Figure 5.23- *Representative SEM images of four phases imaged during the FIB sequential sectioning of two S. aureus cells on 2-hour nanotopography after 3 hours incubation. S. aureus cells were incubated for 3 hours at 37°C on 2-hour nanospikes, fixed, dehydrated and critically point dried. The bacteria were coated with a protective palladium layer and sequential 20 nm slices of the bacteria were cut and imaged using FIB-SEM. B=Area of bacterium.*

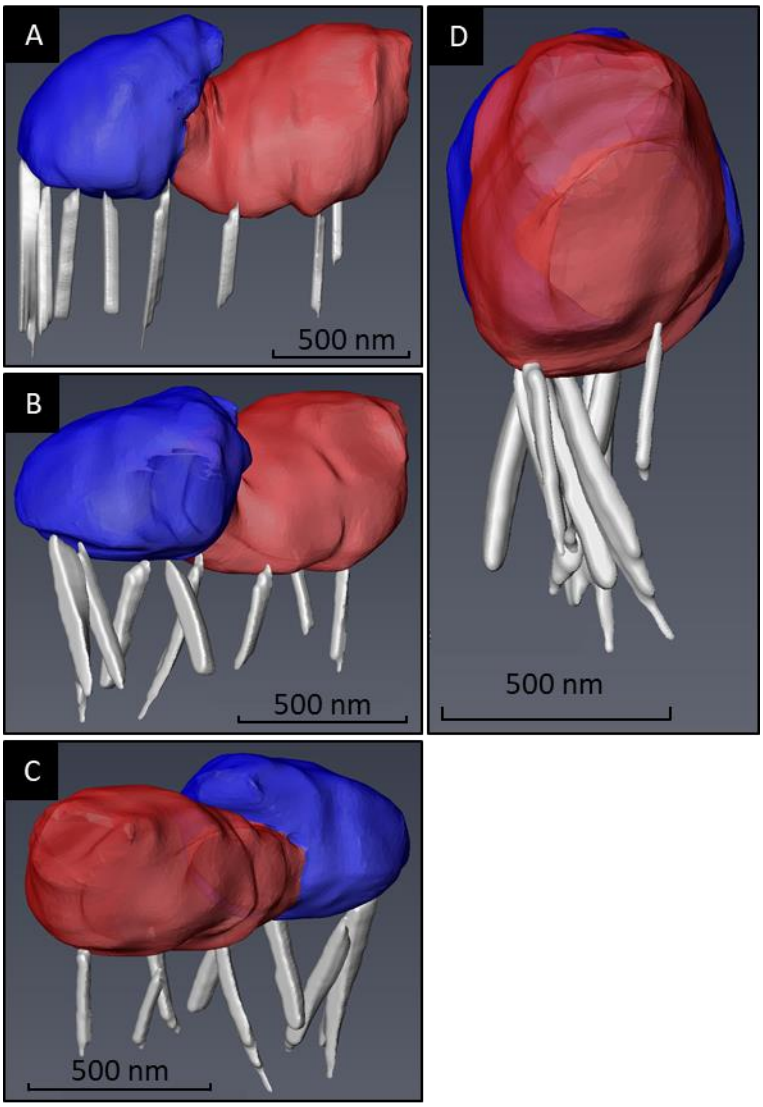

Figure 5.24- *3D model of S. aureus cells on 2-hour nanotopography after 3-hours incubation. S. aureus cells were incubated for 3 hours at 37°C on 2-hour nanospikes, fixed, dehydrated and critically point dried. Sequential 20 nm slices of the bacteria were cut and imaged using FIB-SEM, and a 3D model of the bacteria on nanospikes generated using Avizo software. Images A-D represent different viewpoint angles of the same bacterial cells.*

5.6 Discussion

5.6.1 Comparison of Different Viability Techniques

5.6.1.1 Viability qPCR

Viability qPCR quantifies the amount of amplifiable DNA within a sample. PMA dye enters bacterial cells with a disrupted, permeable membrane, intercalates with DNA and prevents its amplification. Populations of cells that have low levels of amplifiable DNA, should therefore have lower levels of viability (Cangelosi and Meschke, 2014; Nocker and Camper, 2009). The capacity for viability qPCR to distinguish between bacterial cell populations of different viability levels was confirmed here. The results shown in **Section 5.3.1.3** indicated 10% more *P. aeruginosa* deaths on flat titanium (72%), compared to the 2-hour nanospikes (82%). However, it is considered that the quantity of deaths was unreliable for several reasons.

The viable cell populations were underestimated by ~15% as the 50% and 100% viability samples as measured by v-PCR were 36% and 85% viable respectively. In addition, the levels of viable *P. aeruginosa* on the flat titanium control surface were unexpectedly low. Moreover, these data did not correlate with corresponding data using Live/Dead staining, or with previous studies, which reported ~10% cell death on control surfaces (Bhadra *et al.*, 2015; May *et al.*, 2016; Tsimbouri *et al.*, 2016).

There may have been several reasons for this discrepancy. Low concentrations of viable bacteria have been reported to give low levels of viable cell populations, leading to an underestimation of viable bacteria (Liu and Mustapha, 2014; Yáñez *et al.*, 2011). This may be especially pertinent in this project, as only bacteria adhered to the surface were assessed and this population concentration was low, particularly on the control disks. It has also been reported that PMA may, under certain conditions, enter cells with an intact membrane, leading to an overestimation of non-viable cell numbers (Barbau-Piednoir *et al.*, 2014; Cangelosi and Meschke, 2014; Nocker *et al.*, 2007; Nocker and Camper, 2009). Incomplete extraction of DNA from viable cells may lead to lower levels of amplifiable DNA obtained from viable cells, resulting in an underestimation of the viable cell population. The removal of the extracted DNA from the disks involved pipette washing.

Differences in physical and surface chemistry between flat titanium disks and nanotopography may have affected the efficacy of cell lysis and DNA extraction. During photolysis of the PMA stain, the halogen lamp could heat up to high temperatures and as a result, may have caused lysis of the bacteria on the disks, leading to high, non-viable populations being measured. While this effect was mitigated by placing the well plate onto ice, the effects may have been worse for the flat titanium rather than nanotopographies. Due to the significant optimisation that will be

required to potentially obtain sufficient accuracy, confidence, the v-qPCR technique was not considered further for this project.

5.6.1.2 LDH assay

The LDH assay is a colorimetric assay that quantifies the amount of LDH released from a cell when it lyses and was used to investigate the surface bactericidal properties on *P. aeruginosa* and *K. pneumoniae*. The technique has been widely used for quantifying the viability of eukaryotic cells but there are very few studies with bacteria (Kumar *et al.*, 2018; Kaja *et al.*, 2016).

The results suggested a higher proportional of dead cells on the nanotopography than on the flat titanium although the increases were not very significant. However, using *P. aeruginosa*, extremely low viability levels were detected for bacteria incubated on the control surfaces in contrast to data from other techniques and prior studies. It seems likely that these anomalous data were, in part, caused by issues with the need to achieve complete bacterial cell lysis. Bacterial cells are more resistant to cell lysis than mammalian cells, for which the LDH assay was originally developed. As such, detergent Triton X-100 had to be used.

A noticeable colour difference was seen in both the test wells and positive control wells, which may have been indicative of the Triton X-100 interfering with formazan formation and thus the absorbance readings. Overall levels of LDH were also extremely low and likely at, if not below, the optimal sensitivity range for this assay. Given these issues, LDH was not considered suitable for this project.

5.6.1.3 Live/Dead Staining

Live/Dead imaging was used to determine the viability of the bacteria adhering to the surfaces and if there was any bacterial membrane disruption on the nanospikes. This technique has been widely used to assess bacterial viability on interfaces (Lorenzetti *et al.*, 2015; Hasan *et al.*, 2018; Linklater *et al.*, 2019). Compared to techniques such as viability qPCR and CFU enumeration, Live/Dead staining is relatively quick and allows assessment of viability of cell populations via a number of potential platforms such as flow cytometry, in a microplate reader and microscopy (Stocks, 2004; Stiefel *et al.*, 2015).

For this project, Live/Dead staining was used to assess the viability of *K. pneumoniae* and *E. coli* on flat titanium and nanotopography surfaces. However, it is important to recognise that several limitations have been described for this technique. When visualising Live/Dead staining by microscopy, as for this study, only a small area of the sample is considered. Multiple images can

be taken, which can subsequently be combined and quantified, but results may not accurately represent the whole sample. PI stain may sometimes fail to displace SYTO9, resulting in an over-estimation of viable cell numbers (Stocks, 2004; Stiefel *et al.*, 2015). There are also different stages of bacterial viability, such as being viable but non-metabolically active, and Live/Dead stain is unable to distinguish between such states (Quintas Victor, Prada-Lopez and Carmona Inmaculada Tomas, 2014). Given such limitations and to ensure accuracy of data interpretation, it is advisable that Live/Dead stain is not used in isolation to assess bacterial viability.

5.6.1.4 BacTiter-Glo

The BacTiter-Glo test is a measure of the vitality of a bacterial population using luminescence to quantify the level of ATP. ATP is produced during metabolic activity, is not stored within cells and rapidly degrades after cell lysis, making it a good correlate with cell viability (Abelho, 2005; Doll *et al.*, 2016; Sule *et al.*, 2009). With a standard curve of luminescence against CFU, the number of viable cells present within a sample can be estimated (Aragonès *et al.*, 2012).

One of the main advantages offered by the assay for this study was that no washing or sample handling steps were required, unlike for viability qPCR and Live/Dead staining, which potentially leads to inaccurate and unreliable results. The assay could also be used with 24-well plates, enabling multiple samples and experimental replicates to be included at the same time. Incubation time and reading of the samples could be carried out within 10 minutes, and a high sensitivity of detection with as few as 10 bacterial cells has been reported (Promega. 2019). In this study, BacTiter-Glo was successfully used with *E. coli*, *K. pneumoniae* and *S. aureus*.

There were, however, limitations of the assay. As this was an end-point assay, involving the complete lysis of the cells, no further assessment or imaging could be made. Specific time points had to be selected, requiring a high throughput of disks, and the half-life of the luminescence was 30 minutes, so that a co-ordination of sample reading had to be carefully planned to limit discrepancy between samples and repeats (Promega. 2019).

As performed in this study, the assay measured the vitality of the entire bacterial population. While this meant minimal disturbance of the bacteria in contact with the surface, the viability of the bacteria in the planktonic phase directly above the surface versus those adherent to the surface could not be differentiated. This contrasts with the Live/Dead staining and viability qPCR technique, which analysis the adherent bacteria only on the disks.

5.6.1.5 RealTime-Glo

RealTime-Glo enables the continuous monitoring of the vitality of a cell population in real time to give a more accurate representation of changes that may occur over time, this contrasts with assays such as Live/Dead, viability PCR and BacTiter-Glo which are end point assays and only provide a snap point representation at a particular time. As RealTime-Glo allows for the assessment of multiple time points, it also meant that fewer samples were required, in contrast to endpoint techniques such as BacTiter-Glo (Duellman *et al.*, 2015).

RealTime-Glo and BacTiter-Glo assays, although both metabolic assays, measure different aspects of metabolism. RealTime-Glo assesses the reduction potential of a specific substrate while BacTiter-Glo quantifies the amount of ATP in a solution. These processes may be affected differently when the bacteria interact with the surface (Promega, 2016b, 2016a). In this regard, bacterial strain was found to be an important factor in the utility of this assay due to differences in metabolism between the bacterial species (Hoerr *et al.*, 2012). RealTime-Glo was originally designed for use with mammalian cells, which have greater reduction potential than bacterial cells. However, of the bacterial test strains used in this project, only *S. aureus* had sufficient reducing power for RealTime-Glo to be used successfully. Levels of luminescence generated by *E. coli* and *K. pneumoniae* were too low to be reliably measured.

Considering all the methods investigated in this project, it was concluded that Live/Dead staining in combination with BacTiter-Glo were the most appropriate assays for assessing the antimicrobial properties of the nanotopographies. RealTime-Glo was also appropriate for use with *S. aureus.*

5.6.2 Comparison of Different Microscopy Techniques

When imaging *P. aeruginosa* using SEM, very promising images were obtained implying membrane piercing and deflation of the cells, reminiscent of that often illustrated in the literature (Hasan *et al.*, 2013; Ivanova *et al.*, 2012; Truong *et al.*, 2017; Bhadra *et al.*, 2015; Pogodin *et al.*, 2013). However, these observations were not consistent with the data obtained from the Live/Dead staining and metabolic assays, and further investigation confirmed that these effects were in fact an artefact of sample preparation. The sample processing involved hexamethyldisilazane as the final dehydration step with subsequent air drying, and this is believed to have resulted in excessive dehydration and membrane disruption. By optimising the process by a modified fixation and dehydration protocol using critical point drying, it was clear that relatively little piercing on the control or nanotopography surfaces was seen for *E. coli*, *K. pneumoniae* or *S. aureus*.

During air drying or when in a vacuum, evaporation of the liquid within a sample can cause severe sample deformation and structural collapse. This is due to the high surface tension as the liquid evaporates into gas. Critical point drying is a more favourable method of processing, as the critical point is where the liquid and gas phases have the same density and are indistinguishable. The liquid is therefore converted into a gas with minimal cell damage occurring. After sequential dehydration treatment with ethanol, the remaining water in the sample is exchanged with liquid CO_2 within a critical point dryer and brought to its critical point, where it is converted into a gas (Hall, Skerrett and Thomas, 1978; Williams, Clifford and Bray, 2003). There are some studies that suggest the use of hexamethyldisilazane rather than critical point drying produces better images (Jusman, Ng and Abu Osman, 2014; Shively and Miller, 2009). However, the optimal technique will be project-specific, and studies here found that critical point drying was optimal.

FIB-SEM is a well utilised technique to generate 3D models of samples by serial block imaging to give a more accurate representation of a sample. In this project, it was used to model the direct interaction of the nanotopography underneath and inside the bacterial cells, which SEM imaging alone was unable to do. The bacterial samples were sequentially cut and imaged using a ion beam and SEM, with images then collated to produce a 3D image with Avizo software (Schertel *et al.*, 2013; Smith and Starborg, 2019; Beckwith *et al.*, 2015; Svensson *et al.*, 2014).

The numerous steps of the processing for FIB-SEM is to ensure accurate structural preservation of the bacterial cells when subjected to the gallium ion beam. The bacteria are often coated with platinum during FIB scanning to help protect the organic tissue from resulting debris caused by the ion beam and to improve image quality (Martynowycz *et al.*, 2019). In **Figure 5.19** and **Figure 5.22**, ion-beam cuts were made through the bacterial cells with no platinum coating but the structural integrity remained, indicating a good processing technique. Nonetheless, the platinum coating was still used for the 3D imaging due to the quantity and thinness of the slices required.

Both SEM and FIB-SEM require numerous washing steps and transferring of disks into and out of different solutions. For this project, this potentially increased the risk of washing away lysed bacteria and debris, which could then have led to an under-representation of the bactericidal potential of the nanotopography through physical rupture (Kaláb, Yang and Chabot, 2008). As with BacTiter-Glo and Live/Dead staining, SEM and FIB-SEM only provides a snapshot in time. Nonetheless, these microscopy techniques offered a method to assess potential bacterial membrane disruption by the nanospikes at high resolution that could not be provided by other methodologies.

5.6.3 Bacterial Interactions with Nanotopography

A 3-hour timepoint was chosen for the majority of these studies, as previous research had indicated bactericidal activity within this timeframe for similar nanotopographies (Diu *et al.*, 2014; Tsimbouri *et al.*, 2016; Hazell *et al.*, 2018c; Jaggessar *et al.*, 2018b). However, the results presented in this chapter demonstrated that over the 3-hour incubation period, none of the different nanotopographies exhibited significant bactericidal effects, as determined by both metabolic assay and Live/Dead stain. This outcome was further supported by the lack of bacterial membrane penetration by nanospikes seen using SEM and FIB-SEM. Cao *et al*. (2018) reported *S. epidermidis* cell death on topography reminiscent of the 2-hour and 3-hour nanotopography at 47% and 37% respectively after 2 hours incubation. Diu *et al*. (2014) claimed more than 50% death for *P. aeruginosa*, *E. coli* and *B. subtilis* on 2-hour and pocket nanotopography after only 1-hour incubation. Tsimbouri *et al*. (2016) reported around 30% *P. aeruginosa* cell death after 3-hours incubation on 2-hour nanotopography.

Bactericidal potential of a surface will arise from a complex interplay between physical topography characteristics (e.g. height, diameter, density of the nanospikes), surface chemistry (e.g. wettability) and bacterial morphology and phenotype (Luan *et al.*, 2018). As such, it should not be assumed that similar nanotopographies will mediate identical bactericidal effects. Nonetheless, there are some key parameter differences for the Live/Dead assays across these studies that are also likely to have contributed to the discrepancies. Volumes of bacterial suspension differed, with Cao *et al*. (2018) using 0.5 ml, Diu *et al.*, (2014) and Tsimbouri *et al.* (2016) using 2 ml, and 40 µl being used for this project. This would have affected the dynamics of bacterial cell interactions with the surface. Diu *et al*. (2014) and Tsimbouri *et al*. (2016) also used Tris-HCl buffer rather than the growth medium used here. As the former would have not supported bacterial growth, again this will have affected the behaviour of the bacteria.

Although there was no evidence of bactericidal effects mediated by the nanospikes, these data did suggest that the bacteria responded to the nanotopography. This was seen with the different surface profiles of bacteria in contact with flat titanium versus nanotopography, as visualised by SEM. There was also the trend for fewer viable bacteria to adhere to the nanotopography compared to flat surfaces, shown both through BacTiter-Glo and Live/Dead stain. With Live/Dead staining more attachment by *K. pneumoniae* (Figure 5.8) than *E. coli* (Figure 5.9) was visualised after 3 hours incubation. This may be due to the processing and imaging of the samples such as more *E. coli* cells were removed during the washing steps or specific areas of the disk were imaged to give an under-estimation of the adhered cells. Quantification of biomass or cell counts across large areas of the disk could give more accurate representation of bacterial cells adhered to the surface. Differences in between the bacterial species such as motility may also

play a role. *E. coli* being motile while K. pneumoniae being non-motile may enable *E. coli* cells to move away from the nanotopographical surfaces while the K. pneumoniae are unable to (Stocks, 2004; Stiefel *et al.*, 2015; Faruqui *et al.*, 2014; Matthäus, Jagodič and Dobnikar, 2009; Lima *et al.*, 2018). Given the bacterial cell membrane indentation caused by the nanospikes seen using FIB-SEM, it is possible to speculate that mechanosensing systems within the bacteria might be triggered upon contact with the nanospikes.

Furthermore, these data implied that *K. pneumoniae* was most susceptible to the effects of the nanospikes, followed by *E. coli* and then *S. aureus*. This hierarchy may reflect fundamental differences in the cell wall structure of Gram-negative and Gram-positive bacteria. Due to the thicker peptidoglycan layer within the cell wall of Gram-positive bacteria (20-80 nm compared to 1-10 nm), it has been proposed that this confers a more rigid cell envelope with greater resistance to membrane stretching (Pogodin *et al.*, 2013; Ivanova *et al.*, 2013; Elbourne, Crawford and Ivanova, 2017).

The response of bacteria differed across the different nanotopographies and provided good evidence to support the proposal by Cao *et al*. (2018) that the pocket topography may be more effective in deterring bacterial adherence than the nanospikes. Live/Dead imaging and SEM highlighted that bacteria were especially confined to the ridges on the pocket morphology, whereas a more homogenous coverage was seen on the flat titanium and nanospikes. This supports the hypothesis that the pocket topographies may sequester bacteria within the niches and potentially hinder the formation of microcolonies and biofilm formation (Cao *et al.*, 2018).

Nonetheless, RealTime-Glo data for *S. aureus* demonstrated that both well-developed (2 hour) nanospikes and pocket nanotopographies were able to mediate inhibitory effects on bacterial metabolism and growth when incubated for periods of 4 hours or longer. It is possible then that, under the test conditions used for these studies, more time may have been required for bacteria to adhere, respond to and possibly be killed on the nanotopography (Ivanova *et al.*, 2012; Hasan *et al.*, 2013). To determine if these longer-term antimicrobial effects extended to the other test bacterial species, future studies would aim to develop a reliable technique that could be used with Gram-negative bacteria *K. pneumoniae* and *E. coli* over time periods longer than 3 hours.

Based on the nanospike organisation and the capacity for the surface to impair growth of both Gram-negative and -positive bacteria, the 2-hour nanotopography was selected for subsequent functionalisation studies.

6.

FUNCTIONALISATION OF NANOTOPOGRAPHY WITH ANTIMICROBIAL PEPTIDE

Contents

6.1 Introduction

6.1.1 Antimicrobial Peptide Functionalisation

ChoM ('chopped cecropin mutant') is a specifically designed adaptation of the naturally occurring AMP Cecropin B (CecB), first isolated from the haemolymph of the giant silk moth, *Hyalophora cecropia* (**Figure 6.1**).

Figure 6.1- *Adult giant silk moth, Hyalophora cecropia. This moth has a wingspan of approximately 5-7 inches (13-18 cm), and produces AMP cecropin B (BugGuide, 2013).*

Cecropin B is believed to exert its bactericidal effects by a detergent-like carpet mechanism. Above a threshold concentration, the peptide is believed to induce bacterial membrane curvature by inserting below the glycerol backbone of the phospholipid headgroups, leading to stretching

and thinning of the outer bilayer leaflet (Pfeil *et al.*, 2018). CecB has known activity against Gram-negative bacteria such as *P. aeruginosa* and *E. coli*, but little or no activity reported against some Gram-positive bacteria such as *S. aureus* (Wang *et al.*, 2018; Pfeil *et al.*, 2018).

To increase the spectrum of bactericidal activity for CecB, modifications were designed by Pfeil *et al.* (2018) at the National Physical Laboratory (NPL), UK, resulting in ChoM. ChoM was produced for this project during a seven-month placement at NPL. Two modifications were made to the CecB peptide:

1. The C-terminal helix of CecB, consisting of 14 amino acids, was removed. This changed the bactericidal mechanism from detergent-carpet disruption to poration (Pfeil *et al.*, 2018).

2. Substitution of two glycine residues with isoleucine and lysine residues. This further changed the bactericidal mechanism to a non-pore forming exfoliation of the outer bilayer leaflet, which was found to be effective within 10 minutes (Pfeil *et al.*, 2018).

The bactericidal activity of ChoM was effective against both Gram-positive (*S. aureus, B. subtilis, Micrococcus mutans*) and Gram-negative (*P. aeruginosa, E. coli, Salmonella typhimurium*) bacteria. This made it an attractive AMP to use to functionalise the nanotopography for this project.

The properties of both CecB and ChoM are summarised in **Table 6.1** and the helix wheels are illustrated in **Figure 6.2**.

PEPTIDE	NUMBER OF RESIDUES	AMINO ACID SEQUENCE	CHARGE AT Ph 7.2	MASS(m/z)
CecB	35	KWKVFKKIEKMGRNIRNGIVKAGP AIAVLGEAKAL-am	8+	3834.67
ChoM	21	KWKVFKKIEKMIRNIRNKIVK-am	9+	2699.4

Table 6.1- *Properties of the AMPs CecB and ChoM (Pfeil et al., 2018).*

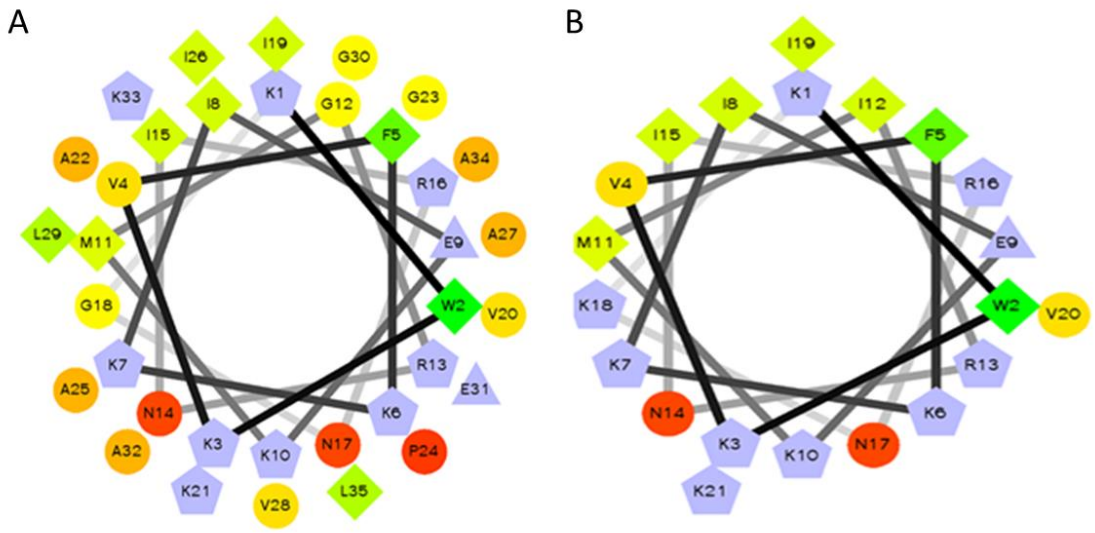

Figure 6.2- *Peptide helix wheels of A) CecB and B) ChoM. Circles-Hydrophilic residues, Diamonds-Hydrophobic residues, Triangles-Negatively charged, Pentagons-Positively charged. Hydrophobicity spectrum-Green, Hydrophilic spectrum-Red, Potentially charged-Blue (Pfeil et al., 2018).*

There are several methods of functionalising interfaces with AMPs. In this project, a physical adsorption method was implemented. This was chosen for several reasons:

1. Simple functionalisation protocol.
2. Allows short term activity with release into the local environment.
3. Allows the peptide to be physically free in solution rather than hindering its activity by tethering.
4. Allows control of the peptide concentration applied.

ChoM was solubilised in water and pipetted at a specific concentration and volume onto the nano-spiked titanium surface. After being left to evaporate under aseptic conditions, the peptide coated the nanotopography.

6.1.2 Biocompatibility and Osteogenic Potential of AMP-Functionalised Nanotopography

Human mesenchymal stem cells (hMSCs) are multipotent fibroblastoid osteoprogenitor cells capable of differentiation into a variety of cell types, from adipocytes to osteoblasts and chondrocytes. hMSCs have been isolated from a range of human tissue, including bone marrow, adipose tissue, umbilical cord matrix, tendon, lung and periosteum (Lee *et al.*, 2017).

Stem cell adhesion to an implant surface is critical for successful tissue development. Under physiological conditions, all adherent cells are surrounded by an extracellular matrix (ECM), which provides support, trophic signalling and biophysical cues. The ECM defines fundamental cell properties such as cell cycling, survival, paracrine activity, motility, homing behaviour and cell fate. These native, inherently mechanical properties dictate stem cell differentiation and function (Dobbenga, Fratila-Apachitei and Zadpoor, 2016; Lee *et al.*, 2017).

Diu *et al.* (2014) reported that on 'brush-type' nanotopography, analogous to the 2-hour nanospikes grown in this project, MG-63 osteoblast-like cells exhibited lower adhesion and arrested proliferation relative to control from 0-7 days. Metabolic activity data (PrestoBlue) indicated that the nanotopography was biocompatible up to 14 days, the longest duration tested. On both the flat titanium and brush-type surfaces, a monolayer of cells was formed, but the morphology of the cells differed. Unrestricted spreading and elongation were seen across the flat titanium surface, while stretched 'teardrop' morphology was more commonly observed on the nanotopography, as the spikes were able to pierce and physically tether the cells, thereby encouraging unidirectional movement.

Tsimbouri *et al.* (2016) further investigated the interactions of bone marrow-derived stem cells (bMSCs) on 2-, 2.5- and 3-hour nanotopography. After one-week incubation on flat titanium, bMSCs had well organised cytoskeletons and formed a monolayer, approaching high confluence. Reduced cell coverage and adhesion were observed on the nanotopography surfaces, with cells appearing smaller with limited spreading, dense tubulin around the nucleus and a less organised cytoskeleton. The expression of osteogenic lineage genes osteopontin (OPN) and osteocalcin (OCN) were significantly upregulated after 35 days and 14 days respectively. Together these papers highlighted that the 2-hour nanotopography was biocompatible and although lower cell adhesion and differing morphology was initially observed, the nanotopography appeared to encourage MSC differentiation along the osteoblastic lineage.

The overall objectives of the studies reported here were to investigate if the antibacterial properties of the nanotopography could be enhanced by AMP functionalisation. A preliminary investigation of the biocompatibility and potential osteogenicity of the 2-hour nanotopography with or without AMP functionalisation was also carried out.

6.2 Synthesis of ChoM

The peptide synthesis process involved six major steps:

1. Solid phase peptide synthesis (SPPS) to generate the peptide chain.
2. Matrix assisted laser desorption/ionisation-time of flight (MALDI-TOF) to confirm presence of the desired product.
3. Reverse phase-high performance liquid chromatography (RP-HPLC) to purify the peptide solution.
4. MALDI-TOF analysis of each of the RP-HPLC fractions to determine purity.
5. Freeze drying of solution to obtain a dry powder.
6. MALDI TOF confirmation and purity quantification with analytical HPLC.

6.2.1 MALDI-TOF Analysis

After the SPPS step, MALDI-TOF analysis was carried out to confirm that the correct peptide product was synthesised based on the molecular weight. The peptide was mixed with a matrix and then subjected to an ultraviolet nitrogen laser beam, which vaporises and ionises the peptide, releasing protonated ions; the speed is a function of the peptide mass to charge ratio (m/z). **Figure 6.3** shows the spectra of the MALDI-TOF analysis with a strong peak at 2700 m/z. This indicated the presence of ChoM, which has a molecular weight of 2699.4. However, as MALDI-TOF is not quantitative, the amount of ChoM could not be calculated. The presence of other peaks indicated impurities. The peaks around 2900 m/z and 2950 m/z corresponded to ChoM + ions such as sodium and potassium from the matrix.

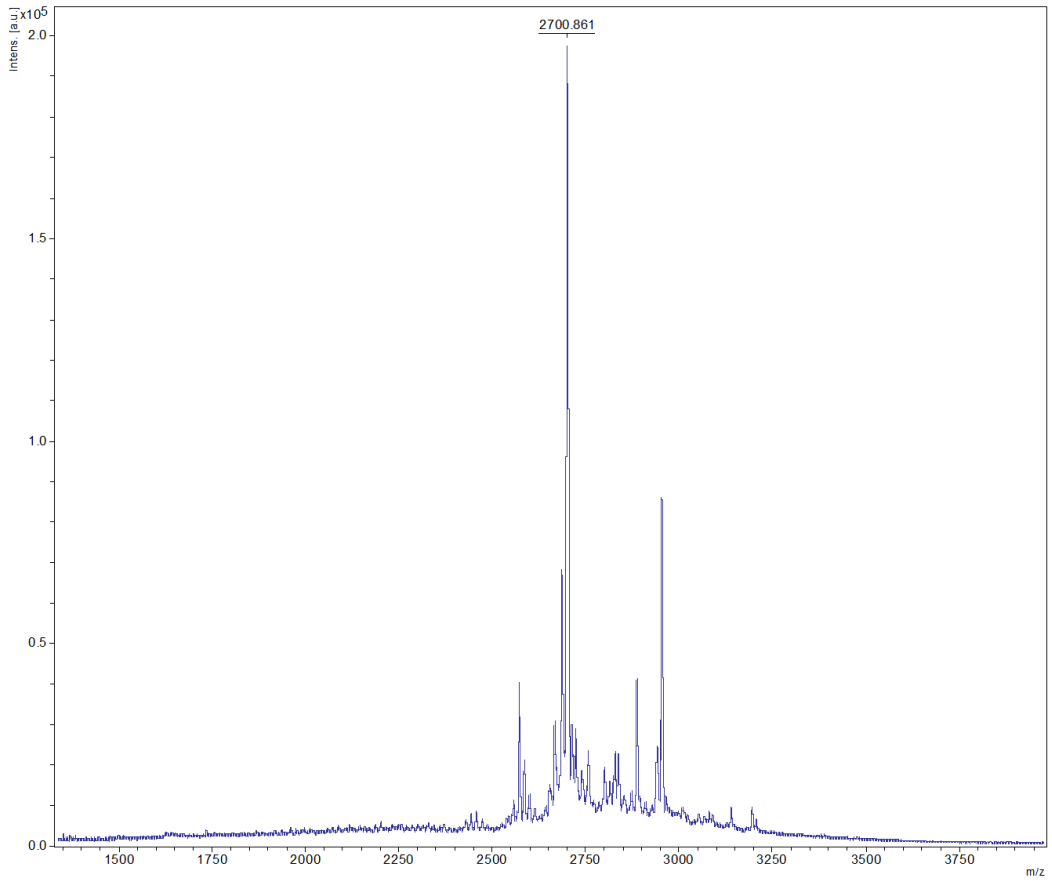

Figure 6.3- *MALDI-TOF spectrum of crude peptide. This highlights the presence of ChoM peptide at ~2699 m/z.*

6.2.2 Purification of Peptide

Reversed-phased high-performance liquid chromatography (RP-HPLC) was used to purify the peptide solution. RP-HPLC is a purification technique used to separate a range of molecules based on their relative hydrophobicity. The peptide is streamed (the mobile phase) through a column permeated by hydrophobic ligands (the stationary phase). Their relative interaction determines the speeds at which each constituent of the sample will travel. The more hydrophobic/non-polar a compound is, the longer it will take to pass through and elute from the column. This is measured as the retention time.

Analysis of the HPLC purification is shown in **Figure 6.4**. The retention time of previous synthesis runs for ChoM was known, so fractions from 20 to 40 minutes were collected into 40 tubes, as shown in blue. The large peak between fractions 11-33 was considered likely to be ChoM and so these fractions were further analysed with MALDI-TOF to determine the qualitative purity of the peptide. The spectra of 4 example fractions are shown in **Figure 6.5**.

ChoM has a molecular weight of 2699. Spectra in **Figure 6.5A-B** had a large peak at this molecular weight, but also other peaks around 2000 m/z and 3100 m/z respectively, which were indicative of impurities. As such, neither fraction was included in the final pooled peptide solution. Spectra in **Figure 6.5C-D** showed few other peaks other than ~2699 m/z, suggesting a high purity. Fractions 14-24 had similar spectra to **Figure 6.5C-D** and so were combined into the final peptide solution. This was freeze dried to produce a white flaky powder, which was stored at -80°C long term. The purity of the final peptide solution was quantitatively measured with analytical HPLC and calculated to be 98.4%.

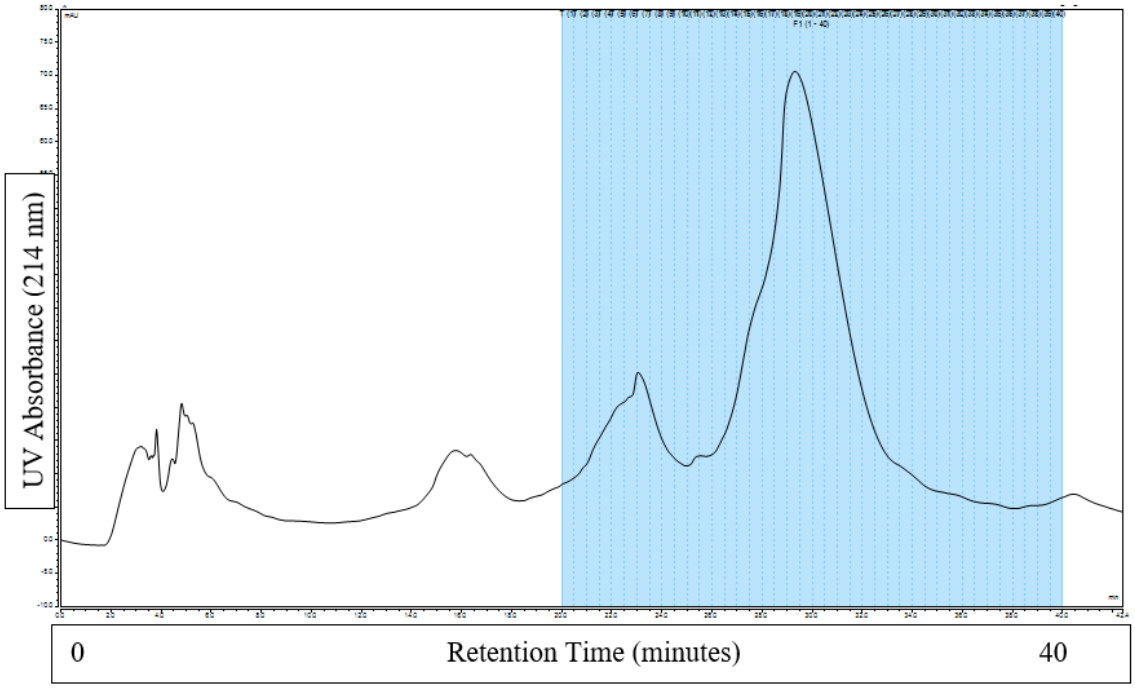

Figure 6.4- *HPLC separation of peptide solution. Highlighted blue region indicates the 40 fractions that were collected.*

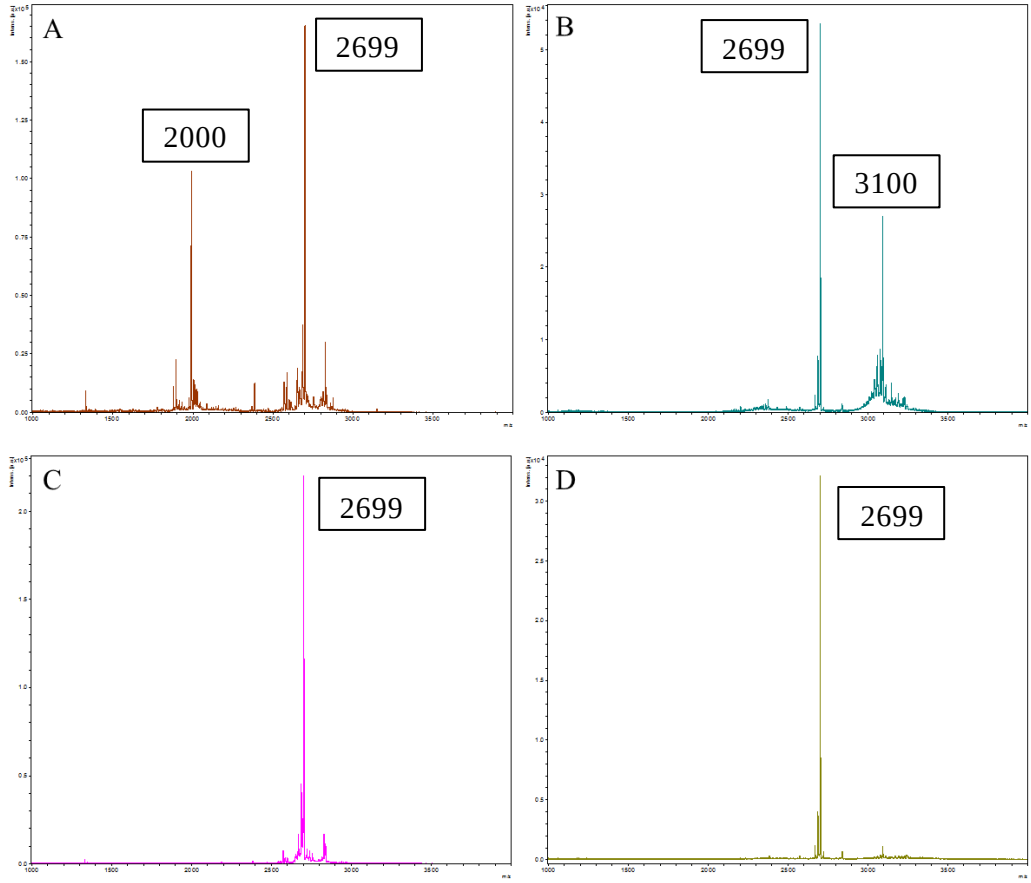

Figure 6.5- *MALDI TOF spectra of HPLC fractions. Fractions shown in A and B were not included in the final peptide solution due to the presence of impurities, as shown by peaks around 2000 m/z and 3100 m/z respectively. Fractions shown in C and D were included in the final peptide solution, as high purity was predicted due to only a few minor peaks seen other than ChoM at 2699 m/z.*

6.3 Antimicrobial Activity of ChoM

6.3.1 Minimum Inhibitory Concentration (MIC)

The minimum inhibitory concentration (MIC) is the lowest peptide concentration required to inhibit the growth of a bacterium. Using a standard two-fold microdilution assay, the MIC for both *E. coli* and *S. aureus* was found to be 25 µM. This established the reference amount of ChoM that, if functionalised onto the titanium, would be expected to inhibit bacterial growth, assuming 100% release. Based on this, ChoM concentrations of 1x, 2x and 4x the MIC were used in subsequent experiments.

6.4 Antimicrobial Peptide Interfacial Release

The flat titanium and 2-hour nanotopography were functionalised with ChoM by physical adsorption. This involved pipetting 40 µl of different concentrations of ChoM onto the surfaces and then allowing them to air dry. A first step was then to investigate the release of ChoM from the flat titanium and 2-hour nanospikes over time.

[N.B. For these studies, surfaces functionalised with ChoM are abbreviated according to the following scheme: flat titanium surface functionalised with 25 µM ChoM = Flat-25, nanospikes functionalised with 25 µM of ChoM = NS-25].

6.4.1 ChoM Release Mechanics

This experiment investigated the release of ChoM into water from the functionalised flat titanium and 2-hour nanospike surfaces over a 3-hour period. The surfaces were functionalised with ChoM at concentrations of 25 µM, 50 µM and 100 µM, these being 1x, 2x and 4x the MIC for *E. coli* and *S. aureus*. Sterilised distilled water (40 µl) was then pipetted onto each surface and after 10 minutes, 30 minutes, 1 hour, 2 hours or 3 hours, 2 µl was removed and the peptide concentration measured using a Nanodrop spectrophotometer at wavelength 280 nm. Studies had to be terminated after 3 hours, as dehydration of the surfaces was observed.

For flat titanium surfaces, there was a burst of ChoM released from all the surfaces tested within the first 10 minutes, with the highest levels of ChoM being released from Flat-50 and Flat-100 (**Figure 6.6**). From 10 minutes onwards, levels of ChoM plateaued for Flat-25 and Flat-50 and from 30 minutes for the Flat-100. This suggested that most of the available ChoM was released within 10-30 minutes in a dose-dependent manner.

For the nanospike surfaces, ChoM was also released most rapidly within the first 10 minutes, but overall levels of peptide released were less than from the flat surfaces over the 3-hour experimental period (**Figure 6.6**). NS-25 exhibited no further release of ChoM after 10 minutes. However, NS-50 and NS-100 saw a gradual increase in peptide level from 10 minutes onwards, and to be approaching the Flat-100 case after 3 hours.

Taken together, these data indicated that ChoM was depleted rapidly (10-30 minutes) from the flat titanium surfaces, but that the nanotopography exhibited a slower release profile of several hours. Thus, ChoM appeared to hinder the ChoM release from the nanospike surface.

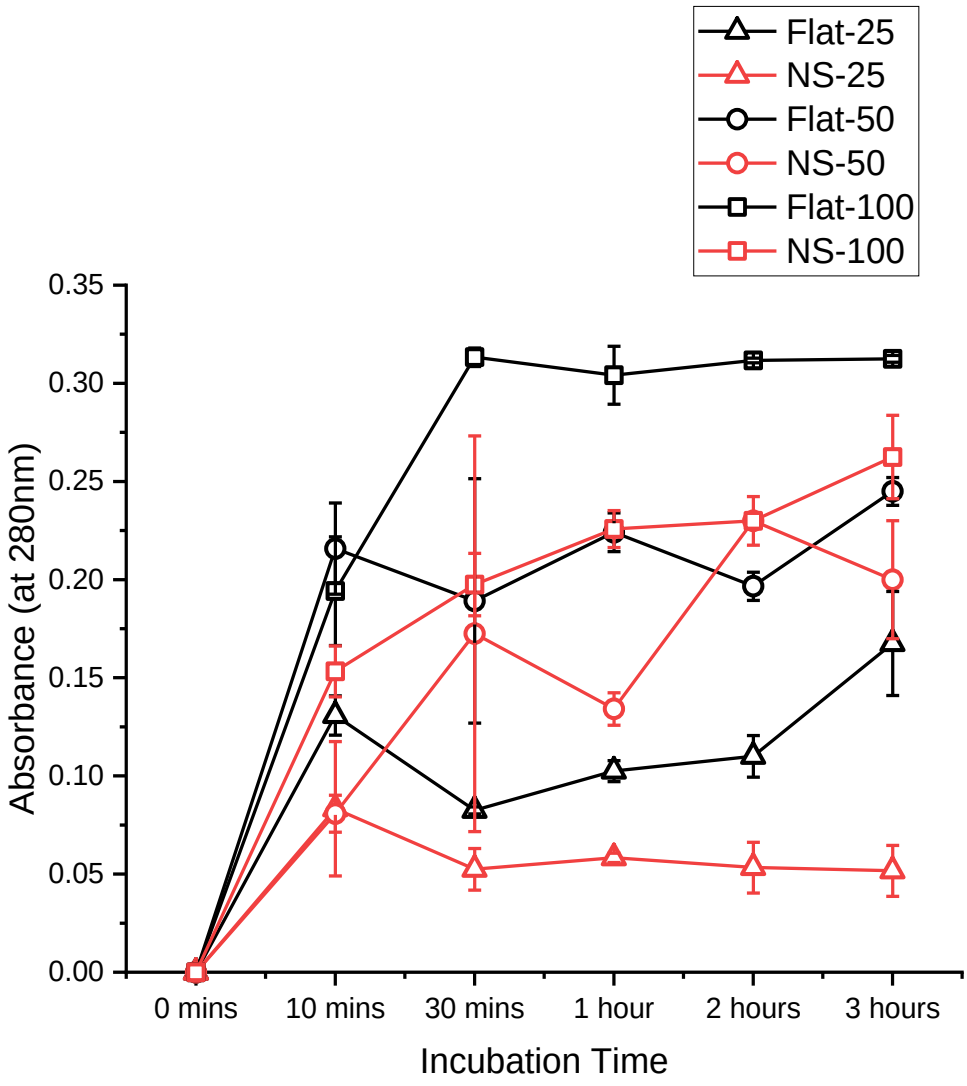

Figure 6.6-*ChoM release mechanics from flat and 2-hour nanospike surfaces. Flat (black) or 2-hour nanospike (red) surfaces were functionalised with 25 µM (triangle), 50 µM (circle) or 100 µM (square) of ChoM. Peptide released into the surrounding distilled water was measured at A280. n= 2 in duplicate*

6.4.2 SEM Imaging of ChoM Coating

SEM was used to image the 50 µM ChoM coating on flat and 2-hour nanospike surfaces after functionalisation to visualise the homogeneity of the coating and its thickness in relation to the nanotopography. Images were also taken of the coating after elution periods of 10 minutes to 3 hours to determine if ChoM release over this time period could be visualised. Mueller Hinton (MH) broth was to be used for the subsequent BacTiter-Glo and RealTime-Glo assays to assess antibacterial activity of the surfaces. Therefore these studies were performed using Mueller Hinton broth rather than distilled water, to ensure the release kinetics of ChoM could be directly related to this later work. At the determined time interval, the broth was removed, and the disks left to air dry, before being sputter coated and observed under SEM.

Differences were seen in the coverage of ChoM on both the flat titanium and 2-hour nanotopography at time zero (**Figure 6.7, Figure 6.8A-B)**. On the flat surface, a more homogenous covering of the peptide was seen, while on the nanotopography, variable levels of ChoM coating could be observed. In some areas there was little peptide coating visible (**Figure 6.8G**), while in others, the coating was relatively thin, with the nanotopography still visible (**Figure 6.8A-G**). Other areas had a very thick coating, which masked the underlying nanotopography (**Figure 6.8G**).

For the flat titanium disk, residual ChoM coating was visible at each of the time points, although this seemed to be very limited by 30 minutes (**Figure 6.7**). By contrast, for the nanospike disks, the peptide coating could still be seen covering the majority of the nanotopography after 10 minutes, with the tips of some of the nanospikes just visible **(Figure 6.9**). Large flake-like matter was also seen on some areas of the disks, which could be dried peptide or remnants from the broth. As the incubation time was increased, there was limited thinning of the peptide coating, but generally the coating remained heterogenous across the surface (**Figure 6.10, Figure 6.11, Figure 6.12** and **Figure 6.13**). Again, flake-like entities were seen at each time interval. These data supported the hypothesis that greater levels of ChoM coating remained on the nanospikes than on the flat titanium surface over the elution period of 3 hours.

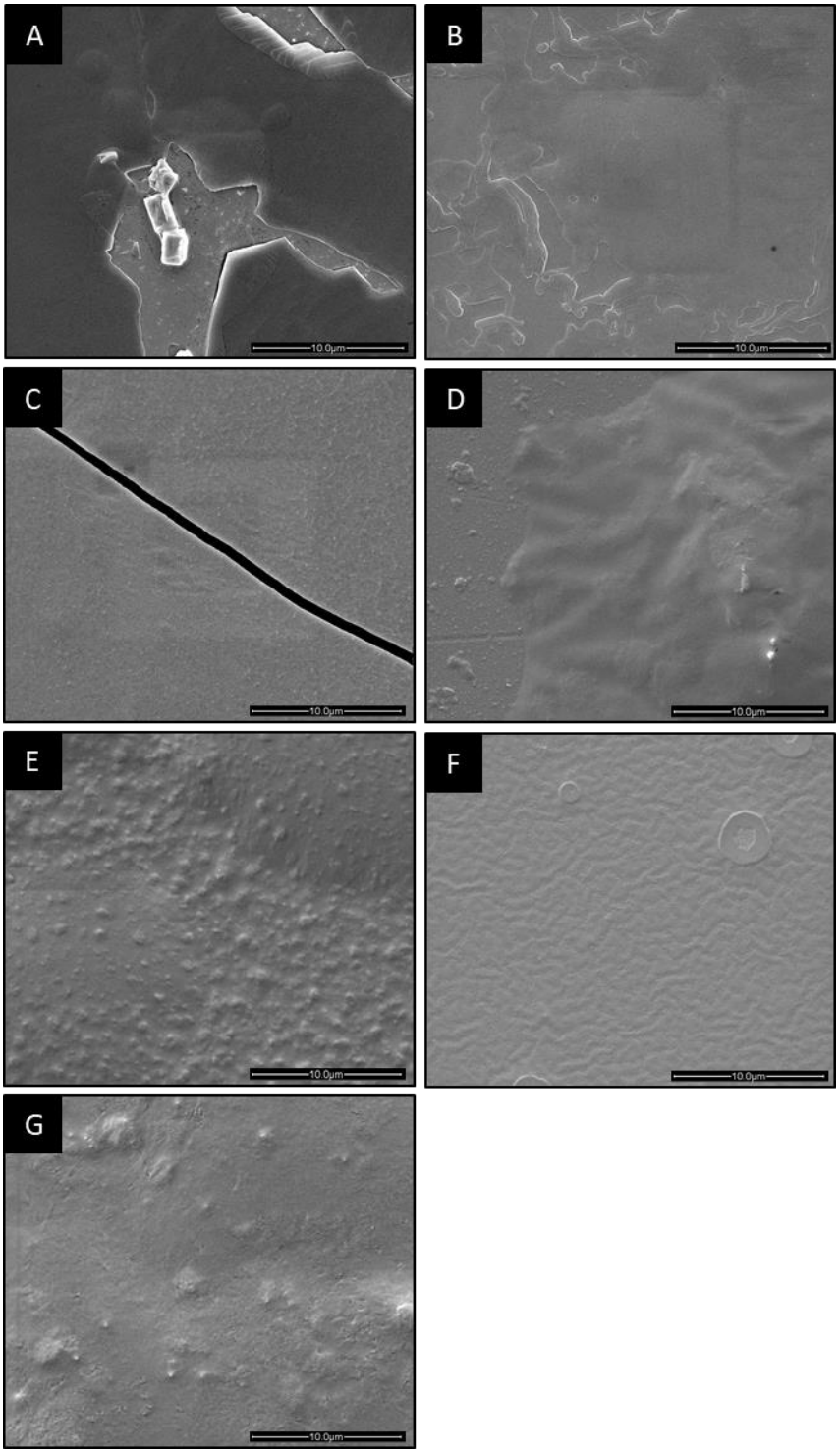

Figure 6.7- *SEM images of 50 µM ChoM coating on flat titanium following elution into MH broth over 3 hours. ChoM was functionalised onto flat titanium and 40 µl MH broth added onto the surface. After A, B) 0 minutes, C) 10 minutes, D) 30 minutes, E) 1 hour, F) 2 hours, or G) 3 hours, the broth was removed and the surfaces were dried and imaged.*

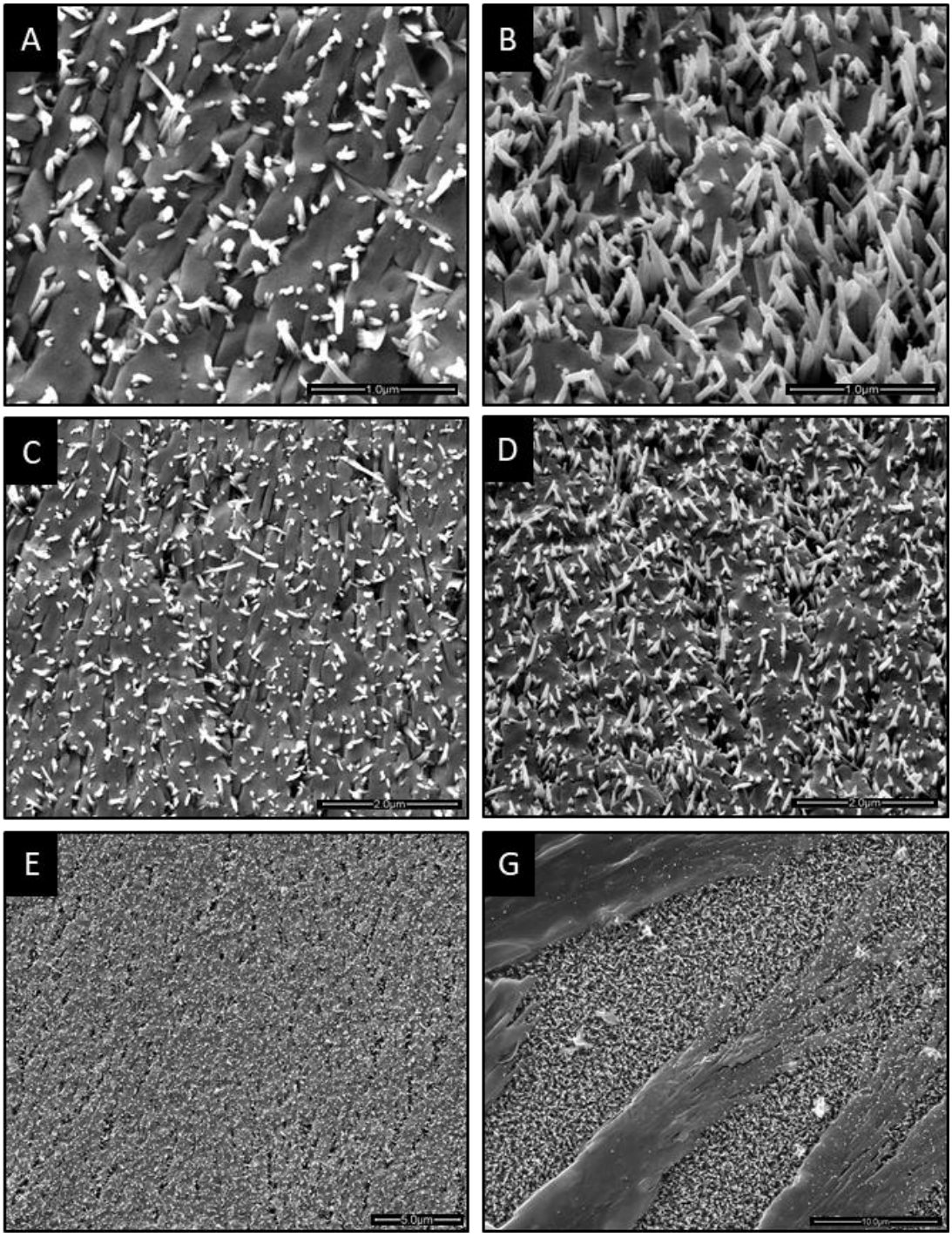

Figure 6.8- *SEM images of 2-hour nanospikes functionalised with 50 µM ChoM at different magnifications. ChoM (40 µl) was pipetted onto 2-hour nanospikes, dried and then imaged. Images B and D are with 30° tilt.*

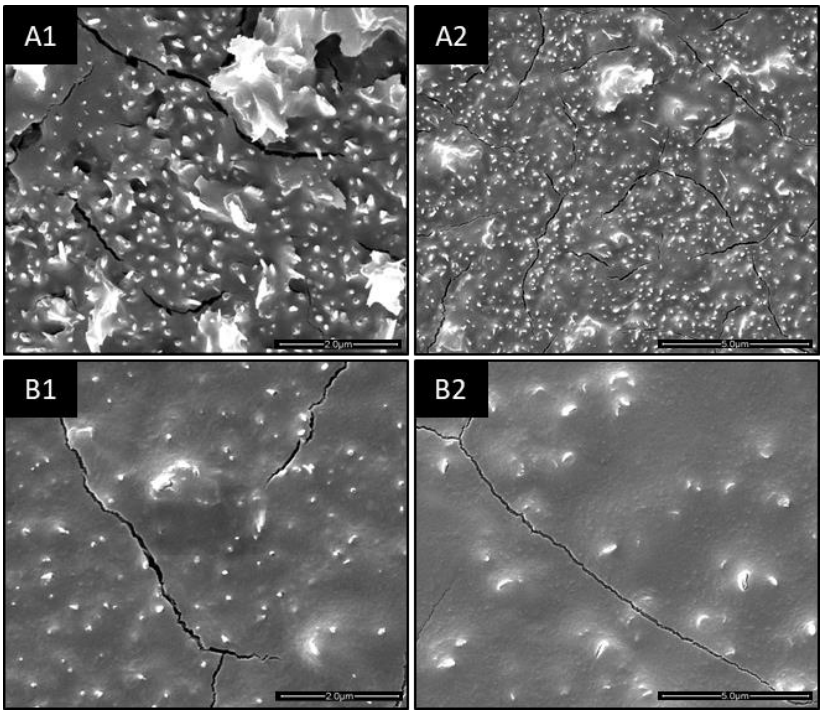

Figure 6.9- *SEM images of 50 µM ChoM coating on 2-hour nanospikes following elution into MH broth over 10 minutes. ChoM was functionalised onto flat titanium and 40 µl MH broth added onto the surface. After 10 minutes, the broth was removed and the surfaces were dried and imaged. Rows A and B are of two different disks. Columns 1 and 2 are different magnifications and regions of the same disk.*

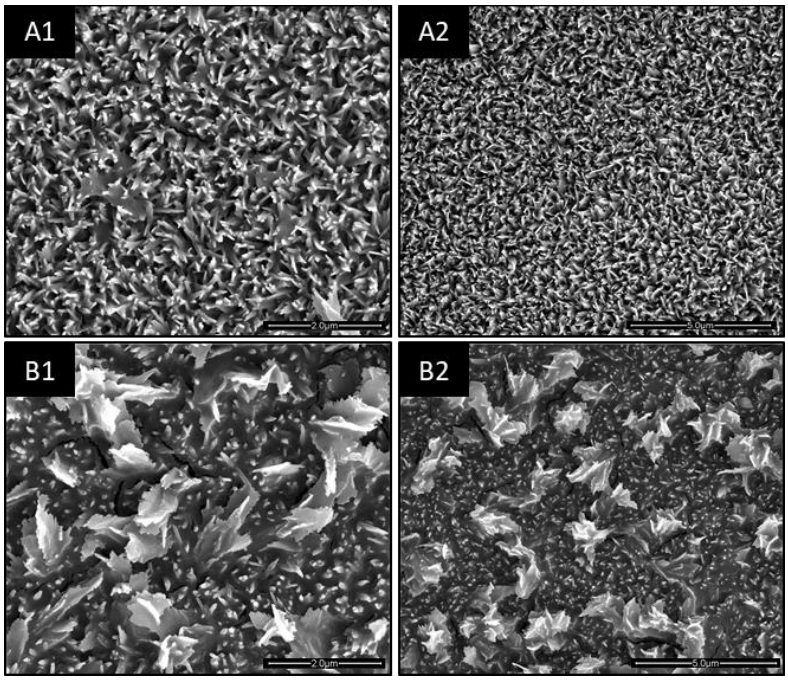

Figure 6.10- *SEM images of 50 µM ChoM coating on 2-hour nanospikes following elution into MH broth over 30 minutes. ChoM was functionalised onto flat titanium and 40 µl MH broth added onto the surface. After 30 minutes, the broth was removed and the surfaces were dried and imaged. Rows A and B are of two different disks. Columns 1 and 2 are different magnifications and regions of the same disk.*

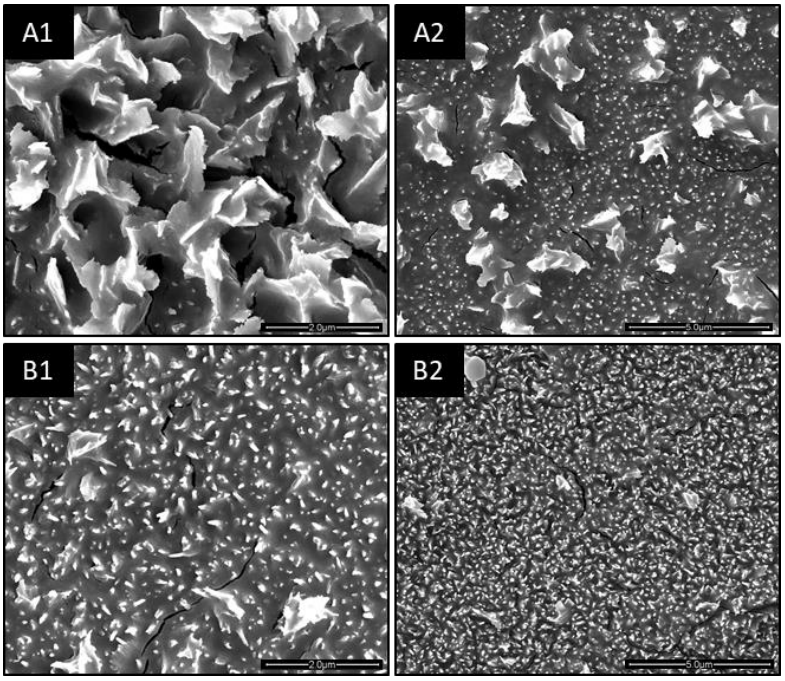

Figure 6.11- *SEM images of 50 µM ChoM coating on 2-hour nanospikes following elution into MH broth over 1 hour. ChoM was functionalised onto flat titanium and 40 µl MH broth added onto the surface. After 1 hour, the broth was removed and the surfaces were dried and imaged. Rows A and B are of two different disks. Columns 1 and 2 are different magnifications and regions of the same disk.*

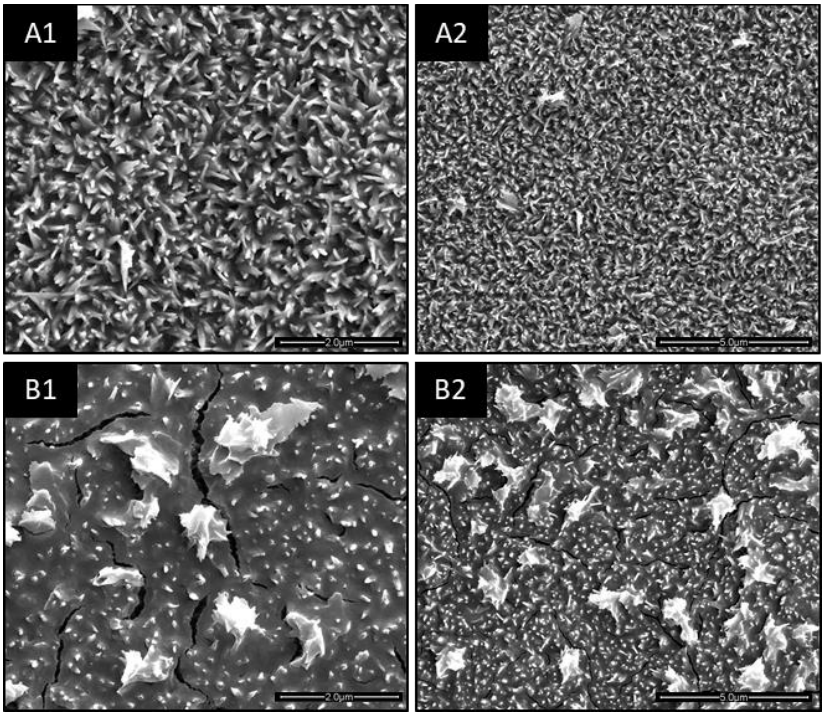

Figure 6.12- *SEM images of 50 µM ChoM coating on 2-hour nanospikes following elution into MH broth over 2 hours. ChoM was functionalised onto flat titanium and 40 µl MH broth added onto the surface. After 2 hours, the broth was removed and the surfaces were dried and imaged. Rows A and B are of two different disks. Columns 1 and 2 are different magnifications and regions of the same disk.*

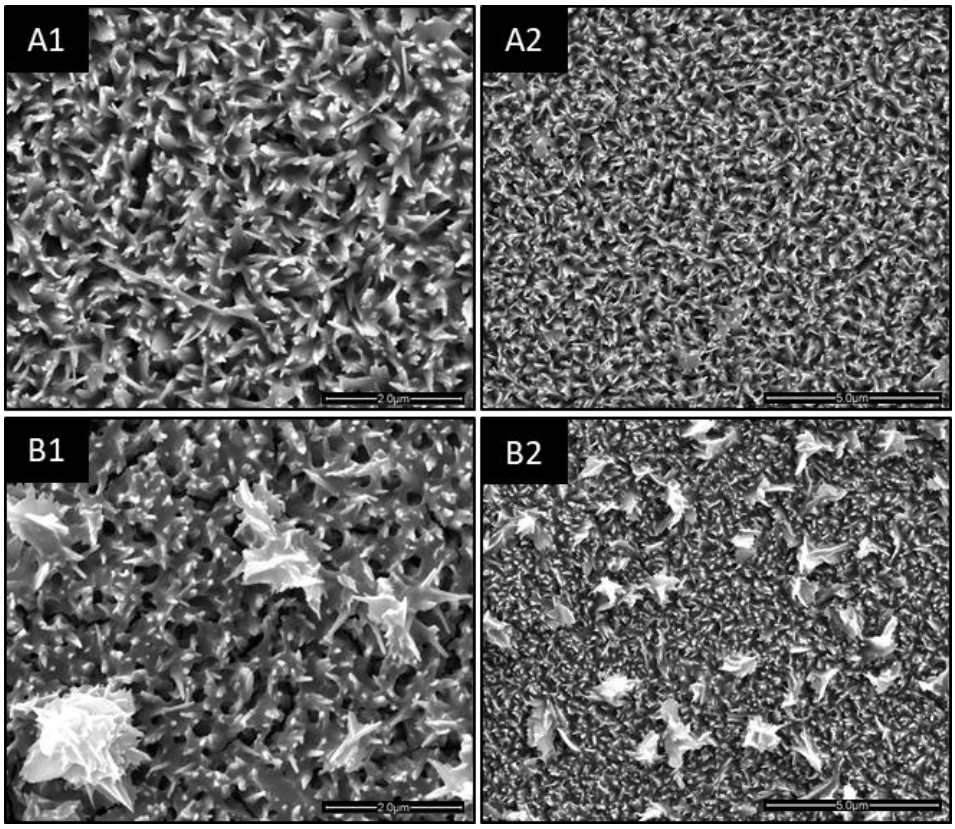

Figure 6.13- *SEM images of 50 µM ChoM coating on 2-hour nanospikes following elution into MH broth over 3 hours. ChoM was functionalised onto flat titanium and 40 µl MH broth added onto the surface. After 3 hours, the broth was removed and the surfaces were dried and imaged. Rows A and B are of two different disks. Columns 1 and 2 are different magnifications and regions of the same disk.*

6.4.3 Antimicrobial Properties of ChoM Released from Functionalised Surfaces

To ensure that ChoM released from the surface of the titanium disks remained functional, its antibacterial activity was monitored following release. This was achieved by testing ChoM eluted from the surface of 50 µM ChoM-functionalised flat titanium surfaces and nano-spikes over 3 hours in a MIC assay. ChoM eluted into 40 µl of MH broth over 3 hours was incubated with mid-exponential phase *E. coli* (10^6 CFU/ml) for 20 hours. Bacterial growth was then quantified by measuring the absorbance at 595 nm.

Levels of ChoM released from the functionalised flat surfaces after 30 minutes onwards were enough to inhibit bacterial growth relative to the controls (**Figure 6.14**). As anticipated from the previous ChoM release experiment, after 3 hours, levels of ChoM released from the functionalised 2-hour nanotopography impair growth of *E. coli*, relative to the controls but were not sufficient for the MIC to be reached (**Figure 6.14**).

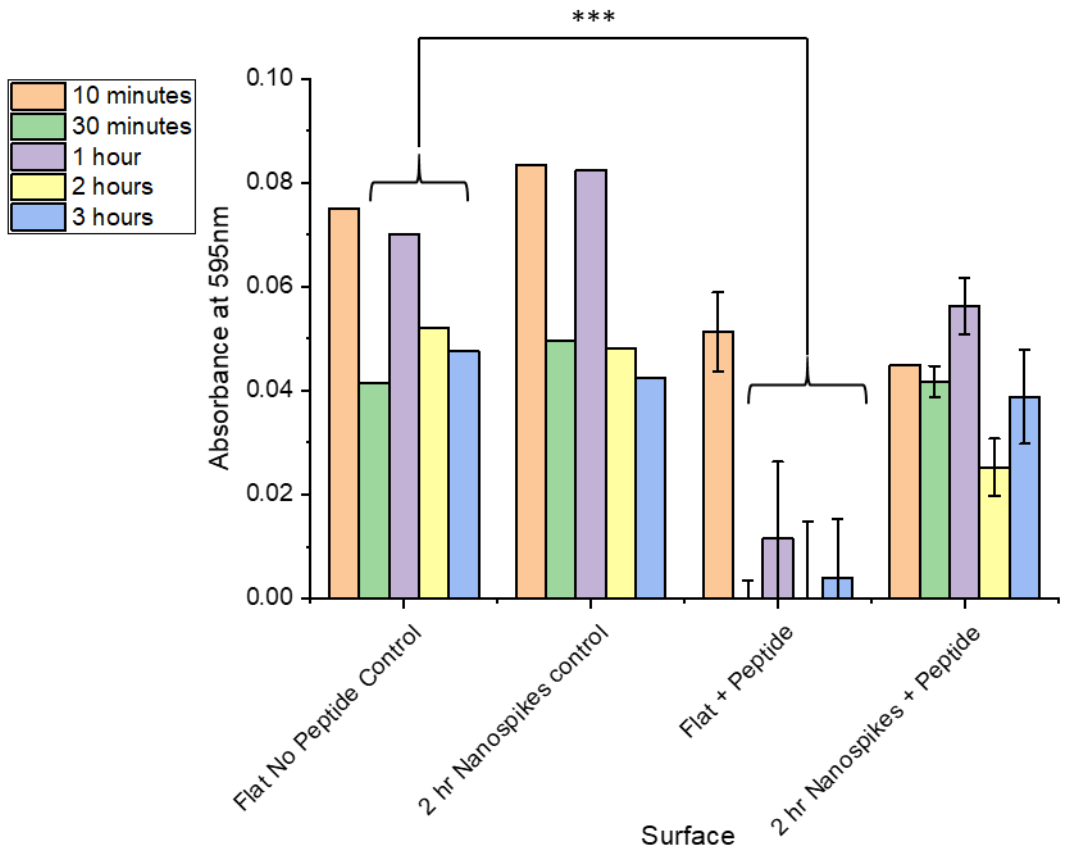

Figure 6.14- *ChoM release as a function of E. coli growth. ChoM (50 µM) was functionalised onto flat and 2-hour nanospike disks. MH broth (40 µl) was then pipetted onto the disks for between 10 minutes and 3 hours, before being recovered and added to a mid-exponential suspension of E. coli. After 20-hours incubation, bacterial growth was measured at A_{595}. ***P<0.001 compared to respective control surface, as determined by ANOVA with post-hoc Tukey and Bonferroni tests; n=2 in duplicate.*

6.4.4 Potential Delayed Release from Nanotopographical Surfaces

The studies performed so far implied that ChoM was being released at a slower rate from nanospike surfaces compared to flat surfaces. As such, there was the potential for greater levels of ChoM to be released from the nanospike surfaces with a longer incubation period. This was assessed by immersing disks in 400 µl broth for 3 or 12 hours. This broth was then recovered and incubated with *E. coli* or *S. aureus* for 3 hours. Levels of bacterial metabolic activity were then determined using BacTiter-Glo, and the levels of luminescence converted into colony forming units (CFU).

Bacteria recovered from the non-functionalised flat titanium and 2-hour nanotopography had relatively high levels of metabolic activity, with evidence of replication. This was seen by the

increase in CFU from the original *E. coli* inoculum of $5x10^5$ CFU/ml to approximately $3x10^6$ CFU/ml for the 3-hour and $5x10^6$ for the 12-hour time points (**Figure 9.4B** and **D**). A similar trend was seen for *S. aureus*, where the bacterial concentration reached around $1x10^6$ CFU/ml (**Figure 9.5B** and **D**).

For the functionalised flat titanium, there was a significant drop in luminescence for the 3- and 12-hour timepoints for *E. coli* compared to non-functionalised, corresponding to a ~10-fold reduction in CFU (**Figure 9.4**). The CFU values after 3 hours were similar to the inoculum but increased after 12 hours to 10^6 CFU/ml. These data also imply that the longer incubation time did not result in ChoM being released. It is possible that nearly all the peptide was released within the initial 30 minutes consistent with the previous time release studies.

In contrast to the flat titanium, no significant reduction was observed in luminescence and CFU for *E. coli* for the 3-hour timepoint from the functionalised 2-hour nanotopography compared to non-functionalised (**Figure 9.4**). This suggests that lower levels of ChoM were released from the 2-hour nanotopography within the initial 3 hours compared to the flat titanium. After 12 hours it was notable that the *E. coli* population had increased by a factor of 3x on the functionalised flat titanium but had remained relatively constant on the nanospikes. This implies peptide was still being released after 3 hours and/or the nanospike surfaces were relatively bactericidal. These results are consistent with the previous peptide time release studies.

For *S. aureus*, there was lower luminescence measured for the functionalised flat titanium compared to the non-functionalised surface for both time points, but this did not correspond to a significant difference in CFU/ml (**Figure 9.5**) As might be expected, a similar trend was seen for the 2-hour nanotopography surfaces. This suggests that insufficient ChoM was released from any of the surfaces to inhibit growth of *S. aureus*. At 3 hours the viability on the functionalised nanospikes was more than for the flat titanium, but less at 12 hours, consistent with the results for *E. coli* and the time release studies.

6.5 Bacterial Interactions with Functionalised Surfaces

Having established that the nanotopography could modulate the release of ChoM relative to a flat surface, a more extensive set of studies were performed to investigate how the release kinetics might be further manipulated.

6.5.1 Effect of Time and Concentration of ChoM

The effects of increasing ChoM concentration and incubation time on the antibacterial activity of functionalised disks was investigated, using *E. coli* metabolic activity as the measure. Bacterial inocula (40 µl; $5x10^5$ CFU/ml) were pipetted on top of the functionalised disks and incubated for 1-3 hours, before being mixed with BacTiter-Glo reagent and luminescence measured (**Figure 9.6A**). Luminescence values were then converted into CFU (**Figure 9.6B**).

Bacterial growth from non-functionalised flat titanium and 2-hour nanotopography showed increasing luminescence and CFU as the duration increased from 1 hour to 3 hours (**Figure 9.6**). There was no statistical difference between growth on flat and 2-hour nanotopography, indicating that the nanotopography had little effect on the vitality of *E. coli* cells at least over the 3-hour period.

For the flat titanium functionalised with 25 µM ChoM, bacterial growth was seen over the 3 hours, but was consistently less than on the non-functionalised surfaces, with a significant reduction being seen by 3 hours (**Figure 9.6**). With higher ChoM concentrations (50 µM, 100 µM), only very low levels of metabolic activity were detected at all time points, and numbers of recovered viable bacteria were static at ~$2x10^4$ CFU. Together, these data indicated a dose-dependent release of ChoM from flat titanium, which, at concentrations of 50 µM or higher, was sufficient to reach the MIC for *E. coli*.

For the nanospike titanium functionalised with ChoM, higher levels of bacterial growth were seen compared to the equivalent flat surfaces. Nonetheless, a significant reduction in CFU was seen at 3 hours for each functionalised surface relative to the non-functionalised nanospike surface, indicating that ChoM released from the nanotopography was able to impair *E. coli* growth. The extent of bacterial growth inhibition increased with increasing ChoM concentration (**Figure 9.6**), indicating a dose-dependent effect on ChoM release, as for flat titanium.

Taken together, these data support the hypothesis that ChoM was released from the nanotopography at a slower rate than from the flat titanium surface, such that the MIC was not reached over the 3-hour period for any of the ChoM concentrations tested although at the highest concentration of 100 M it was probably approaching the MIC. By contrast, peptide release from

the flat titanium was relatively rapid and reached the MIC threshold with a 50 µM ChoM coating within around 1 hour. These results are consistent with the peptide time release experiment (**Section 5.4.1**) which also indicated that after 3 hours the peptide release from the Flat-50 was similar to the NS-100. Further release would also be anticipated from the NS-100 after 3 hours.

6.5.2 Wettability

Differences had been noted between the flat and 2-hour nanospike disks when applying the ChoM solution or bacterial suspensions, which implied variations in regard to their wettability. It was considered that this may be a factor contributing to the difference in the ChoM release profiles between these two disk types. Wettability is the interaction between a fluid and a solid interface and is dependent on the intermolecular forces between the two phases. Water contact angle measurements were therefore carried out on the flat titanium and 2-hour nanotopography to determine if the surfaces were hydrophobic (low wetting) or hydrophilic (high wetting).

Surface wettability was quantified by measuring the contact angle of a deionised water droplet when added to the test surface. If the contact angle is less than 90°, the surface is termed hydrophilic, or if less than 10°, it is classed as super-hydrophilic. If the contact angle is above 90°, it is classified as hydrophobic.

The water droplet formed on mirror polished flat titanium had an average contact angle of 80° and was therefore classified as hydrophilic (**Figure 6.15**). By contrast, the water contact angle on the 2-hour nanotopography was unquantifiable. The water droplet completely spread over the surface with an average angle below 10°, indicating that the 2-hour nanospikes were super-hydrophilic (**Figure 6.15)**. In fact, this super-hydrophilic property was observed for all the nanotopographies generated over 30-minutes to 7-hours. As the contact angle could not be measured, a high-speed video was used to observe the droplet interacting with the 2-hour nanospike surface (**Figure 6.16)**. By 2 seconds, the droplet had completely spread over the surface.

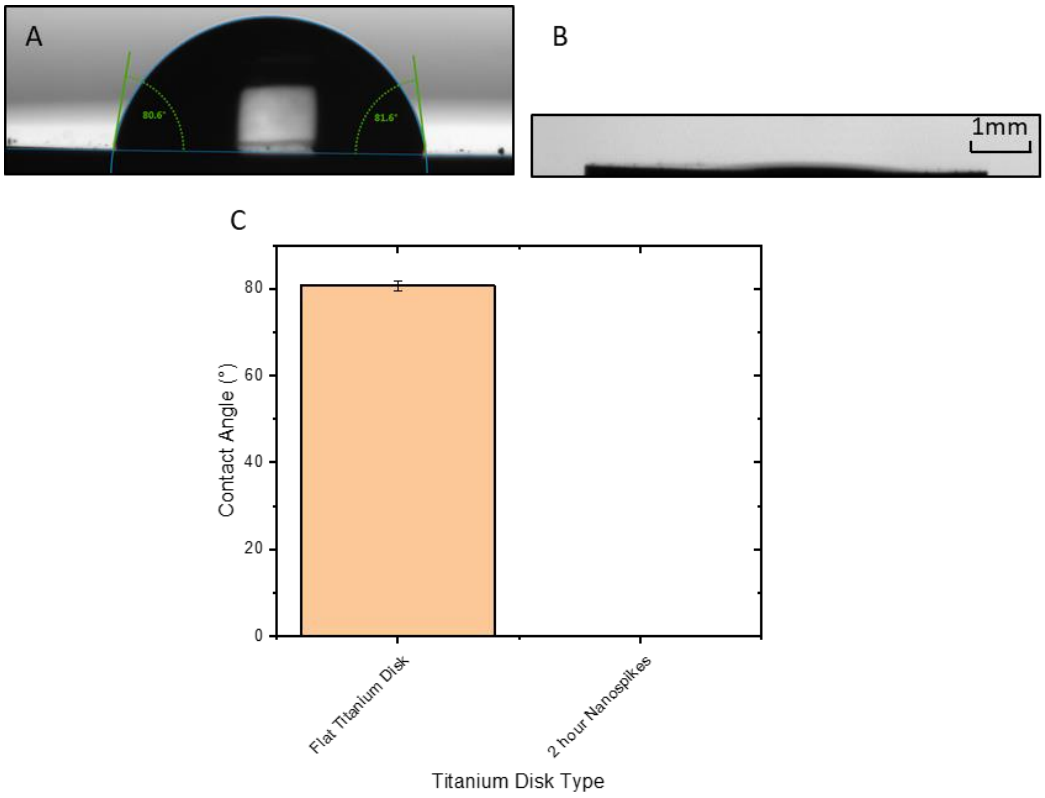

Figure 6.15*- Water contact angle measurements on mirror polished flat titanium surface and 2-hour nanospikes. Nanotopography was grown on pure titanium substrates within a Teflon-lined acid digestion vessel with the conditions of 52 ml 1 M NaOH at 240°C for 2 hours. Water (2 µl) was pipetted onto the disks and the resulting contact angle imaged and measured. A) Water droplet on flat titanium surface, B) Water droplet on 2-hour nanotopography, C) Average contact angle on flat and 2-hour nanotopography (unquantifiable as <10°) (n=3 in triplicate).*

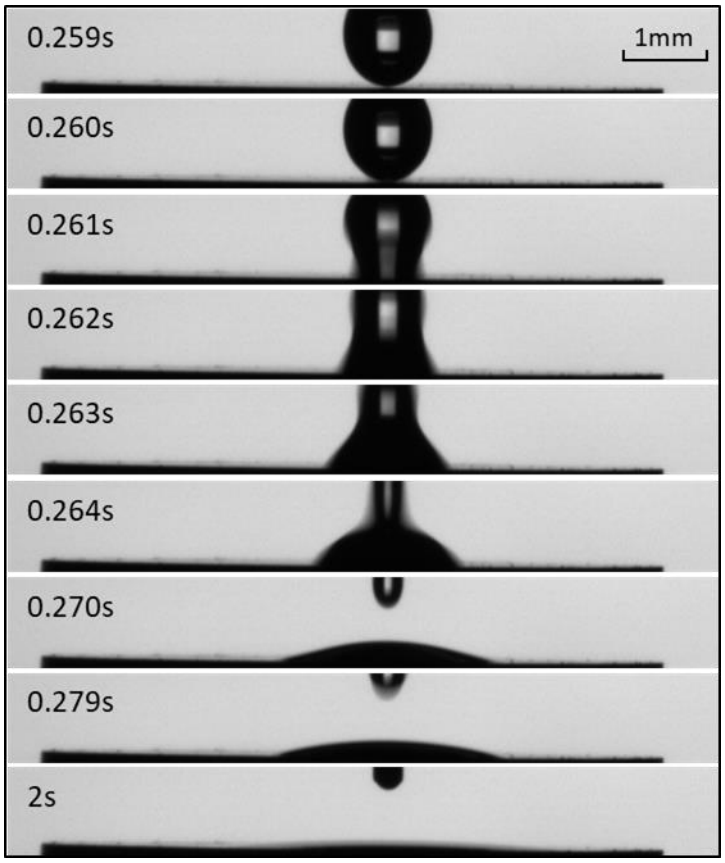

Figure 6.16*- Video images of water droplet interaction on 2-hour nanospikes. Nanotopography was grown on pure titanium substrates within a Teflon-lined acid digestion vessel with the conditions of 52 ml 1 M NaOH at 240°C for 2 hours. Water (2 µl) was pipetted onto the disk and the resulting droplet interaction imaged approximately every 0.001 seconds.*

6.5.3 Effect of Shorter Nanotopography and Elution Environment on Peptide Release

So far, the results indicated that less peptide was released from the nanotopographical surface than the flat titanium surface. It was considered that this may be due to the physical nature of the nanotopography itself and/or may relate to the differences in hydrophilicity between these surface types. The latter meant that on the flat surface, the ChoM/inoculum was present as a meniscus while on the nanotopography, the liquid was completely spread across the disk. It was hypothesised that the meniscus environment may encourage more peptide release by generating a larger diffusion gradient. To investigate these two possibilities, 1-hour nanospikes were tested. These were shorter and it was considered that reducing the topography height might help to promote more rapid release of the peptide. There was also a variant of this 1-hour nanospike surface available that had been stored for 1 year and had become hydrophilic, rather than superhydrophilic, As such, liquid placed onto the surface of this variant formed a meniscus rather

than a completely wetted surface. The peptide release from this surface could therefore be compared to the 'normal' 1-hour nanospikes, where no meniscus was present.

Flat titanium, 1-hour and 2-hour nanospike surfaces were functionalised with 50 µM ChoM, before being incubated with 40 µl of *E. coli* ($5x10^5$ CFU/ml) for 1, 2 and 3 hours. BacTiter-Glo reagent was added, the luminescence read and then converted into CFU.

Over time there was an increase in the number of bacteria on each of the non-functionalised control surfaces, with comparable CFU recovered at each time point (**Figure 9.7**). This indicated similar bacterial growth on each of these surfaces, independent of nanotopography or meniscus environments.

For the functionalised flat titanium, bacterial growth was significantly lower than on the non-functionalised surfaces over the three hours (**Figure 9.7**). Numbers of recovered viable bacteria were static at ~$2x10^4$ CFU, indicating that the MIC threshold for *E. coli* had been reached within the first hour. By contrast, for the functionalised nanospike surfaces, numbers of CFU increased with time. Nonetheless, *E. coli* growth was impaired, with significant reductions in CFU seen from 2 hours for all functionalised nanospike surfaces (**Figure 9.7**).

Comparison of the functionalised 1- and 2-hour nanotopography indicated a significant reduction in CFU recovered at each time point from the 1-hour nanotopography (**Figure 9.7**). This implies that the longer nanospikes may have impeded rapid release of ChoM into the local environment. Furthermore, there was no significant increase in CFU from the 1-hour nanotopography between 2 and 3 hours, in contrast to the 2-hour nanotopography. This suggests that the MIC threshold concentration may have been reached on the 1-hour nanotopography by 2 hours, but not for the 2-hour nanotopography.

Comparison of the functionalised 1-hour nanotopography ± meniscus suggests that the presence of the meniscus assisted early ChoM release, as CFU values were significantly lower from the 1-hour variant than the 'normal', superhydrophilic 1-hour nanospikes (**Figure 9.7**).

Together, these results show that ChoM was released from the 1-hour nanospikes quicker than the 2-hour nanospikes over 3 hours, although the shorter topography still hindered ChoM release compared to the flat titanium surface. The results also suggest that the presence of a meniscus on the flat titanium surface is likely to assist the release of ChoM compared to the superhydrophilic nanospike surface.

6.5.4 Effects of Disk Immersion on Peptide Release

The presence of a meniscus had been shown to influence the different ChoM release profiles seen between the flat titanium and 2-hour nanospike surfaces. To overcome these effects, studies were performed where *E. coli* or *S. aureus* were incubated on functionalised disks that were submerged in a larger volume of growth medium. Functionalised disks were incubated in 400 µl of bacterial suspension for up to 3 hours, after which levels of bacterial metabolic activity were determined by BacTiter Glo. The results for *E. coli* are shown in **Figure 9.8** and *S. aureus* in **Figure 9.9**.

For both *E. coli* (**Figure 9.8**) and *S. aureus* (**Figure 9.9**), cell numbers on non-functionalised flat and 2-hour nanospikes were not significantly different, indicating that the nanotopography did not affect growth of the bacteria over the 3-hour period.

For *E. coli*, functionalising the flat titanium with increasing concentrations of ChoM from 25-200 µM resulted in a progressive, significant decrease in viability compared to the non-functionalised flat surface (**Figure 9.8**). For the functionalised nanotopography there was a similar trend, but a significant reduction in CFU was only seen for surfaces functionalised with 100-200 µM ChoM. At 100 µM ChoM, the CFU values were similar to the original inoculum of $5x10^5$ CFU/ml, indicating that the MIC may have been reached.

A similar trend was seen for *S. aureus*, with the exception that a significant reduction in CFU relative to control was recorded for nanospike surfaces functionalised with 100 µM ChoM (**Figure 9.9**).

These data suggest that disk immersion may have improved ChoM release from the 2-hour nanospike surfaces, since impairment of *S. aureus* growth, as well as that of *E. coli*, was seen. However, differences in peptide release were still seen between flat titanium and 2-hour nanospike disks. This supports the earlier results that ChoM release from nanotopographical surfaces was initially slower than from flat surfaces and suggests that the presence of a meniscus environment was not the only factor that caused the differences in peptide release mechanics.

6.5.5 Vitality of *S. aureus* on Functionalised Surfaces with RealTime-Glo

The previous experiments were generally limited to a 3-hour time period. This assay considered the bactericidal properties of the functionalised and non-functionalised disks over a significantly longer period of up to 11 hours. Beyond 10 hours, *S. aureus* viability decreased on all surfaces, indicating that a factor independent of nanotopography, such as nutrient availability, was affecting bacterial growth. The viability of *S. aureus* cells was assessed on flat titanium and 2-

hour nanospike disks functionalised with 50 µM ChoM. Luminescence was measured at 10-minute intervals by RealTime-Glo.

For the non-functionalised flat titanium surface, a rapid luminescence increase was observed from 4 hours to a maximum of 6 x10^4 RLU at around 10 hours, after which the luminescence started to drop (**Figure 6.17**). By contrast, the non-functionalised nanotopography appeared to impair the vitality of *S. aureus* over time, with a maximum luminescence reading of 2x10^4 RLU recorded at 6 hours. This was significantly lower than the highest luminescence seen on the flat surface.

Growth of *S. aureus* was inhibited on the functionalised flat surface throughout the 11-hour time period, indicating that the MIC had been reached very quickly (**Figure 6.17**). Overall levels of luminescence were similar for the nanospike surfaces ± ChoM. However, for the functionalised nanospike surface, a delayed luminescence increase until around 6 hours was seen compared to that of around 2.5 hours for the non-functionalised nanospikes (**Figure 6.17**).

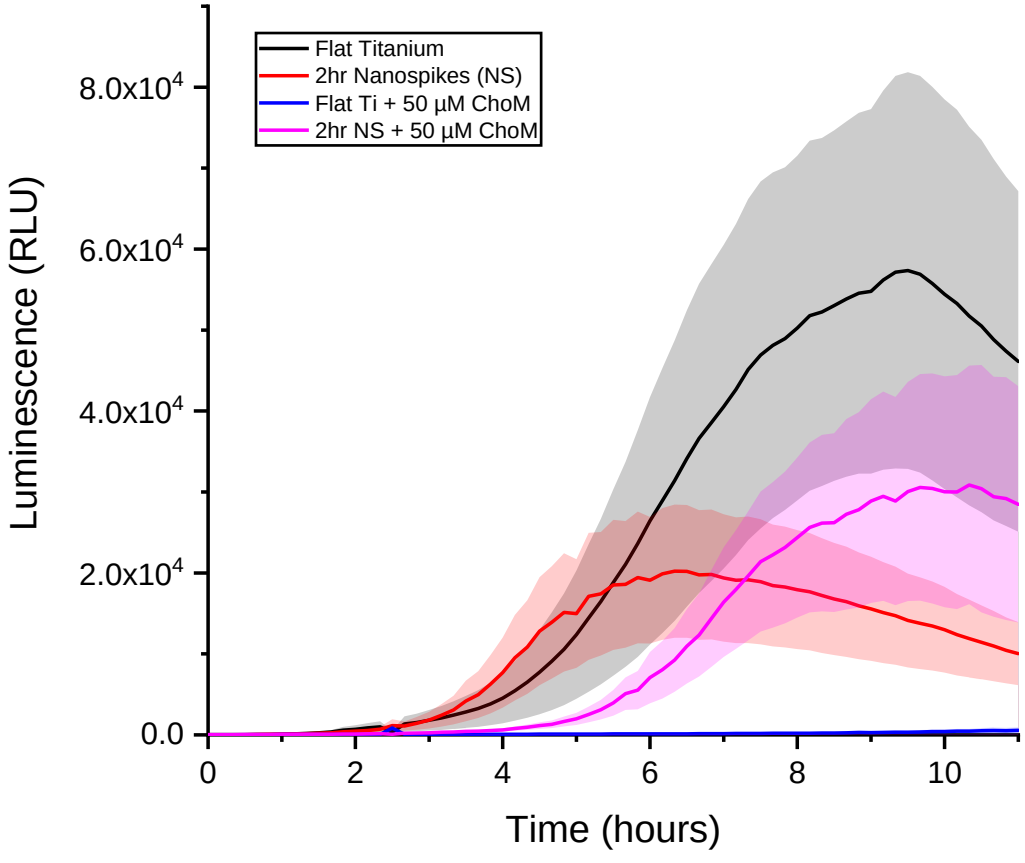

Figure 6.17- *Vitality of S. aureus on functionalised titanium disks as assessed by RealTime-Glo. Flat titanium and 2-hour nanospike disks were functionalised with 50 µM ChoM. RealTime-Glo reagent was added to 40 µl S. aureus suspension and after 1 hour added to functionalised surfaces. The vitality of S. aureus was measured by luminescence every 10 minutes for 11 hours. Light shading is the standard error at each time point. N=2 in duplicate. NS=Nanospikes.*

6.5.6 Promoting Peptide Release with Mechanical Stimulation

6.5.6.1 Promoting Peptide Release using Nanokick

Nanokick is an ultra-low sonication device that has been shown to help stimulate osteogenesis. This device was used to investigate if peptide release from nanotopography could be promoted through a stimulus such as low-level sonication. The experiment was performed using *E. coli* with a 3-hour incubation period with or without nanokick stimulus. Levels of bacterial metabolic activity at 3 hours were determined using BacTiter Glo and luminescence values converted into CFU.

Supporting previous experiments, significant reductions in *E. coli* viability were seen for flat titanium functionalised with 25 µM+ ChoM, and, to a lesser extent, with 50 µM+ ChoM for nanospike surfaces. However, nanokick stimulation did not affect these outcomes (**Figure 6.18**). Somewhat unexpectedly, nanokick stimulation did appear to impact viability of bacteria recovered from both non-functionalised surfaces, although to a very moderate reduction level.

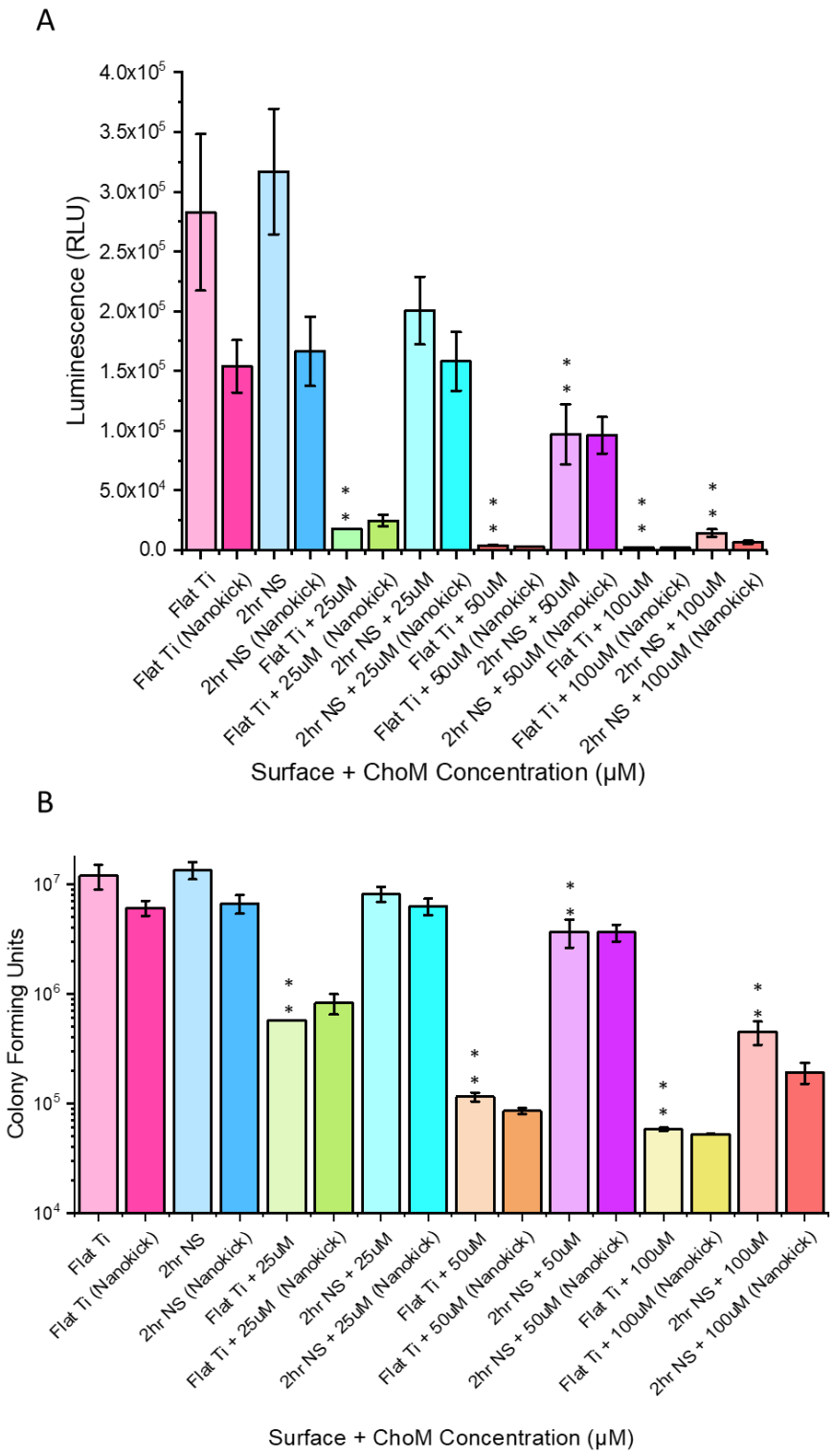

Figure 6.18- *Effects of nanokick stimulation on the antibacterial activity of ChoM against E. coli. Flat titanium and 2-hour nanotopography were functionalised with 25/50/100 µM ChoM and the disks immersed in 400 µl E. coli suspension (5x10^5 CFU/ml) for 3 hours ± continuous nanokick stimulation. Aliquots (40 µl) of the suspension were then mixed with BacTiter-Glo reagent and the metabolic activity of E. coli measured by luminescence (A) and converted into CFU (B). **p≤0.01, compared to respective control surface, as determined by ANOVA with post-hoc Tukey and Bonferroni tests; n=2 in duplicate. NS=Nanospikes.*

6.5.6.2 Promoting Peptide Release with Shaking

As the peptide released from nanotopography was not improved with nanokick, a more rigorous stimulation was tested. Disks were functionalised with 50 µM ChoM and immersed in 400 µl *E. coli* suspension for 3 hours ± shaking at 100 rpm. BacTiter-Glo was then used to measure the metabolic activity of the bacteria, and luminescence values converted into CFU.

Shaking had no significant impact on bacterial viability for the non-functionalised flat and nanospike surfaces (**Figure 6.19**). As expected, there was a significant reduction in CFU for both the Flat-50 and NS-50 surfaces compared to their respective non-functionalised controls (**Figure 6.19**). However, only a minor additional decrease was observed with shaking. This implies that shaking at 100 rpm did not significantly alter the release of ChoM into the local environment.

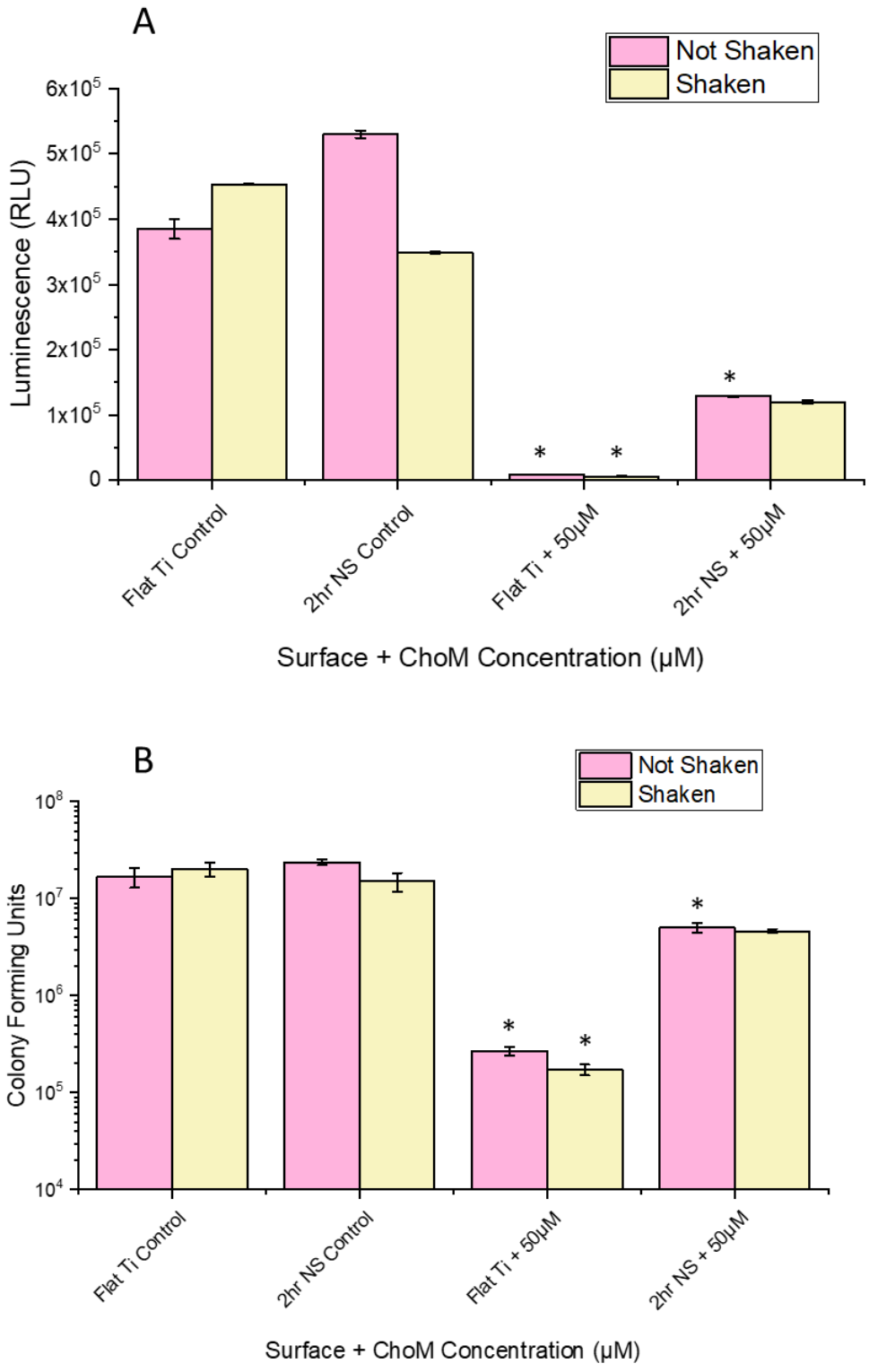

Figure 6.19- *Effects of shaking on the antibacterial activity of ChoM against E. coli. Flat titanium and 2-hour nanotopography were functionalised with 50 µM ChoM and the disks immersed in 400 µl E. coli suspension (5x10^5 CFU/ml) for 3 hours ± continuous shaking. Aliquots (40 µl) of the suspension were then mixed with BacTiter-Glo reagent and the metabolic activity of E. coli measured by luminescence (A) and converted into CFU (B). *p≤0.05, compared to respective control surface, as determined by ANOVA with post-hoc Tukey and Bonferroni tests; n=2 in duplicate. NS=Nanospikes.*

6.5.7 Membrane Disruption caused by ChoM

ChoM is believed to exert its antibacterial mechanism by exfoliating the membrane leading to membrane thinning. It was hypothesised that this may make bacteria more susceptible to being pierced by the underlying nanotopography. To explore this in more detail, SEM was used to visualise bacteria adhered to flat and 2-hour nanospike surfaces ± 50 µM ChoM. After 3 hours incubation on the non-functionalised flat surface, *E. coli* displayed the normal bacillus morphology expected for this species (**Figure 6.20A**), whereas on Flat-50 there were potential pores/indentations present on the membrane (**Figure 6.20B**; highlighted with orange arrows). On the 2-hour nanotopography, the *E. coli* cells exhibited the typical bacillus shape (**Figure 6.20C)**. By contrast, on the functionalised 2-hour nanotopography there was evidence of potential membrane blebbing and cytoplasm leakage (**Figure 6.20D**; highlighted with orange arrows).

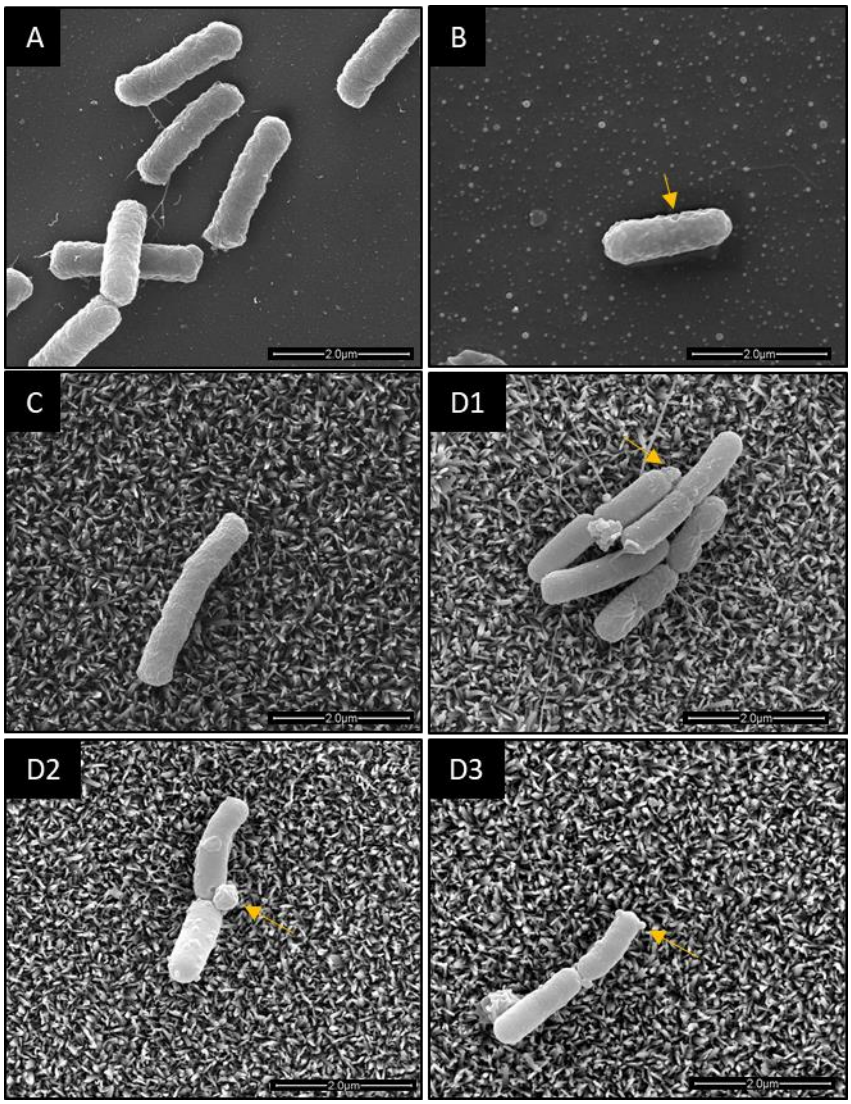

Figure 6.20- *Morphology of E. coli in contact with non-functionalised or ChoM-functionalised surfaces. Flat titanium and 2-hour nanospike surfaces were functionalised with 50 µM ChoM. E. coli suspension ($5x10^5$ CFU/ml; 40 µl) was pipetted onto the disks and incubated for 3 hours. The suspension was then removed, and the samples processed for SEM imaging. A) Non-functionalised flat titanium, B) 50 µM ChoM functionalised flat titanium, C) Non-functionalised 2-hour nanotopography, D1-4) 50 µM functionalised 2-hour nanotopography. Orange arrows indicate blebbing and membrane disruption*

6.6 Biocompatibility of AMP Functionalised Nanotopography

In this section a preliminary investigation of the biocompatibility and potential osteogenicity of the 2-hour nanotopography with or without ChoM-functionalisation was also carried out. The work was carried out by Laila Damiati under the supervision of Professor Matt Dalby at the University of Glasgow. The samples were supplied by the author.

6.6.1 Adhesion of hMSCs to Functionalised Surfaces

Focal adhesions are membrane-associated complexes consisting of several proteins such as talin, vinculin, focal adhesion kinase (FAK) and paxillin. The function of focal adhesions is to link the ECM on the outside of the cell to the actin cytoskeleton on the inside through transmembrane receptors. This facilitates cell survival and movement in response to external environmental cues such as nanotopography (Kim and Wirtz, 2013). When a cell adheres to a favourable surface it spreads, with focal adhesions growing at the periphery of the cell. The elongation of the cell indicates tension along the plane of direction (Seo *et al.*, 2013).

To determine if nanotopography and ChoM functionalisation affected hMSC adherence to the titanium surfaces, immunofluorescent staining was used to visualise focal adhesion formation. hMSCs were seeded onto flat titanium and 2-hour nanospike surfaces ± functionalisation with 100 µM ChoM and incubated for 3 days. Immunofluorescent staining of actin (red), tubulin in the cellular cytoskeleton (green) and the nucleus (blue) then enabled changes to be observed in cell shape and focal adhesion points in response to interaction with the surfaces (**Figure 6.21**).

Cell elongation and a well organised cytoskeleton were visualised on the flat titanium disks, in the presence or absence of ChoM (**Figure 6.21A, C**). Numerous focal points could be seen (in red and highlighted with white arrows), indicating attachment to the titanium surfaces. These adhesion points were observed along the leading edges of the cells, highlighting the movement of the cell in multiple trajectories across the surface. Lamellipodia and filopodia were also present, as the cells spread and sensed the surface.

On both 2-hour nanospike surfaces, smaller hMSCs were observed, with less evidence of cell spreading or motility across the surface (**Figure 6.21B, D)**. Focal adhesion points were not visualised, suggesting only weak interactions with the interface. The cytoskeleton was not well organised, with few tubulin filaments observed, and dense tubulin present around the nuclei for most of the cells. Taken together, these images suggest that after 3 days, the hMSCs preferred to attach and spread on flat titanium rather than the 2-hour nanotopography. The presence of the AMP coating had no discernible effect on these interactions.

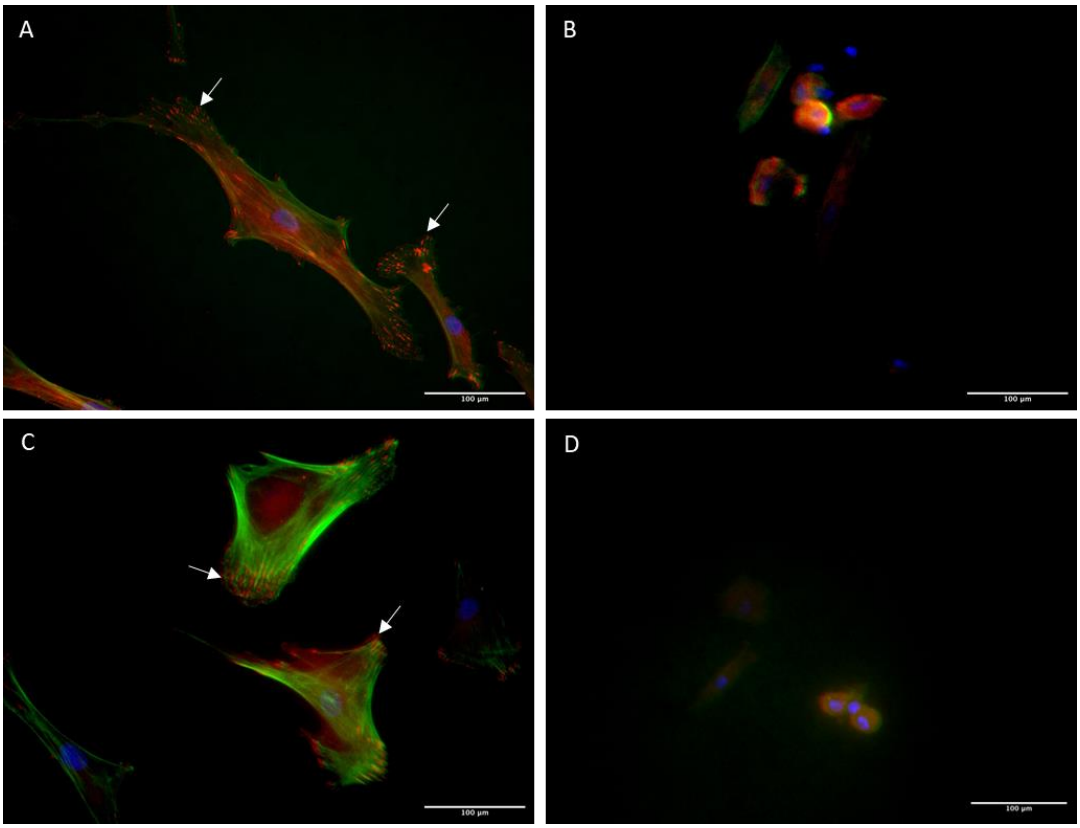

Figure 6.21- *Immunofluorescent staining of hMSCs after 3 days on different surfaces. hMSCs were seeded onto A) non-functionalised flat titanium, B) non-functionalised 2-hr nanospikes, C) ChoM-coated flat titanium, and D) ChoM-coated 2-hr nanospikes at 3000 cells/cm^2 and incubated for 3 days at 37°C in 5% CO_2. Cells were washed, fixed and then stained for vinculin (green) and actin (red). Nuclei were stained with DAPI (blue). White arrows indicate actin focal points.*

6.6.2 Viability of hMSCs

The previous data suggested that the flat titanium may be a more favourable interface for hMSC attachment after 3 days than the 2-hour nanospike surface, and this was ChoM independent. To investigate if cell viability also differed between the two surfaces or in the presence of ChoM, the alamarBlue assay was used. This assay quantitatively determines the viability of mammalian cells by measuring the innate reducing power of a cell. Living cells take up and reduce resazurin into resorufin, which fluoresces red. The experiment was performed over 28 days.

On day 3, hMSC viability was ~60% for uncoated flat titanium and the 2-hour nanotopography, and this was unaffected by AMP functionalisation (**Figure 6.22**). A similar trend was seen at days 7, 14 and 21, with cells on all surfaces exhibiting viability values of ~100%. At 28 days, the longest time point tested, the viability dropped slightly for all the surfaces to around 70%. Again, there was no statistical significance between the surfaces ± ChoM, indicating that the peptide did not cause any cytotoxicity. These results demonstrate that both the flat surface and the 2-hour nanotopography exhibit comparable biocompatibility, at least over a 28-day period. This was not affected by the ChoM peptide coating.

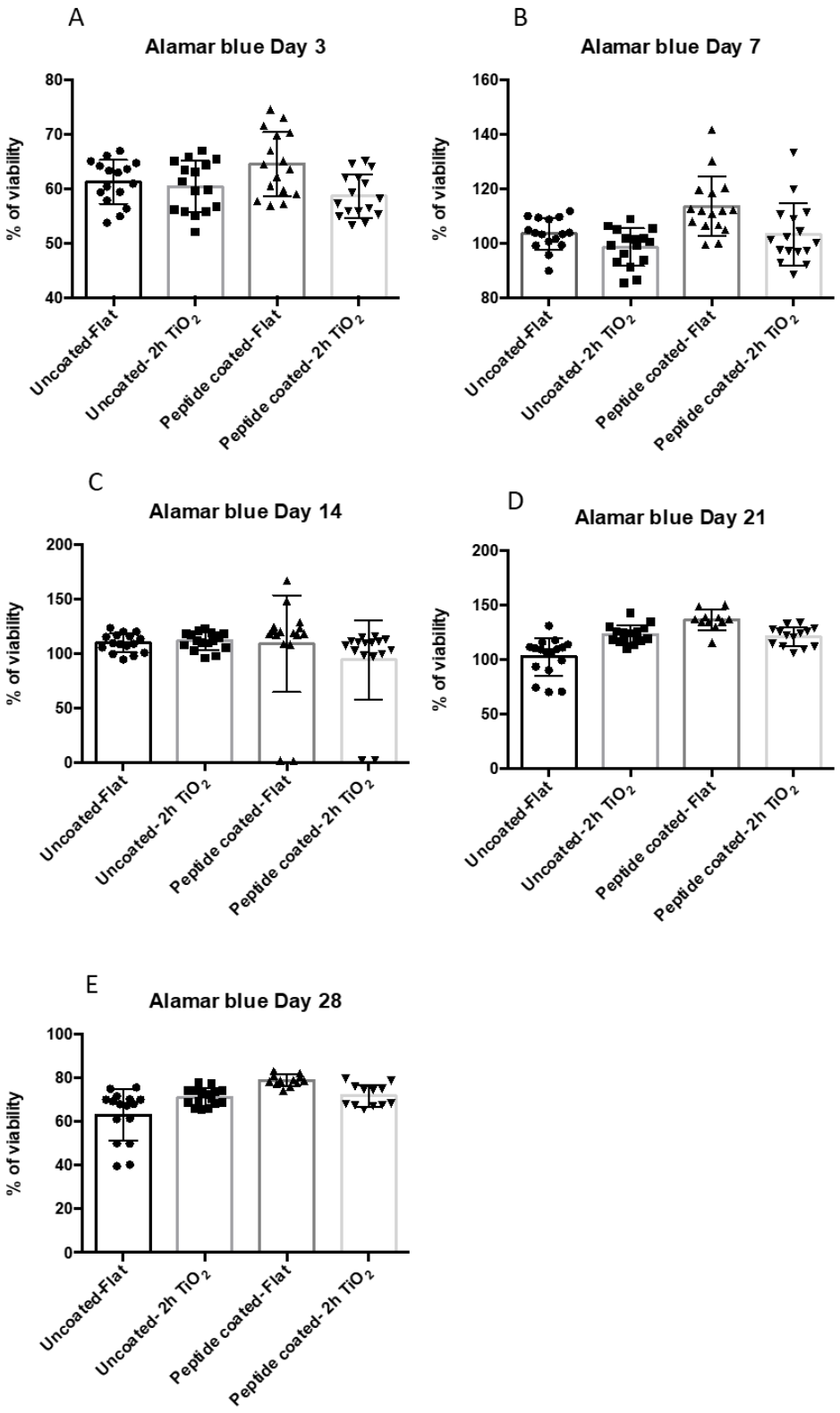

Figure 6.22- *hMSC viability following incubation on different surfaces over 28 days. hMSCs were seeded onto flat titanium and 2-hour nanotopography ± 100 µM ChoM and incubated at 37°C in 5% CO_2 for A) 3 days, B) 7 days, C) 14 days, D) 21 days, and E) 28 days. AlamarBlue solution was then added to each well, incubated for 6 hours at 37°C in 5% CO_2, and the absorbance measured at 570 nm and 600 nm. N=4 in quadruplicate.*

6.7 Cellular Morphology and Qualitative Osteogenic Analysis

Calcium and phosphate are the two main micronutrients involved in bone formation as they are the main constituents of hydroxyapatite (Bonjour, 2011). The presence of phosphate and calcium are indicative of osteoblastic differentiation and their deposition is carried out by osteoblasts during the osseointegration process; this may occur within the first 4 weeks of implantation (Khang *et al.*, 2006). Calcium and phosphate deposition were therefore used as markers to assess the effects of nanotopography and ChoM functionalisation on the osteogenic potential of the titanium surfaces, alongside observing general cellular morphology.

6.7.1 Giemsa Staining

Giemsa staining was used to visualise and assess the morphology and confluency of the hMSCs on each of the surfaces (flat and 2-hour nanospikes ± ChoM ± osteogenic medium) after 28 days' incubation. Osteogenic medium was used as a positive control to generate a highly beneficial environment for hMSC adhesion and proliferation on both flat titanium and 2-hour nanospikes disks.

After 28 days on the flat titanium (**Figure 6.23A, C, E),** the hMSCs were clearly visible, with the nuclei staining dark blue/purple and the cytoplasm a light blue. The cells had formed a dense layer of cells with a range of morphologies, and the majority demonstrated spreading and motility across the surface, with elongated and stretched membranes. The morphology was similar to hMSCs grown in osteogenic medium and did not alter in the presence of ChoM.

Visualisation of cells on the nanotopography with the light microscope was challenging due to the underlying colour of the disks (**Figure 6.24**), which was not seen on the flat surface. There was also high intra-disk and inter-disk variability in colour and patterning. Nonetheless, a dense coverage of hMSCs was seen across the surface, with cell stretching and motility evident in the majority of cells (**Figure 6.23B, D, F)**. There was no observable difference to the morphology seen in the presence of osteogenic medium, and cells were comparable when grown on disks with a peptide coating.

Visualising the Giemsa staining under fluorescence allowed the detection of bone-like nodules, which appear white and are indicative of differentiation and matrix mineralization. All six surfaces (flat and 2-hour nanospikes ± ChoM ± osteogenic medium) displayed a number of white dots, which may be evidence of bone-like nodules. However, the dots may also represent contaminants on the disk that fluoresce dimly.

Together, these results suggest that the hMSCs could adhere and spread across the nanotopography, as well as on the flat surface, regardless of the presence of ChoM, but that in all instances, no significant osteogenic differentiation occurred during the 28-day time period.

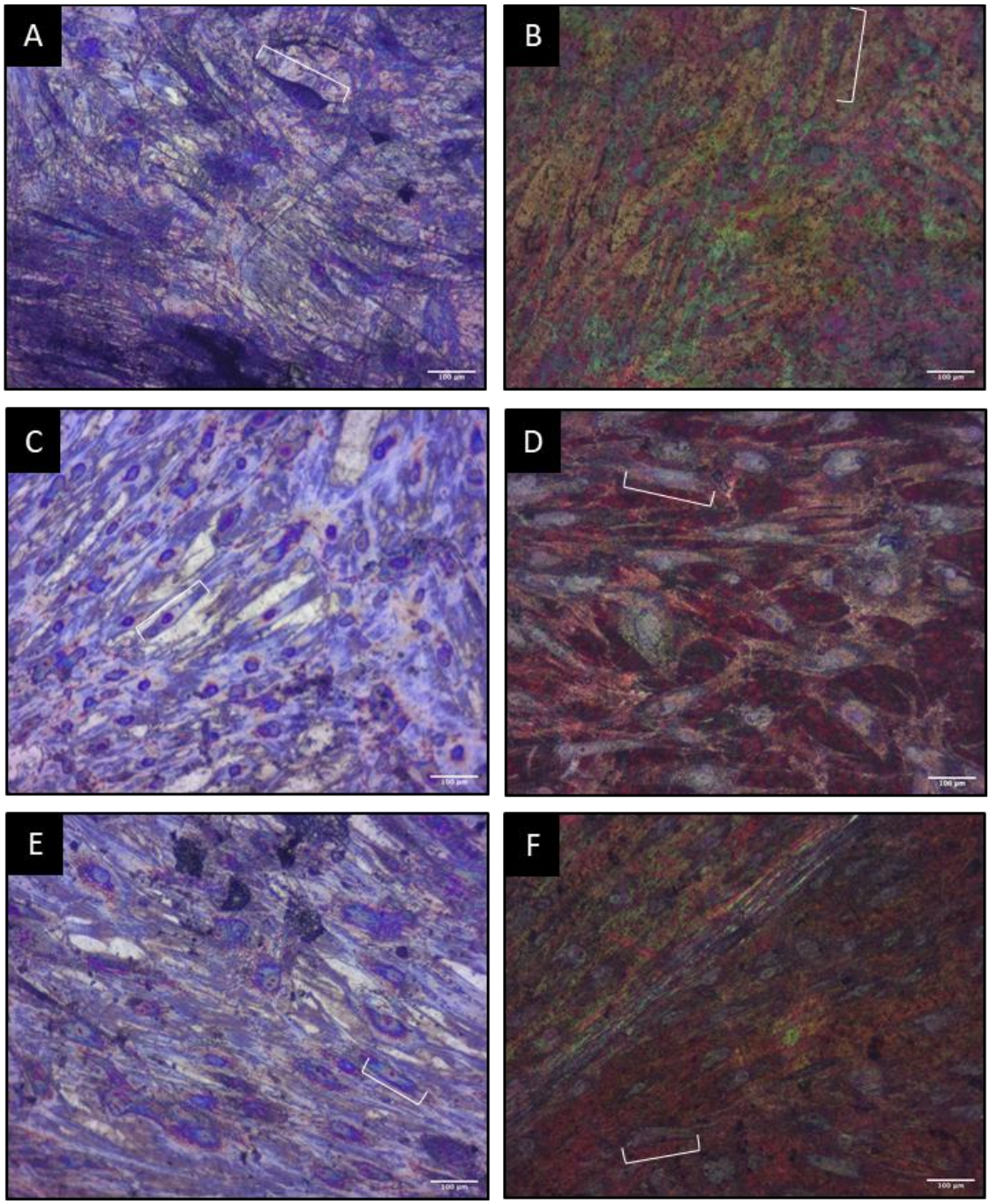

Figure 6.23- *Brightfield imaging of Giemsa-stained hMSCs on different surfaces. hMSCs were seeded onto A) osteogenic medium flat, B) osteogenic medium 2hr-NS, C) non-functionalised flat titanium, D) non-functionalised 2-hr NS, E) ChoM-functionalised flat titanium, and F) ChoM-functionalised 2-hr NS disks. The disks were seeded with 3000 cells/cm^2 and incubated for 28 days at 37°C in 5% CO_2. Cells were washed, fixed and then stained with Giemsa stain. White brackets highlight individual cells.*

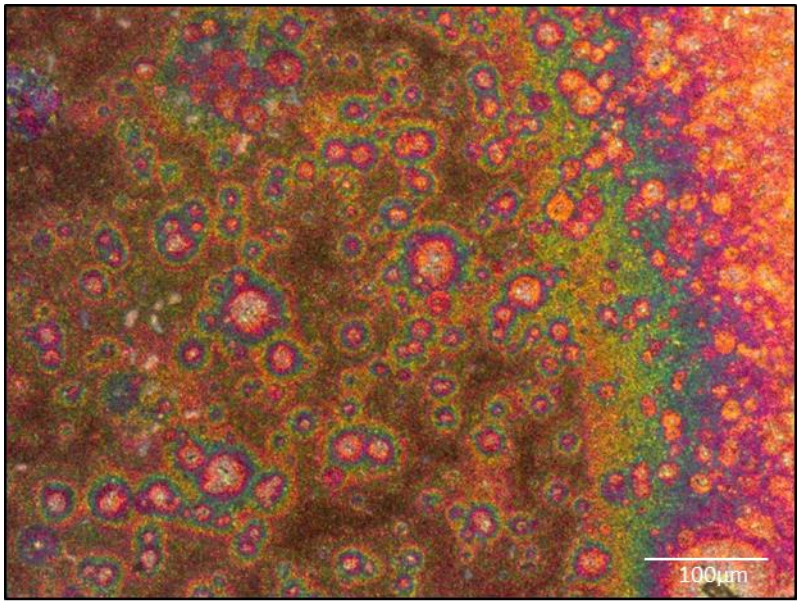

Figure 6.24- *Representative light microscope image of a 2-hour nanospike surface.*

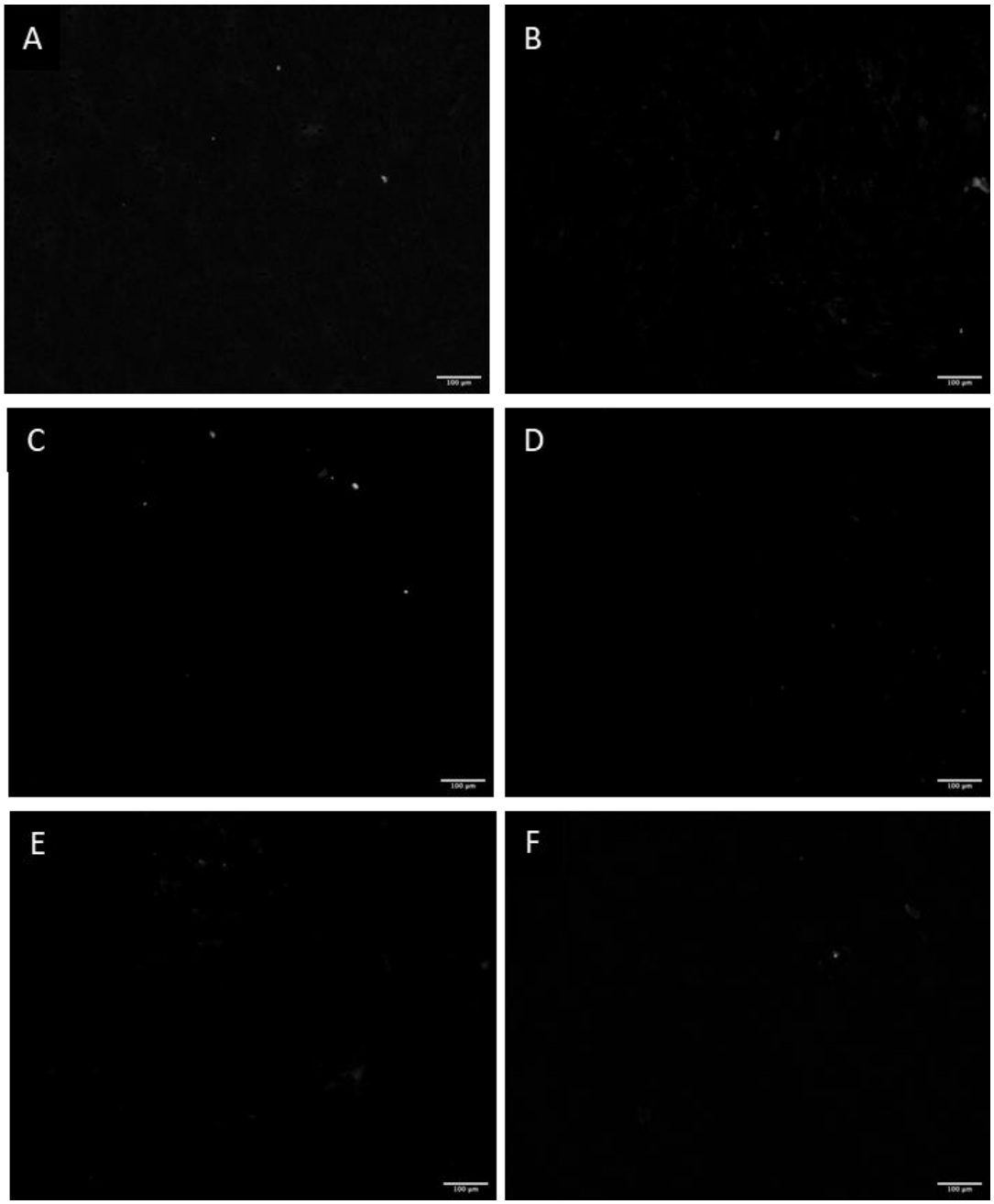

Figure 6.25- *Bone nodule visualisation of Giemsa-stained hMSCs on different surfaces. hMSCs were seeded onto A) osteogenic medium flat, B) osteogenic medium 2hr-NS, C) non-functionalised flat titanium, D) non-functionalised 2-hr NS, E) ChoM-functionalised flat titanium, and F) ChoM-functionalised 2-hr NS disks. The disks were seeded with 3000 cells/cm^2 and incubated for 28 days at 37°C in 5% CO_2. Cells were washed, fixed, stained with Giemsa stain and then visualised by fluorescence microscopy with excitation/emission of 495/519 nm.*

6.7.2 Alizarin Red S Staining

The differentiation of hMSCs into osteoblasts can be qualitatively visualised using the Alizarin Red S stain, which indicates the presence of calcium deposition. Intracellular calcium deposits usually stain bright orange-red. A dense coverage of hMSCs with elongated morphology was seen on all the surfaces (flat and 2-hour nanospikes ± ChoM ± osteogenic medium), as for the Giemsa stain (**Figure 6.26**). No red-stained deposits were observed for the osteogenic medium controls or the non-functionalised or functionalised flat titanium or 2-hour nanospikes. These images provide further evidence that, after 28 days, the surfaces were biocompatible, but there was little evidence of early osteoblastic differentiation.

6.7.3 Von Kossa Staining

Von Kossa staining was used to visualise phosphate deposition within cells as a qualitative indication of osteogenic differentiation. During the staining process, phosphate reacts with silver ions, which photochemically degrade from silver phosphate to silver under light illumination. The silver can then be observed as black dots within the cells. Once again, a dense coverage of stretched hMSCs was seen on all the surfaces (flat and 2-hour nanospikes ± ChoM ± osteogenic medium) (**Figure 6.27**). There were a few black areas on the surfaces (highlighted with white arrows), apart from on the non-functionalised 2-hour nanotopography. It is unclear whether the black areas were due to phosphate deposition, as similar black regions were seen for the Giemsa staining (**Figure 6.23)** and alizarin red S staining (**Figure 6.26).**

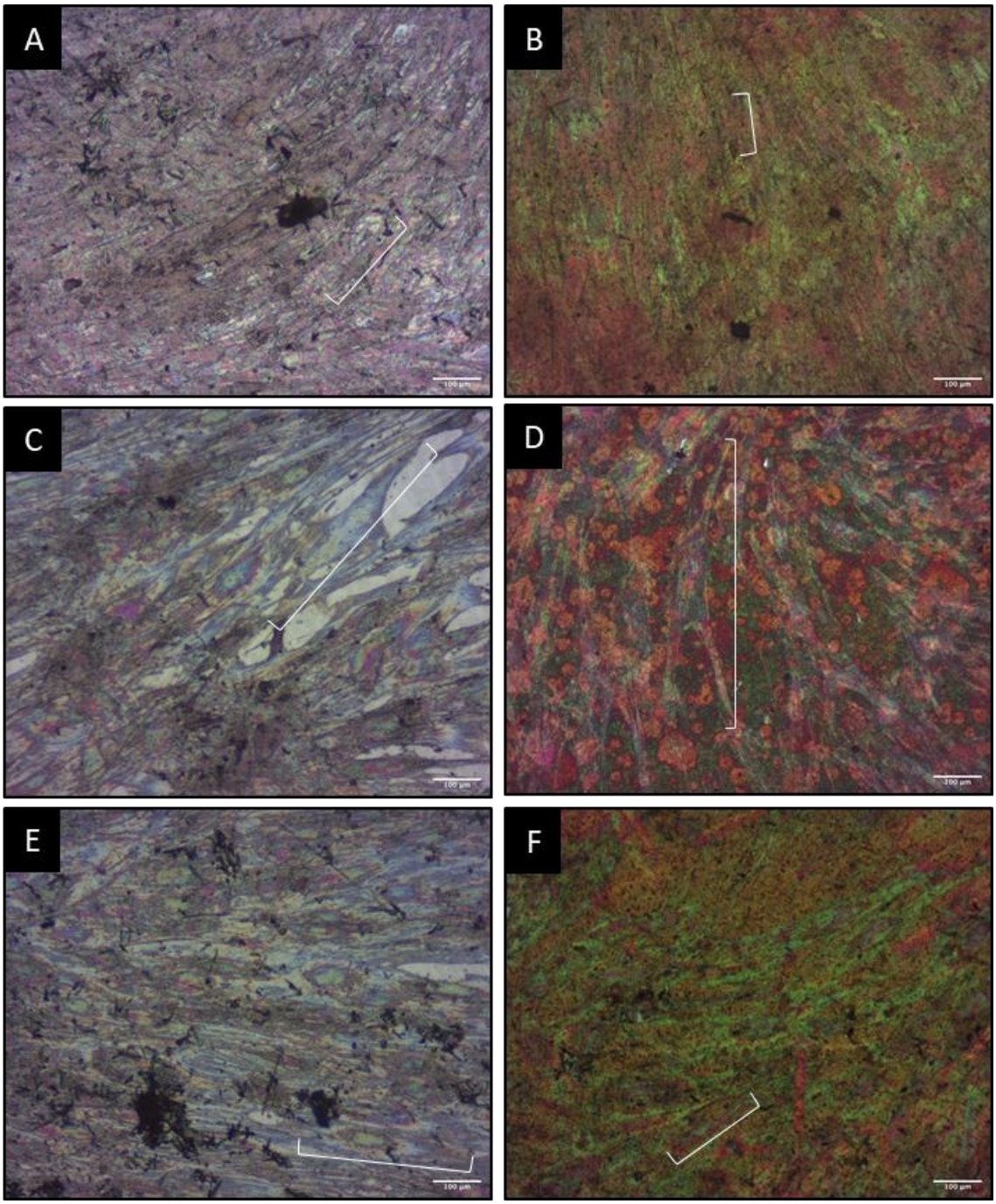

Figure 6.26- *Visualisation of calcium deposition in hMSCs on different surfaces. hMSCs were seeded onto A) osteogenic medium flat, B) osteogenic medium 2hr-NS, C) non-functionalised flat titanium, D) non-functionalised 2-hr NS, E) ChoM-functionalised flat titanium, and F) ChoM-functionalised 2-hr NS disks. The disks were seeded with 3000 cells/cm^2 and incubated for 28 days at 37°C in 5% CO_2. Cells were washed, fixed, stained with alizarin red S stain and then visualised using a phase-contrast microscope. White brackets indicate individual cells.*

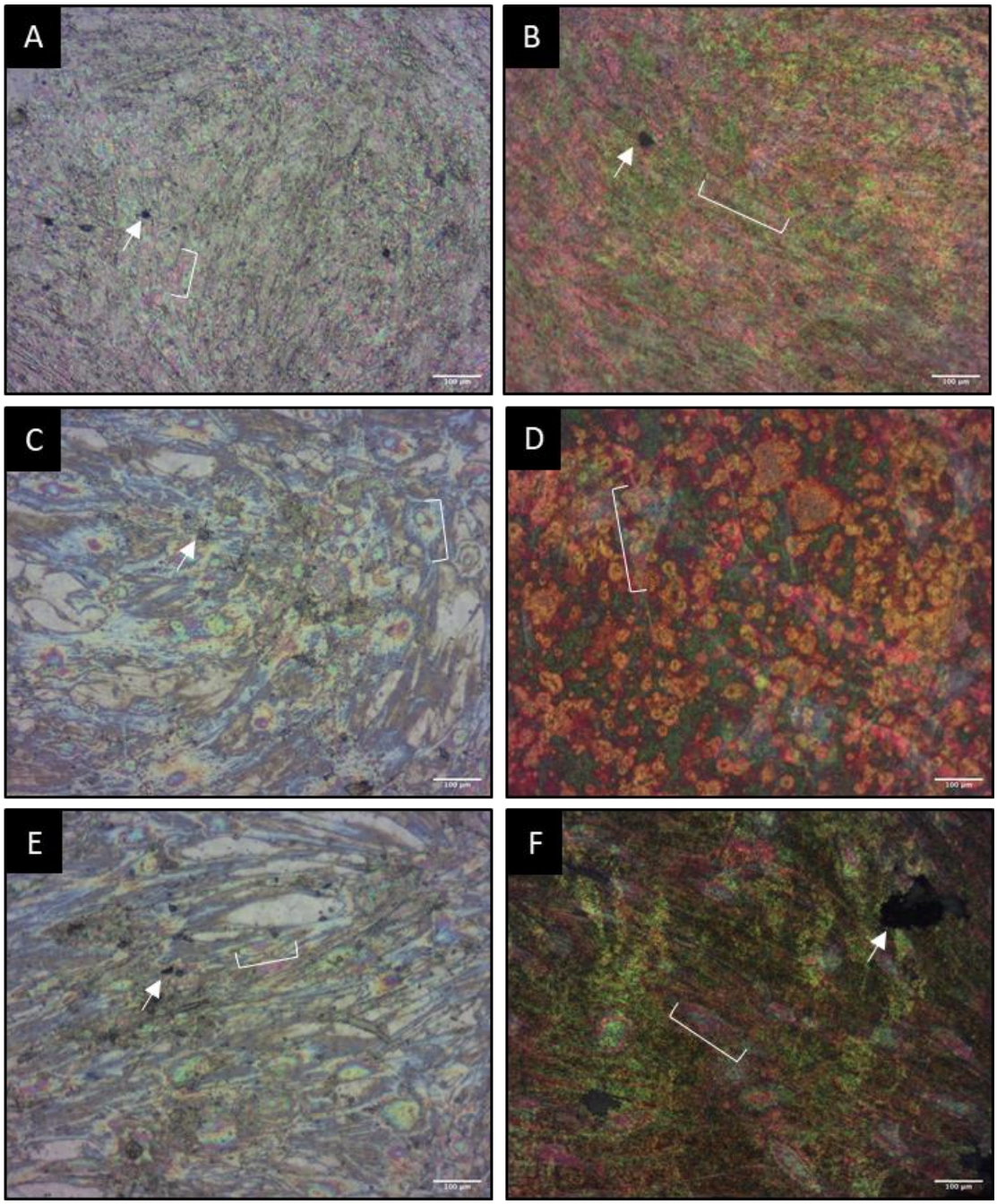

Figure 6.27- *Visualisation of phosphate deposition in Von Kossa-stained hMSCs on different surfaces. hMSCs were seeded onto A) osteogenic medium flat, B) osteogenic medium 2hr-NS, C) non-functionalised flat titanium, D) non-functionalised 2-hr NS, E) ChoM-functionalised flat titanium, and F) ChoM-functionalised 2-hr NS disks. The disks were seeded with 3000 cells/cm^2 and incubated for 28 days at 37°C in 5% CO_2. Cells were washed, fixed, incubated with 5% silver nitrate and exposed to UV light for 30 minutes. Cells were then washed, incubated with 5% sodium thiosulfate for 10 minutes, dehydrated in 70% ethanol and visualised by light microscopy. White brackets indicate individual cells. White arrows indicate potential phosphate deposits.*

6.8 Osteogenic Gene Expression

Osteopontin (OPN) is a protein released by both osteoclasts and osteoblasts and is important in the modulation of osteoclast function, adherence of osseous cells, and modulation of matrix mineralisation (Icer and Gezmen-Karadag, 2018; Tsimbouri, 2015; Tsimbouri *et al.*, 2016). Osteocalcin (OCN) is a protein secreted exclusively by osteoblasts with the primary role to minimise excess bone mineralisation (Zoch, Clemens and Riddle, 2016). Osteonectin (ON) is a collagen binding protein with a role in facilitating the formation of a mineralised matrix involving procollagen processing and collagen cross-linking (Rosset and Bradshaw, 2016). Expression of genes for these proteins is indicative of osteoblastic differentiation.

This was therefore used to further investigate if flat titanium and 2-hour nanospikes were osteogenic, and any potential impact of ChoM-functionalisation, by qPCR. The housekeeping gene, glyceraldehyde 3-phosphate dehydrogenase (GAPDH), was used for normalisation. There were no significant differences in gene expression between the flat surface and 2-hour nanotopography or osteogenic medium controls (**Figure 6.28**). Likewise, functionalisation had no effect on gene expression. As such, there was little indication, from these data, of osteoblast formation for any of the surfaces.

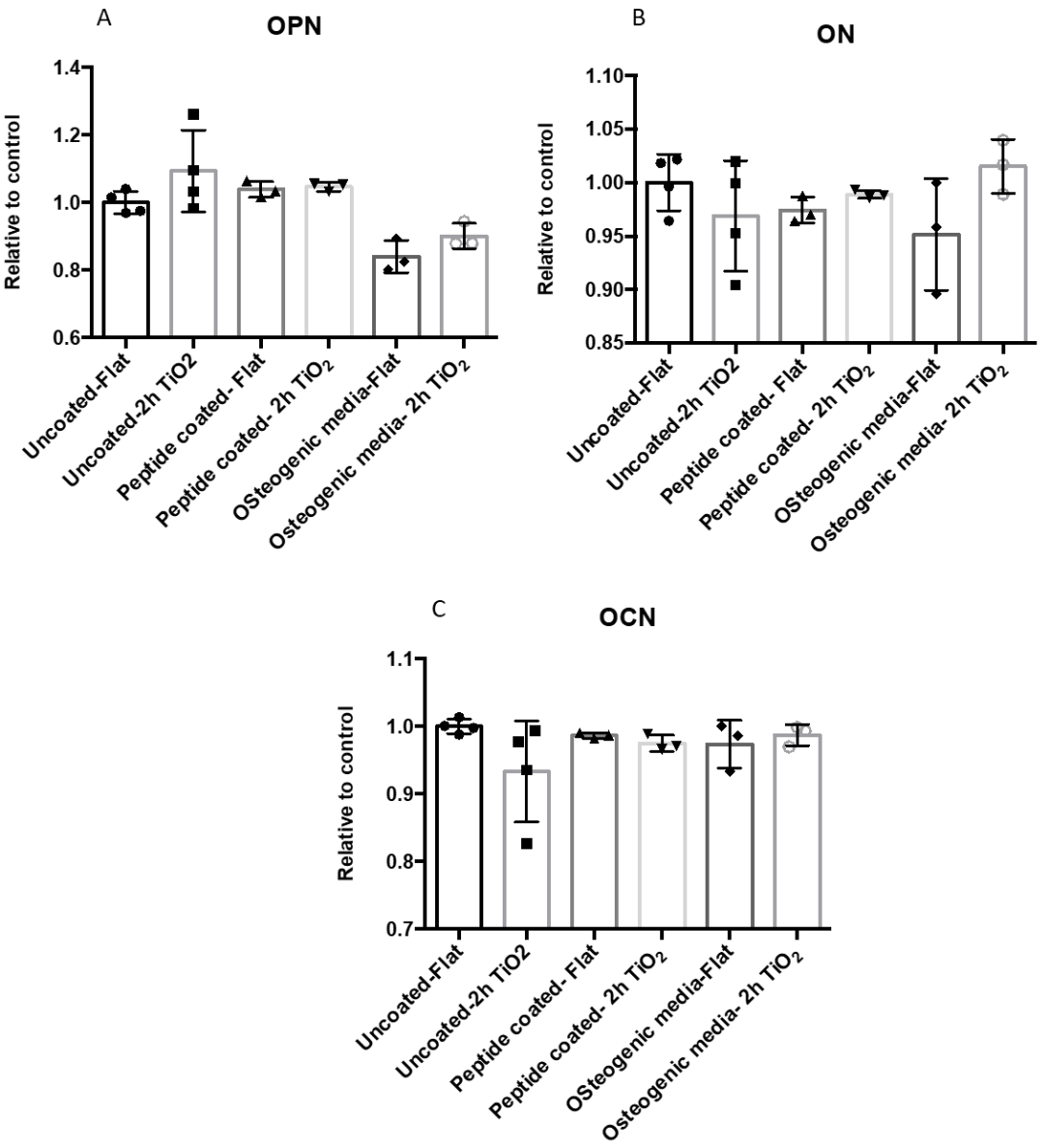

Figure 6.28- *qPCR analysis of the expression of osteogenic genes. hMSCs were seeded onto disks at 3000 cells/cm^2 and incubated for 28 days at 37°C in 5% CO_2. Total RNA was then extracted, and the concentrations normalised for cDNA synthesis. Expression of genes A) osteopontin (OPN), B) osteonectin (ON) and C) osteocalcin (OCN) was normalised against housekeeping gene GAPDH. N=4 in duplicate.*

6.9 Discussion

The main aim of these studies was to determine if the antimicrobial potential of the nanotopography could be enhanced by addition of a coating comprising antimicrobial peptide ChoM, that is if a synergistic effect between nanotopography and ChoM could be seen. Although the bactericidal effects of the ChoM peptide have been previously studied, this project investigated how effectively the peptide may be integrated with different surface nanotopographies, its subsequent release and interaction with bacteria. Pilot work was also performed to assess if the functionalisation impacted the interactions of the titanium surfaces with hMSCs.

6.9.1 Biofunctionalisation of Titanium with ChoM by Physical Adsorption

In this project, physical adsorption was used to functionalise the titanium surfaces with the antimicrobial peptide ChoM. Functionalising the titanium surface involved pipetting a solution of solubilised peptide directly onto the titanium disk and subsequently allowing it to dry under sterile conditions in a flow hood. Adsorption and desorption processes are dependent on a range of factors such as the surface chemistry, solution chemistry, surface area, surface topography, capillary force surface hydrophobicity/hydrophilicity and surface charge (Sevilla, Gil and Aparicio, 2017; Richert *et al.*, 2010).

As there are differences in the properties between the two chosen titanium surfaces: flat mirror polished titanium and 2-hour nanotopography, it might be anticipated that these could influence the functionalisation and interaction of ChoM with the surface, and consequently how, and how rapidly, the peptide was released from the interface into the local environment.

6.9.2 Factors Influencing Adsorption of Peptide

Wettability is the interaction between a fluid and a solid interface dependent on the intermolecular forces between the two phases. Flat titanium was found to be slightly hydrophilic and the 2-hour nanotopography to be super-hydrophilic, with a water contact angle below 10° (Webb, Crawford and Ivanova, 2014).

The super-hydrophilic property of the nanotopography is likely to have been due to an increase in surface roughness and surface area and a change in the surface chemistry, leading to high surface energy. The Wenzel model is proposed to describe the relationship between the apparent

contact angle and the surface roughness (Hazell *et al.*, 2018; Zhao *et al.*, 2015). This model assumes the liquid completely fills the spaces of the rough topography and can be expressed by **Equation 6.1**. The surface roughness factor of the 2-hour nanospike surface, using **Equation 6.2**, was calculated.

The average of the 2-hour nanospike height measurements from SEM and AFM were used, along with the spacing calculated from the density and average nanospike diameter, both quantified by SEM. The calculated roughness factor was 2.8. A surface roughness factor >1 results in a more hydrophilic surface if the surface was hydrophilic originally. The calculated effective water contact angle according to the Wenzel model, using the flat titanium contact angle of 80° and **Equation 6.1** was ~60° (Zhao *et al.*, 2015; Hazell *et al.*, 2018a). This modelled value is still considerably greater than that shown in **Figure 6.15B**, which indicated a contact angle of <10°.

Further hydrophilicity of the nanospike surface is likely to have been conferred by the polar components such as hydroxides present on the surface (Belyaeva *et al.*, 2018). The hydroxide bonds, shown by XPS in **Section 4.4.4**, were present on the surface as a result of the alkaline hydrothermal process. Pre-surface treatments such as ethanol sterilisation and Tris-HCl washing are also likely to have increased surface energy (Drelich and Chibowski, 2010; Bhushan and Her, 2010). Roughness promotes the spread of the liquid, while the large surface area of the nanotopography further enhances the surface wetting (Seo, Kim and Kim, 2015; Roach, Shirtcliffe and Newton, 2008; Zhang, Wang and Zhang, 2013).

$$\mathrm{Cos}\theta_w = r\cos\theta_0$$

Where:

r-roughness factor

θ_0 = contact angle of the flat surface of the same material

θ_w = effective contact angle on a rough surface

Equation 6.1- *Wenzel Model equation* (Zhou *et al.*, 2015; Hazell *et al.*, 2018b)

$$\text{Roughness Factor (r)} = \frac{(R+L)^2 + 4RH}{(R+L)^2}$$

Where:

R=diameter of nanospikes

L=spacing between nanospikes

H=height of nanospikes

Equation 6.2- *Roughness Factor Equation* (Hazell *et al.*, 2018b)

The differences in wettability between the flat titanium and nanospike surfaces led to differences in the interface functionalisation of the peptide. A 40 µl aliquot of ChoM stock solution was used, as this was the maximum volume of liquid that could be pipetted onto the nanotopography disks without the risk of spillage. On the flat titanium surface a meniscus formed due to the poor wettability, resulting in a small, peptide dense area of the titanium disk being functionalised, while the rest of the disk remained non-functionalised, as illustrated schematically in **Figure 6.29**. This would have resulted in a locally thicker, more dense coating of peptide on the surface, and thus less ChoM specifically interacting with the titanium interface, as confirmed by SEM.

Conversely, with the nanotopography, the surface was highly wetting, and the peptide spread across the whole surface (**Figure 6.29**). As a consequence, the peptide coating is likely to have been thinner, with lower and more variable densities of peptide across the disk, exacerbated by the uncontrolled drying of the peptide solution. Again, this was verified by SEM. A thinner coating and lower peptide density, together with the 3D nature of the nanospikes, which increased the surface area by approximately 150%, is likely to have led to more direct interactions between ChoM and the nanotopography surface than the flat surface, where it was layered. In this project, the specific peptide concentration on the surface was not measured, but could be carried out by XPS via the quantification of amine groups (Sun *et al.*, 2019; Karam *et al.*, 2013).

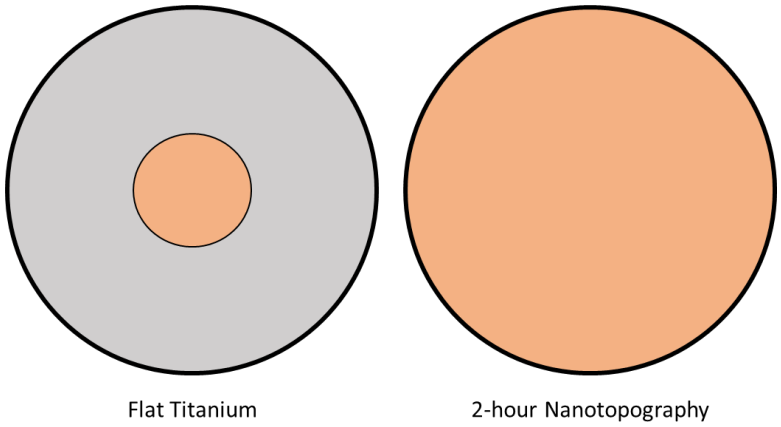

Figure 6.29- *Schematic highlighting differences of potential peptide coverage on flat titanium and 2-hour nanotopography disks due to differences in wettability. Grey indicates base titanium disk. Orange indicates peptide covered area.*

6.9.3 Release Mechanics of Peptide from Functionalised Surfaces

The physical adsorption method permits the free release of peptide from the surface into the local environment or solution, enabling the physically-free peptide to exert effective short-term antimicrobial activity. The results presented here showed that ChoM was released more slowly from the nanotopography than from the flat titanium surfaces, so that the final peptide concentration in the surrounding solution was less from the nanotopography than from the flat surface. Virtually all of the available peptide was found to be released from the flat surfaces within the initial 10-30 minutes, whereas residual ChoM coating could be visualised on the nanotopography even after 3 hours. However, even with an extended period of up to 12 hours, levels of ChoM released from the nanotopography still did not reach those released from the flat surface in the initial 30 minutes, as shown by their failure to achieve the MICs for *E. coli* or *S. aureus*.

6.9.3.1 Factors that Affect Peptide Release

Meniscus Environment

These studies provided evidence that the presence of a meniscus environment may enhance the release of ChoM. As the peptide is solubilised in the broth, a diffusion gradient will be formed, which will be affected by the volume of liquid into which the peptide can diffuse into. For the flat titanium, on which a meniscus of liquid is formed, the ChoM should diffuse easily through it, leading to quicker release and greater initial antimicrobial activity. By contrast, liquid pipetted onto the super-hydrophilic functionalised 2-hour nanotopography disk predictably spread.

This will have resulted in a small volume above the nanospikes into which ChoM could solubilise, resulting in reduced peptide diffusion through the liquid environment (Chan, Li and Li, 2015). Nonetheless, the disk immersion studies (**Section 6.4.4**) indicated that differences in the meniscus environment were not exclusively responsible for the differing ChoM release kinetics between the flat and nanospike surfaces and rather multiple factors are potentially involved.

Hydrophilic and Super-hydrophilic surfaces

Surface hydrophobicity and hydrophilicity are known to affect the adsorption of proteins to an interface. AMPs are more likely to be adsorbed onto hydrophilic surfaces than hydrophobic surfaces due to the higher surface energy (Kubiak, Adamczyk and Cieśla, 2016; Fabre *et al.*, 2018). The nanotopography surface has been shown to be more hydrophilic than the flat titanium surface. If there is a stronger attraction between ChoM and the nanotopography than flat titanium,

the peptide may be released more slowly into the environment. The peptide may also lose some of its secondary structure during adsorption onto the surface and specific amino acids of the peptide chain may interact with the surface (Roccatano, Sarukhanyan and Zangi, 2017).

Capillary force

Due to the reported differences in wettability between the flat and nanospikes surfaces, there are likely to have been variations in how a liquid interacts with the surface and potentially how ChoM was released from the surface due to interfacial tension and capillarity imposed by the nanospikes. As the nanotopography had a relatively high surface energy, it was able to overcome the surface tension, causing the liquid to spread and resulting in a low contact angle. The adhesion of water to the nanotopography was stronger than the cohesive forces between the water, causing a capillary action within the nanotopography. This would have hindered the release of peptide into the surrounding liquid environment (Kosgodagan Acharige, Laurent and Steinberger, 2017).

Surface Charge

The zeta potential of titanium dioxide at physiological pH of 7.2 is usually negative, while the charge of ChoM is positive (Liao, Wu and Liao, 2009; Rapuano and MacDonald, 2011; Pfeil *et al.*, 2018). Due to the opposite charges it is likely there is an electrostatic attraction between the peptide and the titanium surface. This may have led to an enhanced stability of the peptide coating, which may have affected the subsequent release of ChoM from the surface (Sevilla, Gil and Aparicio, 2017; Liao, Wu and Liao, 2009). For this project, the zeta potential of the flat titanium surface and the 2-hour nanotopography surface was not measured, so any differences between the two surfaces and the possible variances on electrostatic interaction was not assessed.

To encourage the release of ChoM from the nanotopography and overcome the potential capillary forces and surface charge that may hinder peptide release, low level vibrations (1 kHz frequency) in the form of the nanokick ultrasound device were used**.** Small differences between 'nanokicked' samples and controls were observed, which may have been due to the low-level frequency used (Childs *et al.*, 2016). However, vigorous shaking at 100 rpm also did not significantly improve the release of ChoM from the nanotopography after 3 hours. Further work is therefore required to investigate the phasing of peptide release from the nanotopography and, if necessary, to devise alternative strategies to encourage enhanced release.

Surface Area

The greater surface area with the more developed nanotopography resulted in lower peptide density and more interactions such as electrostatic forces between the nanospikes and ChoM. The adsorption of the peptide onto the spikes during functionalisation, along with the increased electrostatic interactions, is likely to have impeded early/premature peptide release (Sevilla, Gil and Aparicio, 2017; Hollmann *et al.*, 2018).

Shorter Nanotopography

The physical nature of the nanotopography was hypothesised to inhibit the early release of ChoM and in support of this, peptide release did appear to occur more readily from the shorter nanospikes generated after one hour than the longer 2-hour nanospikes. The shorter nanotopography would have a lower surface area and less peptide interacting directly with the spikes, so ChoM diffusion into the liquid environment would be expected to occur more readily. Surface charge and capillarity factors would also likely be less effective for the 1-hour than 2-hour nanotopography.

In consideration of all of these factors, **Table 5.2** compares some potential differences between the flat titanium and 2-hour nanotopography surfaces that could have influenced the release of ChoM.

FLAT TITANIUM	2-HOUR NANOTOPOGRAPHY
Hydrophilic	Super-hydrophilic
Meniscus environment during drying	Non-meniscus environment during drying
Low peptide surface coverage	High peptide surface coverage
High peptide density	Low peptide density
No capillary force	Capillary force
No 3D structure	3D structure
Low surface area	High surface area

Table 6.2- *Differences between the flat titanium and 2-hour nanotopography properties that potentially affect ChoM release.*

6.9.4 Antimicrobial Activity of ChoM

ChoM was initially made and characterised by Pfeil *et al.* (2018) at NPL, and was chosen for this project due to its antimicrobial activity against a wide range of bacterial species, including Gram-positive bacteria such as *S. aureus* and Gram-negative bacteria such as *E. coli*. The MIC for ChoM against *E. coli* and *S. aureus* in this project was found to be 25 µM. This was higher than that reported by Pfeil *et al.* (2018), who recorded a MIC below 3 µM for both bacterial species. Both assessments were carried out by the two-fold broth dilution method, which is a standard method to measure the bacteriostatic nature of the peptide and widely used due to its simplicity and high reproducibility (Andrews, 2001). Differences in the MIC calculation could therefore be due to variations in batch preparation of ChoM, such as peptide purity and quality, quality of peptide stock after freezing, or accurate measurement of peptide stock and serial dilutions (Andrews, 2001). Nonetheless, the MIC for ChoM of 25 µM was taken forward as the MIC threshold for all experiments performed here, and 50 µM and 100 µM concentrations were used as two-fold and four-fold excess concentrations.

Pfeil *et al.* (2018) considered that ChoM was likely to exert its antimicrobial activity by intercalating underneath the phospholipid head groups and lysing the bacteria through exfoliating and thinning of the lipid bilayer membrane, rather than through pore formation. This mechanism has the potential to act quickly and causes bacterial death potentially within 10 minutes of incubation. Other studies have highlighted the speed of AMP activity (Yasir, Dutta and Willcox, 2019; Dias *et al.*, 2017). Yasir *et al.* (2019) reported membrane disruption in 30 seconds and permeabilization within 5 minutes. Dias *et al.* (2017) reported a more gradual bactericidal effect between 30-180 minutes, dependant on the bacterial species. In this project, the antibacterial effects of ChoM were demonstrated within 1 hour.

The result of ChoM interaction with *E. coli* was visualised by SEM after 3 hours, showing membrane blebbing and cytoplasmic leakage, potentially indicating cell lysis. Blebbing has previously been reported after AMP interaction and can occur at sub-lethal concentrations (Alves *et al.*, 2010; Chileveru *et al.*, 2015; Toyofuku, Nomura and Eberl, 2019). However, membrane blebbing or the production of membrane vesicles can be a natural occurrence and not solely indicative of lytic membrane disruption. Bacteria release membrane vesicles that transport cargo molecules, which have diverse roles in DNA transfer, bacterial communication, transport of virulence factors and antibiotic and eukaryotic host defence factors (Toyofuku, Nomura and Eberl, 2019). Blebbing can also result from the intercalation of hydrophobic molecules inducing cell envelope stress, SOS responses and hampering cell wall biosynthesis (Yin *et al.*, 2012; Toyofuku, Nomura and Eberl, 2019).

6.9.4.1 Importance of ChoM Concentration

For an antimicrobial-releasing biomaterial to be effective, it is important that the MIC threshold is reached as quickly as possible to impair microbial growth. For the titanium surfaces tested here, it was shown that the higher the concentration of ChoM used for functionalisation, the more rapidly the peptide was released, and the more likely that the MIC threshold would be achieved. An excess of peptide above the MIC was also needed for functionalisation, since 100% release of the peptide was not achieved. However, due to the delayed release of ChoM from the nanotopography, only sub-MIC levels of peptide were effective in the first few hours. The results highlighted that below the MIC, growth of the bacteria continued but often at a lower rate to that of the control surfaces.

There are several potential effects of a sub-MIC antimicrobial concentration on bacteria, which may have both positive and negative implications. Sub-MIC concentrations can cause significant changes in bacterial morphology, inhibit enzyme or toxin production, alter growth kinetics, hinder adhesive properties and the transcription of genes, induce mutagenesis and SOS responses (Vasilchenko *et al.*, 2017; Limoli *et al.*, 2014; Reeks *et al.*, 2005). Sub-MIC levels may also provoke changes in membrane architecture, leading to extracellular vesicle formation and the release of virulence factors (Vasilchenko and Rogozhin, 2019).

Beneficial effects have been shown with sub-MIC levels with the potential inhibition of biofilm formation by affecting metabolic regulation, cell surface proteins and virulence proteins (Wang *et al.*, 2016b; Braga, Sasso and Sala, 2000). Conversely other studies have reported a promotion in biofilm formation (Sato *et al.*, 2018). Adverse outcomes from exposing bacteria to sub-MIC levels is the development of resistance due to selection pressures and the promotion of protective mutations (Wistrand-Yuen *et al.*, 2018).

The flat titanium surface functionalised with 50 µM of ChoM was able to suppress *E. coli* growth for at least 9 hours. However, this was in a closed system. Since most ChoM release occurred from flat titanium within 30 minutes, the peptide is susceptible to being flushed away, as might occur during surgery and *in vivo*. In this case even a significant peptide release might fail to reach the MIC.

The peptide adheres longer onto the nanotopography and is released more slowly and therefore potentially remains antimicrobial for an extended period. In this case, if optimised, the longer retention and delayed release of ChoM seen for the nanospike surfaces could prove beneficial extending the duration of antibacterial activity. This would be especially relevant for titanium surgical implants. Further studies should therefore investigate optimisation of the rate of peptide release against possible infections by dynamic modelling of *in vivo* conditions. The release will also be connected to how effectively the peptide is tethered or absorbed onto the nanotopography.

Many of the experiments that investigated peptide release were limited to a 3-hour period due to the potential problems with dehydration for extended durations. The results indicated that initially peptide release into solution from the flat titanium discs was rapid compared to the nanospikes. However, the slower release over long periods of several days has not been sufficiently evaluated.

6.9.5 Biocompatibility and Osteogenic Potential of AMP Functionalised Nanotopography

Following implant surgery, encouraging the attachment of osteoprogenitor cells, ensuring favourable interfacial growth conditions and directing differentiation towards the osteogenic lineage leads to stable tissue fixation between the host-bone and implant surface. This is critical for long-term success of an orthopaedic or dental implant (Dobbenga, Fratila-Apachitei and Zadpoor, 2016). Stem cell behaviour can be modulated by the mechanical and biochemical cues from the surrounding environment and ECM (Stanton, Tong and Yang, 2019; Rutkovskiy, Stensløkken and Vaage, 2016). It was therefore important to consider in this project if ChoM functionalisation affected the interactions of the titanium surfaces with hMSCs.

6.9.5.1 Biocompatibility of the Surface

Data from the focal adhesion and alamarBlue assays provided evidence that both the flat titanium and 2-hour nanotopography surfaces were biocompatible. This correlates with previous work (Diu *et al.*, 2014; Tsimbouri *et al.*, 2016; Nadeem *et al.*, 2013; Karazisis *et al.*, 2016) and the capacity for titanium to form a surface oxide layer. There was some suggestion from the focal adhesion data that the flat titanium surface may initially be more favourable for the attachment of hMSCs than the 2-hour nanospike surface, given differences in cytoskeleton organisation, number of focal adhesions and the prevalence of lamellipodia and filopodia. That hMSCs may initially struggle to have a favourable interaction with the nanotopography supports similar observations reported in previous studies (Diu *et al.*, 2014; Tsimbouri *et al.*, 2016; Loye *et al.*, 2018), and may be related to the diameter of the nanospikes.

The nanospikes in this project were ~40-45 nm in diameter. Goreham *et al.* (2013) reported that spikes of 16 nm in diameter, compared to 38 nm and 68 nm, encouraged adhesion of MG63 and 3T3 cells. Sjöström *et al.* (2009) also found more adhesion and bone matrix formation on titanium nanotopographies with smaller diameters of 28 nm compared to 41 nm and 56 nm. Nonetheless, as shown here and in previous studies (Diu *et al.*, 2014; Tsimbouri *et al.*, 2016; Stanton, Tong and Yang, 2019; Sjöström *et al.*, 2009), greater levels of cellular adhesion on the nanotopography

were seen with longer incubation periods. This is likely due to further deposition of the ECM onto the nanotopography, making the surface more favourable for hMSC attachment.

The data from these studies also indicated that functionalisation with ChoM did not compromise the biocompatibility of the surfaces. This supports the findings of Pfeil *et al.* (2018), who showed that ChoM concentrations <250 µM did not cause adverse effects on blood cells. However, it should be noted that in this project, the growth medium was replenished every 3 days. This would have significantly diminished the concentration of ChoM present from day 4 onwards, particularly for the flat titanium surfaces.

6.9.5.2 Osteogenic Potential of the Surface

Geimsa, Alizarin Red S and von Kossa staining were unable to definitively demonstrate bone nodule formation, calcium or phosphate deposition, respectively, in hMSCs grown on the flat titanium or 2-hour nanotopography, which may imply lack of osteoblastic differentiation. This was further supported by the qPCR data, which found no increase in the expression of genes OPN, OCN or ON. However, no effects were also seen with the positive controls using osteogenic medium, suggesting that there may have been an issue with the promo cells and that further investigation is necessary.

Tsimbouri *et al.* (2016) found upregulation in expression of OCN and OPN genes after 14 days and 35 days respectively in cells grown on an equivalent surface to the 2-hour nanotopography. Osteogenic differentiation may be seen by 28 days, but some studies use 35 or 42 days as a final time point (Matta *et al.*, 2019; Tsimbouri *et al.*, 2016). It is recommended, therefore, to repeat these experiments over a longer time period than the 28 days. In addition, other osteogenic marker genes such as alkaline phosphatase (ALP), bone gamma-carboxyglutamate (BGLAP) and runt-related transcription factor 2 (RUNX2) could be assessed to give further indication of osteogenic differentiation of adherent stem cells (Matta *et al.*, 2019; Westhauser *et al.*, 2019).

7.

CONCLUSIONS AND RECOMMENDED FUTURE WORK

Contents

7.1 Conclusions

7.1.1 Formation and Characterisation of Nanotopography

Alkaline hydrothermal synthesis is an attractive method to fabricate insect-wing mimicking nanospikes on titanium due to its simplicity and environmentally friendly operating systems, together with its high yield of nanostructures and reproducible nanotopography. The process involved submersion of pure titanium in concentrated NaOH, which was then heated under pressure. This was followed by heat treatment, ion exchange in HCl and a final calcination step. SEM images revealed that nanotopographies were formed at the first stage of NaOH submersion and the morphology did not change during the subsequent steps.

Systematic experiments, modifying key growth parameters such as temperature, duration, NaOH volume and concentration, were carried out to form a range of nanotopographical arrays that were subsequently assessed for their bactericidal potential. Over time, the nanotopography grew upwards and by 2 hours of alkaline treatment, the titanium surface had a homogeneous covering of well-developed nanospikes with a conserved diameter. The nanospikes protruded upright from the surface with some variability in orientation. At longer time periods, the nanospikes continued

to elongate but started to bend and intertwine. This further lengthening and interweaving of the nanotopography from 4 hours of treatment formed well developed 'pockets'.

With increasing sodium hydroxide molarity, the nanotopography grew quicker but high concentrations led to malformed structures as a result of enhanced rates of titanium dissolution. Increasing volumes of NaOH resulted in little differences in the nanospike growth, but increasing temperatures led to sharper and separated spikes, possibly due to the promotion of nucleation and crystal growth caused by the increase in pressure. A time duration of 2-hours for the nanospikes and 4-hours for the pocket development with 1 M NaOH concentration at 240°C (close to the maximum advised for the acid digestion vessels) was considered optimal.

The quality and integrity of the Teflon vessels used during alkaline hydrothermal treatment were found to be critical for optimal nanospike growth and reproducibility. The vessels degrade with time and a replacement batch resulted in inferior nanotopography growth due to a larger vessel volume. The addition of the spacer underneath the acid-digestions vessels ensured limited expansion resulting in the characteristic nanospike growth previously observed.

Parameters such as nanospike height, diameter and density, together with surface roughness and surface area, were measured for the range of nanotopographies formed. There were notable differences in the quantified physical characteristics compared with those reported in research papers using similar alkaline hydrothermal parameters. As only one analytical technique is usually used to measure the parameters, and with no standardised approach, such inconsistencies are unsurprising. Differences between batches with the same experimental conditions can also lead to variability in the measurements. In this project, effort was made to utilise several analysis techniques, including SEM, AFM CLSM and OP, to provide a more comprehensive and quantitative physical characterisation of the nanotopography.

AFM and SEM are well suited to quantify the height of nanotopography grown for up to 2 hours. However, for longer growth periods, AFM was not accurate due to tip convolution in randomly orientated and high-aspect ratio structures and SEM overestimated the height. CLSM and OP provided reliable height and roughness measurements for these structures. SEM was appropriate to measure nanospike diameter, density and pocket diameter.

Over time, upward perpendicular growth from the surface occurred and by 2 hours the nanospikes were ~440 nm in height, ~45 nm in diameter with a density of ~40 spikes per μm^2. With further growth the nanospikes began to intertwine. The average diameter of the pockets increased from ~1.5 to 13 µm for the 3-hour and 7-hour nanotopography respectively.

The crystal structure of the nanotopography was analysed at each step of the alkaline hydrothermal method by XRD. The results demonstrated the transformation of the crystal

structure from sodium titanate, to hydrogen titanate and finally to titanium dioxide, consisting primarily of anatase conformation. This was validated by EDX and XPS, which also confirmed the ion exchange success by indicating an absence of sodium.

Nanotopography growth was equally successful on the Ti64 alloy, which is primarily used for orthopaedic implants. However, the nanotopography was found to be easily damaged by scratching or by a human finger and will require optimisation to ensure that the material can survive handling during implant surgery.

7.1.2 Bacterial Interactions with Nanotopography

A key approach to assess the bactericidal properties of a surface is to quantify the number of viable bacteria after a period of incubation. Several methods were utilised, including Live/Dead staining, viability qPCR, LDH, BacTiter-Glo and RealTime-Glo. The surfaces were also visualised by SEM and FIB-SEM. Comparison of the data demonstrated that no single technique should be used in isolation to assess bactericidal performance, especially when applied to surfaces with nanotopography and multiple bacterial strains. Rather, the optimal combination of methodologies to be employed will likely be project-specific and will need to consider the precise research questions being asked. Given the limited microbiological approach taken by much of the literature in the field to date, this raises the question as to whether a standardised set of assays should be developed for such studies going forward. This should improve the accuracy of such work and enable better comparison of studies.

Live/Dead staining *K. pneumoniae* and *E. coli* after 3 hours incubation revealed little membrane permeability and cell lysis when cells adhered to the nanotopography. However, the results demonstrated that the niche/pocket nanotopography had anti-biofouling potential. These results were supported by SEM images of *K. pneumoniae*, *E. coli* and *S. aureus* which also suggested membrane indentations but no evidence of piercing or loss of turgor pressure. This was validated by the 3D FIB-SEM modelling of the bacteria on the 2-hour nanospikes.

These observations are supported by the BacTiter-Glo results for *E. coli*, *K. pneumoniae* and *S. aureus* after 3-hours incubation. Although the results of the nanotopographies were generally not significantly different from the flat titanium over 3-hours of incubation, the most encouraging trend was exhibited by *K. pneumoniae* which indicated up to 50% fewer cells in the solution on the nanotopography than on the flat titanium. The RealTime-Glo data for *S. aureus* demonstrated that there were significant bactericidal effects, although only evident after 4-hours of incubation. The techniques taken together gave consistent results indicating that Gram-negative *K.*

pneumoniae, E. coli were beginning to be affected within 3-hours of incubation, but Gram-positive *S. aureus* was affected only after 4/5 hours.

7.1.3 Functionalisation of Nanotopography with Antimicrobial Peptide

The aim of these studies was to determine if the antimicrobial potential of the 2-hour nanospike surface could be further enhanced by functionalising the nanotopography with ChoM, a synthetic AMP, which was synthesised at NPL. ChoM was functionalised by physical adsorption, which proved extremely time efficient and avoided the need for initial surface treatment. The method also allowed the free release of AMP into the local environment from the surface.

Studying the release kinetics, it was found that from a flat surface, the majority of ChoM was released within the first 10-30 minutes. Release from the nanotopography was delayed, exhibiting reduced concentrations in the surrounding environment, especially for the lower ChoM concentrations in the first 3 hours. Residual peptide on the nanotopography was visualised by SEM and attempts to increase the level of ChoM released by exposing the surface to low level ultrasonication or shaking was found to have little effect. As a result, to have comparable effects, 2-hour nanospikes had to be functionalised with higher concentrations of ChoM than flat titanium. Nonetheless, both surfaces had capacity to release ChoM at levels that exceeded the MIC and so were able to inhibit growth of both *E. coli* and *S. aureus*.

Bactericidal properties of the AMP on the nanotopography were quantified using BacTiter-Glo and visualised by SEM. Most experiments were restricted to 3 hours, but some increased to 12 hours and up to 19 hours (RealTime-Glo assay). The effect of increasing ChoM concentrations from 25 to 200 µM (1 to 8x MIC) was also investigated.

The BacTiter-Glo assays indicated that against *S. aureus,* the functionalised nanotopography is less effective than the flat titanium over a 3-hour period but potentially more effective over a 12-hour period, if the peptide exceeds 100 µM concentration. The assays with *E. coli* also indicated that the flat titanium was more effective up to 3 hours but ineffective between 3 and 12 hours compared to the nanotopography. At longer time periods, it is anticipated that more peptide will be progressively released from the nanotopography as very little residual peptide will remain on the flat titanium disks.

The experiments showed that the peptide is easily flushed from the flat titanium mainly in the initial 10 minutes. If the liquid is then further flushed away from the local area, it will have very limited bactericidal benefit. The peptide adheres longer onto the nanotopography and is released more slowly and therefore potentially remains antimicrobial for an extended period. For titanium

surgical implants it is unlikely that the peptide functionalised on the flat surfaces will have significant bactericidal benefit as it would have been flushed during or very shortly after surgery.

The nature of the local environment influences the release kinetics of ChoM which are affected by differences in the wettability of the flat titanium and 2-hour nanotopography. The flat titanium was hydrophilic, while the 2-hour nanotopography was super-hydrophilic, due to the increased surface roughness, surface area and presence of hydroxide bonds. It is likely that the super-hydrophilicity, electrostatic interactions and greater surface area of the nanospikes results in more peptide interaction with the nanotopography and hence slower release into the environment. A meniscus is present on the flatter surfaces and promotes the earlier release of the peptide than in the case of the super-hydrophilic 2-hour nanospikes and hence is less favourable for peptide retention.

An additional aspect of these studies was to determine the biocompatibility and osteogenic potential of the 2-hour nanospikes and the impact of functionalisation with ChoM. This was an important consideration, as biocompatibility of materials and stem cell adhesion to a surgical implant surface is a requisite for successful tissue development. This work was performed by a collaborator at the University of Glasgow and found that, while hMSCs initially preferred to attach and spread on flat titanium rather than the 2-hour nanotopography, comparable levels of biocompatibility were seen over a 28-day period. This was not affected by ChoM functionalisation. The osteogenic properties of the titanium surfaces were investigated by Giemsa, Alizarin Red S, von Kossa staining and qPCR over a 28-day incubation period. On all surfaces there was a dense coverage of hMSCs with cell stretching and motility evident for the majority of cells, but little evidence of osteogenic differentiation. Again, this was not affected by the presence of the ChoM coating.

7.2 Recommended Future Research

7.2.1 Formation and Characterisation of Nanotopography

In this project, the nanotopography was grown on flat, pure titanium disks. Dental and orthopaedic implants are more commonly made of Ti64 with curved surfaces and potential 3D interfaces with high roughness. Further work is recommended to investigate the reliability and quality of the nanotopographical growth, using the alkaline hydrothermal method, on these clinically relevant substrates and shapes. Further AFM and OP optimisation such as probe speed and line density will result in higher resolution images and more accurate measurements.

The nanotopography is not robust and is easily damaged. More robust surfaces should be developed, and further work carried out on other clinically relevant substrates such as Ti64. Handling procedures including specific areas available to touch should be investigated. Analogous to trabecular implants, procedures may be developed to shield the surfaces during insertion into the body. Implants will be exposed to fluid flow *in vivo* and it will be important to test the surfaces under such shear conditions to determine if the nanotopography is mechanically stable without premature release into the local environment and without any long-term toxicity.

7.2.2 Bacterial Interactions with Nanotopography

The nanotopographies generated impaired bacterial attachment and growth but there is scope for further bactericidal optimisation by systematic investigations into variations of height, nanospike diameter, roughness and density. Longer time periods should also be investigated to better determine the capacity for the nanotopographies to inhibit bacterial biofilm formation. Surface-bacteria interactions should be monitored in the presence of tissue/serous fluid and clinically relevant shear forces. This study used model bacteria that are particularly associated with orthopaedic implant infections. A range of Gram-positive/negative and motile/non-motile species should be investigated including strains more relevant to the dental community such as *Prevotella intermedia* and *Fusobacterium nucleatum* that are associated with peri-implant mucositis or peri-implantitis.

SEM is a widely used technique to visualise bacterial interactions with a surface, but optimisation of processing protocols is essential to avoid false positives. In addition to the critical point drying technique used here, further improvements in the SEM sample processing could be made. The fixation step is critical and involves preserving and stabilizing the structure of the cells in its original state. Rather than using glutaraldehyde as the sole fixative, osmium tetroxide or formaldehyde could be used in combination due to their capability of penetrating the cells faster. In this project the sequential ethanol dehydration steps of the samples were in 20% increments. Smaller increases of 10% could reduce the chance of structural deformation further.

The combination of assays used in these studies investigated the effects of the nanotopography on bacterial adhesion, metabolic activity and the bacterial cell wall. However, little is understood on the dynamics of the bacterial cell interactions with the nanotopography over time. Live imaging of bacteria interacting with the surface over time could be visualised with CLSM or light-sheet microscopy, using bacteria that are tagged, for example, with green fluorescent protein (GFP). Further replicates of experiments such as the RealTime-Glo which were conducted to a n=2 should also be carried out to an n=3.

7.2.3 Functionalisation of Nanotopography with AMP

A number of approaches could be taken to better define the release kinetics of ChoM from the surfaces. A factor controlling the release of ChoM from the 2-hour nanotopography is surface charge, as the titanium dioxide nanospikes are potentially negatively charged compared to the positively charged AMP. The charge could be determined by measuring the zeta potential of pure titanium and the nanotopography with an electrokinetic analyser.

A quartz crystal microbalance (QCM), which measures the adsorption and desorption of molecules to a surface, could be used to assess the detailed release kinetics of ChoM. Fluorescent tagging of ChoM may also enable visualisation of the peptide on the surface and in solution. The functionalised surfaces should ultimately be tested in more clinically relevant models that can be performed over a longer time period and incorporate factors such as tissue fluid flow.

ChoM was selected for this project due to its known antimicrobial activity against both Gram-positive and -negative bacteria. However, the size, structure and charge of an AMP are all factors that will contribute to its release profile. With a spectrum of AMPs available, other AMPs with different characteristics could therefore be functionalised onto the nanotopography and compared to ChoM. While low-level sonication or shaking did not enhance ChoM release from the nanospikes, more powerful sonication could also be tested.

The physical adsorption method used for this project allowed the free release of AMPs into the local environment from the surface, enabling the peptides to exert effective short-term activity. However, for an implant material, a longer period of AMP release may be desirable and other techniques for AMP functionalisation could be explored, such as layer by layer functionalisation, covalent tethering by silanisation or polymer brushing.

To be developed into a clinical product, another consideration for an implant material is its storage capabilities. Investigations should be carried out to assess the stability of the peptide coating after functionalisation. For example, after 1 month stored at 4°C, is the peptide coating as effective as one used immediately after preparation? Such data will help to optimise storage requirements and the long-term stability of the peptide in the dried state. Further replicates of experiments conducted to a n=2 should also be carried out to an n=3.

7.2.4 Biocompatibility and Osteogenic Potential

Investigations on the biocompatibility of the AMP-functionalised surfaces on hMSCs were preliminary and thus considerable further work is required. The experiments were restricted to the 2-hour nanospikes, but the osteogenic potential of the 3-hour and 4-hour nanotopography could also be assessed. Likewise, a wider range of ChoM concentrations could be tested.

The osteogenic potential assays indicated no significant differences between the titanium surfaces. However, as the positive controls also failed, these experiments should be repeated, and over a longer time period than 28 days. Other osteogenic marker genes such as alkaline phosphatase (ALP), bone gamma-carboxyglutamate (BGLAP) and runt-related transcription factor 2 (RUNX2) could also be assessed to give further indication of osteogenic differentiation by the adherent hMSCs.

As the morphology and confluency of the hMSCs on the surfaces were difficult to observe under the light microscope, SEM images may enable better visualisation of the interactions with the surface. In the alamarBlue assay, fluorescence could be measured to give more accurate results due to less interference between the unreduced and reduced alamarBlue spectra.

Ultimately, to better assess the capacity for any nanotopography to be used as an anti-infective implant material, a co-culture model comprising both bacteria and hMSCs should be developed. It would then be possible to determine if the antimicrobial properties of a surface are sufficient to impair bacteria, thereby allowing the hMSCs to bind to the implant surface and initiate the osteointegration process.

8.

References

Abdelraouf, K., Braggs, K.H., Yin, T., Truong, L.D., Hu, M. and Tam, V.H. (2012) Characterization of polymyxin B-induced nephrotoxicity: Implications for dosing regimen design. *Antimicrobial Agents and Chemotherapy* [online]. 56 (9), pp. 4625–4629. Available from: http://www.ncbi.nlm.nih.gov/pubmed/22687519doi:10.1128/AAC.00280-12 [Accessed 3 September 2019].

Abelho, M. (2005) Extraction and quantification of ATP as a measure of microbial biomass. In: *Methods to Study Litter Decomposition: A Practical Guide*. (no place) Springer Netherlands. pp. 223–229. doi:10.1007/1-4020-3466-0_30.

Abu-Amer, Y., Darwech, I. and Clohisy, J.C. (2007) Aseptic loosening of total joint replacements: mechanisms underlying osteolysis and potential therapies. *Arthritis research & therapy* [online]. 9 Suppl 1 (SUPPL.1), pp. S6. Available from: http://www.pubmedcentral.nih.gov/articlerender.fcgi?artid=1924521&tool=pmcentrez&rendertype=abstractdoi:10.1186/ar2170 [Accessed 26 August 2019].

Adamski, Z., Rybska, E. and Błoszyk, J. (2012) Pros and cons of scanning electron microscopy as a research method in acarology *Current Microscopy Contributions to Advances in Science and Technology* [online]. Available from: http://www.formatex.info/microscopy5/book/215-221.pdf.

Agha, M. and Agha, R. (2017) The rising prevalence of obesity: part A: impact on public health. *International journal of surgery. Oncology*. 2 (7), pp. e17. doi:10.1097/IJ9.0000000000000017.

Albright, V., Zhuk, I., Wang, Y., Selin, V., van de Belt-Gritter, B., Busscher, H.J., van der Mei, H.C. and Sukhishvili, S.A. (2017) Self-defensive antibiotic-loaded layer-by-layer coatings: Imaging of localized bacterial acidification and pH-triggering of antibiotic release. *Acta Biomaterialia*. 61 pp. 66–74. doi:10.1016/j.actbio.2017.08.012.

Alencar-Silva, T., Braga, M.C., Santana, G.O.S., Saldanha-Araujo, F., Pogue, R., Dias, S.C., Franco, O.L. and Carvalho, J.L. (2018) Breaking the frontiers of cosmetology with antimicrobial peptides. *Biotechnology Advances*. 36 (8), pp. 2019–2031. doi:10.1016/j.biotechadv.2018.08.005.

Alghamdi, H.S. (2018) Methods to improve osseointegration of dental implants in low quality (type-IV) bone: An overview *Journal of Functional Biomaterials*. doi:10.3390/jfb9010007.

Alhede, M. and Alhede, M. (2014) The biofilm challenge. *EWMA Journal* [online]. 14 (1), pp. 54–59. Available from: http://search.ebscohost.com/login.aspx?direct=true&profile=ehost&scope=site&authtype=crawler&jrnl=16092759&AN=95792245&h=1yEnPzmBQ66PivHMEHVns4x/E1bBqVkfn9OmYTrYebBe7mbTAEVezbisJIuiLYg1NnP2hwjDtlS0bLZSYSsuVQ==&crl=c.

Alibaba.com (2019) *hip joint support of titanium implant, hip joint prosthetic, View hip joint prosthetic, AK Medical Product Details from Beijing AK Medical Co., Ltd. on Alibaba.com*. Available from: https://ak-medical.en.alibaba.com/product/60789857693-801574787/hip_joint_support_of_titanium_implant_hip_joint_prosthetic.html [Accessed 8 September 2019].

Allied Market Research (2018) *Global Antibiotics Market Expected to Reach $50,374 Million by 2025*. Available from: https://www.alliedmarketresearch.com/press-release/antibiotics-market.html [Accessed 4 September 2019].

Alves, C.S., Melo, M.N., Franquelim, H.G., Ferre, R., Planas, M., Feliu, L., Bardají, E., Kowalczyk, W., Andreu, D., Santos, N.C., Fernandes, M.X., Castanho, M.A.R.B., Bardaji, E., Kowalczyk, W., et al. (2010) Escherichia coli cell surface perturbation and disruption induced by antimicrobial peptides BP100 and pepR. *Journal of Biological Chemistry* [online]. 285 (36), pp. 27536–27544. Available from: http://www.jbc.org/cgi/doi/10.1074/jbc.M110.130955doi:10.1074/jbc.M110.130955.

Alves, S.A., Patel, S.B., Sukotjo, C., Mathew, M.T., Filho, P.N., Celis, J.P., Rocha, L.A. and Shokuhfar, T. (2017) Synthesis of calcium-phosphorous doped TiO 2 nanotubes by anodization and reverse polarization: A promising strategy for an efficient biofunctional implant surface. *Applied Surface Science*. 399 pp. 682–701. doi:10.1016/j.apsusc.2016.12.105.

Andersson, D.I.I., Hughes, D. and Kubicek-Sutherland, J.Z.Z. (2016) Mechanisms and consequences of bacterial resistance to antimicrobial peptides. *Drug Resistance Updates* [online]. 26 pp. 43–57. Available from: http://linkinghub.elsevier.com/retrieve/pii/S1368764616300024doi:10.1016/j.drup.2016.04.002.

Andrews, J.M. (2001) Determination of minimum inhibitory concentrations. *Journal of Antimicrobial Chemotherapy* [online]. 48 (suppl_1), pp. 5–16. Available from:

http://academic.oup.com/jac/article/48/suppl_1/5/2473513/Determination-of-minimum-inhibitory-concentrationsdoi:10.1093/jac/48.suppl_1.5 [Accessed 27 July 2019].

Aqua Dental Clinic (2019) *Dental Implants Pinner Mini Dental Implants Northwood*. Available from: https://www.aquadentalclinic.co.uk/dental-implants/ [Accessed 8 September 2019].

Aragonès, L., Escudé, C., Visa, P., Salvi, L. and Mocé-Llivina, L. (2012) New insights for rapid evaluation of bactericidal activity: A semi-automated bioluminescent ATP assay. *Journal of Applied Microbiology*. 113 (1), pp. 114–125. doi:10.1111/j.1365-2672.2012.05320.x.

Aujla, R.S., Bryson, D.J., Gulihar, A. and Taylor, G.J. (2013) Trends in orthopaedic antimicrobial prophylaxis in the UK between 2005 and 2011. *Annals of the Royal College of Surgeons of England*. 95 (7), pp. 495–502. doi:10.1308/003588413X13629960047038.

Aumsuwan, N., Danyus, R.C., Heinhorst, S. and Urban, M.W. (2008) Attachment of ampicillin to expanded poly(tetrafluoroethylene): Surface reactions leading to inhibition of microbial growth. *Biomacromolecules*. 9 (7), pp. 1712–1718. doi:10.1021/bm800176t.

de Avila, E.D., Castro, A.G.B., Tagit, O., Krom, B.P., Löwik, D., van Well, A.A., Bannenberg, L.J., Vergani, C.E. and van den Beucken, J.J.J.P. (2019) Anti-bacterial efficacy via drug-delivery system from layer-by-layer coating for percutaneous dental implant components. *Applied Surface Science* [online]. 488 (April), pp. 194–204. Available from: https://doi.org/10.1016/j.apsusc.2019.05.154doi:10.1016/j.apsusc.2019.05.154.

Badarudeen, S., Shu, A.C., Ong, K.L., Baykal, D., Lau, E. and Malkani, A.L. (2017) Complications After Revision Total Hip Arthroplasty in the Medicare Population. *The Journal of arthroplasty* [online]. 32 (6), pp. 1954–1958. Available from: http://www.ncbi.nlm.nih.gov/pubmed/28236550doi:10.1016/j.arth.2017.01.037 [Accessed 26 August 2019].

Bahraminasab, M. and Farahmand, F. (2017) State of the art review on design and manufacture of hybrid biomedical materials: Hip and knee prostheses. *Proceedings of the Institution of Mechanical Engineers, Part H: Journal of Engineering in Medicine*. 231 (9), pp. 785–813. doi:10.1177/0954411917705911.

Bandara, C.D., Singh, S., Afara, I.O., Wolff, A., Tesfamichael, T., Ostrikov, K. and Oloyede, A. (2017) Bactericidal Effects of Natural Nanotopography of Dragonfly Wing on *Escherichia coli*. *ACS Applied Materials & Interfaces* [online]. 9 (8), pp. 6746–6760. Available from: http://www.ncbi.nlm.nih.gov/pubmed/28139904doi:10.1021/acsami.6b13666 [Accessed 4 September 2019].

Barbau-Piednoir, E., Mahillon, J., Pillyser, J., Coucke, W., Roosens, N.H. and Botteldoorn, N. (2014) Evaluation of viability-qPCR detection system on viable and dead Salmonella serovar Enteritidis. *Journal of Microbiological Methods* [online]. 103 pp. 131–137. Available from: http://dx.doi.org/10.1016/j.mimet.2014.06.003doi:10.1016/j.mimet.2014.06.003.

Barbour, M.E., Gandhi, N., El-Turki, A., O'Sullivan, D.J. and Jagger, D.C. (2009) Differential adhesion of Streptococcus gordonii to anatase and rutile titanium dioxide surfaces with and without functionalization with chlorhexidine. *Journal of Biomedical Materials Research - Part A*. 90 (4), pp. 993–998. doi:10.1002/jbm.a.32170.

Beckwith, M.S., Beckwith, K.S., Sikorski, P., Skogaker, N.T., Flo, T.H. and Halaas, Ø. (2015) Seeing a mycobacterium-infected cell in nanoscale 3D: Correlative imaging by light microscopy and FIB/SEM tomography. *PLoS ONE*. 10 (9), . doi:10.1371/journal.pone.0134644.

Belyaeva, L.A., van Deursen, P.M.G., Barbetsea, K.I. and Schneider, G.F. (2018) Hydrophilicity of Graphene in Water through Transparency to Polar and Dispersive Interactions. *Advanced Materials* [online]. 30 (6), pp. 1703274. Available from: http://doi.wiley.com/10.1002/adma.201703274doi:10.1002/adma.201703274 [Accessed 6 September 2019].

Bencharit, S., Byrd, W.C., Altarawneh, S., Hosseini, B., Leong, A., Reside, G., Morelli, T. and Offenbacher, S. (2014) Development and applications of porous tantalum trabecular metal-enhanced titanium dental implants. *Clinical Implant Dentistry and Related Research*. pp. 817–826. doi:10.1111/cid.12059.

Bennett, J.E., Li, G., Foreman, K., Best, N., Kontis, V., Pearson, C., Hambly, P. and Ezzati, M. (2015) The future of life expectancy and life expectancy inequalities in England and Wales: Bayesian spatiotemporal forecasting. *The Lancet*. 386 (9989), pp. 163–170. doi:10.1016/S0140-6736(15)60296-3.

Bettinger, C.J., Langer, R. and Borenstein, J.T. (2009) Engineering substrate topography at the Micro- and nanoscale to control cell function. *Angewandte Chemie - International Edition*. 48 (30), pp. 5406–5415. doi:10.1002/anie.200805179.

Beyenal, H., Donovan, C., Lewandowski, Z. and Harkin, G. (2004) Three-dimensional biofilm structure quantification. *Journal of Microbiological Methods*. 59 pp. 395–413. doi:10.1016/j.mimet.2004.08.003.

Bhadra, C.M., Khanh Truong, V., Pham, V.T.H.H., Al Kobaisi, M., Seniutinas, G., Wang, J.Y.,

Juodkazis, S., Crawford, R.J. and Ivanova, E.P. (2015) Antibacterial titanium nano-patterned arrays inspired by dragonfly wings. *Scientific Reports* [online]. 5 pp. 16817. Available from: http://www.nature.com/articles/srep16817doi:10.1038/srep16817 [Accessed 7 August 2019].

Bhushan, B. and Her, E.K. (2010) Fabrication of superhydrophobic surfaces with high and low adhesion inspired from rose petal. *Langmuir*. 26 (11), pp. 8207–8217. doi:10.1021/la904585j.

Biotium (2019) *Viability PCR | Biotium*. Available from: https://biotium.com/technology/microbiology/pma-for-viability-pcr/ [Accessed 8 September 2019].

Bixler, G.D., Theiss, A., Bhushan, B. and Lee, S.C. (2014) Anti-fouling properties of microstructured surfaces bio-inspired by rice leaves and butterfly wings. *Journal of Colloid and Interface Science* [online]. 419 pp. 114–133. Available from: http://dx.doi.org/10.1016/j.jcis.2013.12.019doi:10.1016/j.jcis.2013.12.019.

Bjarnsholt, T. (2013) The role of bacterial biofilms in chronic infections. *APMIS. Supplementum* [online]. (136), pp. 1–51. Available from: http://www.ncbi.nlm.nih.gov/pubmed/23635385doi:10.1111/apm.12099.

Boercker, J.E., Enache-Pommer, E. and Aydil, E.S. (2008) Growth mechanism of titanium dioxide nanowires for dye-sensitized solar cells. *Nanotechnology*. 19 (9), pp. 095604. doi:10.1088/0957-4484/19/9/095604.

Bogner, A., Jouneau, P.H., Thollet, G., Basset, D. and Gauthier, C. (2007) A history of scanning electron microscopy developments: Towards 'wet-STEM' imaging. *Micron* [online]. 38 (4), pp. 390–401. Available from: www.elsevier.com/locate/microndoi:10.1016/j.micron.2006.06.008 [Accessed 5 September 2019].

Bonjour, J.-P. (2011) Calcium and phosphate: a duet of ions playing for bone health. *Journal of the American College of Nutrition* [online]. 30 (5 Suppl 1), pp. 438S-48S. Available from: http://www.ncbi.nlm.nih.gov/pubmed/22081690 [Accessed 26 August 2019].

Bosshardt, D.D., Chappuis, V. and Buser, D. (2017) Osseointegration of titanium, titanium alloy and zirconia dental implants: current knowledge and open questions. *Periodontology 2000* [online]. 73 (1), pp. 22–40. Available from: http://www.ncbi.nlm.nih.gov/pubmed/28000277doi:10.1111/prd.12179 [Accessed 7 August 2019].

Braga, P.C., Sasso, M.D. and Sala, M.T. (2000) Sub-MIC concentrations of cefodizime interfere with various factors affecting bacterial virulence. *Journal of Antimicrobial Chemotherapy* [online]. 45 (1), pp. 15–25. Available from: https://academic.oup.com/jac/article-lookup/doi/10.1093/jac/45.1.15doi:10.1093/jac/45.1.15 [Accessed 7 September 2019].

Brånemark, P.I., Breine, U., Adell, R., Hansson, B.O., Lindström, J. and Ohlsson, A. (1969) Intra-osseous anchorage of dental prostheses: I. Experimental studies. *Scandinavian Journal of Plastic and Reconstructive Surgery and Hand Surgery*. 3 (2), pp. 81–100. doi:10.3109/02844316909036699.

Brånemark, P.I., Hansson, B.O., Adell, R., Breine, U., Lindström, J., Hallén, O. and Ohman, A. (1977) Osseointegrated implants in the treatment of the edentulous jaw. Experience from a 10-year period. *Scandinavian journal of plastic and reconstructive surgery. Supplementum.*

Brogden, K. a (2005) Antimicrobial peptides: pore formers or metabolic inhibitors in bacteria? *Nature reviews. Microbiology*. 3 (3), pp. 238–250. doi:10.1038/nrmicro1098.

BugGuide (2013) *Cecropia Moth - Hyalophora cecropia - BugGuide.Net*. Available from: https://bugguide.net/node/view/796869 [Accessed 9 September 2019].

Bunney, P.E., Zink, A.N., Holm, A.A., Billington, C.J. and Kotz, C.M. (2017) Orexin activation counteracts decreases in nonexercise activity thermogenesis (NEAT) caused by high-fat diet. *Physiology and Behavior*. 176 (1), pp. 139–148. doi:10.1016/j.physbeh.2017.03.040.

Busscher, H.J. and van der Mei, H.C. (2012) How do bacteria know they are on a surface and regulate their response to an adhering state? *PLoS Pathogens*. 8 (1), pp. 1–3. doi:10.1371/journal.ppat.1002440.

Butt, A., Hamlekhan, A., Patel, S., Royhman, D., Sukotjo, C., Mathew, M.T., Shokuhfar, T. and Takoudis, C. (2015) A novel investigation of the formation of titanium oxide nanotubes on thermally formed oxide of Ti-6Al-4V. *Journal of Oral Implantology*. 41 (5), pp. 523–531. doi:10.1563/AAID-JOI-D-13-00340.

Byrne, C., Fagan, R., Hinder, S., McCormack, D.E. and Pillai, S.C. (2016) New approach of modifying the anatase to rutile transition temperature in TiO_2 photocatalysts. *RSC Advances* [online]. 6 (97), pp. 95232–95238. Available from: http://xlink.rsc.org/?DOI=C6RA19759Kdoi:10.1039/C6RA19759K [Accessed 5 September 2019].

Campoccia, D., Montanaro, L. and Arciola, C.R. (2013a) A review of the biomaterials

technologies for infection-resistant surfaces. *Biomaterials* [online]. 34 (34), pp. 8533–8554. Available from: http://www.sciencedirect.com/science/article/pii/S0142961213009174doi:10.1016/j.biomaterials.2013.07.089 [Accessed 20 July 2014].

Campoccia, D., Montanaro, L. and Arciola, C.R. (2013b) A review of the clinical implications of anti-infective biomaterials and infection-resistant surfaces. *Biomaterials* [online]. 34 (33), pp. 8018–8029. Available from: http://www.ncbi.nlm.nih.gov/pubmed/23932292doi:10.1016/j.biomaterials.2013.07.048.

Cangelosi, G.A. and Meschke, J.S. (2014) Dead or alive: Molecular assessment of microbial viability *Applied and Environmental Microbiology* 80 (19) p.pp. 5884–5891. doi:10.1128/AEM.01763-14.

Cao, S., Wang, J., Chen, H. and Chen, D. (2011) Progress of marine biofouling and antifouling technologies. *Chinese Science Bulletin*. 56 (7), pp. 598–612. doi:10.1007/s11434-010-4158-4.

Cao, Y., Su, B., Chinnaraj, S., Jana, S., Bowen, L., Charlton, S., Duan, P., Jakubovics, N.S. and Chen, J. (2018) Nanostructured titanium surfaces exhibit recalcitrance towards Staphylococcus epidermidis biofilm formation. *Scientific Reports*. 8 (1), . doi:10.1038/s41598-018-19484-x.

Capitanu, L., Badita, L.., Floresu, V. and Tiganesteanu, C. (2018) Roughness Influence on Initiation of Fretting Fatigue Scar of Ti-6Al-4V Alloy Related content Low temperature ion nitriding of Ti-6Al-4V alloy R D Agzamov, K N Ramazanov, A F Tagirov et al.- Fatigue crack propagation behavior and debris formation in Ti-6Al. *Materials science & engineering*. 295 . doi:10.1088/1757-899X/295/1/012022.

Carreira, A.C., Lojudice, F.H., Halcsik, E., Navarro, R.D., Sogayar, M.C. and Granjeiro, J.M. (2014) Bone morphogenetic proteins: Facts, challenges, and future perspectives. *Journal of Dental Research*. 93 (4), pp. 335–345. doi:10.1177/0022034513518561.

Casciaro, B., Dutta, D., Loffredo, M.R., Marcheggiani, S., McDermott, A.M., Willcox, M.D. and Mangoni, M.L. (2017) Esculentin-1a derived peptides kill Pseudomonas aeruginosa biofilm on soft contact lenses and retain antibacterial activity upon immobilization to the lens surface. *Biopolymers* [online]. Available from: http://www.ncbi.nlm.nih.gov/pubmed/29086910doi:10.1002/bip.23074 [Accessed 7 August 2019].

Chan, T.C., Li, H.T. and Li, K.Y. (2015) Effects of Shapes of Solute Molecules on Diffusion: A

Study of Dependences on Solute Size, Solvent, and Temperature. *The Journal of Physical Chemistry B* [online]. 119 (51), pp. 15718–15728. Available from: https://pubs.acs.org/doi/10.1021/acs.jpcb.5b10550doi:10.1021/acs.jpcb.5b10550 [Accessed 7 September 2019].

Chang, Y., Shao, Y., Liu, Y., Xia, R., Tong, Z., Zhang, J., Zhai, Z., Cheng, W. and Li, H. (2019) Mechanical strain promotes osteogenic differentiation of mesenchymal stem cells on TiO2 nanotubes substrate. *Biochemical and Biophysical Research Communications* [online]. 511 (4), pp. 840–846. Available from: http://www.ncbi.nlm.nih.gov/pubmed/30850158doi:10.1016/j.bbrc.2019.02.145 [Accessed 4 September 2019].

Chee, W. and Jivraj, S. (2007) Failures in implant dentistry. *British dental journal*. 202 (3), pp. 123–129. doi:10.1038/bdj.2007.74.

Chen, C., Zhang, S.M. and Lee, I.S. (2013) Immobilizing bioactive molecules onto titanium implants to improve osseointegration *Surface and Coatings Technology*. doi:10.1016/j.surfcoat.2012.05.112.

Chen, H., Yang, J., Xiao, S., Hu, R., Bhaway, S.M., Vogt, B.D., Zhang, M., Chen, Q., Ma, J., Chang, Y., Li, L. and Zheng, J. (2016a) Salt-responsive polyzwitterionic materials for surface regeneration between switchable fouling and antifouling properties. *Acta Biomaterialia* [online]. 40 pp. 62–69. Available from: http://www.sciencedirect.com/science/article/pii/S1742706116300939doi:10.1016/j.actbio.2016.03.009 [Accessed 11 March 2016].

Chen, R., Willcox, M.D.P., Ho, K.K.K., Smyth, D. and Kumar, N. (2016b) Antimicrobial peptide melimine coating for titanium and its in vivo antibacterial activity in rodent subcutaneous infection models. *Biomaterials*. 85 pp. 142–151. doi:10.1016/j.biomaterials.2016.01.063.

Chen, X., Hirt, H., Li, Y., Gorr, S.U. and Aparicio, C. (2014) Antimicrobial GL13K peptide coatings killed and ruptured the wall of streptococcus gordonii and prevented formation and growth of biofilms. *PLoS ONE*. 9 (11), pp. e111579. doi:10.1371/journal.pone.0111579.

Childs, P.G., Boyle, C.A., Pemberton, G.D., Nikukar, H., Curtis, A.S.G., Henriquez, F.L., Dalby, M.J. and Reid, S. (2016) Use of nanoscale mechanical stimulation for control and manipulation of cell behaviour. *Acta Biomaterialia* [online]. 34 pp. 159–168. Available from: http://dx.doi.org/10.1016/j.actbio.2015.11.045doi:10.1016/j.actbio.2015.11.045.

Chileveru, H.R., Lim, S.A., Chairatana, P., Wommack, A.J., Chiang, I.-L. and Nolan, E.M. (2015) Visualizing attack of Escherichia coli by the antimicrobial peptide human defensin 5. *Biochemistry* [online]. 54 (9), pp. 1767–1777. Available from: http://www.ncbi.nlm.nih.gov/pubmed/25664683doi:10.1021/bi501483q [Accessed 6 September 2019].

Chimutengwende-Gordon, M., Pendegrass, C., Bayston, R. and Blunn, G. (2014) Preventing infection of osseointegrated transcutaneous implants: Incorporation of silver into preconditioned fibronectin-functionalized hydroxyapatite coatings suppresses Staphylococcus aureus colonization while promoting viable fibroblast growth in vitro . *Biointerphases*. 9 (3), pp. 031010. doi:10.1116/1.4889977.

Chooi, Y.C., Ding, C. and Magkos, F. (2019) The epidemiology of obesity. *Metabolism: Clinical and Experimental* [online]. 92 pp. 6–10. Available from: http://www.ncbi.nlm.nih.gov/pubmed/30253139doi:10.1016/j.metabol.2018.09.005 [Accessed 4 September 2019].

Chouirfa, H., Bouloussa, H., Migonney, V. and Falentin-Daudré, C. (2019) Review of titanium surface modification techniques and coatings for antibacterial applications. *Acta Biomaterialia*. 83 pp. 37–54. doi:10.1016/j.actbio.2018.10.036.

Chung, P.Y. and Khanum, R. (2017) Antimicrobial peptides as potential anti-biofilm agents against multidrug-resistant bacteria. *Journal of Microbiology, Immunology and Infection*. 50 (4), pp. 405–410. doi:10.1016/j.jmii.2016.12.005.

Clifford, R.J., Milillo, M., Prestwood, J., Quintero, R., Zurawski, D. V, Kwak, Y.I., Waterman, P.E., Lesho, E.P. and Mc Gann, P. (2012) Detection of bacterial 16S rRNA and identification of four clinically important bacteria by real-time PCR. *PloS one* [online]. 7 (11), pp. e48558. Available from: http://journals.plos.org/plosone/article?id=10.1371/journal.pone.0048558doi:10.1371/journal.pone.0048558.

Cochis, A., Azzimonti, B., Della Valle, C., Chiesa, R., Arciola, C.R. and Rimondini, L. (2015) Biofilm formation on titanium implants counteracted by grafting gallium and silver ions *Journal of Biomedical Materials Research - Part A* 103 (3) p.pp. 1176–1187. doi:10.1002/jbm.a.35270.

Cordeiro, J.M. and Barão, V.A.R. (2016) Is there scientific evidence favoring the substitution of commercially pure titanium with titanium alloys for the manufacture of dental implants? *Materials Science and Engineering: C* [online]. 71 pp. 1201–1215. Available from: http://linkinghub.elsevier.com/retrieve/pii/S0928493116317799doi:10.1016/j.msec.2016.1

0.025 [Accessed 26 August 2019].

Córdoba, A., Hierro-Oliva, M., Pacha-Olivenza, M.Á., Fernández-Calderón, M.C., Perelló, J., Isern, B., González-Martín, M.L., Monjo, M. and Ramis, J.M. (2016) Direct Covalent Grafting of Phytate to Titanium Surfaces through Ti-O-P Bonding Shows Bone Stimulating Surface Properties and Decreased Bacterial Adhesion. *ACS Applied Materials and Interfaces*. doi:10.1021/acsami.6b02533.

Costa, F., Carvalho, I.F., Montelaro, R.C., Gomes, P. and Martins, M.C.L. (2011) Covalent immobilization of antimicrobial peptides (AMPs) onto biomaterial surfaces. *Acta biomaterialia* [online]. 7 (4), pp. 1431–1440. Available from: http://www.sciencedirect.com/science/article/pii/S174270611000512Xdoi:10.1016/j.actbio.2010.11.005 [Accessed 3 September 2015].

Costa, F.M.T.A., Maia, S.R., Gomes, P.A.C. and Martins, M.C.L. (2015) Dhvar5 antimicrobial peptide (AMP) chemoselective covalent immobilization results on higher antiadherence effect than simple physical adsorption. *Biomaterials*. doi:10.1016/j.biomaterials.2015.02.049.

Crawford, R.J., Webb, H.K., Truong, V.K., Hasan, J. and Ivanova, E.P. (2012) Surface topographical factors influencing bacterial attachment *Advances in Colloid and Interface Science* 179–182 p.pp. 142–149. doi:10.1016/j.cis.2012.06.015.

Dalby, M.J., Gadegaard, N., Tare, R., Andar, A., Riehle, M.O., Herzyk, P., Wilkinson, C.D.W. and Oreffo, R.O.C. (2007) The control of human mesenchymal cell differentiation using nanoscale symmetry and disorder. *Nature Materials*. 6 (12), pp. 997–1003. doi:10.1038/nmat2013.

Davidson, H., Poon, M., Saunders, R., Shapiro, I.M., Hickok, N.J. and Adams, C.S. (2015) Tetracycline tethered to titanium inhibits colonization by Gram-negative bacteria. *Journal of Biomedical Materials Research - Part B Applied Biomaterials*. 103 (7), pp. 1381–1389. doi:10.1002/jbm.b.33310.

Dias, S.A., Freire, J.M., Pérez-Peinado, C., Domingues, M.M., Gaspar, D., Vale, N., Gomes, P., Andreu, D., Henriques, S.T., Castanho, M.A.R.B. and Veiga, A.S. (2017) New Potent Membrane-Targeting Antibacterial Peptides from Viral Capsid Proteins. *Frontiers in Microbiology* [online]. 8 pp. 775. Available from: http://journal.frontiersin.org/article/10.3389/fmicb.2017.00775/fulldoi:10.3389/fmicb.2017.00775 [Accessed 7 September 2019].

Diu, T., Faruqui, N., Sjöström, T., Lamarre, B., Jenkinson, H.F., Su, B. and Ryadnov, M.G.

(2014) Cicada-inspired cell-instructive nanopatterned arrays. *Scientific reports* [online]. 4 pp. 7122. Available from: http://www.nature.com/srep/2014/141120/srep07122/full/srep07122.html?WT.ec_id=SREP-639-20141125doi:10.1038/srep07122.

Dobbenga, S., Fratila-Apachitei, L.E. and Zadpoor, A.A. (2016) Nanopattern-induced osteogenic differentiation of stem cells – A systematic review *Acta Biomaterialia* 46 p.pp. 3–14. doi:10.1016/j.actbio.2016.09.031.

Doll, K., Jongsthaphongpun, K.L., Stumpp, N.S., Winkel, A. and Stiesch, M. (2016) Quantifying implant-associated biofilms: Comparison of microscopic, microbiologic and biochemical methods. *Journal of Microbiological Methods*. 130 pp. 61–68. doi:10.1016/j.mimet.2016.07.016.

Dong, L., Cheng, K., Weng, W., Song, C., Du, P., Shen, G. and Han, G. (2011) Hydrothermal growth of rutile TiO2 nanorod films on titanium substrates. *Thin Solid Films* [online]. 519 (15), pp. 4634–4640. Available from: http://dx.doi.org/10.1016/j.tsf.2011.01.008doi:10.1016/j.tsf.2011.01.008.

Dong, W., Zhang, T., Epstein, J., Cooney, L., Wang, H., Li, Y., Jiang, Y.B., Cogbill, A., Varadan, V. and Ryan Tian, Z. (2007) Multifunctional Nanowire Bioscaffolds on Titanium. *Chemistry of Materials*. 19 (1), pp. 4454–4459. doi:10.1021/cm070845a.

Drelich, J. and Chibowski, E. (2010) Superhydrophilic and superwetting surfaces: Definition and mechanisms of control. *Langmuir*. 26 (24), pp. 18621–18623. doi:10.1021/la1039893.

Duellman, S.J., Zhou, W., Meisenheimer, P., Vidugiris, G., Cali, J.J., Gautam, P., Wennerberg, K. and Vidugiriene, J. (2015) Bioluminescent, Nonlytic, Real-Time Cell Viability Assay and Use in Inhibitor Screening. *Assay and Drug Development Technologies*. 13 (8), pp. 456–465. doi:10.1089/adt.2015.669.

Eales, M.G., Ferrari, E., Goddard, A.D., Lancaster, L., Sanderson, P. and Miller, C. (2018) Mechanistic and phenotypic studies of bicarinalin, BP100 and colistin action on Acinetobacter baumannii. *Research in Microbiology* [online]. 169 (6), pp. 296–302. Available from: http://www.ncbi.nlm.nih.gov/pubmed/29751064doi:10.1016/j.resmic.2018.04.005 [Accessed 19 September 2019].

Eger, M., Hiram-Bab, S., Liron, T., Sterer, N., Carmi, Y., Kohavi, D. and Gabet, Y. (2018) Mechanism and Prevention of Titanium Particle-Induced Inflammation and Osteolysis.

Frontiers in immunology. 9 (December), pp. 2963. doi:10.3389/fimmu.2018.02963.

Ekoi, E.J., Gowen, A., Dorrepaal, R. and Dowling, D.P. (2019) Characterisation of titanium oxide layers using Raman spectroscopy and optical profilometry: Influence of oxide properties. *Results in Physics*. 12 pp. 1574–1585. doi:10.1016/j.rinp.2019.01.054.

Elbourne, A., Crawford, R.J. and Ivanova, E.P. (2017) Nano-structured antimicrobial surfaces: From nature to synthetic analogues *Journal of Colloid and Interface Science* 508 p.pp. 603–616. doi:10.1016/j.jcis.2017.07.021.

Epstein, A.K., Wong, T.-S., Belisle, R.A., Boggs, E.M. and Aizenberg, J. (2012) Liquid-infused structured surfaces with exceptional anti-biofouling performance. *Proceedings of the National Academy of Sciences*. doi:10.1073/pnas.1201973109.

Fabre, H., Mercier, D., Galtayries, A., Portet, D., Delorme, N. and Bardeau, J.F. (2018) Impact of hydrophilic and hydrophobic functionalization of flat TiO 2 /Ti surfaces on proteins adsorption. *Applied Surface Science*. doi:10.1016/j.apsusc.2017.08.138.

Faruqui, N., Bella, A., Ravi, J., Ray, S., Lamarre, B. and Ryadnov, M.G. (2014) Differentially instructive extracellular protein micro-nets. *Journal of the American Chemical Society* [online]. 136 (22), pp. 7889–7898. Available from: http://www.ncbi.nlm.nih.gov/pubmed/24825365doi:10.1021/ja411325c.

Feng, B., Chu, X., Chen, J., Wang, J., Lu, X. and Weng, J. (2010) Hydroxyapatite coating on titanium surface with titania nanotube layer and its bond strength to substrate. *Journal of Porous Materials*. doi:10.1007/s10934-009-9307-2.

Ferreira, C., Babu, J., Hamlekhan, A., Patel, S. and Shokuhfar, T. (2017) Efficiency of Nanotube Surface–Treated Dental Implants Loaded with Doxycycline on Growth Reduction of Porphyromonas gingivalis. *The International Journal of Oral & Maxillofacial Implants*. doi:10.11607/jomi.4975.

Flemming, H.-C., Wingender, J., Szewzyk, U., Steinberg, P., Rice, S.A. and Kjelleberg, S. (2016) Biofilms: an emergent form of bacterial life. *Nature reviews. Microbiology* [online]. 14 (9), pp. 563–575. Available from: http://www.ncbi.nlm.nih.gov/pubmed/27510863doi:10.1038/nrmicro.2016.94.

FoaAP (2016) Future of an Ageing Population *The Oxford Institute of Population Ageing* [online]. Available from: https://www.ageing.ox.ac.uk/files/Future_of_Ageing_Report.pdf.

Fouquet, C., Gilles, J.-F., Heck, N., Dos Santos, M., Schwartzmann, R., Cannaya, V., Morel,

M.-P., Davidson, R.S., Trembleau, A. and Bolte, S. (2015) Improving axial resolution in confocal microscopy with new high refractive index mounting media. *PloS one* [online]. 10 (3), pp. e0121096. Available from: http://www.ncbi.nlm.nih.gov/pubmed/25822785doi:10.1371/journal.pone.0121096 [Accessed 2 September 2019].

Gabriel, M., Nazmi, K., Veerman, E.C., Amerongen, A.V.N. and Zentner, A. (2006) Preparation of LL-37-grafted titanium surfaces with bactericidal activity. *Bioconjugate Chemistry*. doi:10.1021/bc050091v.

Gao, G., Lange, D., Hilpert, K., Kindrachuk, J., Zou, Y., Cheng, J.T.J.J., Kazemzadeh-Narbat, M., Yu, K., Wang, R., Straus, S.K., Brooks, D.E., Chew, B.H., Hancock, R.E.W.W. and Kizhakkedathu, J.N. (2011) The biocompatibility and biofilm resistance of implant coatings based on hydrophilic polymer brushes conjugated with antimicrobial peptides. *Biomaterials* [online]. 32 (16), pp. 3899–3909. Available from: http://linkinghub.elsevier.com/retrieve/pii/S0142961211001657doi:10.1016/j.biomaterials.2011.02.013.

Garner, S. and Barbour, M.E. (2015) Nanoparticles for controlled delivery and sustained release of chlorhexidine in the oral environment. *Oral Diseases*. doi:10.1111/odi.12328.

Gaviria, L., Salcido, J.P., Guda, T. and Ong, J.L. (2014) Current trends in dental implants. *Journal of the Korean Association of Oral and Maxillofacial Surgeons* [online]. 40 (2), pp. 50–60. Available from: http://www.pubmedcentral.nih.gov/articlerender.fcgi?artid=4028797&tool=pmcentrez&rendertype=abstractdoi:10.5125/jkaoms.2014.40.2.50.

Geetha, M., Singh, A.K.K., Asokamani, R. and Gogia, A.K.K. (2009) Ti based biomaterials, the ultimate choice for orthopaedic implants - A review. *Progress in Materials Science* [online]. 54 (3), pp. 397–425. Available from: http://dx.doi.org/10.1016/j.pmatsci.2008.06.004doi:10.1016/j.pmatsci.2008.06.004 [Accessed 4 September 2019].

Godoy-Gallardo, M., Mas-Moruno, C., Yu, K., Manero, J.M., Gil, F.J., Kizhakkedathu, J.N. and Rodriguez, D. (2015) Antibacterial properties of hLf1-11 peptide onto titanium surfaces: a comparison study between silanization and surface initiated polymerization. *Biomacromolecules* [online]. 16 (2), pp. 483–496. Available from: http://www.ncbi.nlm.nih.gov/pubmed/25545728doi:10.1021/bm501528x [Accessed 22 December 2015].

Gonzalez-Fernandez, T., Sikorski, P. and Leach, J.K. (2019) Bio-instructive materials for

musculoskeletal regeneration. *Acta Biomaterialia*. doi:10.1016/j.actbio.2019.07.014.

Goodman, S.B., Yao, Z., Keeney, M. and Yang, F. (2013) The future of biologic coatings for orthopaedic implants. *Biomaterials* [online]. 34 (13), pp. 3174–3183. Available from: http://dx.doi.org/10.1016/j.biomaterials.2013.01.074doi:10.1016/j.biomaterials.2013.01.074.

Gopal, R., Kim, Y.G., Lee, J.H., Lee, S.K., Chae, J.D., Son, B.K., Seo, C.H. and Park, Y. (2014) Synergistic effects and antibiofilm properties of chimeric peptides against multidrug-resistant acinetobacter baumannii strains. *Antimicrobial Agents and Chemotherapy*. 58 (3), pp. 1622–1629. doi:10.1128/AAC.02473-13.

Gordon, Y.J., Romanowski, E.G. and McDermott, A.M. (2005) A review of antimicrobial peptides and their therapeutic potential as anti-infective drugs. *Current eye research* [online]. 30 (7), pp. 505–515. Available from: http://www.pubmedcentral.nih.gov/articlerender.fcgi?artid=1497874&tool=pmcentrez&rendertype=abstractdoi:10.1080/02713680590968637.

Goreham, R. V., Mierczynska, A., Smith, L.E., Sedev, R. and Vasilev, K. (2013) Small surface nanotopography encourages fibroblast and osteoblast cell adhesion. *RSC Advances*. 3 (26), pp. 10309–10317. doi:10.1039/c3ra23193c.

Goriainov, V., Hulsart-Billstrom, G., Sjostrom, T., Dunlop, D.G., Su, B. and Oreffo, R.O.C. (2018) Harnessing nanotopography to enhance osseointegration of clinical orthopedic titanium implants-an in vitro and in vivo analysis. *Frontiers in Bioengineering and Biotechnology*. 6 (APR), . doi:10.3389/fbioe.2018.00044.

Goudeli, E. and Pratsinis, S.E. (2017) Surface Composition and Crystallinity of Coalescing Silver-Gold Nanoparticles. *ACS Nano* [online]. 11 (11), pp. 11653–11660. Available from: http://www.ncbi.nlm.nih.gov/pubmed/29112816doi:10.1021/acsnano.7b06727 [Accessed 3 September 2019].

Grotberg, J., Hamlekhan, A., Butt, A., Patel, S., Royhman, D., Shokuhfar, T., Sukotjo, C., Takoudis, C. and Mathew, M.T. (2016) Thermally oxidized titania nanotubes enhance the corrosion resistance of Ti6Al4V. *Materials Science and Engineering C*. doi:10.1016/j.msec.2015.10.056.

Gruenheid, S. and Le Moual, H. (2012) Resistance to antimicrobial peptides in Gram-negative bacteria *FEMS Microbiology Letters* 330 (2) p.pp. 81–89. doi:10.1111/j.1574-6968.2012.02528.x.

Gu, X.N., Guo, H.M., Wang, F., Lu, Y., Lin, W.T., Li, J., Zheng, Y.F. and Fan, Y.B. (2017)

Degradation, hemolysis, and cytotoxicity of silane coatings on biodegradable magnesium alloy. *Materials Letters* [online]. 193 pp. 266–269. Available from: https://www.sciencedirect.com/science/article/abs/pii/S0167577X17301684doi:10.1016/J.MATLET.2017.01.136 [Accessed 4 September 2019].

Guaní-Guerra, E., Santos-Mendoza, T., Lugo-Reyes, S.O. and Terán, L.M. (2010) Antimicrobial peptides: General overview and clinical implications in human health and disease. *Clinical Immunology* [online]. 135 (1), pp. 1–11. Available from: http://dx.doi.org/10.1016/j.clim.2009.12.004doi:10.1016/j.clim.2009.12.004.

Le Guéhennec, L., Soueidan, A., Layrolle, P. and Amouriq, Y. (2007) Surface treatments of titanium dental implants for rapid osseointegration. *Dental materials : official publication of the Academy of Dental Materials* [online]. 23 (7), pp. 844–854. Available from: http://www.sciencedirect.com/science/article/pii/S0109564106001850doi:10.1016/j.dental.2006.06.025 [Accessed 12 November 2014].

Guo, X., Liu, Y., Bai, J., Yu, B., Xu, M., Sun, H., Shen, J., Lin, J., Zhang, H., Wang, D., Geng, D. and Pan, G. (2019) Efficient Inhibition of Wear-Debris-Induced Osteolysis by Surface Biomimetic Engineering of Titanium Implant with a Mussel-Derived Integrin-Targeting Peptide. *Advanced Biosystems*. 3 (2), . doi:10.1002/adbi.201800253.

Guo, Z., Jiang, N., Chen, C., Zhu, S., Zhang, L. and Li, Y. (2017) Surface bioactivation through the nanostructured layer on titanium modified by facile HPT treatment. *Scientific Reports* [online]. 7 (1), pp. 1–11. Available from: www.nature.com/scientificreportsdoi:10.1038/s41598-017-04395-0.

Hall, D.J., Skerrett, E.J. and Thomas, W.D. (1978) Critical point drying for scanning electron microscopy: a semi-automatic method of preparing biological specimens. *Journal of microscopy* [online]. 113 (3), pp. 277–290. Available from: http://www.ncbi.nlm.nih.gov/pubmed/361959 [Accessed 22 August 2019].

Hallab, N.J., Cunningham, B.W. and Jacobs, J.J. (2003) Spinal implant debris-induced osteolysis. *Spine* [online]. 28 (20), pp. S125-38. Available from: http://www.ncbi.nlm.nih.gov/pubmed/14560184doi:10.1097/00007632-200310151-00006 [Accessed 20 August 2019].

Harms, S., Larson, R., Sahmoun, A.E. and Beal, J.R. (2007) Obesity increases the likelihood of total joint replacement surgery among younger adults. *International Orthopaedics*. 31 (1), pp. 23–26. doi:10.1007/s00264-006-0130-y.

Hasan, J., Jain, S. and Chatterjee, K. (2017) Nanoscale Topography on Black Titanium Imparts

Multi-biofunctional Properties for Orthopedic Applications. *Scientific Reports* [online]. 7 (January), pp. 41118. Available from: http://www.nature.com/articles/srep41118doi:10.1038/srep41118 [Accessed 7 August 2019].

Hasan, J., Jain, S., Padmarajan, R., Purighalla, S., Sambandamurthy, V.K. and Chatterjee, K. (2018) Multi-scale surface topography to minimize adherence and viability of nosocomial drug-resistant bacteria. *Materials and Design*. 140 pp. 332–344. doi:10.1016/j.matdes.2017.11.074.

Hasan, J., Webb, H.K., Truong, V.K., Pogodin, S., Baulin, V.A., Watson, G.S., Watson, J.A., Crawford, R.J. and Ivanova, E.P. (2013) Selective bactericidal activity of nanopatterned superhydrophobic cicada Psaltoda claripennis wing surfaces. *Applied Microbiology and Biotechnology*. 97 (20), pp. 9257–9262. doi:10.1007/s00253-012-4628-5.

Hazam, P.K., Goyal, R. and Ramakrishnan, V. (2019) Peptide based antimicrobials: Design strategies and therapeutic potential *Progress in Biophysics and Molecular Biology* 142 p.pp. 10–22. doi:10.1016/j.pbiomolbio.2018.08.006.

Hazell, G., Fisher, L.E., Murray, W.A., Nobbs, A.H. and Su, B. (2018a) Bioinspired bactericidal surfaces with polymer nanocone arrays. *Journal of Colloid and Interface Science*. doi:10.1016/j.jcis.2018.05.096.

Hazell, G., Fisher, L.E., Murray, W.A., Nobbs, A.H. and Su, B. (2018b) Bioinspired bactericidal surfaces with polymer nanocone arrays. *Journal of Colloid and Interface Science* [online]. 528 pp. 389–399. Available from: https://www.sciencedirect.com/science/article/pii/S0021979718306179doi:10.1016/J.JCIS.2018.05.096 [Accessed 6 September 2019].

Hazell, G., May, P.W., Taylor, P., Nobbs, A.H., Welch, C.C. and Su, B. (2018c) Studies of black silicon and black diamond as materials for antibacterial surfaces. *Biomaterials Science*. doi:10.1039/c8bm00107c.

Hernandez-Montelongo, J., Corrales Ureña, Y.R., Machado, D., Lancelloti, M., Pinheiro, M.P., Rischka, K., Lisboa-Filho, P.N. and Cotta, M.A. (2018) Electrostatic immobilization of antimicrobial peptides on polyethylenimine and their antibacterial effect against Staphylococcus epidermidis. *Colloids and Surfaces B: Biointerfaces*. doi:10.1016/j.colsurfb.2018.02.002.

Hickok, N.J. and Shapiro, I.M. (2012) Immobilized antibiotics to prevent orthopaedic implant infections. *Advanced Drug Delivery Reviews* [online]. 64 (12), pp. 1165–1176. Available

from:
http://www.sciencedirect.com/science/article/pii/S0169409X12001111doi:10.1016/j.addr.2012.03.015 [Accessed 14 October 2015].

Hoerr, V., Zbytnuik, L., Leger, C., Tam, P.P.C., Kubes, P. and Vogel, H.J. (2012) Gram-negative and Gram-Positive Bacterial Infections Give Rise to a Different Metabolic Response in a Mouse Model. *Journal of Proteome Research* [online]. 11 (6), pp. 3231–3245. Available from:
http://www.ncbi.nlm.nih.gov/pubmed/22483232doi:10.1021/pr201274r [Accessed 14 September 2019].

Hollmann, A., Martinez, M., Maturana, P., Semorile, L.C. and Maffia, P.C. (2018) Antimicrobial Peptides: Interaction With Model and Biological Membranes and Synergism With Chemical Antibiotics. *Frontiers in chemistry* [online]. 6 pp. 204. Available from:
http://www.ncbi.nlm.nih.gov/pubmed/29922648doi:10.3389/fchem.2018.00204 [Accessed 7 September 2019].

Holmberg, K. V., Abdolhosseini, M., Li, Y., Chen, X., Gorr, S.-U.U. and Aparicio, C. (2013) Bio-inspired stable antimicrobial peptide coatings for dental applications. *Acta Biomaterialia* [online]. 9 (9), pp. 8224–8231. Available from:
http://linkinghub.elsevier.com/retrieve/pii/S1742706113003012doi:10.1016/j.actbio.2013.06.017 [Accessed 22 July 2019].

Holzapfel, B.M., Reichert, J.C., Schantz, J.T., Gbureck, U., Rackwitz, L., Nöth, U., Jakob, F., Rudert, M., Groll, J. and Hutmacher, D.W. (2013) How smart do biomaterials need to be? A translational science and clinical point of view. *Advanced Drug Delivery Reviews* [online]. 65 (4), pp. 581–603. Available from:
http://dx.doi.org/10.1016/j.addr.2012.07.009doi:10.1016/j.addr.2012.07.009.

Horasawa, N., Yamashita, T., Uehara, S. and Udagawa, N. (2015) High-performance scaffolds on titanium surfaces: Osteoblast differentiation and mineralization promoted by a globular fibrinogen layer through cell-autonomous BMP signaling. *Materials Science and Engineering C* [online]. 46 pp. 86–96. Available from:
http://dx.doi.org/10.1016/j.msec.2014.10.025doi:10.1016/j.msec.2014.10.025 [Accessed 26 July 2019].

Hu, C., Ashok, D., Nisbet, D.R. and Gautam, V. (2019) Bioinspired surface modification of orthopedic implants for bone tissue engineering. *Biomaterials*. 219 pp. 119366. doi:10.1016/j.biomaterials.2019.119366.

Huang, J. (2018) A simple accurate formula for calculating saturation vapor pressure of water and ice. *Journal of Applied Meteorology and Climatology*. 57 (6), pp. 1265–1272. doi:10.1175/JAMC-D-17-0334.1.

Ibrahim, M.Z., Sarhan, A.A.D., Yusuf, F. and Hamdi, M. (2017) Biomedical materials and techniques to improve the tribological, mechanical and biomedical properties of orthopedic implants – A review article *Journal of Alloys and Compounds* 714 p.pp. 636–667. doi:10.1016/j.jallcom.2017.04.231.

Icer, M.A. and Gezmen-Karadag, M. (2018) The multiple functions and mechanisms of osteopontin *Clinical Biochemistry* 59 p.pp. 17–24. doi:10.1016/j.clinbiochem.2018.07.003.

Ijadpanah-Saravy, H., Safari, M., Khodadadi-Darban, A. and Rezaei, A. (2014) Synthesis of Titanium Dioxide Nanoparticles for Photocatalytic Degradation of Cyanide in Wastewater. *Analytical Letters* [online]. 47 (10), pp. 1772–1782. Available from: http://www.tandfonline.com/doi/abs/10.1080/00032719.2014.880170doi:10.1080/00032719.2014.880170 [Accessed 3 September 2019].

Ivanova, E.P., Hasan, J., Webb, H.K., Gervinskas, G., Juodkazis, S., Truong, V.K., Wu, A.H.F., Lamb, R.N., Baulin, V.A., Watson, G.S., Watson, J.A., Mainwaring, D.E. and Crawford, R.J. (2013) Bactericidal activity of black silicon. *Nature Communications*. 4 . doi:10.1038/ncomms3838.

Ivanova, E.P., Hasan, J., Webb, H.K., Truong, V.K., Watson, G.S., Watson, J. a., Baulin, V.A., Pogodin, S., Wang, J.Y., Tobin, M.J., L??bbe, C., Crawford, R.J., Löbbe, C., Crawford, R.J., et al. (2012) Natural bactericidal surfaces: Mechanical rupture of pseudomonas aeruginosa cells by cicada wings. *Small*. 8 (16), pp. 2489–2494. doi:10.1002/smll.201200528.

Jaggessar, A., Mathew, A., Wang, H., Tesfamichael, T., Yan, C. and Yarlagadda, P.K. (2018a) Mechanical, bactericidal and osteogenic behaviours of hydrothermally synthesised TiO 2 nanowire arrays. *Journal of the Mechanical Behavior of Biomedical Materials*. 80 pp. 311–319. doi:10.1016/j.jmbbm.2018.02.011.

Jaggessar, A., Mathew, A., Wang, H., Tesfamichael, T., Yan, C. and Yarlagadda, P.K. (2018b) Mechanical, bactericidal and osteogenic behaviours of hydrothermally synthesised TiO2 nanowire arrays. *Journal of the Mechanical Behavior of Biomedical Materials* [online]. 80 pp. 311–319. Available from: https://www.sciencedirect.com/science/article/pii/S1751616118301012 [Accessed 7 August 2019].

Jemat, A., Ghazali, M.J., Razali, M. and Otsuka, Y. (2015a) Surface Modifications and Their Effects on Titanium Dental Implants. *BioMed Research International*. 2015 pp. 1–12. doi:10.1155/2015/791725.

Jemat, A., Ghazali, M.J., Razali, M., Otsuka, Y., Jemat, A., Ghazali, M.J., Razali, M. and Otsuka, Y. (2015b) Surface Modifications and Their Effects on Titanium Dental Implants. *BioMed Research International* [online]. 2015 pp. 1–12. Available from: http://www.hindawi.com/journals/bmri/2015/791725/doi:10.1155/2015/791725.

Jenny Raynor, B.E., Petrie, T.A., García, A.J., Collard, D.M., García, A.J., Petrie, T.A., Collard, D.M. and Raynor, J.E. (2007) Controlling Cell Adhesion to Titanium: Functionalization of Poly[oligo(ethylene glycol)methacrylate] Brushes with Cell-Adhesive Peptides**. *Adv. Mater* [online]. 19 pp. 1724–1728. Available from: www.advmat.dedoi:10.1002/adma.200602129.

Jenssen, H., Hamill, P. and Hancock, R.E.W. (2006) Peptide antimicrobial agents. *Clinical Microbiology Reviews*. 19 (3), pp. 491–511. doi:10.1128/CMR.00056-05.

Jorge-Mora, A., Imaz, N., Garcia-Lecina, E., O'Connor, G.M., Gómez-Vaamonde, R., Alonso-Pérez, A., Franco-Trepat, E., García-Santiago, C., Pino-Minguez, J. and Nieto, D. (2018) In vitro response of bone marrow mesenchymal stem cells (hBMSCs) on laser-induced periodic surface structures for hard tissue replacement: Comparison between tantalum and titanium. *Optics and Lasers in Engineering* [online]. 111 pp. 34–41. Available from: https://www.sciencedirect.com/science/article/abs/pii/S014381661830558Xdoi:10.1016/J.OPTLASENG.2018.07.008 [Accessed 4 September 2019].

Jose, B., Antoci, V., Zeiger, A.R., Wickstrom, E. and Hickok, N.J. (2005) Vancomycin covalently bonded to titanium beads kills Staphylococcus aureus. *Chemistry and Biology*. 12 (9), pp. 1041–1048. doi:10.1016/j.chembiol.2005.06.013.

Junter, G.-A.A., Thébault, P. and Lebrun, L. (2015) Polysaccharide-based antibiofilm surfaces. *Acta Biomaterialia* [online]. 30 pp. 13–25. Available from: http://www.sciencedirect.com/science/article/pii/S1742706115301872doi:10.1016/j.actbio.2015.11.010 [Accessed 9 November 2015].

Jusman, Y., Ng, S.C. and Abu Osman, N.A. (2014) Investigation of CPD and HMDS sample preparation techniques for cervical cells in developing computer-aided screening system based on FE-SEM/EDX. *Scientific World Journal*. 2014 . doi:10.1155/2014/289817.

Kaja, S., Payne, A.J., Naumchuk, Y. and Koulen, P. (2017) Quantification of lactate dehydrogenase for cell viability testing using cell lines and primary cultured astrocytes.

Current Protocols in Toxicology. 2017 pp. 1–10. doi:10.1002/cptx.21.

Kaja, S., Payne, A.J., Singh, T., Ghuman, J.K., Sieck, E.G. and Koulen, P. (2015) An optimized lactate dehydrogenase release assay for screening of drug candidates in neuroscience. *Journal of Pharmacological and Toxicological Methods*. 73 pp. 1–6. doi:10.1016/j.vascn.2015.02.001.

Kaláb, M., Yang, A. and Chabot, D. (2008) Conventional Scanning Electron Microscopy of Bacteria. *Infocus*. pp. 44–61.

Kallala, R.F., Ibrahim, M.S., Sarmah, S., Haddad, F.S. and Vanhegan, I.S. (2015) Financial analysis of revision knee surgery based on NHS tariffs and hospital costs Does it pay to provide a revision service? *Bone and Joint Journal* 97-B (2) p.pp. 197–201. doi:10.1302/0301-620X.97B2.33707.

Kang, S.M., Kong, B., Oh, E., Choi, J.S. and Choi, I.S. (2010) Osteoconductive conjugation of bone morphogenetic protein-2 onto titanium/titanium oxide surfaces coated with non-biofouling poly(poly(ethylene glycol) methacrylate). *Colloids and Surfaces B: Biointerfaces*. doi:10.1016/j.colsurfb.2009.08.039.

Karam, L., Jama, C., Nuns, N., Mamede, A.S., Dhulster, P. and Chihib, N.E. (2013) Nisin adsorption on hydrophilic and hydrophobic surfaces: Evidence of its interactions and antibacterial activity. *Journal of Peptide Science*. doi:10.1002/psc.2512.

Karazisis, D., Ballo, A.M., Petronis, S., Agheli, H., Emanuelsson, L., Thomsen, P. and Omar, O. (2016) The role of well-defined nanotopography of titanium implants on osseointegration: Cellular and molecular events in vivo. *International Journal of Nanomedicine*. 11 pp. 1367–1382. doi:10.2147/IJN.S101294.

Kasuga, T., Hiramatsu, M., Hoson, A. and Sekino, T. (1998) Formation of Titanium Oxide Nanotube. *Langmuir*. 7463 (5), pp. 3160–3163. doi:10.1021/la9713816.

Kaur, M. and Singh, K. (2019) Review on titanium and titanium based alloys as biomaterials for orthopaedic applications *Materials Science and Engineering C* 102 p.pp. 844–862. doi:10.1016/j.msec.2019.04.064.

Kazemzadeh-Narbat, M., Kindrachuk, J., Duan, K., Jenssen, H., Hancock, R.E.W.W. and Wang, R. (2010) Antimicrobial peptides on calcium phosphate-coated titanium for the prevention of implant-associated infections. *Biomaterials* [online]. 31 (36), pp. 9519–9526. Available from: http://dx.doi.org/10.1016/j.biomaterials.2010.08.035doi:10.1016/j.biomaterials.2010.08.035 [Accessed 6 January 2016].

Kelleher, S.M., Habimana, O., Lawler, J., O'reilly, B., Daniels, S., Casey, E. and Cowley, A. (2016) Cicada Wing Surface Topography: An Investigation into the Bactericidal Properties of Nanostructural Features. *ACS Applied Materials and Interfaces*. 8 (24), pp. 14966–14974. doi:10.1021/acsami.5b08309.

Khang, D., Sato, M., Price, R.L., Ribbe, A.E. and Webster, T.J. (2006) Selective adhesion and mineral deposition by osteoblasts on carbon nanofiber patterns. *International journal of nanomedicine* [online]. 1 (1), pp. 65–72. Available from: http://www.ncbi.nlm.nih.gov/pubmed/17722263 [Accessed 26 August 2019].

Kiatkittipong, K., Iwase, A., Scott, J. and Amal, R. (2013) Photocatalysis of heat treated sodium- and hydrogen-titanate nanoribbons for water splitting, H2/O2 generation and oxalic acid oxidation. *Chemical Engineering Science* [online]. 93 pp. 341–349. Available from: http://dx.doi.org/10.1016/j.ces.2013.02.001doi:10.1016/j.ces.2013.02.001.

Kieffer, J. and Karkoulis, D. (2013) PyFAI, a versatile library for azimuthal regrouping. *Journal of Physics: Conference Series* [online]. 425 (PART 20), . Available from: https://hal.archives-ouvertes.fr/hal-01572836doi:10.1088/1742-6596/425/20/202012 [Accessed 29 August 2019].

Kim, D.H. and Wirtz, D. (2013) Focal adhesion size uniquely predicts cell migration. *FASEB Journal*. 27 (4), pp. 1351–1361. doi:10.1096/fj.12-220160.

Kim, W., Kim, D., Park, S., Lee, D., Hyun, H. and Kim, J. (2018) Engineering lotus leaf-inspired micro- and nanostructures for the manipulation of functional engineering platforms. *Journal of Industrial and Engineering Chemistry*. 61 pp. 39–52. doi:10.1016/j.jiec.2017.11.045.

Koch, K., Bhushan, B., Jung, Y.C. and Barthlott, W. (2009) Fabrication of artificial Lotus leaves and significance of hierarchical structure for superhydrophobicity and low adhesion. *Soft Matter*. 5 (7), pp. 1386–1393. doi:10.1039/b818940d.

Koizumi, H., Takeuchi, Y., Imai, H., Kawai, T. and Yoneyama, T. (2019) Application of titanium and titanium alloys to fixed dental prostheses *Journal of Prosthodontic Research* 63 (3) p.pp. 266–270. doi:10.1016/j.jpor.2019.04.011.

Kong, X.Y., Ding, Y., Yang, R. and Wang, Z.L. (2004) Single-Crystal Nanorings Formed by Epitaxial Self-Coiling of Polar Nanobelts. *Science* [online]. 303 (5662), pp. 1348–1351. Available from: http://www.ncbi.nlm.nih.gov/pubmed/14988559doi:10.1126/science.1092356 [Accessed 2 September 2019].

Kosgodagan Acharige, S., Laurent, J. and Steinberger, A. (2017) Capillary force on a tilted cylinder: Atomic Force Microscope (AFM) measurements. *Journal of Colloid and Interface Science*. doi:10.1016/j.jcis.2017.06.095.

Koyanagi, T., Sakamoto, M., Takeuchi, Y., Ohkuma, M. and Izumi, Y. (2010) Analysis of microbiota associated with peri-implantitis using 16S rRNA gene clone library. *Journal of Oral Microbiology*. 2 (2010), pp. 1–7. doi:10.3402/jom.v2i0.5104.

Kubiak, K., Adamczyk, Z. and Cieśla, M. (2016) Fibrinogen adsorption mechanisms at the gold substrate revealed by QCM-D measurements and RSA modeling. *Colloids and Surfaces B: Biointerfaces*. doi:10.1016/j.colsurfb.2015.11.052.

Kumar, P., Nagarajan, A. and Uchil, P.D. (2018) Analysis of Cell Viability by the Lactate Dehydrogenase Assay. *Cold Spring Harbor protocols* [online]. 2018 (6), . Available from: http://www.ncbi.nlm.nih.gov/pubmed/29858337doi:10.1101/pdb.prot095497 [Accessed 22 August 2019].

Lagonegro, P., Trevisi, G., Nasi, L., Paris, L., Manfredi, E., Lumetti, S., Rossi, F., Maculso, G.M., Salviati, G. and Galli, C. (2018) Osteoblasts preferentially adhere to peaks on micro-structured titanium. *Dental Materials Journal*. 37 (2), pp. 278–285. doi:10.4012/dmj.2017-008.

Lai, C.W., Bee Abd Hamid, S., Tan, T.L. and Lee, W.H. (2015) Rapid Formation of 1D Titanate Nanotubes Using Alkaline Hydrothermal Treatment and Its Photocatalytic Performance. *Journal of Nanomaterials*. 2015 pp. 1–8. doi:10.1155/2015/145360.

Lakshmaiah Narayana, J. and Chen, J.-Y. (2015) Antimicrobial peptides: Possible anti-infective agents. *Peptides* [online]. Available from: http://linkinghub.elsevier.com/retrieve/pii/S0196978115001680doi:10.1016/j.peptides.2015.05.012.

Lakshmanan, A., Zhang, S. and Hauser, C.A.E. (2012) Short self-assembling peptides as building blocks for modern nanodevices *Trends in Biotechnology*. doi:10.1016/j.tibtech.2011.11.001.

Lakshminarayanan, R., Tan, W.X., Aung, T.T., Goh, E.T.L., Muruganantham, N., Li, J., Chang, J.Y.T., Dikshit, N., Saraswathi, P., Lim, R.R., Kang, T.S., Balamuralidhar, V., Sukumaran, B., Verma, C.S., et al. (2016) Branched peptide, B2088, disrupts the supramolecular organization of lipopolysaccharides and sensitizes the gram-negative bacteria. *Scientific Reports*. 6 . doi:10.1038/srep25905.

Laverty, G., Gorman, S.P. and Gilmore, B.F. (2011) The Potential of Antimicrobial Peptides as

Biocides. *International Journal of Molecular Sciences* [online]. 12 (12), pp. 6566–6596. Available from: http://www.mdpi.com/1422-0067/12/10/6566/doi:10.3390/ijms12106566.

Lawson, M.C., Hoth, K.C., Deforest, C.A., Bowman, C.N. and Anseth, K.S. (2010) Inhibition of staphylococcus epidermidis biofilms using polymerizable vancomycin derivatives. In: *Clinical Orthopaedics and Related Research*. 2010 (no place) Springer New York. pp. 2081–2091. doi:10.1007/s11999-010-1266-z.

Lee, L.C.Y., Gadegaard, N., de Andrés, M.C., Turner, L.A., Burgess, K. V., Yarwood, S.J., Wells, J., Salmeron-Sanchez, M., Meek, D., Oreffo, R.O.C. and Dalby, M.J. (2017) Nanotopography controls cell cycle changes involved with skeletal stem cell self-renewal and multipotency. *Biomaterials*. doi:10.1016/j.biomaterials.2016.11.032.

Lee, S.J., Heo, D.N., Lee, H.R., Lee, D., Yu, S.J., Park, S.A., Ko, W.K., Park, S.W., Im, S.G., Moon, J.H. and Kwon, I.K. (2015) Biofunctionalized titanium with anti-fouling resistance by grafting thermo-responsive polymer brushes for the prevention of peri-implantitis. *Journal of Materials Chemistry B*. 3 (26), pp. 5161–5165. doi:10.1039/c5tb00611b.

Lemire, J.A., Harrison, J.J. and Turner, R.J. (2013) Antimicrobial activity of metals: Mechanisms, molecular targets and applications *Nature Reviews Microbiology*. doi:10.1038/nrmicro3028.

Li, Y., Xiang, Q., Zhang, Q., Huang, Y. and Su, Z. (2012) Overview on the recent study of antimicrobial peptides: Origins, functions, relative mechanisms and application. *Peptides* [online]. 37 (2), pp. 207–215. Available from: http://dx.doi.org/10.1016/j.peptides.2012.07.001doi:10.1016/j.peptides.2012.07.001.

Liao, D.L., Wu, G.S. and Liao, B.Q. (2009) Zeta potential of shape-controlled TiO2 nanoparticles with surfactants. *Colloids and Surfaces A: Physicochemical and Engineering Aspects*. doi:10.1016/j.colsurfa.2009.07.036.

Lima, W.C., Pillonel, T., Bertelli, C., Ifrid, E., Greub, G. and Cosson, P. (2018) Genome sequencing and functional characterization of the non-pathogenic Klebsiella pneumoniae KpGe bacteria. *Microbes and Infection* [online]. 20 (5), pp. 293–301. Available from: https://doi.org/10.1016/j.micinf.2018.04.001doi:10.1016/j.micinf.2018.04.001.

Limoli, D.H., Rockel, A.B., Host, K.M., Jha, A., Kopp, B.T., Hollis, T. and Wozniak, D.J. (2014) Cationic Antimicrobial Peptides Promote Microbial Mutagenesis and Pathoadaptation in Chronic Infections Frederick M. Ausubel (ed.). *PLoS Pathogens* [online]. 10 (4), pp. e1004083. Available from: http://www.ncbi.nlm.nih.gov/pubmed/24763694doi:10.1371/journal.ppat.1004083

[Accessed 6 September 2019].

Lin, L., Wang, H., Ni, M., Rui, Y., Cheng, T.-Y., Cheng, C.-K., Pan, X., Li, G. and Lin, C. (2014) Enhanced osteointegration of medical titanium implant with surface modifications in micro/nanoscale structures. *Journal of Orthopaedic Translation* [online]. 2 (1), pp. 35–42. Available from: http://www.sciencedirect.com/science/article/pii/S2214031X13000491doi:10.1016/j.jot.2013.08.001.

Linklater, D.P., Juodkazis, S., Crawford, R.J. and Ivanova, E.P. (2019) Mechanical inactivation of Staphylococcus aureus and Pseudomonas aeruginosa by titanium substrata with hierarchical surface structures. *Materialia* [online]. 5 pp. 100197. Available from: https://www.sciencedirect.com/science/article/pii/S2589152918302370#bib0036doi:10.1016/J.MTLA.2018.100197 [Accessed 4 September 2019].

Linklater, D.P., Nguyen, H.K.D., Bhadra, C.M., Juodkazis, S. and Ivanova, E.P. (2017) Influence of nanoscale topology on bactericidal efficiency of black silicon surfaces. *Nanotechnology* [online]. 28 (24), pp. 245301. Available from: http://www.ncbi.nlm.nih.gov/pubmed/28534474doi:10.1088/1361-6528/aa700e [Accessed 7 August 2019].

Listgarten, M.A., Lang, N.P., Schroeder, H.E. and Schroeder, A. (1991) Periodontal tissues and their counterparts around endosseous implants [corrected and republished with original paging, article orginally printed in Clin Oral Implants Res 1991 Jan-Mar;2(1):1-19]. *Clinical oral implants research* [online]. 2 (3), pp. 1–19. Available from: http://www.ncbi.nlm.nih.gov/pubmed/1843462 [Accessed 7 August 2019].

Liu, B., Boercker, J.E. and Aydil, E.S. (2008) Oriented single crystalline titanium dioxide nanowires. *Nanotechnology* [online]. 19 pp. 505604. Available from: http://www.ncbi.nlm.nih.gov/pubmed/19942776doi:10.1088/0957-4484/19/50/505604.

Liu, H., Niinomi, M., Nakai, M., Obara, S. and Fujii, H. (2017) Improved fatigue properties with maintaining low Young's modulus achieved in biomedical beta-type titanium alloy by oxygen addition. *Materials Science and Engineering: A* [online]. 704 pp. 10–17. Available from: https://www.sciencedirect.com/science/article/abs/pii/S092150931730984Xdoi:10.1016/J.MSEA.2017.07.078 [Accessed 4 September 2019].

Liu, N., Chen, X., Zhang, J. and Schwank, J.W. (2014) A review on TiO2-based nanotubes synthesized via hydrothermal method: Formation mechanism, structure modification, and photocatalytic applications. *Catalysis Today* [online]. 225 pp. 34–51. Available from:

http://dx.doi.org/10.1016/j.cattod.2013.10.090doi:10.1016/j.cattod.2013.10.090.

Liu, Y. and Mustapha, A. (2014) Detection of viable Escherichia coli O157: H7 in ground beef by propidium monoazide real-time PCR. *International Journal of Food Microbiology*. 170 pp. 48–54. doi:10.1016/j.ijfoodmicro.2013.10.026.

Liu, Y. and Wang, J. (2017) Influences of microgap and micromotion of implant–abutment interface on marginal bone loss around implant neck. *Archives of Oral Biology* [online]. 83 pp. 153–160. Available from: https://www.sciencedirect.com/science/article/pii/S0003996917302431doi:10.1016/J.ARCHORALBIO.2017.07.022 [Accessed 4 September 2019].

López Zavala, M.Á., Lozano Morales, S.A. and Ávila-Santos, M. (2017) Synthesis of stable TiO2 nanotubes: effect of hydrothermal treatment, acid washing and annealing temperature. *Heliyon* [online]. 3 (11), pp. e00456. Available from: http://dx.doi.org/10.1016/j.heliyon.2017.e00456doi:10.1016/j.heliyon.2017.e00456.

Lorenzetti, M., Dogša, I., Stošicki, T., Stopar, D., Kalin, M., Kobe, S. and Novak, S. (2015) The influence of surface modification on bacterial adhesion to titanium-based substrates. *ACS Applied Materials and Interfaces*. 7 (3), pp. 1644–1651. doi:10.1021/am507148n.

Lotz, E.M., Berger, M.B., Schwartz, Z. and Boyan, B.D. (2018) Regulation of osteoclasts by osteoblast lineage cells depends on titanium implant surface properties. *Acta Biomaterialia*. doi:10.1016/j.actbio.2017.12.039.

Lowin, T., Bleck, J., Schneider, M. and Pongratz, G. (2018) Selective killing of proinflammatory synovial fibroblasts via activation of transient receptor potential ankyrin (TRPA1). *Biochemical Pharmacology* [online]. 154 pp. 293–302. Available from: https://www.sciencedirect.com/science/article/abs/pii/S0006295218302016doi:10.1016/J.BCP.2018.05.015 [Accessed 13 September 2019].

Loye, A.M., Kinser, E.R., Bensouda, S., Shayan, M., Davis, R., Wang, R., Chen, Z., Schwarz, U.D., Schroers, J. and Kyriakides, T.R. (2018) Regulation of Mesenchymal Stem Cell Differentiation by Nanopatterning of Bulk Metallic Glass. *Scientific Reports*. 8 (1), . doi:10.1038/s41598-018-27098-6.

Lozeau, L.D., Alexander, T.E. and Camesano, T.A. (2015) Proposed Mechanisms of Tethered Antimicrobial Peptide Chrysophsin-1 as a Function of Tether Length Using QCM-D. *Journal of Physical Chemistry B*. doi:10.1021/acs.jpcb.5b06883.

Luan, Y., Liu, S., Pihl, M., van der Mei, H.C., Liu, J., Hizal, F., Choi, C.-H., Chen, H., Ren, Y. and Busscher, H.J. (2018) Bacterial interactions with nanostructured surfaces. *Current*

Opinion in Colloid & Interface Science [online]. 38 pp. 170–189. Available from: https://www.sciencedirect.com/science/article/pii/S135902941830089Xdoi:10.1016/J.COCIS.2018.10.007 [Accessed 14 September 2019].

Lutwick, L., Al-Maani, A.S., Mehtar, S., Memish, Z., Rosenthal, V.D., Dramowski, A., Lui, G., Osman, T., Bulabula, A. and Bearman, G. (2019) Managing and preventing vascular catheter infections: A position paper of the international society for infectious diseases *International Journal of Infectious Diseases* 84 p.pp. 22–29. doi:10.1016/j.ijid.2019.04.014.

Mah, T.F.C. and O'Toole, G.A. (2001) Mechanisms of biofilm resistance to antimicrobial agents *Trends in Microbiology* 9 (1) p.pp. 34–39. doi:10.1016/S0966-842X(00)01913-2.

Mahlapuu, M., Håkansson, J., Ringstad, L. and Björn, C. (2016) Antimicrobial Peptides: An Emerging Category of Therapeutic Agents. *Frontiers in cellular and infection microbiology* [online]. 6 pp. 194. Available from: http://www.ncbi.nlm.nih.gov/pubmed/28083516doi:10.3389/fcimb.2016.00194 [Accessed 3 September 2019].

Majhi, S., Arora, A. and Mishra, A. (2019) Surface immobilization of a short antimicrobial peptide (AMP) as an antibacterial coating. *Materialia*. doi:10.1016/j.mtla.2019.100350.

Malanovic, N. and Lohner, K. (2016) Gram-positive bacterial cell envelopes: The impact on the activity of antimicrobial peptides. *Biochimica et Biophysica Acta - Biomembranes* [online]. 1858 (5), pp. 936–946. Available from: http://dx.doi.org/10.1016/j.bbamem.2015.11.004doi:10.1016/j.bbamem.2015.11.004.

Mann, E.E., Manna, D., Mettetal, M.R., May, R.M., Dannemiller, E.M., Chung, K.K., Brennan, A.B. and Reddy, S.T. (2014) Surface micropattern limits bacterial contamination. *Antimicrobial Resistance and Infection Control*. 3 (1), . doi:10.1186/2047-2994-3-28.

Maria-Neto, S., de Almeida, K.C., Macedo, M.L.R. and Franco, O.L. (2015) Understanding bacterial resistance to antimicrobial peptides: from the surface to deep inside. *Biochimica et biophysica acta* [online]. 1848 (11), pp. 3078–3088. Available from: http://www.sciencedirect.com/science/article/pii/S0005273615000577doi:10.1016/j.bbamem.2015.02.017 [Accessed 3 March 2015].

Martynowycz, M.W., Zhao, W., Hattne, J., Jensen, G.J. and Gonen, T. (2019) Qualitative analyses of polishing and pre-coating FIB milled crystals for MicroED. *bioRxiv*. pp. 1–16. doi:10.1101/613042.

Mas-Moruno, C., Espanol, M., Montufar, E.B., Mestres, G., Aparicio, C., Gil, F.J. and Ginebra,

M.P. (2013) Bioactive Ceramic and Metallic Surfaces for Bone Engineering. In: *Biomaterials Surface Science*. doi:10.1002/9783527649600.ch12.

Matta, C., Szűcs-Somogyi, C., Kon, E., Robinson, D., Neufeld, T., Altschuler, N., Berta, A., Hangody, L., Veréb, Z. and Zákány, R. (2019) Osteogenic differentiation of human bone marrow-derived mesenchymal stem cells is enhanced by an aragonite scaffold. *Differentiation*. 107 pp. 24–34. doi:10.1016/j.diff.2019.05.002.

Matthäus, F., Jagodič, M. and Dobnikar, J. (2009) E. coli superdiffusion and chemotaxis-search strategy, precision, and motility. *Biophysical Journal*. 97 (4), pp. 946–957. doi:10.1016/j.bpj.2009.04.065.

Mavrogenis, A.F., Dimitriou, R., Parvizi, J. and Babis, G.C. (2009) Biology of implant osseointegration. *Journal of Musculoskeletal Neuronal Interactions*. 9 (2), pp. 61–71. doi:10.1016/j.joms.2007.05.013.

May, P.W., Clegg, M., Silva, T.A., Zanin, H., Fatibello-Filho, O., Celorrio, V., Fermin, D.J., Welch, C.C., Hazell, G., Fisher, L., Nobbs, A. and Su, B. (2016) Diamond-coated 'black silicon' as a promising material for high-surface-area electrochemical electrodes and antibacterial surfaces. *Journal of Materials Chemistry B*. doi:10.1039/c6tb01774f.

McCloskey, A., Gilmore, B. and Laverty, G. (2014) Evolution of Antimicrobial Peptides to Self-Assembled Peptides for Biomaterial Applications. *Pathogens*. doi:10.3390/pathogens3040791.

Mei, S., Wang, H., Wang, W., Tong, L., Pan, H., Ruan, C., Ma, Q., Liu, M., Yang, H., Zhang, L., Cheng, Y., Zhang, Y., Zhao, L. and Chu, P.K. (2014) Antibacterial effects and biocompatibility of titanium surfaces with graded silver incorporation in titania nanotubes. *Biomaterials*. doi:10.1016/j.biomaterials.2014.02.005.

Meng, Q., Zhang, J., Huo, Y., Sui, Y., Zhang, J., Guo, S. and Zhao, X. (2018) Design of low modulus β-type titanium alloys by tuning shear modulus C44. *Journal of Alloys and Compounds* [online]. 745 pp. 579–585. Available from: https://www.sciencedirect.com/science/article/abs/pii/S0925838818307485doi:10.1016/JJALLCOM.2018.02.259 [Accessed 4 September 2019].

Mi, L. and Jiang, S. (2014) Integrated antimicrobial and nonfouling zwitterionic polymers *Angewandte Chemie - International Edition* 53 (7) p.pp. 1746–1754. doi:10.1002/anie.201304060.

Mishra, B. and Wang, G. (2017) Titanium surfaces immobilized with the major antimicrobial fragment FK-16 of human cathelicidin LL-37 are potent against multiple antibiotic-

resistant bacteria. *Biofouling*. doi:10.1080/08927014.2017.1332186.

Muszanska, A.K., Rochford, E.T.J., Gruszka, A., Bastian, A.A., Busscher, H.J., Norde, W., Van Der Mei, H.C. and Herrmann, A. (2014) Antiadhesive polymer brush coating functionalized with antimicrobial and RGD peptides to reduce biofilm formation and enhance tissue integration. *Biomacromolecules*. 15 (6), pp. 2019–2026. doi:10.1021/bm500168s.

Nadeem, D., Sjostrom, T., Wilkinson, A., Smith, C.-A., Oreffo, R.O.C., Dalby, M.J. and Su, B. (2013) Embossing of micropatterned ceramics and their cellular response. *Journal of biomedical materials research. Part A* [online]. 101 (11), pp. 3247–3255. Available from: http://www.ncbi.nlm.nih.gov/pubmed/23554267doi:10.1002/jbm.a.34622.

Nagasawa, M., Cooper, L.F., Ogino, Y., Mendonca, D., Liang, R., Yang, S., Mendonca, G. and Uoshima, K. (2016) Topography Influences Adherent Cell Regulation of Osteoclastogenesis. *Journal of Dental Research*. doi:10.1177/0022034515616760.

Narayanan, R., Seshadri, S.K., Kwon, T.Y. and Kim, K.H. (2008) Calcium phosphate-based coatings on titanium and its alloys. *Journal of Biomedical Materials Research - Part B Applied Biomaterials*. 85 (1), pp. 279–299. doi:10.1002/jbm.b.30932.

National Joint Registry (2015) 12th Annual Report. *12th Annulary Report*. 12 (December 2014), pp. 81–88.

National Joint Registry (2018) National Joint Registry for England, Wales, Northern Ireland and Isle of Man: 15th Annual Report 2018. *15th Annual Report* [online]. 1821 (December 2017), pp. 218. Available from: http://www.njrcentre.org.uk/njrcentre/default.aspxdoi:10.1038/nmat2505.

Nguyen, L.T., Haney, E.F. and Vogel, H.J. (2011) The expanding scope of antimicrobial peptide structures and their modes of action. *Trends in Biotechnology* [online]. 29 (9), pp. 464–472. Available from: http://dx.doi.org/10.1016/j.tibtech.2011.05.001doi:10.1016/j.tibtech.2011.05.001.

NHS Digital (2018) *Statistics on Obesity, Physical Activity and Diet* [online]. Available from: www.statisticsauthority.gov.uk/assessment/code-of- [Accessed 4 September 2019].

Nie, B., Ao, H., Chen, C., Xie, K., Zhou, J., Long, T., Tang, T. and Yue, B. (2016) Covalent immobilization of KR-12 peptide onto a titanium surface for decreasing infection and promoting osteogenic differentiation. *RSC Advances* [online]. 6 (52), pp. 46733–46743. Available from: www.rsc.org/advancesdoi:10.1039/c6ra06778f.

Nocker, A. and Camper, A.K. (2009) Novel approaches toward preferential detection of viable cells using nucleic acid amplification techniques *FEMS Microbiology Letters* 291 (2) p.pp. 137–142. doi:10.1111/j.1574-6968.2008.01429.x.

Nocker, A., Sossa-Fernandez, P., Burr, M.D. and Camper, A.K. (2007) Use of propidium monoazide for live/dead distinction in microbial ecology *Applied and Environmental Microbiology* 73 (16) p.pp. 5111–5117. doi:10.1128/AEM.02987-06.

Nowlin, K., Boseman, A., Covell, A. and LaJeunesse, D. (2014) Adhesion-dependent rupturing of Saccharomyces cerevisiae on biological antimicrobial nanostructured surfaces. *Journal of the Royal Society Interface*. 12 (102), . doi:10.1098/rsif.2014.0999.

Ofei, F. (2005) Obesity - a preventable disease. *Ghana medical journal* [online]. 39 (3), pp. 98–101. Available from: http://www.ncbi.nlm.nih.gov/pubmed/17299552 [Accessed 26 August 2019].

Office for National Statistics (2017) Overview of the UK Population: March 2017 *ONS (Office of National Statistics)* [online] (March). Available from: https://www.ons.gov.uk/peoplepopulationandcommunity/populationandmigration/populationestimates/articles/overviewoftheukpopulation/mar2017doi:10.1155/APEC.9.9.

Oh, S.L., Shiau, H.J. and Reynolds, M.A. (2019) Survival of dental implants at sites after implant failure: A systematic review *Journal of Prosthetic Dentistry*. doi:10.1016/j.prosdent.2018.11.007.

Oldani, C. and Dominguez, A. (2012) Titanium as a Biomaterial for Implants. *Intechopen* [online]. pp. 149–162. Available from: http://www.intechopen.com/books/recent-advances-in-arthroplasty/titanium-as-a-biomaterial-for-implants%5Cnhttp://www.intechopen.com/source/pdfs/26862/InTech-Titanium_as_a_biomaterial_for_implants.pdfdoi:10.5772/1445.

Onaizi, S. a and Leong, S.S.J. (2011) Tethering antimicrobial peptides: current status and potential challenges. *Biotechnology advances* [online]. 29 (1), pp. 67–74. Available from: http://www.ncbi.nlm.nih.gov/pubmed/20817088doi:10.1016/j.biotechadv.2010.08.012.

Orapiriyakul, W., Young, P.S., Damiati, L. and Tsimbouri, P.M. (2018) Antibacterial surface modification of titanium implants in orthopaedics. *Journal of tissue engineering* [online]. 9 pp. 2041731418789838. Available from: http://www.ncbi.nlm.nih.gov/pubmed/30083308doi:10.1177/2041731418789838 [Accessed 4 September 2019].

Ou, H. and Lo, S. (2007) Review of titania nanotubes synthesized via the hydrothermal

treatment: Fabrication, modification, and application. *Separation and Purification Technology* [online]. 58 (1), pp. 179–191. Available from: http://linkinghub.elsevier.com/retrieve/pii/S1383586607003309doi:10.1016/j.seppur.2007.07.017.

Pajerski, W., Ochonska, D., Brzychczy-Wloch, M., Indyka, P., Jarosz, M., Golda-Cepa, M., Sojka, Z. and Kotarba, A. (2019) Attachment efficiency of gold nanoparticles by Gram-positive and Gram-negative bacterial strains governed by surface charges. *Journal of Nanoparticle Research*. 21 (8), . doi:10.1007/s11051-019-4617-z.

Parithimarkalaignan, S. and Padmanabhan, T. V. (2013) Osseointegration: An update. *Journal of Indian Prosthodontist Society*. 13 (1), pp. 2–6. doi:10.1007/s13191-013-0252-z.

Parvizi, J., Wickstrom, E., Zeiger, A.R., Adams, C.S., Shapiro, I.M., Purtill, J.J., Sharkey, P.F., Hozack, W.J., Rothman, R.H. and Hickok, N.J. (2004) Frank Stinchfield award: Titanium surface with biologic activity against infection. In: *Clinical Orthopaedics and Related Research*. 2004 (no place) Lippincott Williams and Wilkins. pp. 33–38. doi:10.1097/01.blo.0000150116.65231.45.

Pavlukhina, S., Zhuk, I., Mentbayeva, A., Rautenberg, E., Chang, W., Yu, X., Van De Belt-Gritter, B., Busscher, H.J., Van Der Mei, H.C. and Sukhishvili, S.A. (2014) Small-molecule-hosting nanocomposite films with multiple bacteria-triggered responses. *NPG Asia Materials*. doi:10.1038/am.2014.63.

Peng, G., Li, S., Peng, Q., Li, Y., Weng, J., Jia, Z., Kang, J., Lei, X., Zhang, G. and Gao, Y. (2017) Immobilization of native type i collagen on polypropylene fabrics as a substrate for HepG2 cell culture. *Journal of Biomaterials Applications* [online]. 32 (1), pp. 93–103. Available from: http://journals.sagepub.com/doi/10.1177/0885328217709607doi:10.1177/0885328217709607 [Accessed 3 September 2019].

Perron, G.G., Zasloff, M. and Bell, G. (2006) Experimental evolution of resistance to an antimicrobial peptide. *Proceedings of the Royal Society B: Biological Sciences*. 273 (1583), pp. 251–256. doi:10.1098/rspb.2005.3301.

Petersen, G.E., Tang, Y. and Fields, C. (2019) Chemical and in vitro toxicity analysis of a supercritical fluid extract of Kava kava (Piper methysticum). *Journal of Ethnopharmacology* [online]. 235 pp. 301–308. Available from: https://www.sciencedirect.com/science/article/pii/S0378874118340534doi:10.1016/J.JEP.2019.01.032 [Accessed 13 September 2019].

Pfalzgraff, A., Brandenburg, K. and Weindl, G. (2018) Antimicrobial Peptides and Their Therapeutic Potential for Bacterial Skin Infections and Wounds. *Frontiers in pharmacology* [online]. 9 pp. 281. Available from: http://www.ncbi.nlm.nih.gov/pubmed/29643807doi:10.3389/fphar.2018.00281 [Accessed 8 September 2019].

Pfeil, M.P., Pyne, A.L.B., Losasso, V., Ravi, J., Lamarre, B., Faruqui, N., Alkassem, H., Hammond, K., Judge, P.J., Winn, M., Martyna, G.J., Crain, J., Watts, A., Hoogenboom, B.W., et al. (2018) Tuneable poration: host defense peptides as sequence probes for antimicrobial mechanisms. *Scientific Reports*. 8 (1), pp. 1–15. doi:10.1038/s41598-018-33289-y.

Pinto, I.B., dos Santos Machado, L., Meneguetti, B.T., Nogueira, M.L., Espínola Carvalho, C.M., Roel, A.R. and Franco, O.L. (2019) Utilization of antimicrobial peptides, analogues and mimics in creating antimicrobial surfaces and bio-materials *Biochemical Engineering Journal*. doi:10.1016/j.bej.2019.107237.

Pisoni, D.B., Kronenberger, W.G., Harris, M.S. and Moberly, A.C. (2017) Three challenges for future research on cochlear implants. *World Journal of Otorhinolaryngology - Head and Neck Surgery*. 3 (4), pp. 240–254. doi:10.1016/j.wjorl.2017.12.010.

Pogodin, S., Hasan, J., Baulin, V.A., Webb, H.K., Truong, V.K., Phong Nguyen, T.H., Boshkovikj, V., Fluke, C.J., Watson, G.S., Watson, J.A., Crawford, R.J. and Ivanova, E.P. (2013) Biophysical Model of Bacterial Cell Interactions with Nanopatterned Cicada Wing Surfaces. *Biophysical Journal* [online]. 104 (4), pp. 835–840. Available from: http://linkinghub.elsevier.com/retrieve/pii/S0006349513000039doi:10.1016/j.bpj.2012.12.046.

Prasad, S., Ehrensberger, M., Gibson, M.P., Kim, H. and Monaco, E.A. (2015) Biomaterial properties of titanium in dentistry *Journal of Oral Biosciences* 57 (4) p.pp. 192–199. doi:10.1016/j.job.2015.08.001.

Prez Ladrón De Guevara, H., Rodríguez, A.G., Navarro-Contreras, H. and Vidal, M.A. (2007) Nonlinear behavior of the energy gap in Ge1-x Snx alloys at 4 K. *Applied Physics Letters*. 91 (16), . doi:10.1063/1.2800296.

Promega (2016a) *BacTiter-Glo™ Microbial Cell Viability Assay Instructions for Use of Products G8230, G8231, G8232 and G8233* [online]. Available from: https://worldwide.promega.com/-/media/files/resources/protocols/technical-bulletins/101/bactiter-glo-microbial-cell-viability-assay-protocol.pdf?la=en [Accessed 28 August 2019].

Promega (2012) *CytoTox 96® non-radioactive cytotoxicity assay. Instructions for use of product G1780.* [online]. Available from: www.promega.com [Accessed 28 August 2019].

Promega (2016b) *RealTime-Glo™ MT Cell Viability Assay Instructions for Use of Products G9711, G9712 and G9713* [online]. Available from: www.promega.com [Accessed 28 August 2019].

Pye, A.D., Lockhart, D.E.A., Dawson, M.P., Murray, C.A. and Smith, A.J. (2009) A review of dental implants and infection *Journal of Hospital Infection* 72 (2) p.pp. 104–110. doi:10.1016/j.jhin.2009.02.010.

Qi, X., Poernomo, G., Wang, K., Chen, Y., Chan-Park, M.B., Xu, R. and Chang, M.W. (2011) Covalent immobilization of nisin on multi-walled carbon nanotubes: Superior antimicrobial and anti-biofilm properties. *Nanoscale* [online]. 3 (4), pp. 1874–1880. Available from: www.rsc.org/nanoscaledoi:10.1039/c1nr10024f.

Qu, J., Lu, X., Li, D., Ding, Y., Leng, Y., Weng, J., Qu, S., Feng, B. and Watari, F. (2011) Silver/hydroxyapatite composite coatings on porous titanium surfaces by sol-gel method. *Journal of Biomedical Materials Research - Part B Applied Biomaterials*. 97 B (1), pp. 40–48. doi:10.1002/jbm.b.31784.

Querido, M.M., Aguiar, L., Neves, P., Pereira, C.C. and Teixeira, J.P. (2019) Self-disinfecting surfaces and infection control *Colloids and Surfaces B: Biointerfaces* 178 p.pp. 8–21. doi:10.1016/j.colsurfb.2019.02.009.

Quintas Victor, Prada-Lopez and Carmona Inmaculada Tomas (2014) Analyzing the oral biofilm using fluorescence-based microscopy: what's in a dye? *Microscopy: advances in scientific research and education*. doi:10.13140/2.1.2104.5762.

Raikar, S., Talukdar, P., Kumari, S., Panda, S.K., Oommen, V.M. and Prasad, A. (2017) Factors affecting the survival rate of dental implants: A retrospective study. *Journal of International Society of Preventive and Community Dentistry*. 7 (6), pp. 351–355. doi:10.4103/jispcd.JISPCD_380_17.

Ramanauskaite, A. and Juodzbalys, G. (2016) Diagnostic Principles of Peri-Implantitis: a Systematic Review and Guidelines for Peri-Implantitis Diagnosis Proposal. *Journal of Oral and Maxillofacial Research* [online]. 7 (3), pp. e8. Available from: http://www.ncbi.nlm.nih.gov/pubmed/27833733doi:10.5037/jomr.2016.7308 [Accessed 2 September 2019].

Raphel, J., Holodniy, M., Goodman, S.B. and Heilshorn, S.C. (2016a) Multifunctional coatings to simultaneously promote osseointegration and prevent infection of orthopaedic implants.

Biomaterials [online]. 84 pp. 301–314. Available from: http://www.sciencedirect.com/science/article/pii/S0142961216000181doi:10.1016/j.biomaterials.2016.01.016.

Raphel, J., Karlsson, J., Galli, S., Wennerberg, A., Lindsay, C., Haugh, M.G., Pajarinen, J., Goodman, S.B., Jimbo, R., Andersson, M. and Heilshorn, S.C. (2016b) Engineered protein coatings to improve the osseointegration of dental and orthopaedic implants. *Biomaterials* [online]. 83 pp. 269–282. Available from: http://dx.doi.org/10.1016/j.biomaterials.2015.12.030doi:10.1016/j.biomaterials.2015.12.030.

Rapuano, B.E. and MacDonald, D.E. (2011) Surface oxide net charge of a titanium alloy: modulation of fibronectin-activated attachment and spreading of osteogenic cells. *Colloids and surfaces. B, Biointerfaces* [online]. 82 (1), pp. 95–103. Available from: http://www.ncbi.nlm.nih.gov/pubmed/20884181doi:10.1016/j.colsurfb.2010.08.023 [Accessed 26 July 2019].

Ready, D., Theodoridis, G., Green, I., Ciric, L., Pratten, J., Tay, W. and McDonald, A. (2015) In vitro evaluation of the antibiofilm properties of chlorhexidine and delmopinol on dental implant surfaces. *International Journal of Antimicrobial Agents*. doi:10.1016/j.ijantimicag.2015.01.020.

Reeks, B.Y., Champlin, F.R., Paulsen, D.B., Scruggs, D.W. and Lawrence, M.L. (2005) Effects of sub-minimum inhibitory concentration antibiotic levels and temperature on growth kinetics and outer membrane protein expression in Mannheimia haemolytica and Haemophilus somnus. *Canadian journal of veterinary research = Revue canadienne de recherche vétérinaire* [online]. 69 (1), pp. 1–10. Available from: http://www.pubmedcentral.nih.gov/articlerender.fcgi?artid=1142163&tool=pmcentrez&rendertype=abstract [Accessed 4 December 2015].

Reyneke, B., Dobrowsky, P.H., Ndlovu, T., Khan, S. and Khan, W. (2016) EMA-qPCR to monitor the efficiency of a closed-coupled solar pasteurization system in reducing Legionella contamination of roof-harvested rainwater. *Science of The Total Environment* [online]. 553 pp. 662–670. Available from: https://www.sciencedirect.com/science/article/pii/S0048969716303084doi:10.1016/J.SCITOTENV.2016.02.108 [Accessed 13 September 2019].

Ribeiro, M., Monteiro, F.J. and Ferraz, M.P. (2012) Infection of orthopedic implants with emphasis on bacterial adhesion process and techniques used in studying bacterial-material interactions. *Biomatter* [online]. 2 (4), pp. 176–194. Available from:

http://www.pubmedcentral.nih.gov/articlerender.fcgi?artid=3568104&tool=pmcentrez&rendertype=abstractdoi:10.4161/biom.22905 [Accessed 22 February 2016].

Richert, L., Variola, F., Rosei, F., Wuest, J.D. and Nanci, A. (2010) Adsorption of proteins on nanoporous Ti surfaces. *Surface Science*. doi:10.1016/j.susc.2010.05.007.

Roach, P., Shirtcliffe, N.J. and Newton, M.I. (2008) Progess in superhydrophobic surface development. *Soft Matter*. 4 (2), pp. 224. doi:10.1039/b712575p.

Robertson, J., McGoverin, C., Vanholsbeeck, F. and Swift, S. (2019) Optimisation of the protocol for the liVE/DEAD®BacLightTM bacterial viability kit for rapid determination of bacterial load. *Frontiers in Microbiology*. 10 (APR), . doi:10.3389/fmicb.2019.00801.

Roccatano, D., Sarukhanyan, E. and Zangi, R. (2017) Adsorption mechanism of an antimicrobial peptide on carbonaceous surfaces: A molecular dynamics study. *Journal of Chemical Physics* [online]. 146 (7), pp. 074703. Available from: http://aip.scitation.org/doi/10.1063/1.4975689doi:10.1063/1.4975689 [Accessed 29 July 2019].

Romero-Brey, I. and Bartenschlager, R. (2015) Viral infection at high magnification: 3D electron microscopy methods to analyze the architecture of infected cells. *Viruses* [online]. 7 (12), pp. 6316–6345. Available from: http://www.ncbi.nlm.nih.gov/pubmed/26633469doi:10.3390/v7122940 [Accessed 15 September 2019].

Rosenberg, M., Azevedo, N.F. and Ivask, A. (2019) Propidium iodide staining underestimates viability of adherent bacterial cells. *Scientific Reports*. 9 (1), . doi:10.1038/s41598-019-42906-3.

Rosset, E.M. and Bradshaw, A.D. (2016) SPARC/osteonectin in mineralized tissue *Matrix Biology* 52–54 p.pp. 78–87. doi:10.1016/j.matbio.2016.02.001.

Rupp, F., Liang, L., Geis-Gerstorfer, J., Scheideler, L. and Hüttig, F. (2018) Surface characteristics of dental implants: A review *Dental Materials* 34 (1) p.pp. 40–57. doi:10.1016/j.dental.2017.09.007.

Rutkovskiy, A., Stensløkken, K.-O. and Vaage, I.J. (2016) Osteoblast Differentiation at a Glance. *Medical Science Monitor Basic Research*. 22 pp. 95–106. doi:10.12659/msmbr.901142.

Salwiczek, M., Qu, Y., Gardiner, J., Strugnell, R.A., Lithgow, T., McLean, K.M. and Thissen, H. (2014) Emerging rules for effective antimicrobial coatings. *Trends in Biotechnology*

[online]. 32 (2), pp. 82–90. Available from: http://dx.doi.org/10.1016/j.tibtech.2013.09.008doi:10.1016/j.tibtech.2013.09.008.

Samuelsen, Ø., Haukland, H.H., Jenssen, H., Krämer, M., Sandvik, K., Ulvatne, H. and Vorland, L.H. (2005) Induced resistance to the antimicrobial peptide lactoferricin B in Staphylococcus aureus. *FEBS Letters*. 579 (16), pp. 3421–3426. doi:10.1016/j.febslet.2005.05.017.

Sánchez-Gómez, S. and Martínez-de-Tejada, G. (2017) Antimicrobial Peptides as Anti-biofilm Agents in Medical Implants. *Current topics in medicinal chemistry* [online]. 17 (5), pp. 590–603. Available from: http://www.ncbi.nlm.nih.gov/pubmed/27411324 [Accessed 26 August 2019].

Santajit, S. and Indrawattana, N. (2016) Mechanisms of Antimicrobial Resistance in ESKAPE Pathogens *BioMed Research International* 2016. doi:10.1155/2016/2475067.

Santivañez-Veliz, M., Pérez-Silanes, S., Torres, E. and Moreno-Viguri, E. (2016) Design and synthesis of novel quinoxaline derivatives as potential candidates for treatment of multidrug-resistant and latent tuberculosis. *Bioorganic & Medicinal Chemistry Letters* [online]. 26 (9), pp. 2188–2193. Available from: https://www.sciencedirect.com/science/article/pii/S0960894X16302864doi:10.1016/J.BMCL.2016.03.066 [Accessed 13 September 2019].

Sargolzaie, N., Moeintaghavi, A. and Shojaie, H. (2017) Comparing the Quality of Life of Patients Requesting Dental Implants Before and After Implant. *The Open Dentistry Journal*. 11 (1), pp. 485–491. doi:10.2174/1874210601711010485.

Sartori, M., Giavaresi, G., Parrilli, A., Ferrari, A., Aldini, N.N., Morra, M., Cassinelli, C., Bollati, D. and Fini, M. (2015) Collagen type I coating stimulates bone regeneration and osteointegration of titanium implants in the osteopenic rat. *International Orthopaedics*. doi:10.1007/s00264-015-2926-0.

Sato, Y., Unno, Y., Ubagai, T. and Ono, Y. (2018) Sub-minimum inhibitory concentrations of colistin and polymyxin B promote Acinetobacter baumannii biofilm formation. *PloS one* [online]. 13 (3), pp. e0194556. Available from: http://www.ncbi.nlm.nih.gov/pubmed/29554105doi:10.1371/journal.pone.0194556 [Accessed 7 September 2019].

Scarborough, P., Bhatnagar, P., Wickramasinghe, K.K., Allender, S., Foster, C. and Rayner, M. (2011) The economic burden of ill health due to diet, physical inactivity, smoking, alcohol and obesity in the UK: an update to 2006-07 NHS costs. *Journal of public health (Oxford,*

England) [online]. 33 (4), pp. 527–535. Available from: http://www.ncbi.nlm.nih.gov/pubmed/21562029doi:10.1093/pubmed/fdr033 [Accessed 26 August 2019].

Schertel, A., Snaidero, N., Han, H.M., Ruhwedel, T., Laue, M., Grabenbauer, M. and Möbius, W. (2013) Cryo FIB-SEM: Volume imaging of cellular ultrastructure in native frozen specimens. *Journal of Structural Biology*. 184 (2), pp. 355–360. doi:10.1016/j.jsb.2013.09.024.

Schlenoff, J.B. (2014) Zwitteration: Coating surfaces with zwitterionic functionality to reduce nonspecific adsorption *Langmuir* 30 (32) p.pp. 9625–9636. doi:10.1021/la500057j.

Seo, C.H., Jeong, H., Furukawa, K.S., Suzuki, Y. and Ushida, T. (2013) The switching of focal adhesion maturation sites and actin filament activation for MSCs by topography of well-defined micropatterned surfaces. *Biomaterials* [online]. 34 (7), pp. 1764–1771. Available from: http://www.ncbi.nlm.nih.gov/pubmed/23219606doi:10.1016/j.biomaterials.2012.11.031 [Accessed 10 September 2019].

Seo, K., Kim, M. and Kim, D.H. (2015) Re-derivation of Young's Equation, Wenzel Equation, and Cassie-Baxter Equation Based on Energy Minimization. In: *Surface Energy*. (no place) InTech. doi:10.5772/61066.

Seo, M.-D., Won, H.-S., Kim, J.-H., Mishig-Ochir, T. and Lee, B.-J. (2012) Antimicrobial Peptides for Therapeutic Applications: A Review. *Molecules*. 17 (10), pp. 12276–12286. doi:10.3390/molecules171012276.

Seriwala, H.M., Khan, M.S., Munir, M.B., Riaz, I. bin, Riaz, H., Saba, S. and Voigt, A.H. (2016) Leadless pacemakers: A new era in cardiac pacing *Journal of Cardiology* 67 (1) p.pp. 1–5. doi:10.1016/j.jjcc.2015.09.006.

Sevilla, P., Gil, J. and Aparicio, C. (2017) Relevant Properties for Immobilizing Short Peptides on Biosurfaces. *IRBM*. doi:10.1016/j.irbm.2017.06.003.

Shah, F.A., Trobos, M., Thomsen, P. and Palmquist, A. (2016) Commercially pure titanium (cp-Ti) versus titanium alloy (Ti6Al4V) materials as bone anchored implants — Is one truly better than the other? *Materials Science and Engineering: C* [online]. 62 pp. 960–966. Available from: http://www.sciencedirect.com/science/article/pii/S0928493116300315doi:10.1016/j.msec.2016.01.032 [Accessed 7 February 2016].

Shahali, H., Hasan, J., Mathews, A., Wang, H., Yan, C., Tesfamichael, T. and Yarlagadda,

P.K.D.V. (2019) Multi-biofunctional properties of three species of cicada wings and biomimetic fabrication of nanopatterned titanium pillars. *Journal of Materials Chemistry B*. 7 (8), pp. 1300–1310. doi:10.1039/C8TB03295E.

Shi, J., Liu, Y., Wang, Y., Zhang, J., Zhao, S. and Yang, G. (2015) Biological and immunotoxicity evaluation of antimicrobial peptide-loaded coatings using a layer-by-layer process on titanium. *Scientific Reports*. 5 . doi:10.1038/srep16336.

Shively, S. and Miller, W.R. (2009) The use of HMDS (hexamethyldisilazane) to Replace Critical Point Drying (CPD) in the Preparation of Tardigrades for SEM (Scanning Electron Microscope) Imaging. *Transactions of the Kansas Academy of Science*. 112 (3–4), pp. 198–200. doi:10.1660/062.112.0407.

Shokuhfar, T., Arumugam, G.K., Heiden, P.A., Yassar, R.S. and Friedrich, C. (2009) Direct compressive measurements of individual titanium dioxide nanotubes. *ACS Nano*. doi:10.1021/nn900202x.

Sidambe, A. (2014) Biocompatibility of Advanced Manufactured Titanium Implants—A Review. *Materials* [online]. 7 (12), pp. 8168–8188. Available from: http://www.mdpi.com/1996-1944/7/12/8168/doi:10.3390/ma7128168.

Silhavy, T.J., Kahne, D. and Walker, S. (2010) The bacterial cell envelope. *Cold Spring Harbor perspectives in biology* [online]. 2 (5), pp. a000414. Available from: http://www.pubmedcentral.nih.gov/articlerender.fcgi?artid=2857177&tool=pmcentrez&rendertype=abstractdoi:10.1101/cshperspect.a000414 [Accessed 23 January 2015].

Silverman, B.M., Wieghaus, K.A. and Schwartz, J. (2005) Comparative Properties of Siloxane vs Phosphonate Monolayers on A Key Titanium Alloy. *Langmuir* [online]. 21 (1), pp. 225–228. Available from: https://pubs.acs.org/doi/10.1021/la048227ldoi:10.1021/la048227l [Accessed 8 August 2019].

Simović, B., Dapčević, A., Zdravković, J., Tasić, N., Kovač, S., Krstić, J. and Branković, G. (2019) From titania to titanates: Phase and morphological transition in less alkaline medium under mild conditions. *Journal of Alloys and Compounds*. 781 pp. 810–819. doi:10.1016/j.jallcom.2018.12.039.

Sjöström, T., Dalby, M.J., Hart, A., Tare, R., Oreffo, R.O.C.C. and Su, B. (2009) Fabrication of pillar-like titania nanostructures on titanium and their interactions with human skeletal stem cells. *Acta Biomaterialia*. 5 (5), pp. 1433–1441. doi:10.1016/j.actbio.2009.01.007.

Sjöström, T., Nobbs, A.H. and Su, B. (2016) Bactericidal nanospike surfaces via thermal

oxidation of Ti alloy substrates. *Materials Letters*. 167 pp. 22–26. doi:10.1016/j.matlet.2015.12.140.

Skovdal, S.M., Jørgensen, N.P., Petersen, E., Jensen-Fangel, S., Ogaki, R., Zeng, G., Johansen, M.I., Wang, M., Rohde, H. and Meyer, R.L. (2018) Ultra-dense polymer brush coating reduces Staphylococcus epidermidis biofilms on medical implants and improves antibiotic treatment outcome. *Acta Biomaterialia*. 76 pp. 46–55. doi:10.1016/j.actbio.2018.07.002.

Slotta, C., Storm, J., Pfisterer, N., Henkel, E., Kleinwächter, S., Pieper, M., Ruiz-Perera, L.M., Greiner, J.F.W., Kaltschmidt, B. and Kaltschmidt, C. (2018) IKK1/2 protect human cells from TNF-mediated RIPK1-dependent apoptosis in an NF-κB-independent manner. *Biochimica et Biophysica Acta (BBA) - Molecular Cell Research* [online]. 1865 (8), pp. 1025–1033. Available from: https://www.sciencedirect.com/science/article/pii/S0167488918300600doi:10.1016/J.BBAMCR.2018.04.003 [Accessed 13 September 2019].

Smart, N.J., Marshall, M. and Daniels, I.R. (2012) Biological meshes: A review of their use in abdominal wall hernia repairs *Surgeon* 10 (3) p.pp. 159–171. doi:10.1016/j.surge.2012.02.006.

Smith, D. and Starborg, T. (2019) Serial block face scanning electron microscopy in cell biology: Applications and technology *Tissue and Cell* 57 p.pp. 111–122. doi:10.1016/j.tice.2018.08.011.

Soares, J.W., Kirby, R., Doherty, L.A., Meehan, A. and Arcidiacono, S. (2015) Immobilization and orientation-dependent activity of a naturally occurring antimicrobial peptide. *Journal of peptide science : an official publication of the European Peptide Society* [online]. 21 (8), pp. 669–679. Available from: http://www.ncbi.nlm.nih.gov/pubmed/26018607doi:10.1002/psc.2787 [Accessed 7 August 2019].

Soares, P., Mikowski, A., Lepienski, C.M., Santos, E., Soares, G.A., Swinka Filho, V. and Kuromoto, N.K. (2008) Hardness and elastic modulus of TiO2 anodic films measured by instrumented indentation. *Journal of Biomedical Materials Research - Part B Applied Biomaterials*. 84 (2), pp. 524–530. doi:10.1002/jbm.b.30900.

Soliman, H.H., Maksoud, T.M.A., Elewa, I.M., Koura, M.M. and Gadelmawla, E.S. (2002) Roughness parameters. *Journal of Materials Processing Technology*. 123 (1), pp. 133–145. doi:10.1016/s0924-0136(02)00060-2.

Sommerfeld Ross, S., Tu, M.H., Falsetta, M.L., Ketterer, M.R., Kiedrowski, M.R., Horswill,

A.R., Apicella, M. a., Reinhardt, J.M. and Fiegel, J. (2014) Quantification of confocal images of biofilms grown on irregular surfaces. *Journal of Microbiological Methods*. 100 (1), pp. 111–120. doi:10.1016/j.mimet.2014.02.020.

Song, H., Jiang, H., Liu, T., Liu, X. and Meng, G. (2007) Preparation and photocatalytic activity of alkali titanate nano materials A2TinO2n+1 (A = Li, Na and K). *Materials Research Bulletin*. 42 (2), pp. 334–344. doi:10.1016/j.materresbull.2006.05.025.

Song, Z., Xu, H., Li, K., Wang, H. and Yan, H. (2005) Hydrothermal synthesis and photocatalytic properties of titanium acid H2Ti2O5·H2O nanosheets. *Journal of Molecular Catalysis A: Chemical*. 239 (1–2), pp. 87–91. doi:10.1016/j.molcata.2005.06.005.

Souza, J.C.M., Sordi, M.B., Kanazawa, M., Ravindran, S., Henriques, B., Silva, F.S., Aparicio, C. and Cooper, L.F. (2019) Nano-scale modification of titanium implant surfaces to enhance osseointegration *Acta Biomaterialia* 94 p.pp. 112–131. doi:10.1016/j.actbio.2019.05.045.

Spurr, R.A. and Myers, H. (1957) Quantitative Analysis of Anatase-Rutile Mixtures with an X-Ray Diffractometer *Analytical Chemistry* 29 (5). doi:10.1021/ac60125a006.

Stanton, A.E., Tong, X. and Yang, F. (2019) Extracellular matrix type modulates mechanotransduction of stem cells. *Acta Biomaterialia*. doi:10.1016/j.actbio.2019.06.048.

Stiefel, P., Schmidt-Emrich, S., Maniura-Weber, K. and Ren, Q. (2015) Critical aspects of using bacterial cell viability assays with the fluorophores SYTO9 and propidium iodide *BMC Microbiology* 15 (1) p.pp. 36. doi:10.1186/s12866-015-0376-x.

Stocks, S.M. (2004) Mechanism and use of the commercially available viability stain, BacLight. *Cytometry Part A*. 61 (August), pp. 189–195. doi:10.1002/cyto.a.20069.

Su, R., Bechstein, R., Sø, L., Vang, R.T., Sillassen, M., Esbjörnsson, B., Palmqvist, A. and Besenbacher, F. (2011) How the anatase-to-rutile ratio influences the photoreactivity of TiO 2. *Journal of Physical Chemistry C*. 115 (49), pp. 24287–24292. doi:10.1021/jp2086768.

Sule, P., Wadhawan, T., Carr, N.J., Horne, S.M., Wolfe, A.J. and Prüß, B.M. (2009) A combination of assays reveals biomass differences in biofilms formed by Escherichia coli mutants. *Letters in Applied Microbiology*. 49 (3), pp. 299–304. doi:10.1111/j.1472-765X.2009.02659.x.

Sun, Y., George Ndifor-Angwafor, N., Jason Riley, D. and Ashfold, M.N.R. (2006) Synthesis

and photoluminescence of ultra-thin ZnO nanowire/nanotube arrays formed by hydrothermal growth. *Chemical Physics Letters* [online]. 431 (4–6), pp. 352–357. Available from: https://www.sciencedirect.com/science/article/abs/pii/S0009261406014643?via%3Dihubdoi:10.1016/J.CPLETT.2006.09.100 [Accessed 2 September 2019].

Sun, Y., Kunc, F., Balhara, V., Coleman, B., Kodra, O., Raza, M., Chen, M., Brinkmann, A., Lopinski, G.P. and Johnston, L.J. (2019) Quantification of amine functional groups on silica nanoparticles: a multi-method approach. *Nanoscale Advances*. doi:10.1039/c9na00016j.

Svensson, S., Forsberg, M., Hulander, M., Vazirisani, F., Palmquist, A., Lausmaa, J., Thomsen, P. and Trobos, M. (2014) Role of nanostructured gold surfaces on monocyte activation and Staphylococcus epidermidis biofilm formation. *International Journal of Nanomedicine*. 9 (1), pp. 775–794. doi:10.2147/IJN.S51465.

Swiatkowska, I., Martin, N. and Hart, A.J. (2019) Blood titanium level as a biomarker of orthopaedic implant wear *Journal of Trace Elements in Medicine and Biology* 53 p.pp. 120–128. doi:10.1016/j.jtemb.2019.02.013.

Tan, X.W., Goh, T.W., Saraswathi, P., Nyein, C.L., Setiawan, M., Riau, A., Lakshminarayanan, R., Liu, S., Tan, D., Beuerman, R.W. and Mehta, J.S. (2014) Effectiveness of antimicrobial peptide immobilization for preventing perioperative cornea implant-associated bacterial infection. *Antimicrobial agents and chemotherapy* [online]. 58 (9), pp. 5229–5238. Available from: http://aac.asm.org/content/58/9/5229.fulldoi:10.1128/AAC.02859-14 [Accessed 7 January 2016].

Telli, A.E. and Doğruer, Y. (2019) Discrimination of viable and dead Vibrio parahaemolyticus subjected to low temperatures using Propidium Monoazide – Quantitative loop mediated isothermal amplification (PMA-qLAMP) and PMA-qPCR. *Microbial Pathogenesis*. 132 pp. 109–116. doi:10.1016/j.micpath.2019.04.029.

Terheyden, H., Lang, N.P., Bierbaum, S. and Stadlinger, B. (2012) Osseointegration - communication of cells. *Clinical Oral Implants Research*. doi:10.1111/j.1600-0501.2011.02327.x.

The Review on Antimicrobial Resistance (2016) The Review on Antimicrobial Resistance *Https://Amr-Review.Org/* [online]. Available from: https://amr-review.org/sites/default/files/160525_Final paper_with cover.pdfdoi:10.1016/j.jpha.2015.11.005 [Accessed 4 September 2019].

Toyofuku, M., Nomura, N. and Eberl, L. (2019) Types and origins of bacterial membrane vesicles. *Nature Reviews Microbiology* [online]. 17 (1), pp. 13–24. Available from: www.nature.com/nrmicrodoi:10.1038/s41579-018-0112-2 [Accessed 6 September 2019].

Trampuz, A. and Widmer, A. (2006) *Infections_associated_with_orthopedic_implants_Mis.pdf*.

Transparency Market Research (2017) *Dental Implants Market by Product, Material, End Users & Forecast - 2025 | Transparency Market Research*. Available from: https://www.transparencymarketresearch.com/dental-implants-market.html [Accessed 4 September 2019].

Trebse, R., Pisot, V. and Trampuz, A. (2005) Treatment of infected retained implants *Journal of Bone and Joint Surgery - Series B* 87 (2) p.pp. 249–256. doi:10.1302/0301-620X.87B2.15618.

Tripathy, A., Sen, P., Su, B. and Briscoe, W.H. (2017) Natural and bioinspired nanostructured bactericidal surfaces *Advances in Colloid and Interface Science* 248 p.pp. 85–104. doi:10.1016/j.cis.2017.07.030.

Truc, N.T., Minh, H.H., Khanh, L.L., Thuy, V.M., Van Toi, V., Van Man, T., Nam, H.C.N., Quyen, T.N. and Hiep, N.T. (2018) Modification of type I collagen on TiO2 surface using electrochemical deposition. *Surface and Coatings Technology*. doi:10.1016/j.surfcoat.2018.03.038.

Truong, V.K., Geeganagamage, N.M., Baulin, V.A., Vongsvivut, J., Tobin, M.J., Luque, P., Crawford, R.J. and Ivanova, E.P. (2017) The susceptibility of Staphylococcus aureus CIP 65.8 and Pseudomonas aeruginosa ATCC 9721 cells to the bactericidal action of nanostructured Calopteryx haemorrhoidalis damselfly wing surfaces. *Applied Microbiology and Biotechnology*. 101 (11), pp. 4683–4690. doi:10.1007/s00253-017-8205-9.

Tschang, C.-Y.T. and Thoma, M. (2019) Biofilm inactivation by synergistic treatment of atmospheric pressure plasma and chelating agents. *Clinical Plasma Medicine* [online]. 15 pp. 100091. Available from: https://www.sciencedirect.com/science/article/pii/S2212816618300374doi:10.1016/J.CPME.2019.100091 [Accessed 13 September 2019].

Tsimbouri, P. (2015) Adult Stem Cell Responses to Nanostimuli. *Journal of Functional Biomaterials*. 6 (3), pp. 598–622. doi:10.3390/jfb6030598.

Tsimbouri, P.M., Fisher, L., Holloway, N., Sjostrom, T., Nobbs, A.H., Meek, R.M.D., Su, B. and Dalby, M.J. (2016) Osteogenic and bactericidal surfaces from hydrothermal titania

nanowires on titanium substrates. *Scientific Reports* [online]. 6 (November), pp. 36857. Available from: http://www.nature.com/articles/srep36857doi:10.1038/srep36857.

Ucer, C., Wright, S., Slade, K., Drysdale, C., Feran, K., Friel, P., Henderson, S., Parker, C. and Speechley, D. (2012) *A Dentist's Guide to Implantology* C Ucer, S Wright, and K Slade (eds.). [online]. (no place) Association of Dental Implantology. [Accessed 26 August 2019].

Unosson, E., Rodriguez, D., Welch, K. and Engqvist, H. (2015) Reactive combinatorial synthesis and characterization of a gradient Ag-Ti oxide thin film with antibacterial properties. *Acta Biomaterialia*. 11 (1), pp. 503–510. doi:10.1016/j.actbio.2014.09.048.

Vanhegan, I.S., Malik, A.K., Jayakumar, P., Ul Islam, S. and Haddad, F.S. (2012) A financial analysis of revision hip arthroplasty: the economic burden in relation to the national tariff. *The Journal of bone and joint surgery. British volume* [online] 94 (5) p.pp. 619–623. Available from: http://www.bjj.boneandjoint.org.uk/content/94-B/5/619.shortdoi:10.1302/0301-620X.94B5.27073.

Vasilchenko, A.S. and Rogozhin, E.A. (2019) Sub-inhibitory Effects of Antimicrobial Peptides. *Frontiers in Microbiology* [online]. 10 pp. 1160. Available from: https://www.frontiersin.org/article/10.3389/fmicb.2019.01160/fulldoi:10.3389/fmicb.2019.01160 [Accessed 6 September 2019].

Vasilchenko, A.S., Vasilchenko, A. V., Pashkova, T.M., Smirnova, M.P., Kolodkin, N.I., Manukhov, I. V., Zavilgelsky, G.B., Sizova, E.A., Kartashova, O.L., Simbirtsev, A.S., Rogozhin, E.A., Duskaev, G.K. and Sycheva, M. V. (2017) Antimicrobial activity of the indolicidin-derived novel synthetic peptide In-58. *Journal of Peptide Science* [online]. 23 (12), pp. 855–863. Available from: http://www.ncbi.nlm.nih.gov/pubmed/29193518doi:10.1002/psc.3049 [Accessed 6 September 2019].

Vassallo, E., Pedroni, M., Silvetti, T., Morandi, S., Toffolatti, S., Angella, G. and Brasca, M. (2017) Bactericidal performance of nanostructured surfaces by fluorocarbon plasma. *Materials Science and Engineering C*. doi:10.1016/j.msec.2017.05.111.

Vasudevan, R., Kennedy, A.J., Merritt, M., Crocker, F.H. and Baney, R.H. (2014) Microscale patterned surfaces reduce bacterial fouling-microscopic and theoretical analysis. *Colloids and Surfaces B: Biointerfaces* [online]. 117 pp. 225–232. Available from: http://dx.doi.org/10.1016/j.colsurfb.2014.02.037doi:10.1016/j.colsurfb.2014.02.037.

Venault, A., Subarja, A. and Chang, Y. (2017) Zwitterionic Polyhydroxybutyrate Electrospun

Fibrous Membranes with a Compromise of Bioinert Control and Tissue-Cell Growth. *Langmuir*. 33 (9), pp. 2460–2471. doi:10.1021/acs.langmuir.6b04683.

Venkateswarlu, G., Sharada, R., M, B.R., Heavy, B., Limited, E. and Puram, R.C. (2014) Polytetrafluoroethylene (PTFE) based composites. *Journal of Chemical and Pharmaceutical Research* [online]. 6 (10), pp. 508–517. Available from: http://www.jocpr.com/articles/polytetrafluoroethylene-ptfe-based-composites.pdf [Accessed 14 September 2019].

Wang, B., Shi, S., Nan, K., Xu, Q., Ye, Z., Chen, H., Liu, H. and Wang, Z. (2017) A self-defensive antibacterial coating acting through the bacteria-triggered release of a hydrophobic antibiotic from layer-by-layer films. *Journal of Materials Chemistry B*. doi:10.1039/C6TB02614A.

Wang, C., Zhang, X., Zhang, Y., Jia, Y., Yang, J., Sun, P. and Liu, Y. (2011) Hydrothermal growth of layered titanate nanosheet arrays on titanium foil and their topotactic transformation to heterostructured TiO2 photocatalysts. *Journal of Physical Chemistry C*. 115 (45), pp. 22276–22285. doi:10.1021/jp2093719.

Wang, G., Li, J., Lv, K., Zhang, W., Ding, X., Yang, G., Liu, X. and Jiang, X. (2016a) Surface thermal oxidation on titanium implants to enhance osteogenic activity and in vivo osseointegration. *Scientific Reports*. 6 . doi:10.1038/srep31769.

Wang, G., Li, X. and Wang, Z. (2016) APD3: the antimicrobial peptide database as a tool for research and education. *Nucleic Acids Research* [online]. 44 (D1), pp. D1087–D1093. Available from: https://academic.oup.com/nar/article-lookup/doi/10.1093/nar/gkv1278doi:10.1093/nar/gkv1278 [Accessed 3 September 2019].

Wang, S., Yang, Y., Zhao, Y., Zhao, H., Bai, J., Chen, J., Zhou, Y., Wang, C. and Li, Y. (2016b) Sub-MIC Tylosin Inhibits Streptococcus suis Biofilm Formation and Results in Differential Protein Expression. *Frontiers in microbiology* [online]. 7 pp. 384. Available from: http://www.ncbi.nlm.nih.gov/pubmed/27065957doi:10.3389/fmicb.2016.00384 [Accessed 7 September 2019].

Watson, G.S., Green, D.W., Schwarzkopf, L., Li, X., Cribb, B.W., Myhra, S. and Watson, J.A. (2015) A gecko skin micro/nano structure - A low adhesion, superhydrophobic, anti-wetting, self-cleaning, biocompatible, antibacterial surface. *Acta Biomaterialia* [online]. 21 pp. 109–122. Available from: http://dx.doi.org/10.1016/j.actbio.2015.03.007doi:10.1016/j.actbio.2015.03.007.

Webb, H.K., Crawford, R.J. and Ivanova, E.P. (2014) Wettability of natural superhydrophobic

surfaces *Advances in Colloid and Interface Science* 210 p.pp. 58–64. doi:10.1016/j.cis.2014.01.020.

Webb, H.K., Truong, V.K., Hasan, J., Crawford, R.J. and Ivanova, E.P. (2011) Physico-mechanical characterisation of cells using atomic force microscopy - Current research and methodologies. *Journal of Microbiological Methods* [online]. 86 (2), pp. 131–139. Available from: http://dx.doi.org/10.1016/j.mimet.2011.05.021doi:10.1016/j.mimet.2011.05.021.

Wei, F., Li, M., Crawford, R., Zhou, Y. and Xiao, Y. (2019) Exosome-integrated titanium oxide nanotubes for targeted bone regeneration. *Acta Biomaterialia* [online]. 86 pp. 480–492. Available from: https://www.sciencedirect.com/science/article/pii/S1742706119300170doi:10.1016/J.ACTBIO.2019.01.006 [Accessed 4 September 2019].

Wennerberg, A., Jimbo, R., Stübinger, S., Obrecht, M., Dard, M. and Berner, S. (2014) Nanostructures and hydrophilicity influence osseointegration: A biomechanical study in the rabbit tibia. *Clinical Oral Implants Research*. doi:10.1111/clr.12213.

Wennerberg, A., Svanborg, L.M., Berner, S. and Andersson, M. (2013) Spontaneously formed nanostructures on titanium surfaces. *Clinical Oral Implants Research*. doi:10.1111/j.1600-0501.2012.02429.x.

Westhauser, F., Karadjian, M., Essers, C., Senger, A.S., Hagmann, S., Schmidmaier, G. and Moghaddam, A. (2019) Osteogenic differentiation of mesenchymal stem cells is enhanced in a 45S5-supplemented β-TCP composite scaffold: An in-vitro comparison of Vitoss and Vitoss BA. *PLoS ONE*. 14 (2), . doi:10.1371/journal.pone.0212799.

Widmer, A. (2006) *Clin Infect Dis.-2006-Musher-421-7* [online] p.pp. 1–7. Available from: papers://19cf457c-68ad-4d71-babe-ad8992c3079c/Paper/p286.

Williams, J.R., Clifford, A.A. and Bray, D. (2003) Critical Point Drying of Biological Specimens for Scanning Electron Microscopy. In: *Supercritical Fluid Methods and Protocols*. (no place) Humana Press. pp. 235–243. doi:10.1385/1-59259-030-6:235.

Wimley, W.C. (2010) Describing the Mechanism of Antimicrobial Peptide Action with the Interfacial Activity Model. *ACS Chemical Biology* [online]. 5 (10), pp. 905–917. Available from: http://www.ncbi.nlm.nih.gov/pubmed/20698568doi:10.1021/cb1001558 [Accessed 3 September 2019].

Wimley, W.C. and Hristova, K. (2011) Antimicrobial Peptides: Successes, Challenges and Unanswered Questions. *The Journal of Membrane Biology* [online]. 239 (1–2), pp. 27–

34. Available from: http://www.ncbi.nlm.nih.gov/pubmed/21225255doi:10.1007/s00232-011-9343-0 [Accessed 3 September 2019].

Wistrand-Yuen, E., Knopp, M., Hjort, K., Koskiniemi, S., Berg, O.G. and Andersson, D.I. (2018) Evolution of high-level resistance during low-level antibiotic exposure. *Nature Communications* [online]. 9 (1), pp. 1599. Available from: http://www.ncbi.nlm.nih.gov/pubmed/29686259doi:10.1038/s41467-018-04059-1 [Accessed 7 September 2019].

Wong, C.L., Tan, Y.N. and Mohamed, A.R. (2011) A review on the formation of titania nanotube photocatalysts by hydrothermal treatment. *Journal of Environmental Management* [online]. 92 (7), pp. 1669–1680. Available from: http://dx.doi.org/10.1016/j.jenvman.2011.03.006doi:10.1016/j.jenvman.2011.03.006.

Wronska, M.A., O'Connor, I.B., Tilbury, M.A., Srivastava, A. and Wall, J.G. (2016) Adding Functions to Biomaterial Surfaces through Protein Incorporation. *Advanced Materials*. doi:10.1002/adma.201504310.

Wu, Y.K., Cheng, N.C. and Cheng, C.M. (2019) Biofilms in Chronic Wounds: Pathogenesis and Diagnosis *Trends in Biotechnology* 37 (5) p.pp. 505–517. doi:10.1016/j.tibtech.2018.10.011.

Xu, H., Zhang, G., Xu, K., Wang, L., Yu, L., Xing, M.M.Q. and Qiu, X. (2018) Mussel-inspired dual-functional PEG hydrogel inducing mineralization and inhibiting infection in maxillary bone reconstruction. *Materials Science and Engineering: C* [online]. 90 pp. 379–386. Available from: http://www.ncbi.nlm.nih.gov/pubmed/29853103doi:10.1016/j.msec.2018.04.066 [Accessed 8 September 2019].

Xu, Q., Li, X., Jin, Y., Sun, L., Ding, X., Liang, L., Wang, L., Nan, K., Ji, J., Chen, H. and Wang, B. (2017) Bacterial self-defense antibiotics release from organic-inorganic hybrid multilayer films for long-term anti-adhesion and biofilm inhibition properties. *Nanoscale*. doi:10.1039/c7nr07106j.

Yáñez, M.A., Nocker, A., Soria-Soria, E., Múrtula, R., Martínez, L. and Catalán, V. (2011) Quantification of viable Legionella pneumophila cells using propidium monoazide combined with quantitative PCR. *Journal of Microbiological Methods*. 85 (2), pp. 124–130. doi:10.1016/j.mimet.2011.02.004.

Yao, Q., Ye, Z., Sun, L., Jin, Y., Xu, Q., Yang, M., Wang, Y., Zhou, Y., Ji, J., Chen, H. and Wang, B. (2017) Bacterial infection microenvironment-responsive enzymatically

degradable multilayer films for multifunctional antibacterial properties. *Journal of Materials Chemistry B*. doi:10.1039/c7tb02114c.

Yasir, M., Dutta, D. and Willcox, M.D.P. (2019) Comparative mode of action of the antimicrobial peptide melimine and its derivative Mel4 against Pseudomonas aeruginosa. *Scientific Reports* [online]. 9 (1), pp. 7063. Available from: http://www.nature.com/articles/s41598-019-42440-2doi:10.1038/s41598-019-42440-2 [Accessed 7 September 2019].

Yin, L.M., Edwards, M.A., Li, J., Yip, C.M. and Deber, C.M. (2012) Roles of Hydrophobicity and Charge Distribution of Cationic Antimicrobial Peptides in Peptide-Membrane Interactions. *Journal of Biological Chemistry* [online]. 287 (10), pp. 7738–7745. Available from: http://www.ncbi.nlm.nih.gov/pubmed/22253439doi:10.1074/jbc.M111.303602 [Accessed 6 September 2019].

Yu, Q., Ista, L.K. and López, G.P. (2014) Nanopatterned antimicrobial enzymatic surfaces combining biocidal and fouling release properties. *Nanoscale* [online]. 6 (9), pp. 4750–4757. Available from: http://www.ncbi.nlm.nih.gov/pubmed/24658328doi:10.1039/c3nr06497b [Accessed 13 January 2016].

Zhang, B., Wang, J. and Zhang, X. (2013) Effects of the hierarchical structure of rough solid surfaces on the wetting of microdroplets. *Langmuir*. 29 (22), pp. 6652–6658. doi:10.1021/la400800u.

Zhang, F., Shi, Z.L., Chua, P.H., Kang, E.T. and Neoh, K.G. (2007) Functionalization of titanium surfaces via controlled living radical polymerization: From antibacterial surface to surface for osteoblast adhesion. In: *Industrial and Engineering Chemistry Research*. 2007 doi:10.1021/ie070795j.

Zhang, Y. and Jordan, J.M. (2010) Epidemiology of osteoarthritis. *Clinics in geriatric medicine* [online]. 26 (3), pp. 355–369. Available from: http://www.ncbi.nlm.nih.gov/pubmed/20699159doi:10.1016/j.cger.2010.03.001 [Accessed 4 September 2019].

Zhao, W., Zhang, X., Tian, C. and Gao, Z. (2015) Analysis of Wetting Characteristics on Microstructured Hydrophobic Surfaces for the Passive Containment Cooling System. *Science and Technology of Nuclear Installations* [online]. 2015 pp. 1–6. Available from: http://www.hindawi.com/journals/stni/2015/652731/doi:10.1155/2015/652731 [Accessed 6 September 2019].

Zhou, L., Lai, Y., Huang, W., Huang, S., Xu, Z., Chen, J. and Wu, D. (2015) Biofunctionalization of microgroove titanium surfaces with an antimicrobial peptide to enhance their bactericidal activity and cytocompatibility. *Colloids and Surfaces B: Biointerfaces* [online]. 128 pp. 552–560. Available from: http://linkinghub.elsevier.com/retrieve/pii/S0927776515001423doi:10.1016/j.colsurfb.2015.03.008 [Accessed 1 August 2019].

Zhou, P., Xie, G., Liang, T., Yu, B., Aguilar, Z. and Xu, H. (2019) Rapid and quantitative detection of viable emetic Bacillus cereus by PMA-qPCR assay in milk. *Molecular and Cellular Probes* [online]. pp. 101437. Available from: https://linkinghub.elsevier.com/retrieve/pii/S0890850819301690doi:10.1016/j.mcp.2019.101437 [Accessed 22 August 2019].

Ziegler, N., Sengstock, C., Mai, V., Schildhauer, T.A., Köller, M. and Ludwig, A. (2019) Glancing-Angle Deposition of Nanostructures on an Implant Material Surface. *Nanomaterials*. doi:10.3390/nano9010060.

Zimmerli, W. (2014) Clinical presentation and treatment of orthopaedic implant-associated infection *Journal of Internal Medicine* 276 (2) p.pp. 111–119. doi:10.1111/joim.12233.

Zoch, M.L., Clemens, T.L. and Riddle, R.C. (2016) New insights into the biology of osteocalcin. *Bone* [online]. 82 pp. 42–49. Available from: http://www.ncbi.nlm.nih.gov/pubmed/26055108doi:10.1016/j.bone.2015.05.046 [Accessed 14 September 2019].

9.

APPENDICES

9.1 Lactate Dehydrogenase Assay

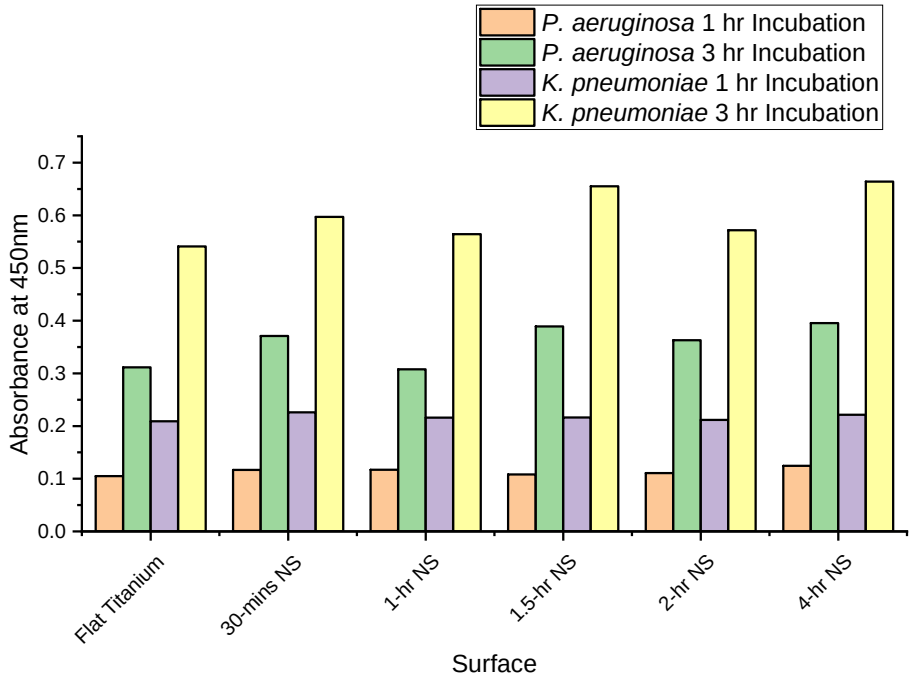

Figure 9.1- *LDH assay for P. aeruginosa and K. pneumoniae after 1-hour and 3-hours incubation on flat titanium and five nanotopographical surfaces. Disks were immersed in 400 µl bacterial inoculum for 1 or 3 hours at 37°C. Aliquots of the suspension were then removed and tested for the presence of LDH by absorbance measurements at 450 nm. N=1 in duplicate.*

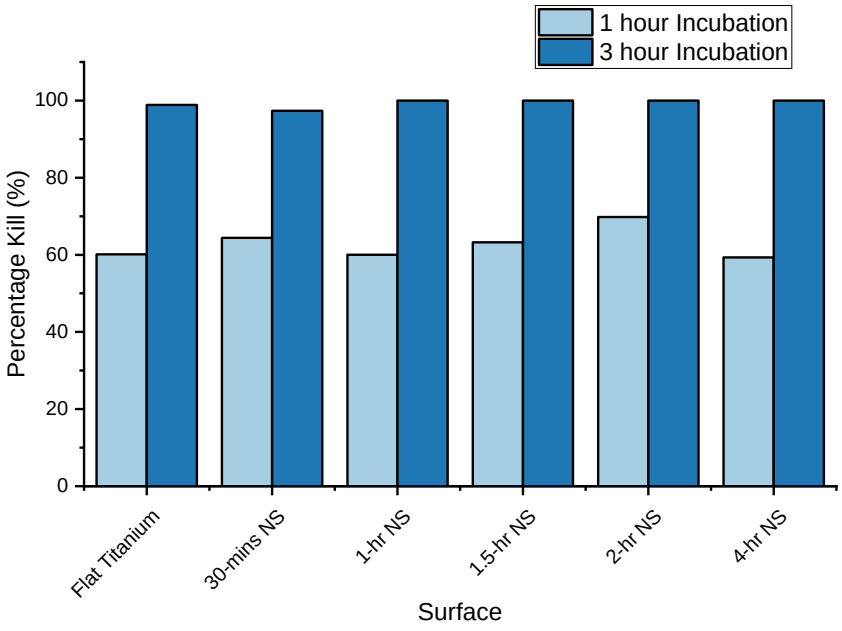

Figure 9.2- *Percentage kill for P. aeruginosa after 1- and 3-hours incubation on flat titanium and five different nanotopographical surfaces. Disks were immersed in 400 µl bacterial inoculum for 1 or 3 hours at 37°C. Aliquots of the suspension were then removed and tested for the presence of LDH by absorbance measurements at 450 nm. Values were converted to % kill against a total lysis control. N=1 in duplicate.*

9.2 RealTime-Glo

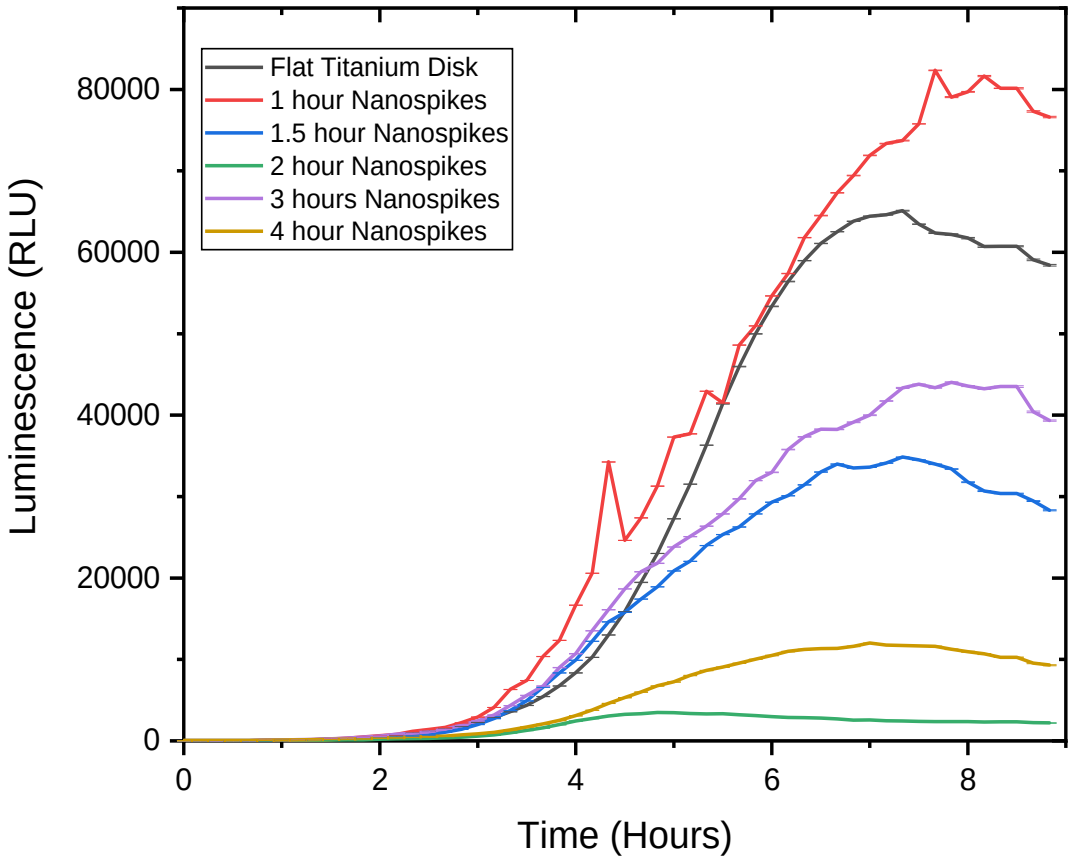

Figure 9.3- *Vitality of S. aureus on different nanotopographical surfaces as assessed by RealTime-Glo. Bacterial inocula (40 µl) containing RealTime-Glo MT Cell Viability substrate and NanoLuc enzyme were pipetted onto six different surfaces and placed into a plate reader at 37°C. Luminescence was read every 10 minutes for approximately 9 hours. N=2 in duplicate.*

9.3 Potential Delayed Release from Nanotopographical Surfaces

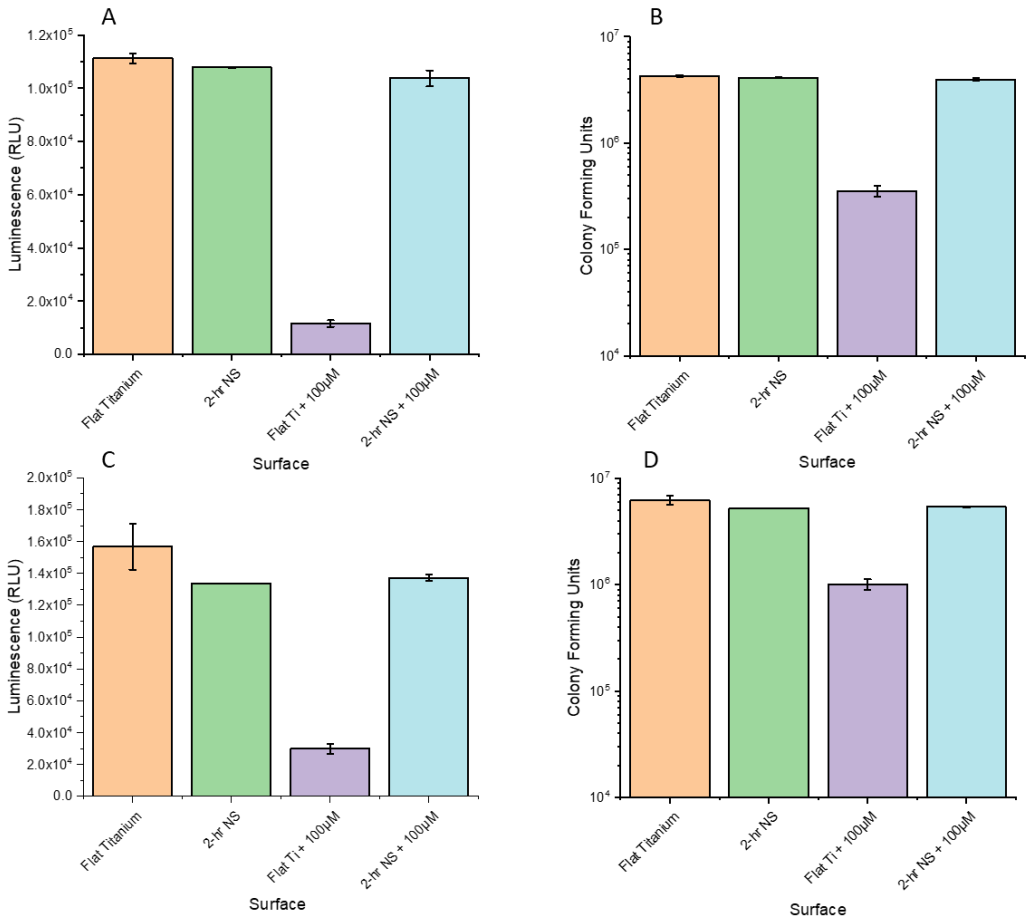

Figure 9.4- *Antibacterial activity of ChoM released over 3 and 12 hours against E. coli. ChoM (100 µM) was functionalised on flat and 2-hour nanospike disks, which were then immersed in 400 µl of MH broth. After 3 (A, C) or 12 (B, D) hours, 50 µl aliquots were recovered and mixed with a mid-exponential suspension of E. coli (10^6 CFU/ml). Samples were incubated at 37°C for 3 hours, after which the metabolic activity of the suspension was assessed by BacTiter-Glo (A, C) and luminescence values converted into viable counts (B, D). n=2 in duplicate. NS=Nanospikes.*

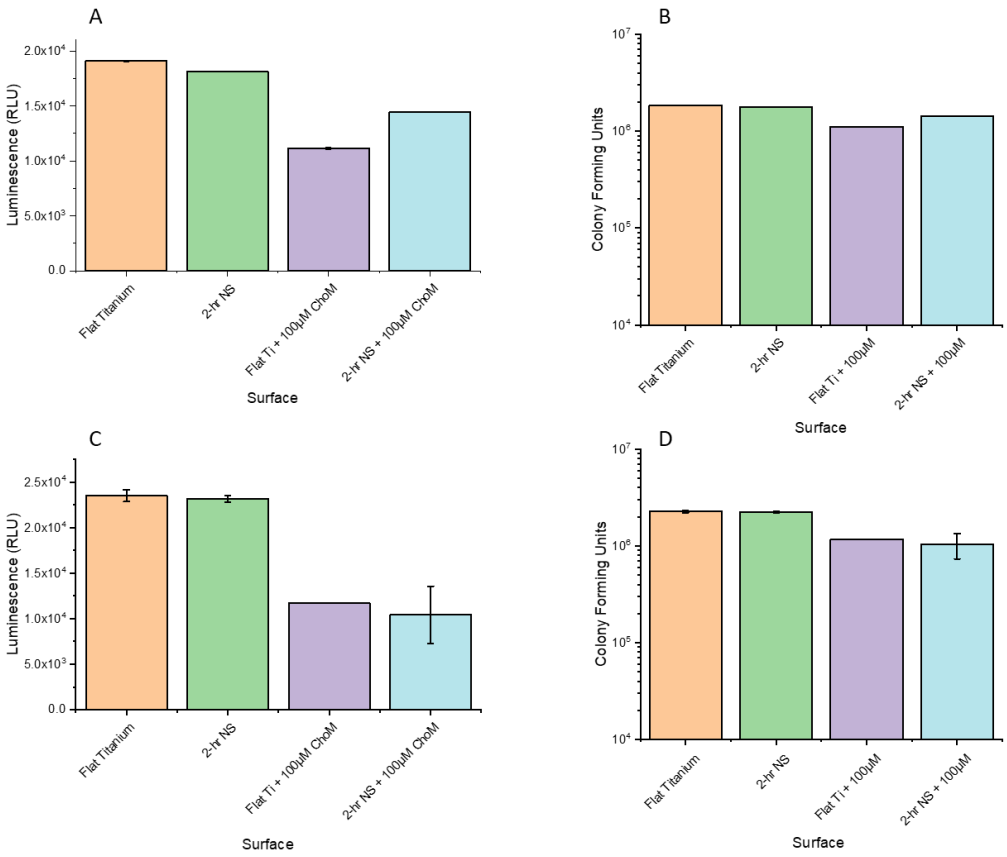

Figure 9.5- *Antibacterial activity of ChoM released over 3 and 12 hours against S. aureus. ChoM (100 µM) was functionalised on flat and 2-hour nanospike disks, which were then immersed in 400 µl of MH broth. After 3 (A, C) or 12 (B, D) hours, 50 µl aliquots were recovered and mixed with a mid-exponential suspension of S. aureus (10^6 CFU/ml). Samples were incubated at 37°C for 3 hours, after which the metabolic activity of the suspension was assessed by BacTiter-Glo (A, C) and luminescence values converted into viable counts (B, D). n=2 in duplicate. NS=Nanospikes.*

9.4 Effect of Time and Concentration of ChoM

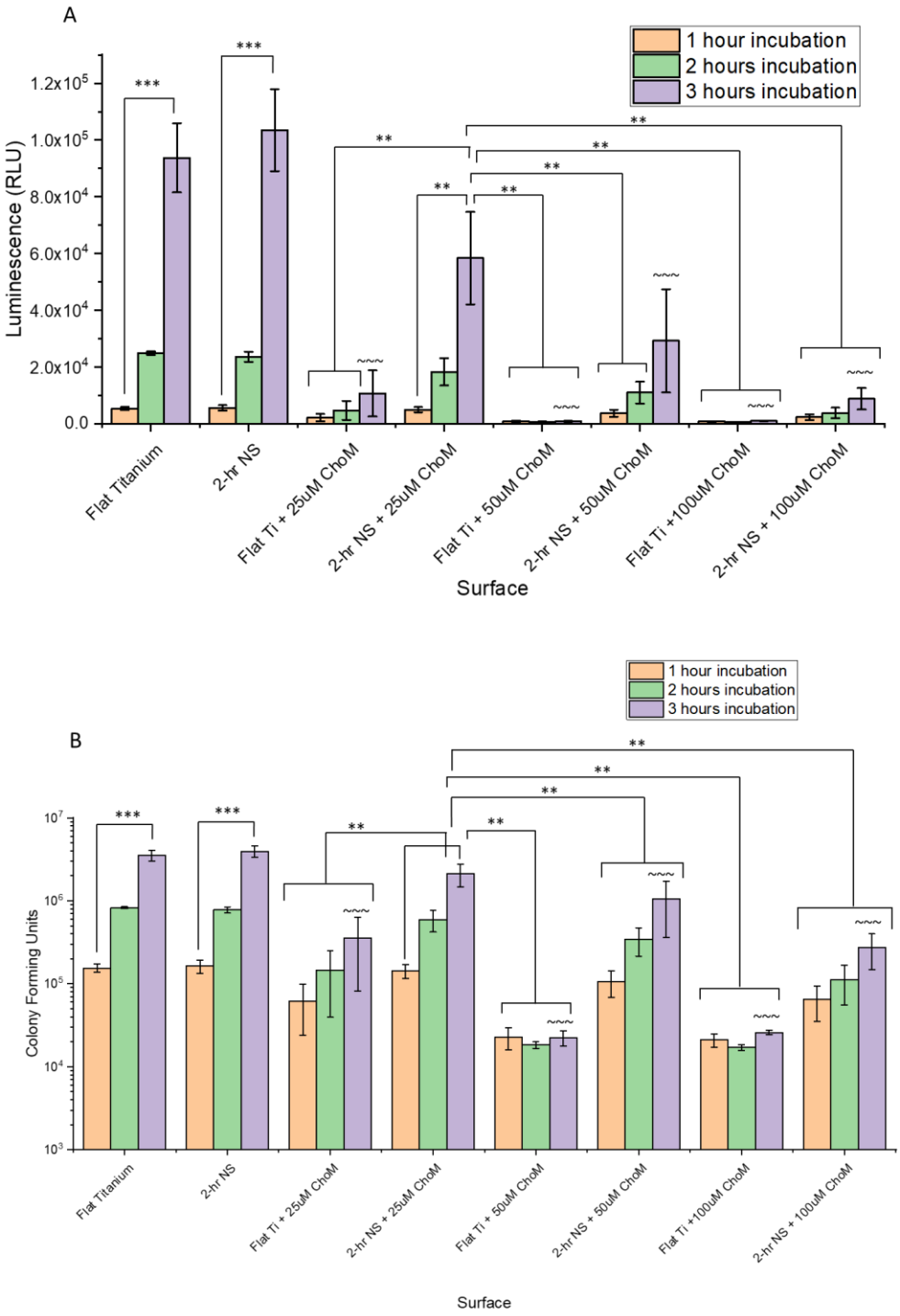

Figure 9.6- *Effects of time and concentration on the antibacterial activity of ChoM against E. coli. Flat titanium and 2-hour nanospikes were functionalised with 25/50/100 µM ChoM. E. coli (5x10^5 CFU/ml; 40 µl) was then pipetted onto the disks and incubated for 1-3 hours, after which BacTiter-Glo reagent was added, and luminescence measured (A) and converted into CFU (B). ~ =p≤0.05, ~~=p≤0.01, ~~~=p≤0.001 compared to respective control surface, and * =p≤0.05, **=p≤0.01, ***=p≤0.001 between illustrated surfaces as determined by ANOVA with post-hoc Tukey and Bonferroni tests; n=2 in duplicate. NS=Nanospikes.*

9.5 Effect of Shorter Nanotopography and Elution Environment on Peptide Release

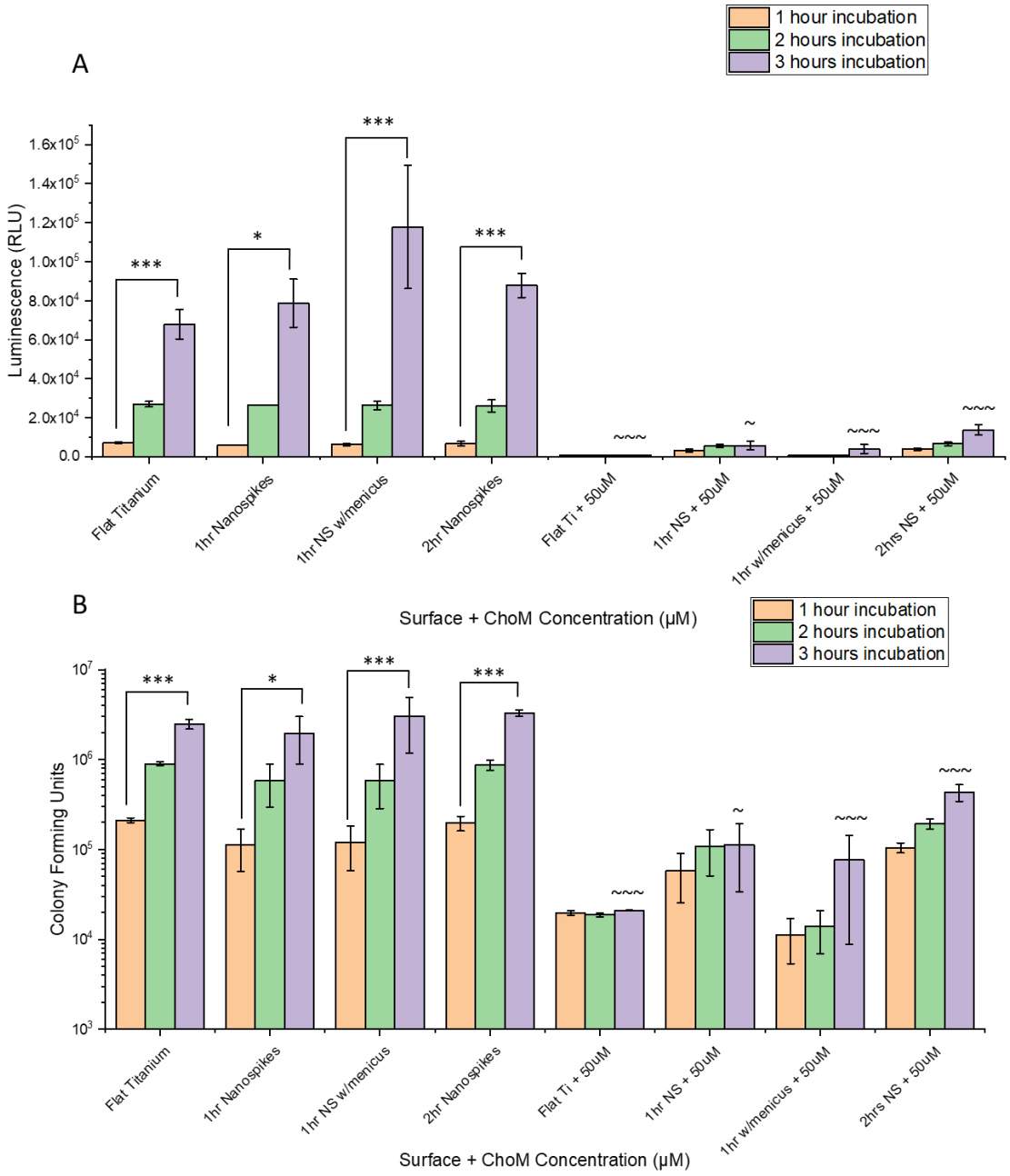

Figure 9.7- *Effects of shorter nanospikes and a meniscus environment on the antibacterial activity of ChoM against E. coli. Flat titanium, 1-hour nanospike ± meniscus and 2-hour nanospike surfaces were functionalised with 50 µM ChoM. E. coli (5x10^5 CFU/ml; 40 µl) was then pipetted onto the disks and incubated for 1-3 hours, after which BacTiter-Glo reagent was added, and luminescence measured (A) and converted into CFU (B). ~ =p≤0.05, ~~=p≤0.01, ~~~=p≤0.001 compared to respective control surface, and * =p≤0.05, **=p≤0.01, ***=p≤0.001 between illustrated surfaces as determined by ANOVA with post-hoc Tukey and Bonferroni tests; n=2 in duplicate. NS=Nanospikes.*

9.6 Effects of Disk Immersion on Peptide Release

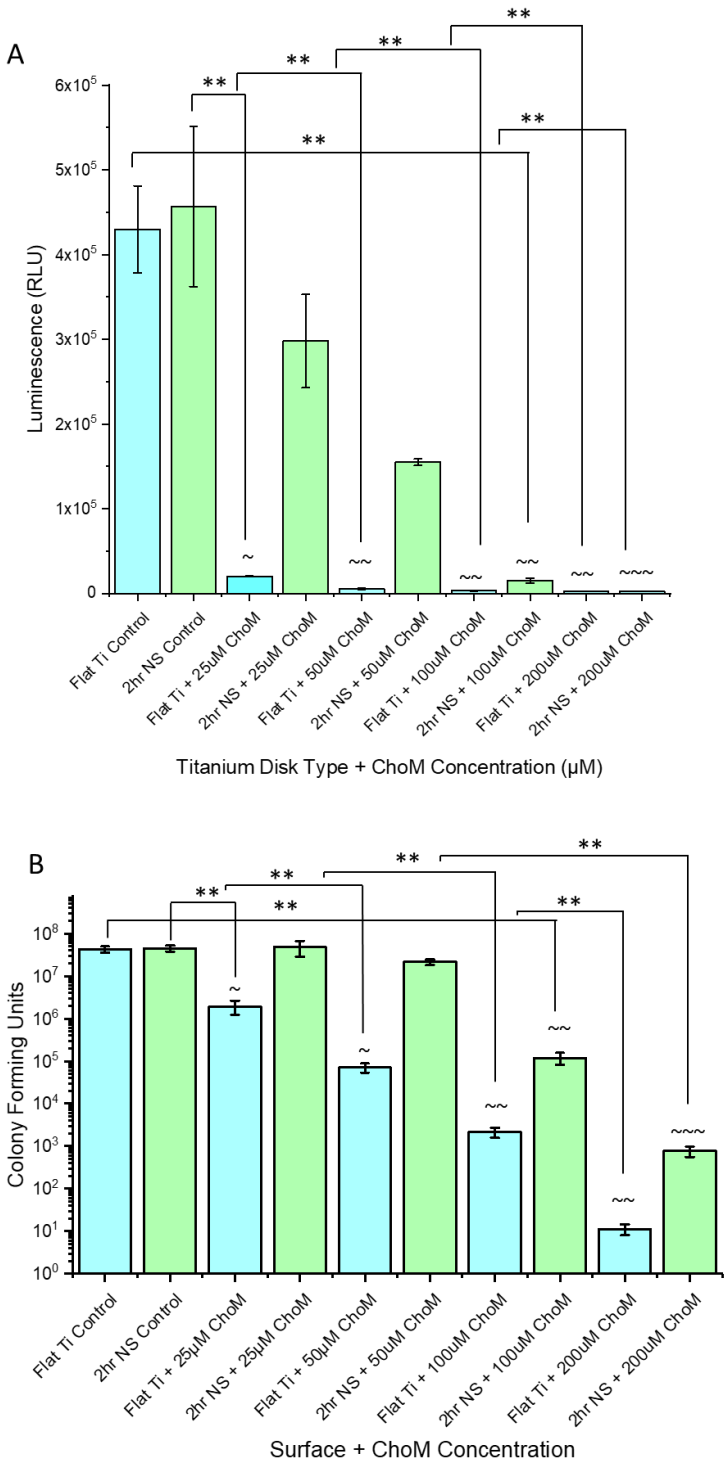

Figure 9.8- *Effects of disk immersion on the antibacterial activity of ChoM against E. coli. Flat titanium and 2-hour nanospikes were functionalised with 25/50/100/200 µM ChoM, and the disks immersed in 400 µl of E. coli suspension (5x10^5 CFU/ml) for 3 hours. Aliquots (40 µl) of the suspension were then removed and the metabolic activity of E. coli was assessed by BacTiter-Glo (A) and luminescence values converted into viable counts (B). ~ =p≤0.05, ~~=p≤0.01, ~~~=p≤0.001 compared to respective control surface, and * =p≤0.05, **=p≤0.01, ***=p≤0.001 between illustrated surfaces as determined by ANOVA with post-hoc Tukey and Bonferroni tests; n=2 in duplicate. NS=Nanospikes.*

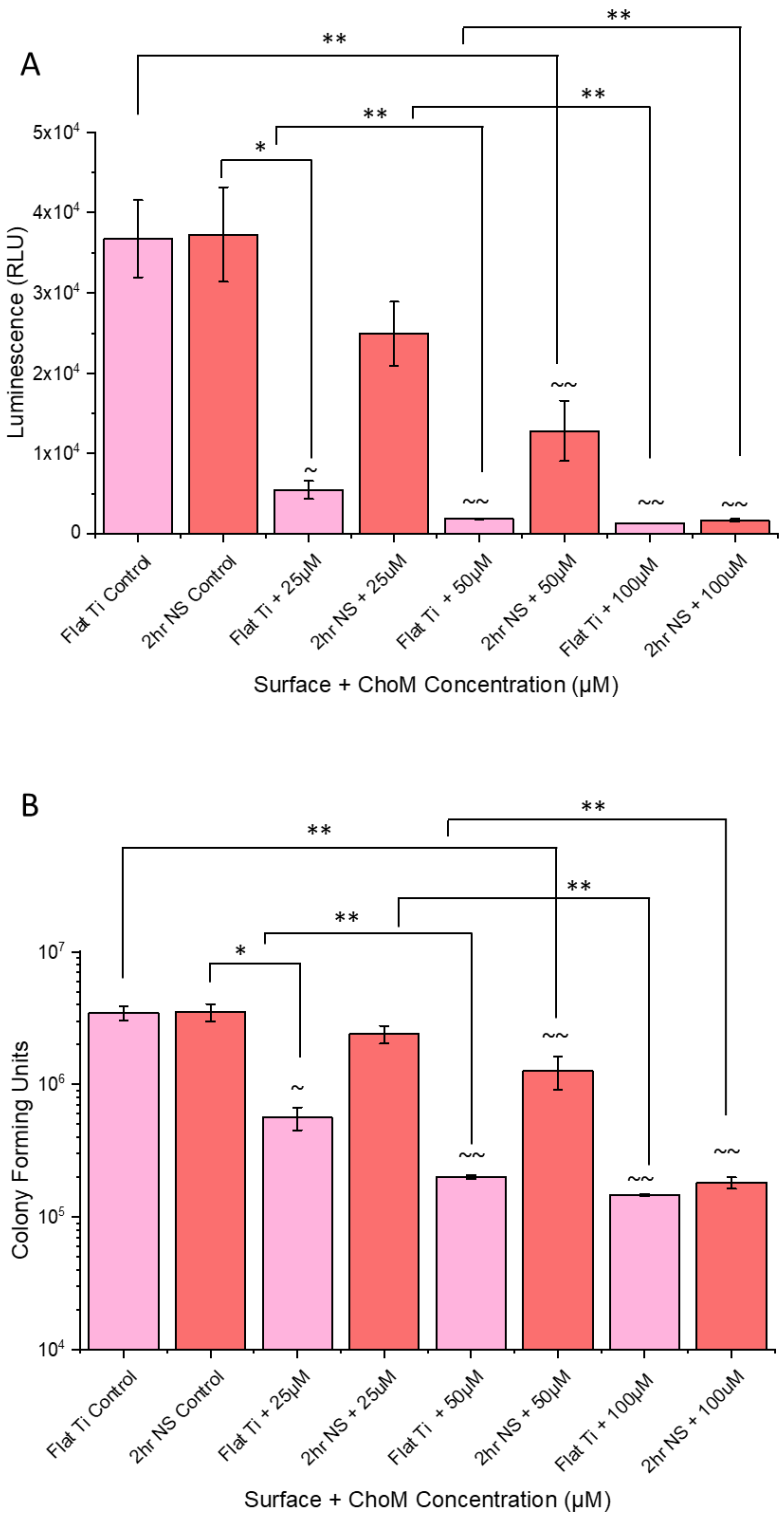

Figure 9.9- *Effects of disk immersion on the antibacterial activity of ChoM against S. aureus. Flat titanium and 2-hour nanospikes were functionalised with 25/50/100 µM ChoM, and the disks immersed in 400 µl of S. aureus suspension (5x10^5 CFU/ml) for 3 hours. Aliquots (40 µl) of the suspension were then removed and the metabolic activity of S. aureus was assessed by BacTiter-Glo (A) and luminescence values converted into viable counts (B). ~ =p≤0.05, ~~=p≤0.01, ~~~=p≤0.001 compared to respective control surface, and * =p≤0.05, **=p≤0.01, ***=p≤0.001 between illustrated surfaces as determined by ANOVA with post-hoc Tukey and Bonferroni tests; n=2 in duplicate. NS=Nanospikes.*